ELECTRONIC STRUCTURE OF PEROVSKITES AND RELATED COMPOUNDS

Thesis submitted for the degree of

Doctor of Philosophy (Science)

in

Physics (Theoretical)

by

Anita Halder

Department Physics
University of Calcutta
2019

To

my grandfather...

Acknowledgements

A journey becomes easier if you are blessed by the people around you. Here I want to take the opportunity to acknowledge all my well wishers who have supported me directly or indirectly during this long duration of my Ph.D days.

First of all I want to express my sincere gratitude to my supervisor Prof. Tanusri Saha-Dasgupta for her constant support, motivation and endless enthusiasm. Her integral view on research and her aim for providing high-quality work has always inspired me. During my years of doctoral study I have tried to learn many things from her specially her way of thinking, systematic way of handling critical problem, time management and her dedication towards science. Her guidance always helped me to keep focus. Without her continuous push I would not be able to complete my research work within limited time frame.

I would like to convey my thanks to my officiating co-supervisor Prof. Anjan Barman for his help in handling administrative related matter.

I also want to thank Dr. Prabudhha Sanyal, Prof. Sugata Ray and Prof. Karsten Held for collaborating in different projects and giving useful insights. I would like to thank Prof. Jeron van den Brink at IFW Dresden and Prof. Giorgio Sangiovanni at Wurzburg University for giving me the opportunity to visit their groups and for scientific discussions. I am really grateful to them for their help and hospitality during my stay in Germany.

I feel lucky due to my dynamic group members like Kartik, Hrishit, Dhani, Poulami, Shreya, Edwin, Aurab, Raghvendra, Shiladitya, Tilak, Sudipta and Ransell. I specially want to thank my closest senior Hrishit who has always helped me in any matter at any situation and I have learnt many computational skills from him. I also want to mention the name of one of my juniors, Shiladitya for helping me in every possible way. I am very fortunate to work with young people like Aishwarya, I would not have been able to finish my last project without his constant help and patience.

I would like to convey my acknowledgement to S. N. Bose National Centre for Basic Sciences. I spent a long time in this institute as I joined in integrated Ph.D programme in 2011. To me, this institute is like my second home. I want to thank all administrative and non academic staffs of this institute. Specially I want to thank Mr. Abhijit Ghosh for all computer related technical help. I will miss the nice library environment where I spent hours since my M.Sc days.

During my long stay in S. N. Bose, I made many good friends. Among seniors,

I have nice memories with Sreemoyee, Sunandan, Arpan, Debmalya, Subrata. I want to thank my batch mates Rakesh, Sadhu, Debasish, Sumanta, Poonam for always helping me. I had nice time with my juniors Debasmita, Suraka, Sumanti, Kajal, Indrani, Avik, Sidhartho, Debayan, Anupam, Swarnali, Sudip, Indranil, Swarup and Subhamita. I want to thank SNB mess and cooking team for providing delicious food, specially I will be going to miss breakfast menu and morning gossip.

I would like to give a special thank to Dr. Saurabh Ghosh from SRM University for his scientific discussion which have greatly enriched my knowledge.

I want to convey my regards to my school teachers Mr. Saibal Banerjee, Mr. Prankrishna Sahu, Ms. Soma Banerjee and Dr. Srimanta Sinha Roy for developing my initial interest in science.

I am very blessed that I belong from a very supportive family. I want to express my heartfelt gratitude to my family for their understanding and patience. My grandfather to whom I dedicated my thesis was my friend, philosopher and guide. I got my primary education from him. My higher education would not be possible without my parents sacrifice. My words are less to express their contribution in my life. I want to thank my uncles Sukanta and Jagabandhu for their endless support. I really enjoyed the curiosity of my little brother Sonu about my research work. I also want to thank my in-laws for being supportive.

Finally, I want to thank my best friend, my husband Sourav for being with me in my ups and downs. I always enjoy discussing basic physics with him. I really appreciate his love, patience and care for me.

Anita Halder
Kolkata, India
August, 2019.

List of Publications

1.* *Magnetism in Sr_2CrMoO_6 : A Combined Ab-initio and Model Study*, Prabuddha Sanyal, **Anita Halder**, L. Si, M. Wallerberg, K. Held and Tanusri Saha-Dasgupta, *Phys. Rev. B* **94**, 035132 (2016).

2.* *Computer Predictions on Rh-based Double Perovskites with Unusual Electronic and Magnetic Properties*, **Anita Halder**, Dhani Nafday, Prabuddha Sanyal and Tanusri Saha-Dasgupta, *npj Quantum Materials* **3**, 17 (2018).

3.* *Magnetism in Cation Disordered 3d-4d/5d Double Perovskites*, **Anita Halder**, Prabuddha Sanyal and Tanusri Saha-Dasgupta, *Phys. Rev. B (Rapid Communications)* **99**, 020402 (2019).

4.* *Machine-learning Assisted Prediction of Magnetic Double Perovskites* **Anita Halder**, Aishwaryo Ghosh and Tanusri Saha-Dasgupta. (Accepted in Phys. Rev. Materials.)

5. *Covalency driven stereochemical activity of lone pair in Pb based langasite compounds*, Rafikul Ali Saha, **Anita Halder**, Tanusri Saha-Dasgupta, Desheng Fu, Mitsuru Itoh and Sugata Ray. (Under preparation.)

Publications marked with * are reported in this thesis.

Contents

List of Figures

List of Tables

Chapter 1

Introduction

Material science is an interdisciplinary research area at the intersection of physics, chemistry and engineering which has attracted attention due to its importance in advancement of technology. A branch of this, known as material physics aims at microscopic understanding of properties of existing materials, and use of the understanding thus gained in designing of new materials. Therefore without any doubt, it is one of the most promising field of research for last few decades. The present thesis work falls in this domain.

1.1 Transition metal oxides

This thesis in particular focuses on the transition metal (TM) oxides, [1] which occur in a variety of structures and exhibit various different interesting properties. The unique nature of unfilled d shell of transition metals is responsible for their unusual electronic and magnetic properties. This class of materials is composed of metal-oxygen polyhedra, TMO_n, in which TM is surrounded by n (an integer) number of oxygens (O). Some examples of metal oxygen polyhedra are octahedra, square pyramid, square planar, tetrahedra, pentagonal bipyramid, trigonal bipyramid etc. The charge distribution of surrounding anions (O^{2-}) produces static electric field which breaks the five-fold degeneracy of the d orbitals of an isolated TM ion. The repulsive interactions between all the the electrons of TM and oxygen are not same, and this results into splitting of d orbitals, known as crystal field splitting. This splitting depends on the following factors:

- The oxidation state of transition metal. Higher the oxidation state larger is the splitting.
- The arrangement of oxygen in metal-oxygen polyhedra.
- Strength of covalancy between TM and O.

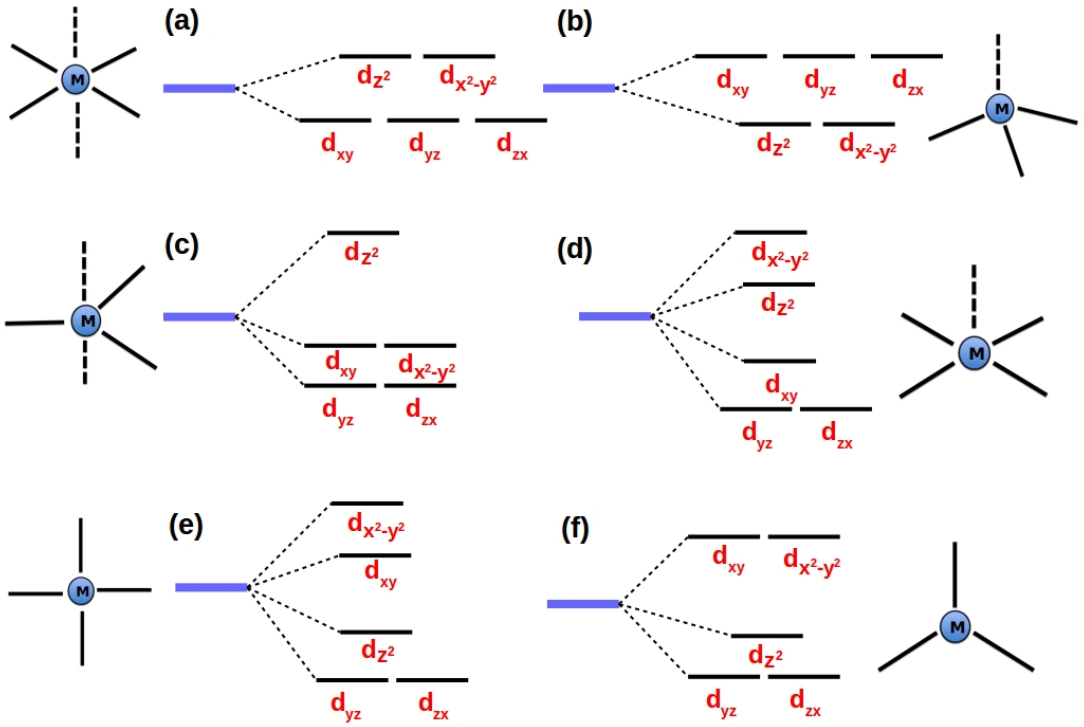

Figure 1.1: Crystal field splitting in different metal oxygen polyhedra: (a) octahedra (b) tetrahedra (c) trigonal bipyramidal (d) square pyramidal (e) square planner (f) trigonal.

The crystal field splitting provides stability, as the presence of ligand field splits d orbitals in such a way that some of them are lower in energy compared to the previous situation. The most commonly observed coordination is octahedral arrangement which is shown in panel (a) of Fig. (1.1). In this case, d orbitals split into two levels : (i) the lower level collectively known as t_{2g} which is formed by three degenerate d orbitals namely, d_{xy}, d_{xz} and d_{yz} (ii) the upper level e_g consisting of two degenerate d orbitals, $d_{x^2-y^2}$ and d_{z^2}. The electrons in the e_g orbitals feel strong electrostatic repulsion due to the electrons of O^{2-} ions, as the lobes of e_g orbitals are pointed along oxygen atoms. Thus e_g orbitals gain energy. On the other hand the lobes of d_{xy}, d_{xz} and d_{yz} in t_{2g}, are not pointed directly towards the oxygen atoms but in between two atoms. As a result, the electrons in these orbitals feel less Coulomb repulsion due to oxygen atoms and hence lower in energy with respect to e_g orbitals. If the e_g orbitals are partially occupied, then they tend to lower the energy by lifting the degeneracy of e_g. This can be

achieved by the distortion of octahedra and two corresponding vibrational modes are Q_2 and Q_3 as shown in Fig. (1.2). Such kind of structural distortion has been pointed by Hermann Jahn and Edward Teller and is known as Jahn-Teller effect. [2] In tetrahedral geometry, the situation is completely opposite to that of

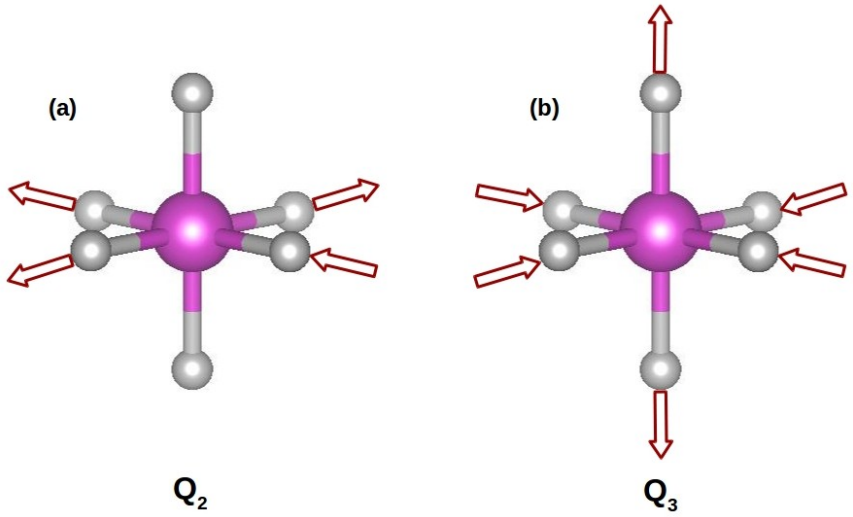

Figure 1.2: Illustration of two breathing modes (a) Q_2 and (b) Q_3 in Jahn-Teller distortion of metal oxygen octahedra.

octahedral geometry. In this case e_g orbitals are energetically lower compared to t_{2g} as shown in Fig. (1.1-b). The other possible geometry is trigonal bipyramidal [cf. Fig. (1.1-c)], which can be thought of two tetrahedral geometry merged along their common face. The two interesting coordinations are square pyramidal and square planar. The first one is with five-fold coordination number which can be obtained by removing one of the apical oxygen from octahedral geometry and the second one is with four fold coordination as obtained by removing both apical oxygens of an octahedra. The corresponding splitting are shown in Fig. (1.1-d) and (1.1-e). The energy levels corresponding to trigonal geometry with three fold coordination is shown in Fig. (1.1-f).

In transition metal oxides, the electrons at TM sites occupy the d levels in such a way, so that the total energy of the system gets minimized. The two factors on which the filling of levels depends on, are crystal field splitting (Δ) and Hund's coupling (J_H). To explain this let us consider a system with 4 electrons in regular octahedral arrangement. In this case, first three electrons will occupy three lowest lying t_{2g} levels and the fourth electron can occupy any of the doubly degenerate e_g states with parallel spin arrangement to t_{2g} or it can occupy any of t_{2g} states with opposite spin alignment. The energy gain in the first case is $E_{Hund} = -3J_H$ but it costs an amount of energy Δ due to crystal field splitting.

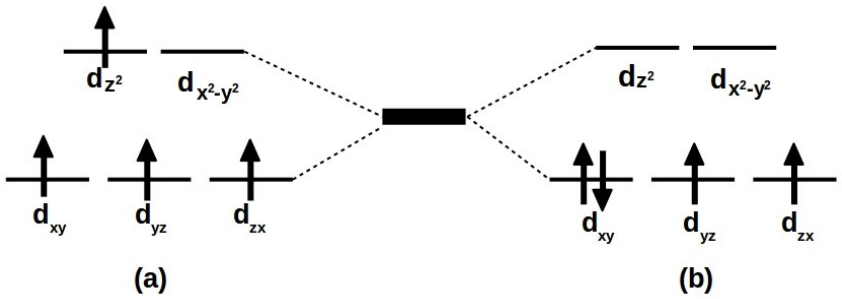

Figure 1.3: d^4 configuration in (a) high spin state when crystal field splitting $\Delta < H_{Hund}$ (b) low spin state in case of $\Delta > H_{Hund}$.

If $\Delta < 3J_H$ then then putting forth electron onto e_g level saves energy. Such kind of configurations are known as high spin state as shown in Fig. (1.3-a). On the other hand, if $\Delta > 3J_H$, the forth electron will occupy any of three t_{2g} levels with opposite spin and leads to low-spin state (Fig. (1.3-b)). The $3d$ transition metals generally favor high spin state, though there are many examples of low-spin state specially in case of late $3d$ transition metals. Some of the examples can be found in Chapter 6. On the other hand, $4d$ and $5d$ TMs are generally found in low spin state as the crystal field splittings in these cases are larger compared to $3d$ ions.

Among the transition metal oxide family, the compounds crystallizing in perovskite structure are widely studied in solid state physics and chemistry due to their interesting physical and chemical properties. The perovkites can have electronic properties ranging from insulating to metallic, superconducting or even half metallic with spin-polarized electrical conductivity. [3] The perovskites can also show magnetic ordering ranging from anti-ferromagnetic to ferro and ferrimagnetic as well as exotic spin structures. In the next section we will discuss about the structural, electronic and magnetic properties of perovskite compounds.

1.2 Perovskite compounds

This family of compounds is named after a particular mineral $CaTiO_3$. The mineral was first found by Gustav Rose in Russia in 1939 and the name was given in tribute of Russian mineralogist Lev Perovski. [4] Since then these compounds attracted considerable attention due to variety of applications in different fields.

1.2.1 Crystal structure

The general formula of perovskite compounds is ABO_3; where A: rare-earth/alkaline earth metals, B: transition metals. In perovskite, the B cations are in 6-fold co-

ordination surrounded by oxygen anions forming BO_6 octahedra and A cations in 12-fold cubo-octahedral coordinaton. The ideal form of perovskite can be described as array of corner shared BO_6 octahedra, as shown in Fig. (1.4). The void space created by eight BO_6 octahedra is occupied by a large A cation. In

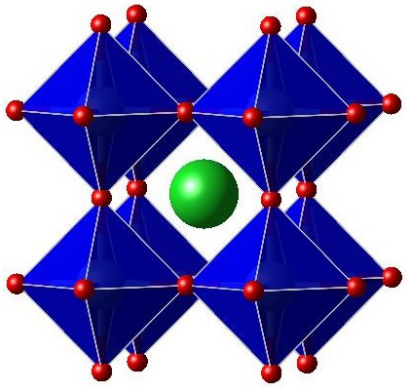

Figure 1.4: Ideal crystal structure of cubic perovskite ABO_3. Oxygen atoms are represented by small red balls, green ball indicates A cation, B transition metals are inside the blue BO_6 octahedra.

ideal perovskite compounds, the structure is cubical with ∠B-O-B of 180^o in the corner-shared geometry. However most of the perovskites are distorted. Therefore they do not have ideal cubic structure and ∠B-O-B deviates from 180^o. The distortion arises mainly due to the mismatch between A and B cation′s ionic radii.

Goldschmidt′s tolerance factor t [5] which is a dimensionless quantity that determines the stability and distortion from ideal perovskite structure. It can be estimated from the ratio of the ionic radii : $t = \frac{r_A + r_O}{\sqrt{2}(r_B + r_O)}$, where, r_A, r_B and r_O denote the ionic radii of A cation, B cation, and O^{2-} anion respectively. Cubic structure is obtained for $t = 1$ or close to 1 which is the ideal case with symmetry Pm-3m. The distorted perovskite structure with $t < 1$ leads to lowering the symmetry giving rise to space groups like Pnmm ($NaNbO_3$), Pbnm ($YAlO_3$, $DyAlO_3$, $GdFeO_3$), R3c ($BiFeO_3$) and R-3c ($BaTbO_3$, $LiTaO_3$, $LaCoO_3$) etc. [6] Within the low symmetry structures, orthorhomic $GdFeO_3$ kind of distortion where BO_6 octahedra is tilted about a and b axis and rotated about c axis is the most common one. The compounds with $t > 1$ are generally found to exhibit hexagonal symmetry.

1.2.2 Properties of Perovskites

As already mentioned, perovskite oxides show a variety of interesting physical properties. The different combinations of nominal oxidation states of A and B

cations ($A^{3+}B^{3+}$, $A^{2+}B^{4+}$, $A^{1+}B^{5+}$) drive the wide range of rich electronic and magnetic properties.

They can be insulating ($NaTiO_3$, $SrRuO_3$, $SrTiO_3$, $BaTiO_3$ etc.), metallic ($LaTiO_3$, $KMnO_3$, $LaWO_3$ etc.) or semiconducting ($LaRhO_3$, $GdTiO_3$, $CaCrO_3$ etc.). Many of these compounds undergo metal to insulator transition depending upon external factors like doping, temperature or pressure etc. One typical example is $La_{1-x}A_xMnO_3$ [7] with A = Sr, Ca or Ba. It is seen that for extreme values of x, the compounds are insulating whereas for the value of x between 0.2 and 0.4, the compounds show good electrical conductivity.

Magnetism in these compounds are generally described by superexchange mechanism. Within this mechanism hopping is mediated through the non magnetic oxygen atoms between two neighbouring transition metal sites. In this case tilting of BO_6 octahedra plays a major role. Depending upon different occupancies of d orbitals, different magnetic properties are found in this class of compounds. The compounds with d^0 configuration are generally insulators and non-magnetic ($CaTiO_3$, $BaZrO_3$, $BaHfO_3$ etc.). [8] With d^1 and d^2 configurations, the compounds are generally metallic and show Pauli paramagnetism. There is one exception in case of $GdTiO_3$ [8] which is found to be ferromagnetic semiconductor. The compounds with d^3 and d^5 electron configurations are generally conventional antiferromagnet with insulating property. The compound like $LaCoO_3$ [8] with d^6 electrons can arise in two spin states like S=0 and S=2 according to low spin and high spin configurations. $SrRuO_3$ with S=2 [9] is an example of ferromagnetic metal.

These compounds also exhibit different dielectric properties like ferroelectricity ($BaTiO_3$, $KNbO_3$ etc), piezoelectricity ($NaTiO_3$) etc. Some of the perovskite compounds also exhibit multiferroic properties like ferroelectric - ferromagnetic ($BiMnO_3$), ferroelectric - antiferromagnetic ($BiCoO_3$), antiferroelectric - antiferromagnetic ($BiFeO_3$) , ferroelectric - semiconductor ($SrTiO_3$) etc. [10]

1.3 Naturally occurring Multi component perovskites

Starting from the perovskite compounds with ABO_3 composition several different variants of perovskite family can be derived through chemical and structural modifications as shown in Fig. (1.5). This not only expands this family of compounds but also opens up possibility to engineer new compounds with desired properties. The perovskite derived compounds can be classified into three broad categories, (a) multi component perovskites including more than one elements at A or B or both A and B sites (b) $ABO_3/AB'O_3$ super lattices and (c) compounds found to be formed by partial or complete replacement of oxygen anion through mixed anion chemistry route. In this subsection we will discuss perovskite derived

multi-component compounds.

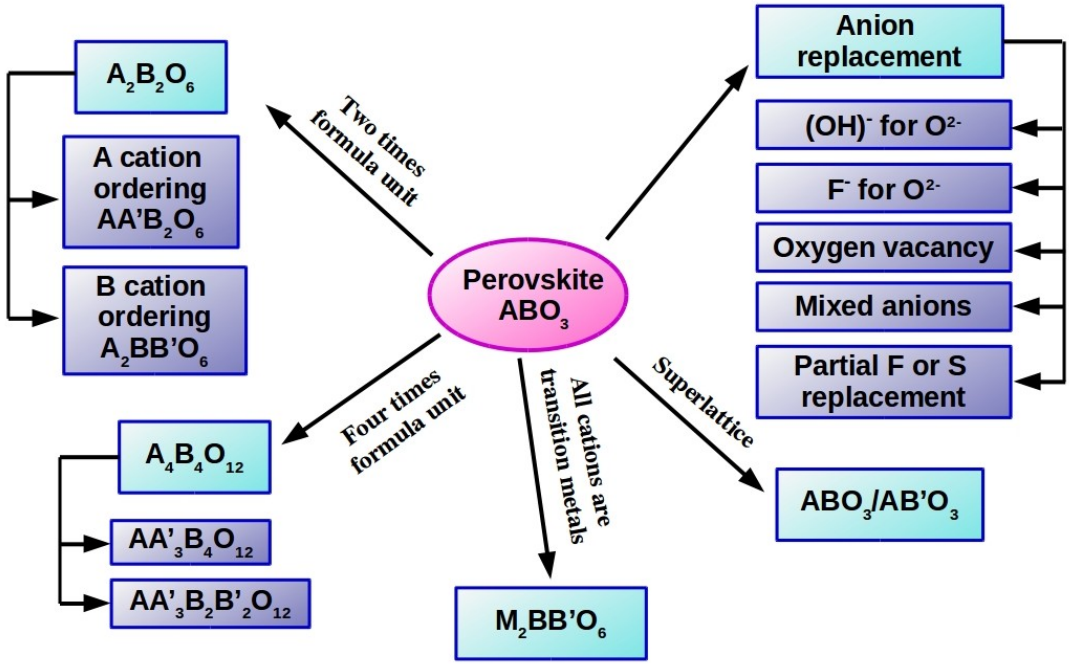

Figure 1.5: Perovskite derived compounds. The compounds can be broadly divided into three categories: multi-component perovskite compounds, superlattices and compounds obtained from anion replacement.

1.3.1 Double perovskite

The formula obtained by doubling the unit cell of perovskite is $A_2B_2O_6$, in which substitution of A or B cations in different ways helps to expand this family of compound into a large extent. Compounds can be formed by cation ordering at A site where two different A elements (A and A′) are hosted in a ordered manner giving rise to general formula $AA'B_2O_6$. Such kind of ordering is not very common in literature as the difference of the charge states between A and A′ can only have few possible values. A site ordering in $AA'B_2O_6$ is possible in three different ways [11] as illustrated in Fig. (1.6) : rock-salt, layered and columnar, among which layered ordering is favored than rock salt or columnar arrangement. On the other hand the group of compounds which are generally known as double perovskites (DP) with stoichiometry $A_2BB'O_6$ as shown in Fig. (1.7-a), which can be obtained by replacing one of the B TMs in $A_2B_2O_6$ by another TM B′, are extensively studied in this thesis. We will discuss their crystal structure and

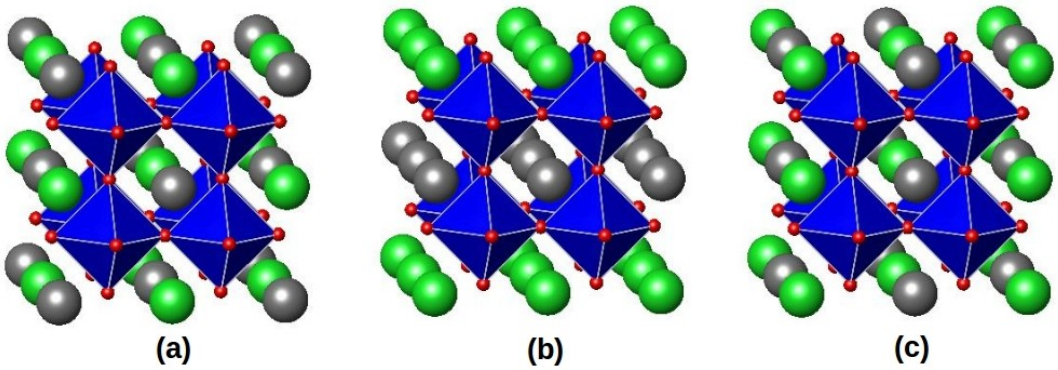

Figure 1.6: Different types of A cation ordering in perovskite compounds (a) Rock-Salt (b) Layered (c) Columnar. A and A′ cations are shown by green and grey balls respectively and oxygen atoms are represented by small red balls.

properties in detail in section 1.4. It is seen that A site ordering gets stabilized in the presence of B cation ordering in the compounds like $AA'BB'O_6$. [12]

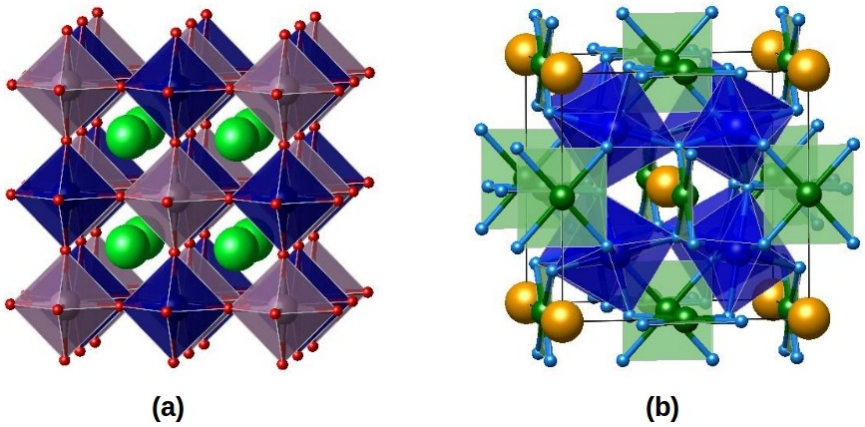

Figure 1.7: Different multicomponent perovskite compounds (a) B cation ordered double perovskite in rocksalt arrangement (b) Quadruple perovskite.

1.3.2 Quadruple perovskite

Quadrupole perovskites are four times the formula unit of simple perovskite. One interesting class of this compounds is $AA'_3B_4O_{12}$ where A cations are ordered in 1:3 ratio. In simple perovskite, A cations are generally large alkali metal ions,

whereas in quadruple perovskite one quarter of the A sites are occupied by conventional alkali metals and remaining three forth of the A sites are filled by transition metals with smaller ionic radii. Therefore one forth of the A sites are in icosahedral coordinate like in normal perovskite and rest form square planner geometry as shown in Fig. (1.7-b). This cationic mismatch at A site force to tilt the BO_6 octahedra in order to stabilize the structure. This family of compounds was first discovered by Bochu et al. [13] In recent times these compounds are studied theoretically and experimentally as it shows wide variety of structural as well as intriguing physical properties like multiferroicity, colossal magnetoresistance, intermetallic charge transfer, charge disproportionation etc. [14] The choice of magnetic ions in which Jahn teller distortion is active at A′ site is favourable for the stability of A′ cation in square planner geometry. The complex magnetic interactions between the magnetic ions at A′ and B site give rise to different interesting electronic and magnetic properties as observed in this family of compounds. Recently, both A site and B site ordered quadruple peroskites $AA'_3B_2B'_2O_{12}$ have been prepared and studied where one can combine the intriguing properties of both A site ordered quadruple perovskite and B site ordered double perovskite. In these compounds A site cations are ordered in 1:3 ratio, while B and B′ cations are corner shared and arranged in alternate manner. The compounds from this family are reported to show half metallic property with high magnetic transition temperature. [15]

1.3.3 All magnetic cations perovskite compounds

Double perovskites like Sr_2FeMoO_6 [16] with large core spin of $3d$ TM and small induced spin on $4d/5d$ TM offer ferromagnetism with high degree of spin polarized conduction. In such compounds, if one introduces magnetic cation at A site, then it is possible to increase magnetization to a large extent compared to simple double perovskite. Such a new double perovskite with all magnetic cation Mn_2FeReO_6 was reported by Attfield et al. [17] The new compound is found to be ferrimagnetic with high Curie temperature and enhanced saturation magnetization. A novel magnetoresistance switching is also discovered in this compound and thus offering new possibilities for spintronic devices. Another such example is Mn_2MnReO_6 or Mn_3ReO_6, [18] which is the first example in this family where all the transition metal cations are ordered antiferromagnetically.

1.4 B site ordered double perovskite ($A_2BB'O_6$)

As already mentioned in subsection 1.3.1, in this thesis we have extensively studied B cation ordered double perovskite with general formula $A_2BB'O_6$. In this section we provide a detailed description of the structures and properties of such

compounds. These compounds are in the limelight due to their attractive properties like multiferroicity, [19] [20] magnetodielectric and magnetocapacitive property, [21] [22] complex spin behavior, [23] magnetostructural coupling, [24] room-temperature low-field magnetoresistance [16] [25] etc. Some of them also show half-metallicity associated with high magnetic transition temperature (T_c) which is desirable for designing spintronics materials operating at room-temperature. In double perovskite $A_2BB^{'}O_6$, presence of two transition metals instead of a single transition metal as in the case of simple perovskite, enhances tunability and provides a variety of intriguing properties. Specially the DPs with one transition metal from $3d$ TM elements and another from $4d/5d$ elements are of special interest as these compounds show wide range of magnetic properties.

In this thesis, we have studied the electronic and magnetic structure of both existing and new DP compounds using combination of techniques like density functional theory (DFT) and model Hamiltonian approach. We have furthermore used genetic algorithm to predict the crystal structure of yet-to-be synthesized DP compounds as well as machine learning techniques in prediction of possible new DP compounds. In the following subsections we discuss the structural, electronic and magnetic properties of DP compounds.

1.4.1 Crystal Structure

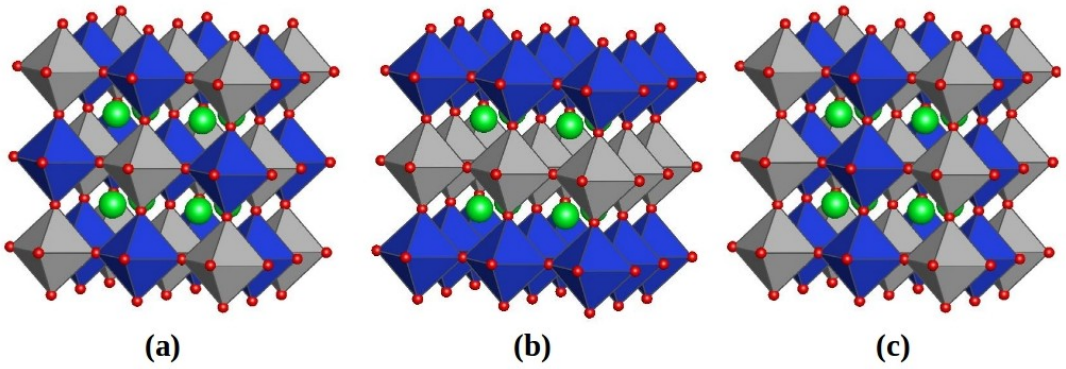

Figure 1.8: Different types of ordering of B and B′ sites in a double perovskite (a) Rock-Salt (b) Layered (c) Columnar. B and B′ centred octahedra are shown in grey and blue. A site cations and oxygen atoms are represented by green and small red balls respectivley.

In ordered double perovskites, the B and $B^{'}$ cations can be arranged in three [26] different ways:

- **Rocksalt arrangement:** This is most common arrangement as shown in Fig. (1.8-a) where BO_6 and $B'O_6$ octahedra are corner shared and alternately arranged in all three directions.

- **Layered arrangement:** In this case, BO_6 and $B'O_6$ octahedra are found in layers and they alternate only in one direction [cf. Fig. (1.8-b)]. The first observed layered DP is La_2CuSnO_6 [27] and other examples are R_2CuSnO_6 and R_2CuZnO_6 where R= Nd, Pr and Sm. [28]

- **Columnar arrangement:** The third possible arrangement is columnar like structure [cf. Fig. (1.8-c)], where B and B$'$ cations alternate in two directions. This one is rare case and has only been found when A sites are also occupied by two different elements. [11]

There are plenty of DP compounds which are synthesized and studied till the date. Fig. 1.9 shows a list of almost 800 double perovskite [26] compounds where A sites are Ca, Sr, Ba or La. Most of the compounds were synthesized in ambient pressure and some compounds required high pressure for stabilization. Several attempts were made with double perovskite stoichiometry, but either non-perovskite compounds were formed or compounds did not form. There are many possibilities left where no experimental or theoretical studies are available. We predicted many stable DP compounds out of them. The details are discussed in chapters 5 and 6.

$'A'$ cation in DP can be either divalent (examples: Sr, Ca, Ba etc.) or trivalent (examples: La, Bi). There are only three examples of monovalent A cation: Na_2ZrTeO_6 [29] synthesized in ambient pressure and Na_2BTeO_6 [30] where B = Ti/Sn formed in high pressure. Most of the DPs, around 700 in literature are found with divalent A cations. The divalent A cations are favorable than trivalent A cations due to larger size of A^{2+} compared to A^{3+}. The possible combination of oxidation states of B and B$'$ cations with a divalent A cation are B^{4+}/B'^{4+}, B^{3+}/B'^{5+}, B^{2+}/B'^{6+}, B^{1+}/B'^{7+}. So one can have the flexibility to choose B cations with oxidation states between one to seven. This leads to huge number of possibilities in case of divalent A cation compounds. Among the above mentioned combinations of B and B$'$, the B site cation ordering depends on the difference between the oxidation states of B and B$'$, $\triangle Z_{BB'}$. [27] It is found that generally $\triangle Z_{BB'} <| 2 |$ [11, 31] leads to fully disordered situation whereas the compounds are found to be ordered for $\triangle Z_{BB'} >| 2 |$. Thus complete ordering is observed in B^{2+}/B'^{6+}, B^{1+}/B'^{7+} combinations, however among the compounds of type B^{3+}/B'^{5+}, various degrees of ordering are found to be formed. The dependency of ordering on $\triangle Z_{BB'}$ can be explained in terms of Madelung energy. It is found that Madelung energy is proportion to $\triangle Z^2_{BB'}$. Hence larger $\triangle Z_{BB'}$ enhances the probability of complete cation ordering. [32] 4+/4+ combination leads to completely disordered structure in most of the cases with few exceptions. [33]

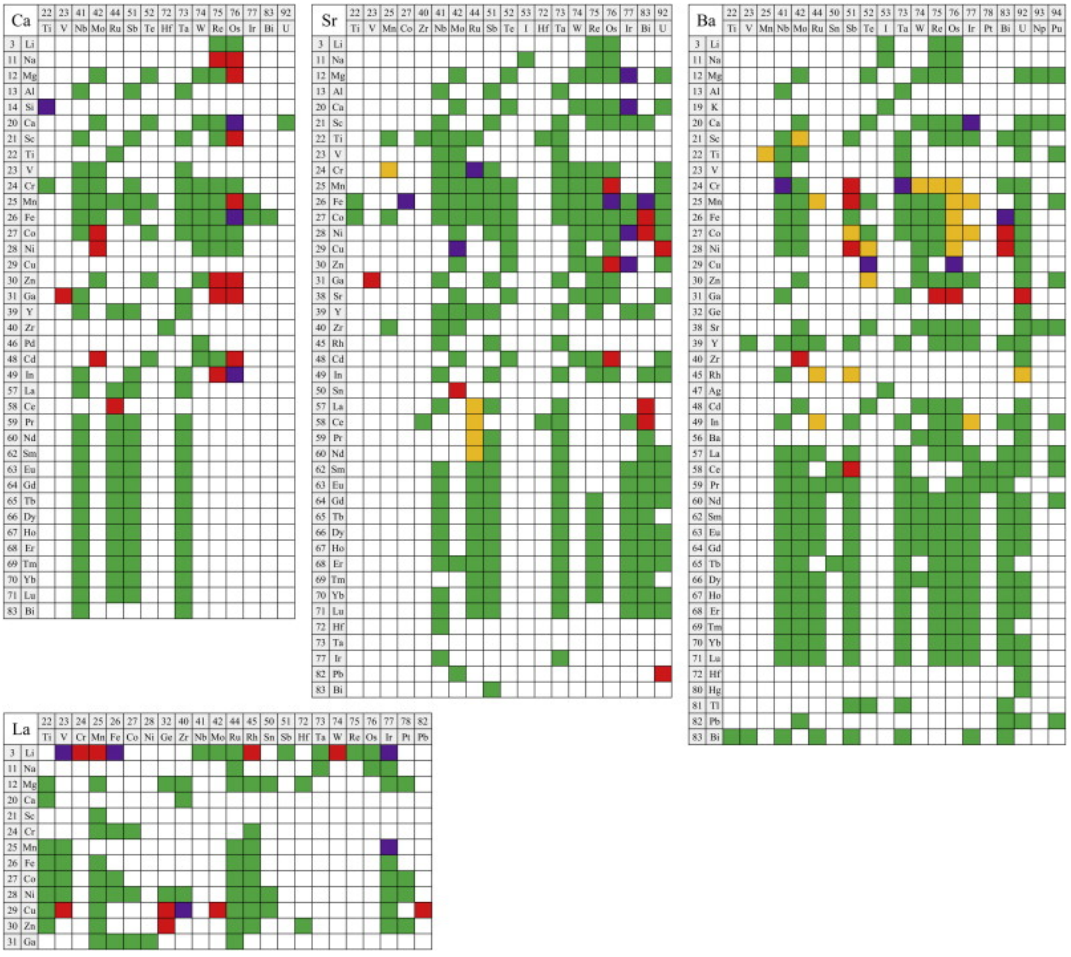

Figure 1.9: Compounds with composition $A_2BB'O_6$ reported in literature. Here, A cations are Ca, Sr, Ba and La. The green boxes represent the compounds which are double perovskites synthesized in ambient pressure, whereas the compounds which are stabilized by high pressure synthesis are marked in purple, the yellow boxes represent hexagonal nonperovskite compounds with similar stoichiometry, the red boxes indicate the compounds did not form in double perovskite structure. The figure is taken from Ref [26].

Another factor which can affect the cation ordering is the difference of ionic radii of B and B′, $\triangle r_{BB'}$. It has been observed that cation ordering is probable with large value of $\triangle r_{BB'}$. It was reported by Galasso and Darby [34] that for the compounds like $A_2B^{3+}B'^{5+}O_6$, the value of $\triangle r_{BB'}$ greater than the critical percentage 7-17%, would be favourable for ordering of B cations. Fig 1.10 and Table 1.1 show a general trend of cation ordering with ionic radius difference and charge difference.

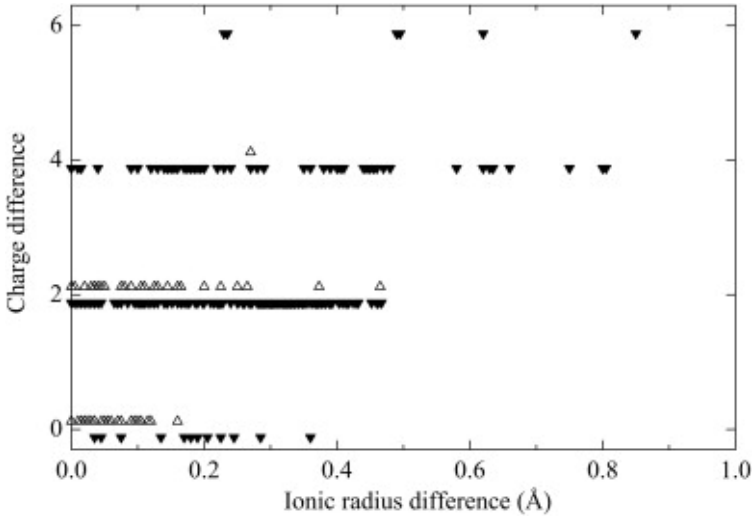

Figure 1.10: Plot of charge difference vs difference of ionic radius of B and B′ cations. The filled triangles represent ordered DP compounds and open triangles represent disordered compounds. For the sake of clarity the symbols of ordered (disordered) compounds are shifted down (up). The figure is adopted from Ref [26].

The tolerance factor t in case of DP can be defined as,

$$t = \frac{r_A + r_O}{\sqrt{2}(\frac{(r_B + r'_B)}{2} + r_O)}$$

where, r_A, r_B, $r_{B'}$ and r_O are the ionic radii [35] of A, B, B′ and O^{2-} ions respectively. The structure of an ideal DP compound is cubic with $t = 1$ or close to 1. The compounds with $t < 1$, show TM octahedra tilts which lower the symmetry of the crystal. It is seen from literature [26] that most of the compounds are found around $t \sim$ (0.93-1.01), where the ionic radii are very close to ideal case. There are very few number of compounds for $t > 1.01$. In this case the A-site cation is too large for the perovskite structure, and various non-perovskite hexagonal structures are often formed.

In rock salt arrangement, ideal cubic ordered DP has space group symmetry Fm-3m. Group theoretical work [36,37] shows that tilting of octahedra can lower the symmetry to some specific space groups. The most common space groups are cubic Fm-3m ($a^0a^0a^0$), rhombohedral R-3 ($a^-a^-a^-$), tetragonal I4/m and tetragonal I4/mmm ($a^0a^0c^-$), monoclinic $P2_1/n$ ($a^+b^-b^-$), monoclinic I2/m ($a^0b^-b^-$), with rare examples of tetragonal P4/mnc ($a^0a^0c^+$) and monoclinic I-1 ($a^-b^-c^-$). The crystal symmetry of these compounds have correspondence on the tolerance factor t as shown in Fig. (1.11), though due to large overlapping the trend is not

$\triangle Z_{BB'}$	Charge on A cation	Compound	Ordering
0	2	B^{4+}/B'^{4+}	Disordered with $\triangle r_{BB'} < 0.17$ Å. Ordered otherwise
0	3	B^{3+}/B'^{3+}	Disordered
2	1	B^{2+}/B'^{6+}	Ordered
2	2	B^{3+}/B'^{5+}	Disordered, partially ordered or ordered with increasing $\triangle r_{BB'}$
4	2	B^{2+}/B'^{6+}	Mostly highly ordered
4	3	B^{1+}/B'^{5+}	Ordered
6	2	B^{1+}/B'^{7+}	Ordered

Table 1.1: Cation ordering found in double perovskite compounds for different charge states of A, B and B′ cations. Taken from [26].

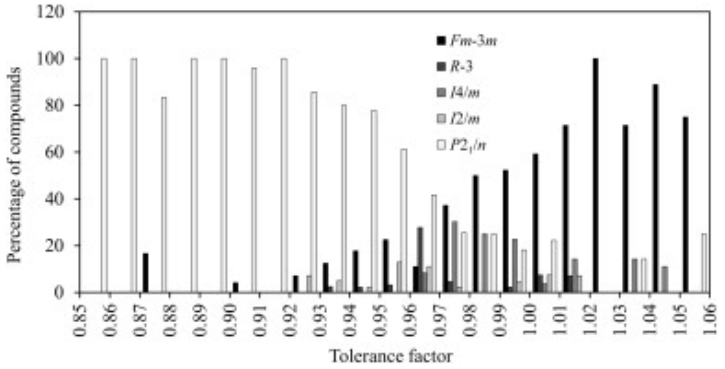

Figure 1.11: Percentage of DP compounds found with different space group symmetries as a function of tolerance factor t. [26]

very clear. In broad sense it can be concluded that the crystal is monoclinic with space group $P2_1/n$ for $t < 0.97$ and cubic having space group *Fm-3m* with $t > 0.97$. The remaining three most common symmetries are found for the intermediate values of *t*. Rhombohedral (*R-3*) structures are found at $t = 0.96$-0.97 and tetragonal ($I4/m$) at around $t = 0.97$-1.00, whereas the compounds with monoclinic space group having *I2/m* symmetry are found at slightly lower values of $t = 0.95$-0.97.

The electronic structure can also drive structural distortion in this family of compounds:

- Jahn-Teller distortion: Double perovskites having Jahn-Teller active ions like Cu^{2+} ($3d^9$; $t_{2g}^6\ e_g^3$) and Mn^{3+} ($3d^4$; $t_{2g}^3\ e_g^1$), often exhibit octahedral distortion which removes the octahedral degeneracy and helps in structure

stabilization. Coupling between Jahn-Teller distortion and octahedral tilting plays an important role, though the interaction between these two is not clearly understood. Most of the compounds where Mn is in 3+ oxidation state are disordered. However, orbital ordering is found in Sr_2MnRuO_6 and Sr_2MnSbO_6. [38] Among the Cu^{2+} based compounds, Sr_2CuMO_6, [38] where M = W, Te, Mo in rocksalt arrangement and La_2CuSnO_6 in layered arrangement are the examples where Jahn-Teller distortion is present. In Co compounds like Sr_2CoMO_6 (M = Fe, Os), [39, 40] a weak Jahn-Teller distortion is present.

- In some double perovskites, ferroelectric displacement can also lead to octahedral distortion. Presence of lone pair active cation like Pb^{2+} or Bi^{3+} at A site may drive ferroic distortion. Some examples are Bi_2NiMnO_6, [41, 42] Bi_2CoMnO_6, [41] Pb_2CoWO_6 [43] and $Pb_2MgTeWO_6$ [44] etc.

1.4.2 Disorder in double perovskites

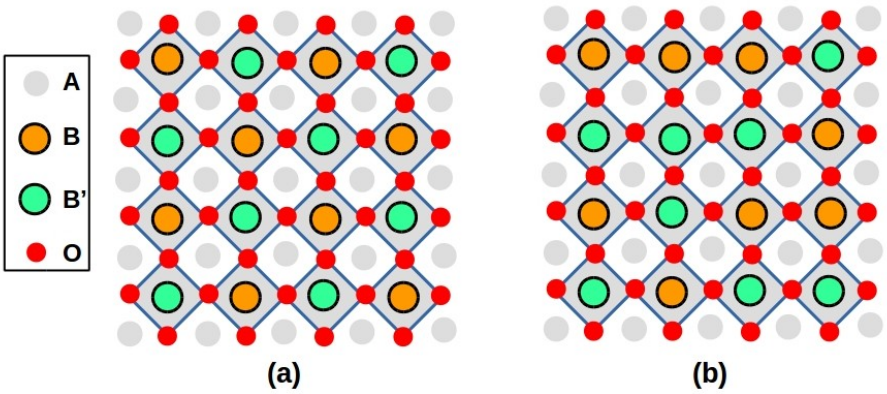

Figure 1.12: Two dimensional visualization of B and B′ cations (a) ordered situation (b) antisite disorder.

Presence of defects or imperfection which is unavoidable during experimental synthesis can affect the fascinating properties of double perovskites. The tendency of B and B′ cations to choose similar location promotes defect formation. In order to get a clear idea, let us consider a two dimensional visualization of rock salt arrangement. In perfectly ordered case B and B′ octahedra are arranged in alternate manner in all direction (Fig. (1.12-a)). In case of imperfections, the most commonly observed one is known as antisite disorder, in which some B and B′ pairs switch their positions. As a result, similar TM (either B-B or B′-B′) will become nearest neighbour as shown in Fig. (1.12-b).

There are various ways to characterize antisite disorder, one of them being,

$$disorder\% = \frac{number\,of\,wrong\,bonds\,(B - B/B' - B')}{total\,number\,of\,bonds} \times 100\%$$

Sometimes it is also defined as $S = 1 - 2x$, [45] where x is the fraction of B or B′ cations in the wrong sites. It can be easily understood that S = 1 and S = 0 correspond to perfectly ordered and completely disordered situation respectively.

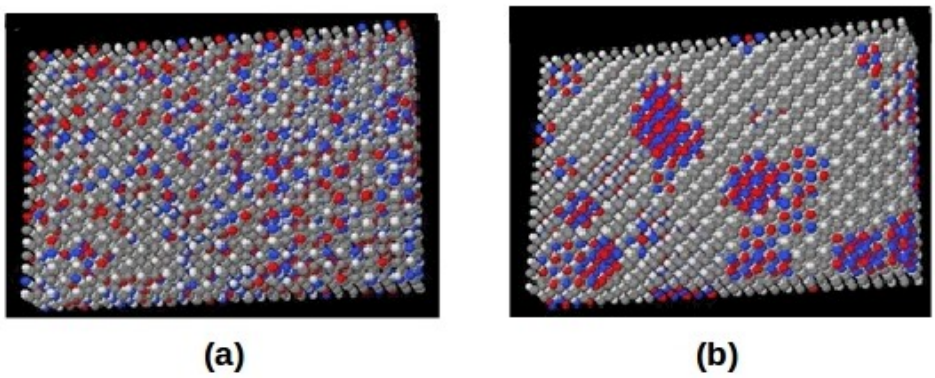

Figure 1.13: Model representation of Fe/Mo cubic lattices. (a) Homogeneous/random distribution of antisite disorder (b) small patchy domains of antisite disorder. Here the light and dark grey sites represent Fe/Mo atoms in ordered position whereas blue and red sites indicates the imperfection of Fe sites replaced by Mo sites or vice versa. The figure is adopted from Ref [47].

The wrong site occupancies of B and B′ cations can occur in a completely random manner. However, experiments showed that spatial correlation exists in antisite disordered situation, where locally ordered domains are separated from each other by antiphase boundary (APB).

Several experimental observations are available on the antisite disorder of Sr_2FeMoO_6. Navarro et al. [46] showed the existence of antiphase domains from high resolution electron microscopy study. In a different observation, Meneghini et al. [47] studied correlation of disorder on polycrystalline Sr_2FeMoO_6 sample. Fig. (1.13) shows the distribution of antisite disorder in two different situations. In Fig. (1.13-a), it is seen that disorder is homogeneous or random throughout the lattice, whereas in Fig. (1.13-b), disorder forms small patches and within the patchy domain short range ordering is present. Overall experimental observations suggest the presence local ordering in a antisite disordered sample without any long range ordering. This also supports the formation of patches or domains which are favoured than the random distribution of antisite disorder.

1.5 Properties of double perovskites

As mentioned earlier, double perovskite compounds are studied extensively due to their various interesting properties and application in the technological sector. In this section, we discuss some of their important properties.

1.5.1 Electronic properties

In double perovskite compounds, the electronic structure is mainly driven by the cations at B site. Specially the combination of $3d$ and $4d/5d$ elements gives rise to a broad range of fascinating electronic properties. The electronic property in these compounds mainly depends on two factors : intra-atomic Coulomb repulsion (U) and electronic bandwidth (w).

In case of partially occupied d orbitals, the electrons are localized if $w <$ U and the electrons are itinerant in case of $w >$ U. The band width w depends on extend of overlap of wavefunctions at two sites. Generally $3d$ TMs have narrow band width with respect to $4d/5d$ TMs. As a consequence, intra-atomic coulomb repulsion is more in $3d$ TMs and it is found to be decreased in case of $4d/5d$ TMs. So in the DP compound with $3d - 4d/5d$ combination, localized behaviour of electrons is observed in $3d$ metals at B site and electrons from $4d/5d$ metals at B$'$ site show itinerant character. In terms of crystal field splitting, $4d/5d$ TMs have large splitting than $3d$ metals. Due to the consequence of large intra-atomic repulsion and small crystal field splitting, high spin state is observed in $3d$ metals. On the other hand, due to small intra-atomic repulsion and large crystal field splitting, $4d/5d$ TMs are generally found in low spin state. In double perovskite compounds, $4d/5d$ TMs are observed with high oxidation state which results fewer electrons in d orbitals and these electrons mostly occupy lower t_{2g} levels, whereas $3d$ TMs at B site are with lower oxidation state prefer high spin symmetry. [26]

In DP compounds, sometimes unusual high oxidation state of $4d/5d$ cation at B$'$ site gets stabilized by the formation of oxygen ligand hole. In this mechanism, oxygens donate electrons to the less electro-positive B$'$ cation. Strong covalency between B$'$-O compared to B-O, effectively shifts the energy levels of d orbitals of B cation away from O p states. This enhances the overlapping between B$'$-O states and as a result, uncommon oxidation state of B$'$ cation gets stabilized, which is commonly known as inductive effect [48,49] as represented in Fig. (1.14).

The third factor which also plays important role in determining electronic state is spin orbit interaction (SOC). [50, 51] It is found that SOC is more pronounced in case of $4d/5d$ TMs compared to $3d$ TMs. Specially in the DP compounds with Ir^{4+} or Ir^{5+}, SOC is found to play a major role in determining the electronic structure. The degeneracy of t_{2g} orbitals can be lifted in presence of spin orbit interaction. [52]

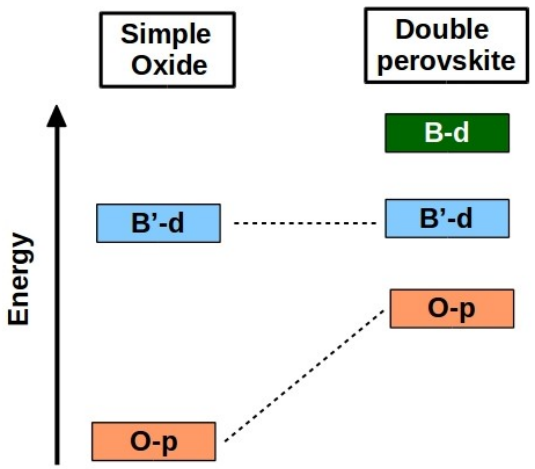

Figure 1.14: Schematic representation of stabilization of unusual valance state of B′ cation through inductive effect. [49]

1.5.2 Magnetic properties

The presence of two TM cations in double perovskite compound leads to improved magnetic properties compared to simple perovskite with single TM cation. For example Sr_2FeMoO_6 compounds exhibit a large magnetoresistance [16] making them useful for spintronics application. In double perovskites, two important interactions are 90^o nearest neighbour (NN) B-O-B and 180^o next nearest neighbour (NNN) B-O-B′-O-B. B-O-B interaction competes with long range B-O-B′-O-B interaction. Apparently one can expect short range B-O-B interaction to be dominating but in some cases like in Sr_2BOsO_6 (B = Fe, Co, Ni and Cu), [53–57] B-O-B interaction is found to be weaker. In some double perovskites specially with $3d$-$4d/5d$ combinations, mechanism of magnetism is not simple superexchange (SE) but it is governed by hybridization driven (HD) mechanism. [58] In the latter mechanism, the core spin is provided by a large spin at B site and the mobile electron is provided by the conduction electron which is oppositely aligned to the core spin and it is delocalized over B-B′ network. This mechanism was first proposed to explain the parallel alignment of Fe ions in widely discussed compound Sr_2FeMoO_6 as shown in Fig. (1.15). This mechanism is operative if the energy levels of B′ (Mo) t_{2g} fall within the exchange split B (Fe) t_{2g} energy levels. As a result of hybridization between B and B′ t_{2g} levels, a negative spin splitting develops at B′ site, which helps to stabilize the parallel arrangement of spins in B sublattices.

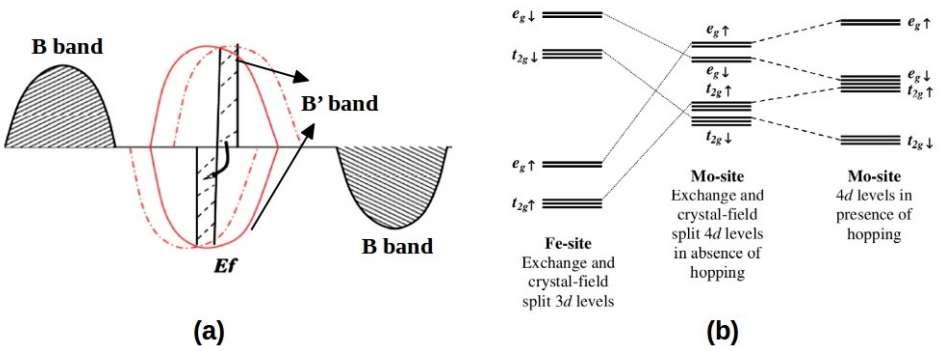

Figure 1.15: (a) Schematic representation of hybridization driven mechanism showing negative spin splitting at B′ site. The B bands are represented by shaded semicircle and B ′ bands are represented by red solid semicircle before switching on the hybridization and red dashed semicircle after switching on the hybridization. This figure is taken from Ref [59]. (b) The energy level positions for Sr_2FeMoO_6. Here Mo t_{2g} levels are placed in between the exchange split of Fe t_{2g} levels. As a result, after switching on the hybridization, Mo t_{2g} up state is pushed up and the Mo t_{2g} down state is pushed further down, which produces negative spin splitting at Mo site. (Adopted from Ref [58].)

In some compounds the mechanism of magnetism is found to be driven by combined double exchange and superexchange mechanism. [60–62] In these compounds HD mechanism is arising from coupling between large core spin and delocalized itinerant electron along with SE coupling between core spin at B site and intrinsic spin at B′ site.

The factors which can affect the magnetic properties of double perovskite materials are crystal field splitting, spatial overlap between different ions which depends on the structure, Jahn-Teller distortion, spin orbit interaction etc.

Different types of magnetic ordering have been observed in double perovskite compounds such as antiferromagnetism and ferromagnetism. In the following we provide some of the examples.

- Antiferromagnetism (AFM) : Most of the reported double perovskites are antiferromagnetic. Different types of antiferromagnetic ordering are possible in double perovskite compounds depending on the spin arrangement of B cations in the lattice. [26] Examples are La_2MgIrO_6, [63] La_2ZnIrO_6, [63] Ca_2CoTeO_6, [64] Sr_2CoTeO_6, [65] A_2MnTeO_6 (where A = Sr, Ba) [26] etc. Some compounds show weak ferromagnetism as in La_2ZnIrO_6, Sr_2ErRuO_6 etc. which is mainly due to Dzyalosky-Moriya interactions [66, 67] and spin canting. [68]

- Ferromagnetism (FM) : In some double perovskites, ferromagnetic arrangement of B cations are driven by hybridization driven mechanism, in which B and B′ cations are arranged in anti-parallel manner, examples are Sr_2CrWO_6, [60] Sr_2FeMoO_6, [58] Sr_2CrMoO_6, [61] Ca_2CrWO_6 [69] etc. These compounds are of special interest as most of them show half metallic properties with high transition temperature (T_c) as shown in Fig. (1.16) and hence useful for spintronics application. In some compounds, ferromagnetic ordering is driven by superexchange mechanism. This kind of ordering is found in the combination of Co^{2+}/Ni^{2+} and Mn^{4+}, where e_g orbitals of Co^{2+}/Ni^{2+} are partially filled and e_g orbitals of Mn^{4+} are empty driving ferromagnetism within superexchange interaction. Such compounds show low T_c, some exceptions are La_2NiMnO_6, [70–72] La_2CoMnO_6 [73] etc.

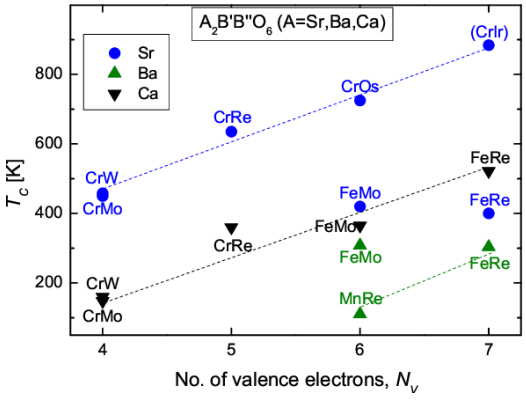

Figure 1.16: Double perovskites $A_2BB'O_6$ where B cations are from $3d$ transition metals and B′ cations are from $4d/5d$ transition metals, are reported with high transition temperature. Here A cations are Ca, Sr or Ba. The figure is taken from Ref. [74].

1.5.3 Half metallicity and magnetoresistance property

Half metallic materials [75] are promising candidate for the development of future electronic devices. Half metals offer 100% spin polarization at Fermi energy as the compounds show metallic behaviour in one spin channel and insulating behaviour in the other spin channel as illustrated in Fig (1.17). The most discussed property of double perovskite compounds is probably half metallicity. Examples are Sr_2FeMoO_6, [76, 77] Sr_2CrMoO_6, [61] Sr_2CrWO_6, [60] Sr_2CrReO_6, [60] Ba_2FeMoO_6 [78] and many more. We have also predicted some half metallic double perovskites, as discussed in chapters 5 and 6.

Magnetoresistance (MR) [79] is a well known phenomena defined as the change in electrical resistance with the application of external magnetic field. Half metals

are ideal materials as high spin polarization enhances MR value. [80]

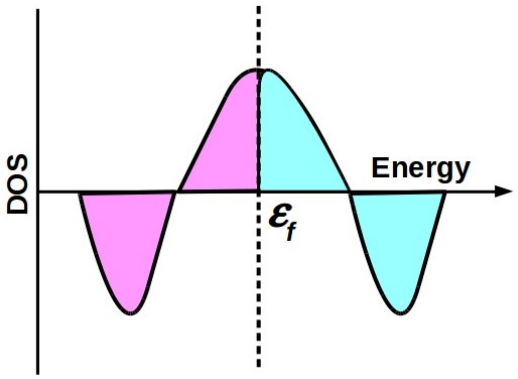

Figure 1.17: Schematic representation of half metallicity, in the up spin channel the band is crossing the Fermi energy whereas in the down spin channel a gap exists at Fermi energy.

Perhaps the most discussed double perovskite in this regard is Sr_2FeMoO_6, [58,81] which gained much attention after the discovery of significant negative tunnelling magnetoresistance (TMR) behaviour even at room temperature. The unusual magnetoresistance with high magnetic transition temperature makes this compound distinct from other perovskite compounds. The high transition temperature in this compound has been explained in terms of aforementioned hybridization driven mechanism. In the series of compounds A_2FeMoO_6, with A = Sr, Ca, Ba and Pb, [52,76] the magnetoresistance is affected by A cations. It is seen that best result is obtained for Sr and Ca compounds, and for Ba, the effect is found to be reduced. For Pb at A site, the compound is insulator. Sr_2CrWO_6 shows half metallic property and MR effect is similar to Sr_2FeMoO_6. The presence of antisite disorder can hinder half metallicity and reduce the MR effect. Another important factor is spin orbit interaction which can also effect the half metallicity, as seen in case of Sr_2FeReO_6 [82, 83] for the presence of strong SOC at Re site.

1.5.4 Superconductivity

Perovskite related layered compound La_2CuO_4 undergoes superconducting phase under temperature 33 K. Despite of the fact similar layered structure has been found in the double perovskite La_2CuSnO_6, the compound is not superconducting. The reason has been explained by Anderson et al. [84] in terms of positioning of Cu orbitals in these two compounds. However some double perovskite compounds with rock salt ordering such as $Sr_2Y(Ru_{1-x}Cu_x)O_6$ with $x = 0.05$-0.2, [85,86] show superconducting property with $T_c \approx 30$ - 40 K.

1.5.5 Dielectric and ferroelectric property

Many of the reported double perovskites are insulators and therefore can have application as dielectrics. The series of compounds as reported by Takata and kageyama [87] where A cations are Ca, Sr or Ba, B = La, Nd and Sm, and B′ = Nd or Ta show high values of dielectric constant.

Ferroelectric materials possess a spontaneous electronic polarization which can be switched by applying electric field. Though there are perovskite compounds showing ferroelectric property due the presence of lone pair at A site, only a few double perovskite compounds like $Pb_2ScB'O_6$ where B = Nb or Ta [88] to be reported as ferroelectric material. La_2NiMnO_6 and La_2CoMnO_6 [89–92] have been discussed as magnetodielectric materials. High pressure synthesis of Bi_2NiMnO_6 [19] opened the door for DPs showing multiferroicity.

1.6 Overview of present thesis

It is clearly understood from the previous section that double perovskite compounds can show variety of interesting structures and intriguing properties. First principle calculations are the best choice to understand the structures as well as the properties of these compounds at the microscopic level. A complete understanding of different magnetic ordering, charge states, orbital degrees of freedom can guide us to design new materials with desired properties. Moreover, several combinations of B and B′ have remained unexplored which may give rise to stable double perovskite compounds. Improved computational techniques and resources can help us to predict new double perovskite compounds with promising properties and can guide experimentalists for future synthesis of the compounds.

In this thesis, a variety of double perovskite compounds have been studied. The study can be divided into two broad classes. In the first part, known double perovkites are studied while the other deals with yet to be synthesized double perovskite compounds. The contents of different chapters discussed in this thesis can be summarized as follows:

Chapter 2 : In this chapter, we discuss the theoretical methodology employed in our calculations. This contains discussion on density functional theory as well as its implementation in solving many electron Hamiltonian in practice. In addition we discuss dynamical mean field theory to handle electronic correlation. We also describe genetic algorithm which has been used to predict the structure of unknown compounds. For finite temperature calculation, we used few methods such as Monte Carlo (MC) simulation and exact diagonalization along with Monte Carlo (ED-MC), which are also discussed in this chapter. Additionally, we provide a brief overview of machine learning algorithm which has been employed to scan new stable compounds from a large possibilities.

Chapter 3 : In this work, we carried out a microscopic analysis using a com-

bination of first-principles calculation and exact diagonalization study of first-principle derived model to calculate the magnetic properties of a known half-metallic double perovskite compound, Sr_2CrMoO_6, which is a sister compound of the much discussed material Sr_2FeMoO_6. The electronic structure of Sr_2CrMoO_6, which appears similar to Sr_2FeMoO_6 at a first glance, shows non trivial differences. The shift of Cr d states with respect to Fe d suppresses the hybridization between Cr t_{2g} and Mo t_{2g} driven by the change in charge transfer energy between Cr and Mo sites. This suppressed hybridization in Sr_2CrMoO_6 makes the Mo t_{2g} electrons more localized compared to Sr_2FeMoO_6. This in turn opens up an additional, super-exchange contribution to magnetism. To explain the high value of the magnetic transition temperature of Sr_2CrMoO_6 in spite of the dehybridization, additional super-exchange contribution has to be taken into account which arises due to the finite intrinsic moment developing at Mo site. We also examined the effect of correlation beyond DFT, through dynamical mean field theory (DMFT) calculations carried out in the Wannier function basis derived from DFT. The DMFT calculations confirmed the half-metallicity of Sr_2CrMoO_6, implying its robustness against correlation effect.

Chapter 4 : This particular chapter is devoted to the investigation of the effect of B site cationic disorder in a number of $A_2BB'O_6$ double perovskite compounds containing $3d$ transition metal at B sites and $4d$ or $5d$ transition metal ion at B$'$ sites. In particular we used exact diagonalization along with Monte Carlo technique to solve the first-principles derived model Hamiltonian. Our exhaustive study revealed that B cation antisite disorder influences the magnetic properties such as magnetic transition temperature and saturation magnetization, which strongly depends on the underlying mechanism of magnetism. The impact on magnetic properties is severe in the compounds where superexchange is present along with double exchange than the compounds where mechanism of magnetism is solely driven by double exchange. We further observed that it also depends on the nature of antisite disorder. Magnetism is severely affected in case of homogeneous or random disorder especially for the compounds where superexchange is present, whereas correlated or patchy disorder preserves the magnetic properties to quite a large extent even in case of extreme disorder. Finally our findings helped to solve the puzzling report of CrRu oxides, where despite of any cation ordering, the compound maintains its magnetic ordering with a high transition temperature of around 400 K.

Chapter 5 : In this chapter, our search for new magnetic materials among yet-to-be synthesized Rh based double perovskites, $Sr(Ca)_2BRhO_6$ (B = Cr, Mn, Fe) is described. For this purpose, we employed genetic algorithm to predict the crystal structure. Then using density functional theory we studied the electronic and magnetic properties of these compounds. Our study shows that all the compounds are in nominal valance state of B^{3+}/Rh^{5+} and this unusual valence of Rh^{5+} may be stabilized through the formation of oxygen ligand hole, the forma-

tion of which crucially depends on the proper description of d levels at B site. We also studied the ground state magnetic configuration of these compounds. Cr-Rh and Mn-Rh compounds are predicted to be ferromagnetic half-metals whereas the Fe-Rh compounds are rare examples of antiferromagnetic metals. Using the finite temperature Monte Carlo study of the DFT derived model Hamiltonian, we further calculated the magnetic transition temperatures of the predicted compounds, which are found to be reasonable. We also identified the favorable growth conditions through extensive thermodynamic stability analysis which might be helpful for future synthesis of these compounds.

Chapter 6 : Continuing on the same theme as in chapter 5, in this particular chapter, we provide description of our work which employ machine learning (ML) technique for screening of stable double perovskite candidates, evolutionary algorithm to predict the structure of new stable compounds and first-principles calculations for characterization of electronic and magnetic properties. We are mainly interested in prediction of yet-to-be synthesized magnetic double-perovskites with $3d$ and $4d$ or $5d$ transition metals at B and B$^{'}$ sites respectively. Initially we chose 412 B/B$^{'}$ combinations, out of which 33 compounds were scanned by ML algorithm and predicted to be formed in stable double-perovskite structure. We further considered 25 compounds among them for characterization of their structure, assigning of nominal valences of B and B$^{'}$, electronic and magnetic state, and magnetic transition temperatures. Based on our computation, we predicted 21 double-perovskites of varying magnetic and electronic properties, ranging from ferromagnetic half-metals to ferri- and antiferro-magnetic insulators to ferromagnetic metals and rare example of antiferromagnetic metals. Our computational study is expected to help in discovering new magnetic double perovskites.

Chapter 7 : In this chapter, we provide a summary of results obtained from the study of various known and yet to be synthesized double perovskite compounds. In addition, future scope of work is also discussed.

Bibliography

[1] C.N.R. Rao, *Annu. Rev. Phys. Chem*, **40**, 291-326 (1980).

[2] H. Jahn and E. Teller, Phys. Rev. **49**, 874 (1936).

[3] A.S. Bhalla, R. Guo, R. Roy, *Materials Research Innovations*, **4**, 3-26, (2000).

[4] D. G. Marc and M. E. McHenry, Structure of Materials: an introduction to crystallography, diffraction and symmetry, Cambridge University Press. ISBN 978-0-521-65151-6 (2007).

[5] Victor M. Goldschmidt, "Die Gesetze der Krystallochemie". Die Naturwissenschaften, **21**, 477- 485, (1926), Xiang Chun Liu, Rongzi Hong and Changsheng Tian, Journal of Materials Science: Materials in Electronics, **20**, 323-327 (2012).

[6] A. M. Glazer, Acta Cryst. (1972). B**28**, 3384-3392 (1972).

[7] C. Zener, Phys. Rev. **82**, 3 (1951).

[8] J. B. Goodenough, Progr. Solid State Chern. **5**, 149-399 (1971).

[9] M. Imada, A. Fujimori, Y. Tokura, Rev. Mod. Phys. **70**, 1039 (1998).

[10] L. E. Cross and R.E. Newham, History of Ferroelectrics, Ceramics and Civilization, Volume 111. (1987) by The American Ceramic Society.

[11] G. King and P. M. Woodward, J. Mater. Chem., **20**, 5785 (2010).

[12] M. C. Knapp and P. M. Woodward, Journal of Solid State Chemistry, **179**, 1076 (2006).

[13] B. Bochu , J. Chenavas, JC. Joubert, et al., J Solid State Chem., **11**, 8893 (1974).

[14] I. Yamada, Science and Technology of Advanced Materials, **18**, 541 (2017).

[15] W. Chen, M. Mizumaki, H. Seki, M. S. Senn, T. Saito, D. Kan, J. Paul Attfield and Y. Shimakawa, Nature Communications, **5**, 3909 (2014).

[16] K.-I. Kobayashi, T. Kimura, H. Sawada, K. Terakura, and Y. Tokura, *Nature (London)* **395**, 677 (1998).

[17] A. M. Arévalo-López, G. M. McNally, J. P. Attfield, Angewandte Chemie, **54**, 12074 (2015).

[18] A. M. Arévalo-López, F. Stegemanna and J. P. Attfield, Chem. Commun., **52**, 5558 (2016).

[19] M. Azuma, K. Takata, T. Saito, S. Ishiwata, Y. Shimakawa, M. Takano, *J. Am. Chem. Soc.*, **127**, 8889 (2005).

[20] Vivien S. Zapf et al., *Phys. Rev. B*, **93**, 134431 (2016).

[21] Hena Das, Umesh V. Waghmare, T. Saha-Dasgupta, D. D. Sarma, *Phys. Rev. Lett.*, **100**, 186402 (2008).

[22] Santu Baidya and T. Saha-Dasgupta *Phys. Rev. B*, **84**, 035131 (2011).

[23] S. Kanungo, B. Yan, C. Felser, M. Jansen, *Phys. Rev. B*, **93**, 161116(R) (2016)

[24] D. Yang, R. J. Harrison, J. A. Schiemer, G. I. Lampronti, X. Liu, F. Zhang, H. Ding, Y. Liu, and M. A. Carpenter, *Phys. Rev. B*, **93**, 024101 (2016).

[25] Prabuddha Sanyal, Hena Das, and T. Saha-Dasgupta, *Phys. Rev. B* **80**, 224412 (2009).

[26] S. Vasala, M. Karppinen, Prog. in Solid State Chem. **43**, 1-36 (2015).

[27] M. T. Anderson, K. R. Poeppelmeier, Chem. Mater. **3**, 476 (1991).

[28] M. Azuma, S. Kaimori, M. Takano, Chem. Mater. **10**, 3124 (1998).

[29] PJ. Saines, B. J. Kennedy, M. M. Elcombe, H. H. Harris, L -Y. Jang, Z. Zhang, J Solid State Chem **181**, 2941 (2008).

[30] J-H. Park, J.B. Parise, P.M. Woodward, I. Lubomirsky, O. Stafsudd, J Mater Res, **14**, 3192 (1999).

[31] P. M. Woodward, R. D. Hoffmann, A. J. Sleight, Mater Res **9**, 2118 (1994).

[32] E. J. Cussen, P. D. Battle, J Mater Chem **12**, 1210 (2003).

[33] C. De, Á. M. Arévalo-López, F. Orlandi, P. Manuel, J.P. Attfield and A. Sundaresan, Angew. Chem. Int. **57**, 16099 (2018).

[34] F. Galasso, W. Darby, J Phys Chem, **66**, 131 (1962).

[35] R. D. Shannon, Acta Crystallogr. A, **32** 751 (1976).

[36] P.M. Woodward, Acta Crystallogr Sect B Struct Sci, **53**, 32 (1997).

[37] C.J. Howard, B.J. Kennedy and P.M. Woodward, Acta Crystallogr Sect B Struct Sci, **59**, 463 (2003).

[38] M. W. Lufaso, P. M. Woodward, Acta Crystallogr Sect B Struct Sci, **60**, 10 (2004).

[39] R. Pradheesh, H. Nair, V. Sankaranarayanan, K. Sethupathi., Eur Phys J B Condens Matter, **85**, 1 (2012).

[40] R. Morrow, R. Mishra, O.D. Restrepo, M. R. Ball, W. Windl, S. Wurmehl, et al. J Am Chem Soc **135**, 18824 (2013).

[41] K. Takata, M. Azuma, Y. Shimakawa, M. Takano, J Jpn Soc Powder Powder Metall **52**, 913 (2005).

[42] M. Azuma, K. Takata, T. Saito, S. Ishiwata, Y. Shimakawa, M. Takano, J Am Chem Soc **127**, 8889 (2005).

[43] G. Baldinozzi, G. Calvarin, P. Sciau, D. Grebille, E. Suard, Acta Crystallogr Sect B Struct Sci **56**, 570 (2000).

[44] Y. Y. Tomashpolśkii, E. V. Zubova, K. P. Burdina, Y. N. Venevtsev, Sov Phys Crystallogr **13**, 859 (1969).

[45] The impact of antisite disorder on magnetism and transport in the double perovskites, Viveka Nand Singh, Harish-Chandra Research Institute, Allahabad, June 2012.

[46] J. Navarro, L. Balcells, F. Sandiumenge, M. Bibes, A. Roig, B. Martnez, and J. Fontcuberta, J. Phys. Cond. Matt. **13**, 8481 (2001).

[47] C. Meneghini, S. Ray, F. Liscio, F. Bardelli, S. Mobilio, and D. D. Sarma, Phys. Rev. Lett. **103**, 046403 (2009).

[48] J. Etourneau, J. Portier, F. Ménil, J. Alloys Compd., **188**, 1-7 (1992).

[49] Joshua A. Kurzman, Solid state chemistry of platinum group and noble metal oxides: Implications for heterogeneous catalysis, University of California, Santa Barbara. Chemistry, (2011).

[50] B. C. Jeon, C. H. Kim, S. J. Moon, W. S. Choi, H. Jeong, Y. S. Lee, et al. J. Phys. Condens. Matter. **22**, 345602 (2010).

[51] J. H. Choy, D. K. Kim, J. Y. Kim, Solid State Ionics **108**, 159 (1998).

[52] G. Cao, T. F. Qi, L. Li, J. Terzic, S. J. Yuan, L. E. DeLong, et al. Phys. Rev. Lett. **112**, 56402 (2014).

[53] A. K. Paul, M. Reehuis, V. Ksenofontov, B. Yan, A. Hoser, D. M. Tobbens, P. M. Abdala, M. Jansen, C. Felser, P. Adler, Phys. Rev. Lett. **111**, 167205 (2013).

[54] R. Morrow, J. W. Freeland, P. M. Woodward, Inorg. Chem. **53**, 7983-7992 (2014).

[55] R. Morrow, R. Mishra, O. R. Restrepo, M. R. Ball, W. Windl, S. Wurmehl, U. Stockert, B. Bchner, P. M. Woodward, J. Am. Chem. Soc. **135**, 18824-18830 (2013).

[56] R. Macquart, S. J. Kim, W. R. Gemmill, J. K. Stalick, Y. Lee, T. Vogt, H. C. Zur Loye, Inorg. Chem. **44**, 9676-9683 (2005).

[57] M. W. Lufaso, W. R. Gemmill, S. J. Mugavero, S. J. Kim, Y. Lee, T. Vogt, H. C. zur Loye, J. Solid State Chem. **181**, 623-627 (2008).

[58] D. D. Sarma, P. Mahadevan, T. Saha-Dasgupta, S. Ray, and A. Kumar, Phys. Rev. Lett. **85**, 2549 (2000).

[59] T. Saha-Dasgupta, J Supercond Nov Magn **26**, 1991 (2013).

[60] H. Das, P. Sanyal, T. Saha-Dasgupta and D.D. Sarma, *Phys. Rev. B*, **83**, 104418 (2011).

[61] P. Sanyal, A. Halder, Liang Si, M. Wallerberger, K. Held and T. Saha-Dasgupta, Phys. Rev. B. **94**, 035132 (2016).

[62] A. Halder, P. Sanyal and T. Saha-Dasgupta, Phys. Rev. B, **99**(R), 020402 (2019).

[63] G. Cao, A. Subedi, S. Calder, J. Q. Yan, J. Yi, Z. Gai, L. Poudel, D. J. Singh, M. D. Lumsden, A. D. Christianson, B. C. Sales, D. Mandrus, Phys. Rev. B **87**, 155136 (2013).

[64] L. Martin Ortega-San, J. P. Chapman, L. Lezama et al. J Mater Chem **15**, 183 (2005).

[65] M. S. Augsburger, M. C. Viola, J. C. Pedregosa et al. J Mater Chem **15**, 993 (2005).

[66] I. Dzyaloshinskii, Journal of Physics and Chemistry of Solids **4**, 241 (1958).

[67] T. Moriya, Physical Review **120**, 91 (1960).

[68] Q. Lin, M. Greenblatt, M. Croft, J. Solid State Chem. **178**, 1356 (2005).

[69] P. Majewski, S. Gepraegs, A. Boger, M. Opel, A. Erb, R. Gross, G. Vaitheeswaran, V. Kanchana, A. Delin, F. Wilhelm, A. Rogalev, L. Alff, Phys. Rev. B, **72**, 132402 (2005).

[70] H. Das, U. V. Waghmare, T. Saha-Dasgupta, and D. D. Sarma, Phys. Rev. B, **79**, 144403 (2009).

[71] H. Das, U. V. Waghmare, T. Saha-Dasgupta, and D. D. Sarma, Phys. Rev. Lett. **100**, 186402 (2008).

[72] S. F. Mater, M. A. Subramanian, A. Villesuzanne, V. Eyert,and M. H. Whangbo, J. Magn. Magn. Mater. **308**, 116 (2007).

[73] S. Baidya and T. Saha-Dasgupta, Phys. Rev. B **84**, 035131 (2011).

[74] T. K. Mandal, C. Felser, M. Greenblatt and Jrgen Kbler, Phys. Rev. B **78**, 134431 (2008).

[75] J. M. D. Coey, M. Venkatesan, J. Appl. Phys. **91**, 8345 (2002).

[76] D. Serrate, J. M. De Teresa and M. R. Ibarra, J. Phys.: Condens. Matter. **19**, 023201 (2007).

[77] J. B. Philipp, P. Majewski, L. Alff, A. Erb, R. Gross, T. Graf, et al. Phys. Rev. B **68**, 144431 (2003).

[78] O. Sahnouna, H. Bouhani-Benzianea, M. Sahnouna, M.Drizb, Journal of Alloys and Compounds, **714**, 704 (2017).

[79] William Thomson (Lord Kelvin), Proc. Royal Soc. London **8**, 546-550 (1857).

[80] D. D. Sarma and Sugata Ray, Proc. Indian Acad. Sci. (Chem. Sci.), **113**, 515 (2001).

[81] J. Kanamori and K. Terakura, J. Phys. Soc. Jpn. **70**, 1433 (2001).

[82] J. M. De Teresa, J. M. Michalik, J. Blasco, P. A. Algarabel, M. R. Ibarra, C. Kapusta C, et al., Appl. Phys. Lett. **90**, 252514(2007).

[83] M. Sikora, C. Kapusta, M. Borowiec, C. J. Oates, V. Prochazka, D. Rybicki, et al. Appl. Phys. Lett. **89**, 62503 (2006).

[84] M. T. Anderson, K. R. PoeS. M. Rao, J. K. Srivastava, M. K. Wu, B. H. Mok, C. L. Chen, M. C. Ling, et al. Nov. Magn. **24**, 1249 (2011).

[85] S. M. Rao, J. K. Srivastava, M. K. Wu, B. H. Mok, C. L. Chen, M. C. Ling, et al. Nov. Magn. **24**, 1249 (2011).

[86] G. Long, M. DeMarco, D. Coffey, M. K. Toth, M. S. Torikachvili, Phys. Rev. B **87**, 24416 (2013).

[87] M. Takata, K. Kageyama, J Am Ceram Soc **72**, 1955 (1989).

[88] P. K. Davies, H. Wu, A. Y. Borisevich, I. E. Molodetsky, L. Farber, Annu Rev Mater Res **38**, 369 (2008).

[89] H. Das, U. V. Waghmare, T. Saha-Dasgupta, and D. D. Sarma, *Phys. Rev. Lett.*, **100**, 186402 (2008).

[90] N. S. Rogado, J. Li, A. W. Sleight, and M. A. Subramanian, Adv. Mater. Weinheim, Ger. **17**, 2225 (2005).

[91] Y. Q. Lin, X. M. Chen, X. Q. Liu. Solid State Commun **149**, 784 (2009).

[92] Y. Q. Lin, X. M.Chen. J Am Ceram Soc **94**, 782 (2011).

Chapter 2

Methodology

2.1 Introduction

In this chapter we summarize the methods used to understand and predict various structural, electronic and magnetic properties of perovskite compounds. The methods used in this thesis are as follows:

- Zero temperature calculation:
  - We primarily used density functional theory (DFT) to carry out most of the theoretical calculations. To handle the strong electronic correlation, we considered supplemented Hubbard U calculation within static mean field theory and dynamical mean field theory (DMFT).
  - For prediction of crystal structure, genetic algorithm is used based on DFT total energy calculation.
- Finite temperature calculation:
  - Monte Carlo simulation
  - Exact Diagonalization along with Monte Carlo

Additionally, for prediction of new stable compounds, scanned from a large number of possibilities to be feasible, we used Machine learning technique.

In the following, we present a brief summary of each methods used in this thesis.

2.2 Many electron Hamiltonian

Matter can be thought of as a collection of interacting atoms and molecules, existing either in gas phase (molecules and clusters) or in a solid/condensed phase

(like in bulk solid or surfaces). In all cases these systems can be described as a collection of heavy positively charged nuclei and lighter negatively charged electrons interacting via electrostatic coulomb interaction. The general form of many body Hamiltonian for such system can be expressed as,

$$H = -\sum_{I=1}^{P} \frac{\hbar^2}{2M_I}\nabla_I^2 - \sum_{i=1}^{N} \frac{\hbar^2}{2m_i}\nabla_i^2 + \frac{e^2}{2}\sum_{I=1}^{P}\sum_{J\neq I}^{P} \frac{Z_I Z_J}{|\mathbf{R_I} - \mathbf{R_J}|}$$

$$+\frac{e^2}{2}\sum_{i=1}^{N}\sum_{j\neq i}^{N} \frac{1}{|\mathbf{r_i} - \mathbf{r_j}|} - e^2\sum_{I=1}^{P}\sum_{i=1}^{N} \frac{Z_I}{|\mathbf{R_I} - \mathbf{r_i}|}, \tag{2.1}$$

where the ions with charge Z_I and mass M_I are indicated by upper case subscripts and lower case subscripts indicate electrons with mass m_i and charge e. The first and second term of the Hamiltonian are kinetic energy terms of ion (T_n) and electrons (T_e) respectively. The coulomb interactions between electron-ion (V_{ne}), electron-electron (V_{ee}) and ion-ion (V_{nn}) are represented by the last three terms respectively. Therefore to obtain many body wavefunction $\Psi_i(\mathbf{r}, \mathbf{R})$ one needs to solve the following time independent Schrödinger's Equation:

$$H\Psi_i(\mathbf{r}, \mathbf{R}) = E_i\Psi_i(\mathbf{r}, \mathbf{R}). \tag{2.2}$$

The exact analytical solution of Eq. (2.2) is possible only for hydrogen like atoms. Due to many body nature of Coulomb interaction, the above equation becomes non-separable. Therefore to solve this Hamiltonian in realistic cases one needs to do approximations at different stages. The first step towards a reasonable approximation is *Born-Oppenheimer Approximation*. [1] Within this approximation, the electronic and nuclear motion can be decoupled as the electrons are much lighter than nuclei and hence time-scale associated with ions is much shorter than that of electrons. Therefore, the ions can be assumed to remain stationary with respect to motion of the electrons. Thus the electronic part of the Hamiltonian can be written for a fixed nuclei configuration as:

$$H_e = T_e + U_{ee} + V_{ne} + U_{nn}, \tag{2.3}$$

where the last term U_{nn} is a constant term arising from ion-ion interaction which is known as Madelung energy and can be obtained classically. This major approximation reduces to the many electron and many nuclear Hamiltonian to only many electron Hamiltonian, but even after this further approximations are required to exactly solve Eq. (2.3) due to the interacting nature of the electrons.

Independent Electron Approximation is the next level approximation which maps the interacting electrons into a system of non-interacting electrons that effectively resemble the original system. There are two different approaches : (a) The wavefunction based approach as implemented by Hartree, [2], Hartree-Fock

[3], configuration-interaction [4] *etc.*, (b) The density functional based approach as implemented by density functional theory (DFT). [5–7] The main disadvantage of wavefunction based method is the heavy computational cost even for a simple system, which increases exponentially with system size for capturing the detailed wavefunction. On the other hand, DFT is much less expensive. The theoretical framework followed in this thesis is primarily based on DFT.

2.3 Density Functional Theory

Density functional theory is one of the most powerful approach and being successfully used to determine the structural as well as electronic properties in a wide class of materials. Within DFT, the many body wavefunction which is a function of 3N variable can be replaced by the electronic charge density $\rho(\mathbf{r})$ which is a function of 3 variables. The electronic charge density is defined as,

$$\rho(\mathbf{r}_1) = N \int \Psi^*(\mathbf{r}_1, \mathbf{r}_2, ..., \mathbf{r}_N)\Psi(\mathbf{r}_1, \mathbf{r}_2, ..., \mathbf{r}_N)d\mathbf{r}_2 d\mathbf{r}_3 ... d\mathbf{r}_N. \tag{2.4}$$

Although the basic idea of DFT is rooted in the Thomas Fermi model [8, 9] as proposed in 1921, but two fundamental mathematical theorem as proposed and proved by Hohenberg and Kohn are considered as the back bone of modern DFT.

2.3.1 The Hohenberg-Kohn (HK) theorems

Theorem 1

The ground state wavefunction has unique correspondence with the ground state electron density $\rho(\mathbf{r})$ and external potential V_{ne}. The ground state wavefunction unequivocally determines the external potential, upto an additive constant. Therefore for any observable $\hat{O}$, its ground state expectation value is also an unique functional of the ground state density ρ_0,

$$\langle \Psi | \hat{O} | \Psi \rangle = O[\rho_0].$$

Theorem 2

For any given external potential, a density variational principle can be formulated, i.e. there exists a functional, called "energy functional" $E[\rho]$ such that:

$$E[\rho] \geq E_0.$$

where E_0 is the ground-state energy. The equality sign holds if and only if $\rho[\mathbf{r}] = \rho_{\mathbf{0}}[\mathbf{r}]$, where $\rho_0[\mathbf{r}]$ is the ground state density. There exists a universal

functional $F[\rho]$ for any many electron systems, such that the energy functional can be written as

$$E[\rho] = F[\rho] + \int v_{ext}[\mathbf{r}]\rho[\mathbf{r}]d\mathbf{r},$$

where

$$H = T + U + V,$$

and

$$F[\rho] = \langle \Psi[\rho]|T + U|\Psi[\rho]\rangle.$$

However the exact form of $F[\rho]$ remains unknown and it has no dependency on external potential.

2.3.2 Kohn-Sham Equations

In 1965, the equations proposed by Kohn and Sham [6] transform DFT into a useful tool. They introduced a further development by mapping of kinetic energy of interacting electrons to an equivalent non-interacting system in such a way the density of true interacting system remains unaltered as that of fictitious non-interacting system. For such non-interacting fictitious electrons the universal functional can be written as,

$$F[\rho(\mathbf{r})] = T_0[\rho(\mathbf{r})] + \frac{e^2}{2}\int\int \frac{\rho(\mathbf{r}_1)\rho(\mathbf{r}_2)}{\mathbf{r}_{12}} d\mathbf{r}_1 d\mathbf{r}_2 + \int v(\mathbf{r})\rho(\mathbf{r})d\mathbf{r} + E_{XC}[\rho(\mathbf{r})]. \quad (2.5)$$

The exact kinetic energy functional of interacting electrons is replaced by the kinetic energy of a system of non interacting particles $T_0[\rho]$. The second term is the classical electrostatic contribution known as Hartree term and $E_{XC}[\rho]$, known as exchange-correlation (XC) energy includes all the contribution due to many body effect. Hence one can write the energy functional as,

$$E[\rho] = \int v_{ext}(\mathbf{r})\rho(\mathbf{r})d\mathbf{r} + T_0[\rho(\mathbf{r})] + \frac{e^2}{2}\int\int \frac{\rho(\mathbf{r}_1)\rho(\mathbf{r}_2)}{\mathbf{r}_{12}} d\mathbf{r}_1 d\mathbf{r}_2 + \int v(\mathbf{r})\rho(\mathbf{r})d\mathbf{r} + E_{XC}[\rho(\mathbf{r})] \quad (2.6)$$

Now to obtain the non-interacting K.E. functional $T_0[\rho]$ for a certain $\rho(\mathbf{r})$, one has to consider the solution of the one particle Schrödinger's equations,

$$[-\frac{1}{2}\nabla^2 + \lambda(\mathbf{r})]\psi_i = \epsilon_i\psi_i, \quad (2.7)$$

with a suitable choice of $\lambda(\mathbf{r})$ the resulting orbitals produce the density as,

$$\rho(\mathbf{r}) = \sum_{\mathbf{i}} |\psi_{\mathbf{i}}|^{\mathbf{2}},$$

and henceforth evaluating the functional as,

$$T_0[\rho] = \sum_i \epsilon_i - \int d\mathbf{r}\lambda(\mathbf{r})\rho(\mathbf{r}). \tag{2.8}$$

The energy functional for determining equilibrium density then becomes,

$$E[\rho] = \sum_i \epsilon_i - \int d\mathbf{r}\lambda(\mathbf{r})\rho(\mathbf{r}) + \int v_{ext}(\mathbf{r})\rho(\mathbf{r})d\mathbf{r} + E_{coul}[\rho] + E_{XC}[\rho]. \tag{2.9}$$

The functional minimization produces,

$$\lambda(\mathbf{r}) = v(\mathbf{r}) + \frac{\delta E_{coul}[\rho]}{\delta\rho(\mathbf{r})} + \frac{\delta E_{XC}[\rho]}{\delta\rho(\mathbf{r})}, \tag{2.10}$$

which clearly shows that if $\lambda(\mathbf{r})$ is chosen by the above expression, the correct density for the system will be obtained from the single particle Schrödinger's equation. Hence one arrives to a set of N-nonlinear integro-differential equations known as *Kohn-Sham* (KS) equations, which are needed to be solved instead of many body Schrödinger's equation given by,

$$[-\frac{1}{2}\nabla^2 + v_{eff}(\mathbf{r};\rho)]\psi_i = \epsilon_i\psi_i, \tag{2.11}$$

where the effective potential can be written as

$$v_{eff}(\mathbf{r}) = v(\mathbf{r}) + \int \frac{\rho(\mathbf{r}')}{|\mathbf{r}-\mathbf{r}'|}d\mathbf{r}' + \frac{\delta E_{XC}}{\delta\rho(\mathbf{r})} = v(\mathbf{r}) + v_{Hartree}[\rho(\mathbf{r})] + \mathbf{v_{XC}}[\rho(\mathbf{r})]. \tag{2.12}$$

The Kohn-sham equations are required to be solved in an iterative manner until the self consistency is reached. The procedure can be summarized as follows: One needs to start with an initial guess ρ_0, which can build up the initial KS equation. After solving the eigen value equation, a new density can be obtained and if the new density differs from the previous one by a threshold value then in the next step another new density is evaluated by mixing these two densities. The Hamiltonian for the next iteration will be produced by this density and it will again produce the density for this iteration and so on. The procedure will repeat until the densities of two consecutive steps produce same solution within a specified error margin. The flowchart is shown in Fig. (2.1).

2.3.3 Exchange correlation functional

Up to this point the theory does not need any approximation, hence Kohn-Sham equation is exact in principle. But the main problem lies with the term $E_{XC}[\rho]$, the exact expression of which is unknown and the approximations are needed. Among the different successful approximate methods, the local density approximation (LDA) and the generalized gradient approximation (GGA) are most popular. A brief description of these approximations is provided below.

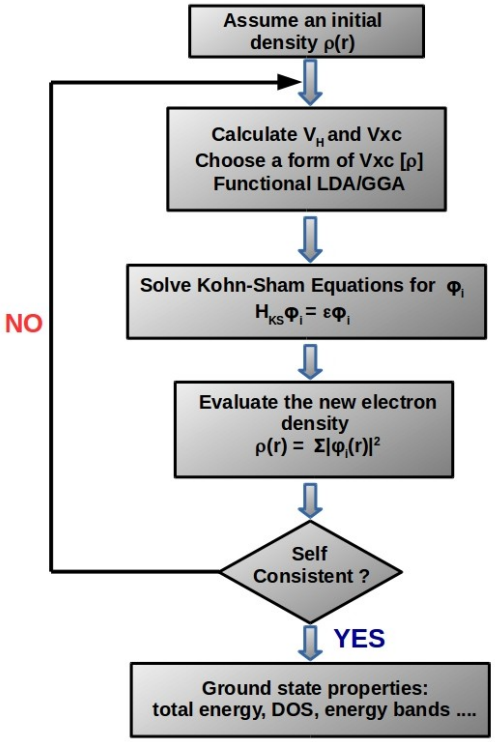

Figure 2.1: Self consistent cycle in DFT

Local density approximation (LDA)

This is one of the simplest approximation made by Kohn and Sham [6], although its basic idea is rooted in the Thomas-Fermi-Dirac theory. [8, 9] Within this approximation, it is assumed that the exchange-correlation energy has only local dependence on electron density $\rho(\mathbf{r})$. The functional form can be written as,

$$E_{XC}^{LDA} = \int \rho(\mathbf{r})\epsilon_{XC}[\rho(\mathbf{r})]d\mathbf{r}, \tag{2.13}$$

where $\epsilon_{XC}[\rho(\mathbf{r})]$ corresponds to the exchange and correlation energy density of a homogeneous electron gas with density $\rho(\mathbf{r})$. In practice, within LDA the ϵ_{XC} can be calculated as the individual sum of contributions coming from exchange and correlation part.

$$\epsilon_{XC}[\rho(\mathbf{r})] = \epsilon_X[\rho(\mathbf{r})] + \epsilon_C[\rho(\mathbf{r})]. \tag{2.14}$$

where the exchange part can be obtained from the Dirac's expression,

$$E_X[\rho(\mathbf{r})] = -C_X \int \rho^{\frac{4}{3}}(\mathbf{r})d\mathbf{r}. \tag{2.15}$$

The functional form of correlation part has been estimated by Ceperley-Alder [10] using numerical quantum Monte Carlo simulation for homogeneous electron gas which has turned out to be exact within numerical accuracy and further different parametrizations have been done by Perdew and Zunger [11], John P. Perdew and Yue Wang correlation (PWC) [12] etc. Though LDA was designed for the systems where the variation of charge density is slow, but surprisingly the outcome is quite good even for non-homogeneous system. [13] Main drawback of this approximation is overestimation of bond energies and underestimation of equilibrium bond length than what obtained in experimental values.

Generalized gradient approximation (GGA)

A next step improvement of LDA has been incorporated in Generalized gradient approximation, where the functional depends on the spatial variation (gradient) of the density,

$$E_{XC}[\rho] = \int \rho(\mathbf{r})\epsilon_{XC}[\rho(\mathbf{r})]d\mathbf{r} + \int F_{XC}[\rho(\mathbf{r}), \nabla\rho(\mathbf{r})]d\mathbf{r}, \tag{2.16}$$

where F_{xc} is known as enhancement factor which modifies the LDA expression. Different versions of GGA functional are available depending upon the choice of the enhancement factor such as Langreth-Mehl(LM) [14], Perdew-Wang (PW'86 and PW'91) [15] [16], Becke '88 (B88) [17] exchange functional, Lee-Yang-Parr (LYP) correlation functional, [18] Pedew-Burke-Ernzerhof (PBE) [19] etc. Among them the last one has been widely used to calculate the ground state properties. GGA is able to rectify some drawbacks of LDA and in general provides better description of properties like binding energy, total energy, structural, and magnetic properties of real materials. But it fails to describe the long range behaviour ($1/R^6$) and provides overestimated result for electric polarization in polar system. Especially, the approximation does not hold good for the systems which are strongly correlated and therefore, it is necessary to consider a more accurate treatment of electron electron correlation.

2.4 General band structure methods

Solution of Kohn-Sham equation demands the wavefunction to be expressed in a suitable basis set. In this thesis, we have used three different basis sets, namely

- Muffin tin orbital(MTO) based Linear MTO (LMTO) [20,21] and Nth order MTO method. [22]
- Plane wave based method as implemented in Vienna ab initio simulation package (VASP). [23]

- Full potential linear augmented plane wave based method [24]. We used Wien 2k for this purpose. [25]

The brief description of each method is provided in the following section.

2.4.1 Linearized Muffin-Tin Orbital method (LMTO)

LMTO is computationally lighter and efficient method to solve the Kohn-Sham equation. In this method, Muffin-tin (MT) sphere approximation is used, where the actual crystal potential is replaced by muffin tin potential as shown in Fig. (2.2). This approximation divides the crystal into MT sphere (atom-centred sphere) and interstitial region.Therefore the external potential has two parts

- a spherically symmetric potential $v(\mathbf{r}_R)$ within a atom centred sphere of radius S_R
- a constant potential in the interstitial region as expressed in the following equation:

$$v(\mathbf{r}_R) = \begin{cases} v(r_R) & \text{for } r_R \leq S_R, r_R = |\mathbf{r} - \mathbf{R}| \\ -v_0 & \text{for } r_R > S_R \end{cases} \tag{2.17}$$

The radial part of Schrödinger's Equation within MT sphere can be written as,

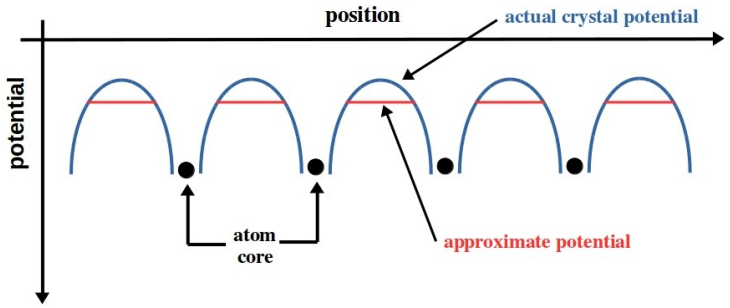

Figure 2.2: Schematic diagram of Muffin-tin potential which can be described by spherically symmetric potential within MT radius and constant potential in outside interstitial region between two neighbouring MT potential wells.

$$[\frac{d^2}{dr_R^2} + \frac{l(l+1)}{r_R^2} - \kappa^2] r_R \theta_{RL}(r_R, \epsilon) = 0. \tag{2.18}$$

In the interstitial region the radial part becomes,

$$[\frac{d^2}{dr_R^2} + \frac{l(l+1)}{r_R^2} - \kappa^2] r_R \theta_{RL}(r_R, \epsilon) = 0, \tag{2.19}$$

where $\kappa^2 = \epsilon - v_0$. Inside the MT sphere, the solution of Eq. (2.19) is a partial wave which is product of radial part and spherical harmonics and outside the sphere the solution becomes plane wave where the expansion can be made in terms of Neumann and Bessel Functions. These two solution must have continuous and smooth matching at the sphere boundary. Though this approach is accurate but computationally heavy as the basis set are energy dependent. Following Anderson's proposal of lineraization, [26] the muffin tin spheres are replaced by the space filling atomic spheres. This approximation is known as atomic sphere approximation(ASA). Within ASA, the basis function can be written as,

$$\chi^{\alpha}_{RL}(r_R) = \phi_{Rl}(r_R) + \sum \dot{\phi}^{\alpha}_{R'L'}(r_{R'}) h^{\alpha}_{R'L',RL}, \tag{2.20}$$

where $\dot{\phi}^{\alpha}$ is the linear combinations of the ϕ's and its energy derivatives $\dot{\phi}'$s The matrix h^{α} is given by,

$$h = C^{\alpha} - \epsilon_{\nu} + (\Delta^{\alpha})^{1/2} S^{\alpha}(\Delta^{\alpha}), \tag{2.21}$$

where C^{α} and Δ^{α} are the diagonal potential matrices commonly known as band centre and band width respectively. They depend on the potential inside the sphere, chosen screening parameter α and on sphere radii. S is known as the structure matrix which depends on the representation and the geometrical arrangement of the atomic sites.

2.4.2 Nth Order Muffin Tin Orbital (NMTO) - a downfolding method

The single electron part like hopping integrals or the onsite terms of a correlated Hamiltonian can be calculated from the low energy, few band calculation instead of full Hamiltonian which can be achieved through downfolding technique. In this technique the basis set is divided into two parts (lower $|l>$ and upper $|s>$) and full Hamiltonian is reducted into the lower subset H_{ll} in such a way that the lower l eigenvalues of original Hamiltonian and the eigenvalues of H_{ll} are similar. This introduces additional energy dependency which can be overcome by linearizaton procedure in LMTO method. The execution of downfolding technique method in LMTO does not reach the accuracy for massive downfolding technique as downfolded bands span in a small energy window. A betterment has been done by Nth order MTO or NMTO method which treats the interstitial region in a more accurate way and goes beyond linear approximation. Like LMTO, NMTO also considers the partial waves within atomic spheres. Screened spherical waves (SSW) replace Neumann functions in the interstitial regions. The Kinked partial waves (KPWs) are defined by the combination of partial waves and screened spherical waves. The basis set is constructed by the Lagrange interpolation of partial waves at (N+1) energy points. Therefore the basis set is energy selective

and hence it is possible to consider a narrow energy window from the full DFT band structure. In this method, one can integrate out the irrelevant orbitals and the effect of re-normalization from integrated out orbitals is taken into account. Thus the renormalized effective few orbitals low energy Hamiltonian can serve as Wannier like orbitals. The effective hopping parameters, on-site energies can be obtained from the real space representation of this downfolded Hamiltonian.

2.4.3 The plane wave based method

In the plane basis, the Kohn-Sham wavefunction can be expanded as

$$\Psi_{kn}(\mathbf{r}) = e^{i\mathbf{k}.\mathbf{r}} \sum_{G} C_G(\mathbf{kr}) e^{i\mathbf{G}.\mathbf{r}}, \tag{2.22}$$

where $\mathbf{G}$ is the reciprocal lattice vector and $C_{(G)}(\mathbf{kr})$ is the plane wave coefficient with normalization condition $\sum_G |C_G(\mathbf{kr})|^2 = 1$. In reality computational implementation needs a truncation of the sum upto a finite cut-off. The cut-off is defined in terms of plane wave kinetic energy cut-off as:

$$\hbar \frac{|\mathbf{k} + \mathbf{G}|^2}{2m_e} \leq E_{cut}. \tag{2.23}$$

The physical quantities are calculated after checking the convergence in terms of energy cut-off. The main advantages of plane wave basis set are

- The basis set does not depend on the atomic positions and species.
- The forces acting on the atoms known as the Hellman-Feynman forces can easily be calculated and no basis set correction is required.
- It has the advantage of changing real space representation to momentum space representation using Fast Fourier transformation (FFT).

The main disadvantage of plane wave basis set is that one needs a large number of plane waves to accurately describe the wavefunctions in the core region as the electrons in this region are tightly bound to the nucleus and the wavefunctions are highly oscillating due to the orthogonality constraints with the electrons in the valence state.

This difficulty can be overcome through the pseudopotential approximation. The basic idea of pseudopotential can be explained as following. The actual potential is deep and attractive in the core region. Valence electrons gain kinetic energy due to the rapid oscillation in the core region, which behaves as repulsive potential. The valence wavefunctions can be considered as smooth nodeless pseudowavefunction within the core region which is identical to the actual wavefunction outside the core region as shown in Fig. (2.3). Hence far less plane waves are required to describe the valence wavefunctions.

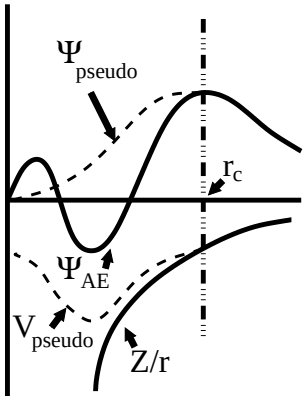

Figure 2.3: Comparison between all electron (solid line) and pseudo (dashed line) wavefunction and potential. After a cut-off radius r_c, they match with each other. The picture is adapted from wikipedia.

Various methods have been developed to construct more accurate and efficient pseudo-potentials (PS) in last few decades. Three kinds of pseudopotentials exist which are widely used in electronic structure calculation using plane wave basis.

- **Norm conserving pseudopotential:** It has an extra constraint that the norm of the pseudo-wave function [27] within the core radius must be equal to all-electron (AE) wavefunction and outside the core region these two should be identical. In real situation, it needs a large plane waves for strongly localized orbitals like $3d$ and rare earth elements making the situation computationally expensive.

- **Utltrasoft pseudopotential:** The previously mentioned situation was improved by Vanderbilt [28], where the constraint of norm-conservation was relaxed and localized atom centred augmentation charges were introduced to compensate the charge deficit. The charge density difference between the AE and the PS wavefunction is considered as the augmentation charge. Only for the augmentation charges, the moments and the charge distribution of the AE wavefunction can be restored accurately within a small cut-off radius.

- **Projector augmented wave (PAW) method:** The method was introduced by Bloch [29] and it is widely used to determine the electronic structure calculation for transition metal oxides within plane waves due to high accuracy, light computational cost with respect to other methods. The detailed description can be found in section 2.4.5. In our calculation we considered PAW method as implemented in VASP. [23]

2.4.4 The Linearized Augmented Plane Wave (LAPW) method

Augmented Plane Wave (APW) basis set is more useful for the information that inherently lies in the region near the nucleus than pseudo potential methods. The behaviour of the electrons can be described by atomic like wavefunctions in the region close to nuclei, whereas the electrons are de-localized in the region far from the nuclei and can be described by plane waves. So the space can be divided into muffin tin spheres and interstitial region as was discussed in the LMTO method in the previous section. The linearized version of Augmented Plane Wave (LAPW) basis, following Andersen's linearization approach [26], is expressed as,

$$\chi_q(\mathbf{r},\epsilon) = \begin{cases} \Sigma_{l,m}(A^q_{lm,R}\Phi_{LR}(r_R,\epsilon_v)+ & (B^q_{lm;R}\dot{\Phi}_{LR}(r_R,\epsilon_v)) \text{for } r_R \leq S_R \\ e^{i(\mathbf{q}.\mathbf{r})} & \text{for } r_R > S_R \end{cases} \tag{2.24}$$

where the coefficients $A^q_{lm;R}$ and $B^q_{lm;R}$ can be obtained by matching boundary conditions. It can be achieved by expanding the plane wave solution in the interstitial in terms of Bessel functions $j_l(r_R;q)$. In principle exact matching requires a large number of l values, but to simplified the problem it is truncated at some value l_{max}. Therefore l_{max} is a crucial parameter in band structure calculations using LAPW basis set and a reasonable choice is required and the condition is

$$R_i K_{max} = l_{max},$$

where R_i is the radius of i^{th} MT sphere and the cut-off for the plane waves is determined by K_{max}. The term $R_i^{min}K_{max}$ controls the accuracy of the basis where R_i^{min} is the smallest MT sphere radius in the unit cell.

In LAPW, the core states that do not participate in chemical bonding, are treated as in free atoms, but subject to the potential due to the valence states. The problem arises in order to treat the semi-core states, which lie in between core and valence states. In order to solve this problem an additional set of basis functions can be added. They are known as "local orbitals" and consist of a linear combination of two radial functions at two different energies and one energy derivative at one of these energies:

$$\phi^{LO}_{lm} = A_{lm;R}\phi_{LR}(r_R;\epsilon_{\nu 1}) + B_{lm;R}\dot{\phi}_{LR}(r_R;\epsilon_{\nu 1}) + C_{lm;R}\phi_{LR}(r_R;\epsilon_{\nu 2}).$$

The coefficients are determined by the requirements that ϕ^{LO} should be normalized and should have zero value and slope at the sphere boundary. Though adding local orbitals increases the LAPW basis set size, still their number is quite small compared to typical LAPW basis set size of a few hundred functions. The problem with the APW method was the energy dependence of the basis set, which is removed in the LAPW+LO method, however at the cost of a somewhat larger basis set size.

2.4.5 The Projector Augumented Wave (PAW) method

PAW method [29] connects the idea of LAPW method with existing plane wave pseudopotential approach. Within this formalism, a linear transformation τ maps the PS wavefunction $\tilde{\Psi}_n$ to AE wavefunction Ψ_n

$$\Psi_n = \tau\tilde{\Psi}_n. \tag{2.25}$$

The transformation υ has a contribution from atom-centred part τ_R apart from identity

$$\tau = 1 + \sum_R \tilde{\tau}_R. \tag{2.26}$$

An augmentation region Ω_R is considered surrounding atom in which the local contribution $\tilde{\tau}_R$ can act. This augmentation region is equivalent to muffin tin sphere in linear methods and core region in pseudopotential method. So, outside this region AE and PS wavefunction are same. The AE wave function as transformed from the PS wavefunction can be written as

$$|\Psi_n\rangle = |\tilde{\Psi}_n\rangle + \sum_i (|\phi_i\rangle - |\tilde{\phi}_i\rangle)\langle\tilde{p}_i|\tilde{\Psi}_n\rangle, \tag{2.27}$$

where ϕ_i and $\tilde{\phi}_i$ corresponds to AE and PS partial waves respectively. p_i is known as the projector function and it must satisfies the relation $\langle\tilde{p}_i|\tilde{\phi}_j\rangle = \delta_{ij}$ within Ω_R for each PS partial wave. If we consider any operator A in AE space, the above transformation can be used to evaluate operator in PS space as

$$\tilde{A} = \tau^* A\tau. \tag{2.28}$$

The Kohn-Sham equation can also be transformed in the similar manner,

$$(\tilde{H} - \varepsilon\tilde{S})|\tilde{\Psi}_i\rangle = 0, \tag{2.29}$$

where $\tilde{H} = \tau^* H\tau$ and $S = \tau^*\tau$ is known as pseudopotential overlap operator.

2.5 Beyond DFT exchange-correlation

2.5.1 LDA+U

"LDA+U" is one of the methods which is used to describe the strongly correlated system. It considers the strong on site coulomb interaction (known as Hubbard U) at highly localized orbitals like d or f 4 electrons along with the standard LDA functional for the rest. Within this method, the energy of a system with total number of d electrons $N = \sum n_i$ can be written as,

$$E = E_{LDA} + \frac{U}{2}\sum_{i\neq j} n_i n_j - \frac{UN(N-1)}{2} \tag{2.30}$$

The second term is Hubbard term and double counting is avoided by subtracting the third term. The orbital energies can be written as

$$\varepsilon_i = \frac{\delta E}{\delta n_i} = \varepsilon_{LDA} + U(\frac{1}{2} - n_i). \tag{2.31}$$

This makes occupied orbital for which $n_i = 1$ is shifted by $-\frac{U}{2}$ and the unoccu-

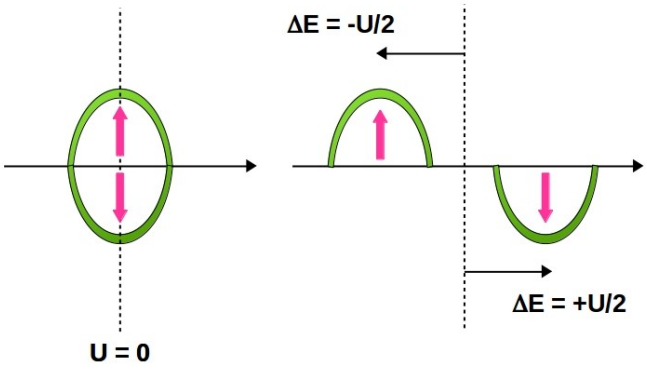

Figure 2.4: Schematic representation of the effect of U in LDA electronic structure. In the presence of Hubbard U, there is shifting of occupied and unoccupied orbitals with respect to each other.

pied orbital ($n_i = 0$) is shifted by $\frac{U}{2}$ as shown in Fig. (2.4). It produces lower and upper Hubbard bands which are separated by coulomb parameter U. Therefore this method can qualitatively capture the underlying physics of strongly correlated system. The two popular methods of LDA+U approach are:

- **Liechestein method** This method was proposed by Liechtenstein et al. [30] in which generalized form of LDA+U functional for multiorbital correlated site was introduced as follows:

  $$E^{LDA+U}[\rho^\sigma(\mathbf{r}), \{n^\sigma\}] = E^{LDA}[\rho^\sigma(\mathbf{r})] + E^U[\{n^\sigma\}] - E_{dc}[\{n^\sigma\}], \tag{2.32}$$

  where ρ^σ is the charge density for spin σ, n^σ_m are the orbital occupancies of correlated atoms, m denoting magnetic quantum number. The first term $\mathrm{E}^{LDA}[\rho^\sigma(\mathbf{r})]$ is the standard LDA functional and the orbital polarization is included in the second term $\mathrm{E}^U[\{n^\sigma\}]$ which is absent in LDA. It can be written as,

  $$E^U[\{n^\sigma\}] = \frac{1}{2}\sum_{\{m\}\sigma}\{\langle m, m^{''}|V_{ee}|m^{'}, m^{'''}\rangle n^\sigma_{m,m'}, n^{-\sigma}_{m',m'''}$$

$$-(\langle m, m^{''}|V_{ee}|m^{'}, m^{'''}\rangle) - \langle m, m^{''}|V_{ee}|m^{'''}, m^{'}\rangle)n^{\sigma}_{m,m'}, n^{\sigma}_{m',m'''}\}, \quad (2.33)$$

where V_{ee} represents for the screened Coulomb interactions among nl-electrons(n and l are principle and orbital quantum number respectively).

The last term is considered to avoid double counting and can be expressed as,

$$E_{dc}[\{n^{\sigma}\}] = \frac{1}{2}UN(N-1) - \frac{1}{2}J[N^{\uparrow}(N^{\uparrow}-1) + N^{\downarrow}(N\downarrow -1)], \quad (2.34)$$

where N^{σ}= Tr($n^{\sigma}_{mm'}$) and $N = N^{\uparrow}$+N$^{\downarrow}$. U and J are screened Coulomb and exchange parameters [31, 32] respectively.

- **Dudarev method** The prescription given by Dudarev et al. [33], is a much simplified treatment, which is the rotationally invariant approach to the LDA+U. Within this approach LDA+U energy functional can be written as,

$$E^{LSDA+U} = E^{LSDA} + \frac{U-J}{2}\sum_{\sigma}\left[\sum_{m} n^{\sigma}_{m,m} - \sum_{m,m'} n^{\sigma}_{m,m'}n^{\sigma}_{m',m}\right], \quad (2.35)$$

where U and J are represented by the spherically averaged matrix elements of the screened Coulomb electron-electron interaction. Total number of electron can be obtained from N^{σ}= $\sum_m n_{m,\sigma}$.In this approach the parameters U and J are not considered separately, only the meaningful parameter is their difference $U - J$.

2.6 Dynamical mean field theory (DMFT)

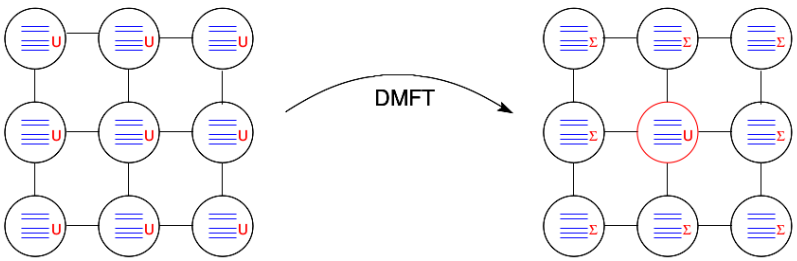

Figure 2.5: The DFMT replaces a the full lattice with interaction U onto single impurity site coupled to a self consistent bath (adopted from Ref. [38]).

The standard approach of incorporating electronic correlation beyond LDA as mentioned in the previous section is LDA+U, based on the simplified idea of static treatment of electron-electron correlation considering movement of electron within a time-averaged density created by other electrons. Despite of huge success of LDA+U in describing correlated magnetic insulators, such description fails for correlated metals for which dynamical correlation effect is important. Specially both LDA and LDA+U unable to capture the quasiparticle physics present in strongly correlated metal along with lower and upper Hubbard band. Dynamical mean field theory, a non-perturbative method primarily developed by Metzner and Vollhardt [35], Müller-Hartmann [36], Georges and Kotliar [34], and Jarrell [37] is able to describe the strongly correlated metals as well as Mott-insulator in a single framework.

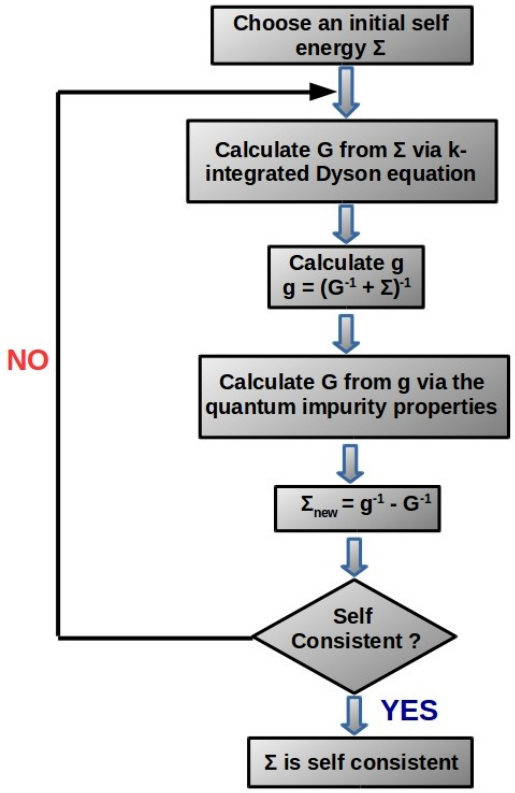

Figure 2.6: Flow diagram of the DMFT self-consistency cycle.

DMFT maps the many body lattice problem with interaction U present on every site onto a single site impurity problem, where the self energy Σ replaces the interaction U except for a single site as shown in Fig. (2.5). The mapping is exact for infinite dimension. The related local Greens function can be calculated

via the k -integrated Dyson equation as,

$$G(\omega_n) = \sum_k [(\omega_n + \mu)I - H^{LDA}(k) - \Sigma(\omega_n)]^{-1}, \tag{2.36}$$

where, H^{LDA} denotes the Hamiltonian defined in few band description of LDA band structure in Wannier function basis, chemical potential μ is determined through the total number of electron in a self consistent way. In the above equation Matsubara finite-temperature formalism is used with frequencies $\omega_n = (2n+1)\pi/\beta$ where $\beta = 1/k_B T$. The local Green function $G(\omega)$ and self energy Σ are related to the impurity Green function g, by the following equation,

$$g^{-1} = (\Sigma + G^{-1})^{-1}. \tag{2.37}$$

The self consistent DMFT scheme can be summarized as follows. At first a trial self energy Σ is considered from which one can calculate the local green function G using Dyson equation. Then g needs to be calculated from Eq. (2.37). In the next step which is most crucial step is the solution of G from by solving Anderson impurity model. Different solvers are used like iterated perturbation theory [39] self-consistent perturbation theory [40], quantum Monte Carlo simulations [41], exact diagonalization [42] etc. Then a new self energy can be obtained using Eq. (2.37). The algorithm stops iteration when the convergence criteria is reached. The flow chart is shown in Fig. (2.6).

2.7 Genetic algorithm for structure prediction

The structural information of a crystalline solid is essential to calculate many physical properties using quantum chemical approach. The conventional way of finding crystal structure is experimental synthesis which is time-consuming and expensive. At high temperature and pressure, experimental data are often poor and incomplete. The better alternative is theoretical structure prediction based on the knowledge of chemical compositions and it has become increasingly popular as it opens new ways to design materials with desired properties. Search of the most stable structure by minimizing energy at given external conditions (such as pressure and temperature) is one of the long-standing challenges in theoretical solid state physics, chemistry, and materials science. Among the other optimization based methods like simulated annealing [43], metadynamics [44] and minima hopping [45], the evolutionary algorithm for crystal structure prediction has been highly successful and popular as a method for the discovery of minerals and materials. [46] The genetic algorithm we used in this thesis to investigate the structures of yet-to-be synthesized compounds, is Universal Structure Predictor: Evolutionary Xtallography(USPEX). [47,48] The key mechanism of USPEX is to search structure on the basis of fitness value which is defined as energy obtained

from ab-inito calculation of locally optimized structure in a evolutionary way. Though from computational perspective, such calculations are expensive but it provides high accuracy in predicting structures of new compounds without any prior assumption. It also helps to avoid trapping in local minima, and is able to compare a large variety of structures in a wide energy landscape. The critical part of any evolutionary algorithm is to find new samples in each generation. In a crystal the atomic positions of neighbouring atoms hold the most important information. The crucially chosen fraction of the atomic position can provide a significant information present in the entire crystal. Therefore rearranging such fragments of ′parent′ structure would provide a way to obtain new samples of ′offspring′ structures and thus help to search the structure of the desired compound in all possible way. In following section we describe the basic steps followed by USPEX to predict the ground state structure of yet to be synthesized compounds.

2.7.1 Evolutionary Algorithm

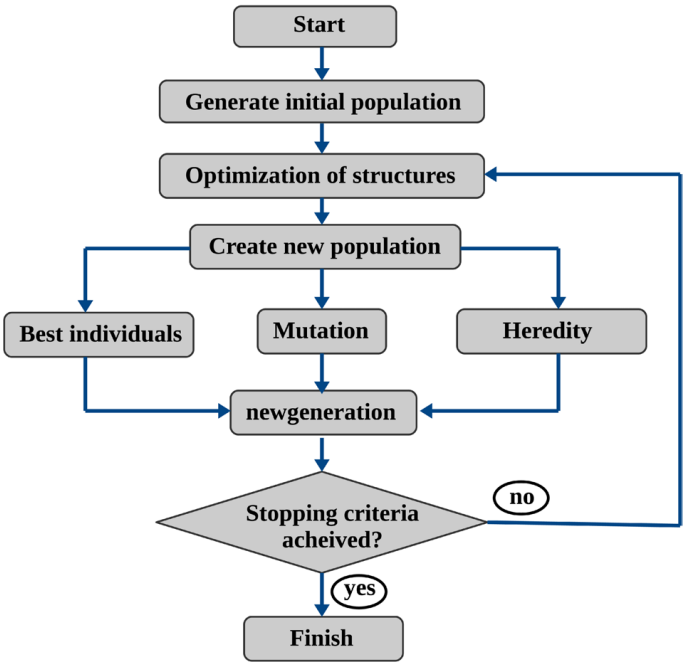

Figure 2.7: Flow-chart of genetic algorithm

The flowchart of a typical evolutionary algorithm is shown in Fig. (2.7). In the first generation structures are randomly created for a given chemical composition. The hard constraints such as minimal inter-atomic distances, restriction of cell angles between 60° and 120°, least lattice vector length are checked for all the

structures and the individuals disobeying any of the above mentioned conditions are discarded.

Though initial population is usually created randomly but one can narrow down the search space by providing some information such as likely candidate structures, lattice parameters, or possible space groups etc. All the individuals created by the algorithm are then relaxed by some external code interfaced with this algorithm. We used plane wave based method as implemented in VASP [23] to calculate fitness parameter. All the structures are ranked on the basis of fitness parameter. After optimization, few weak structures are rejected and rest of the individuals are considered as parent for the next generation. In the succeeding generations, the offspring structures are produced from the parent structure employing different variational operators like heredity, mutation, permutation etc. Among them heredity is the most important operator. Mutation helps in finding immediate intermediate of a good structure which can be useful if metastable structures are present and it may be neglected. A brief description of these operators is given below.

Heredity

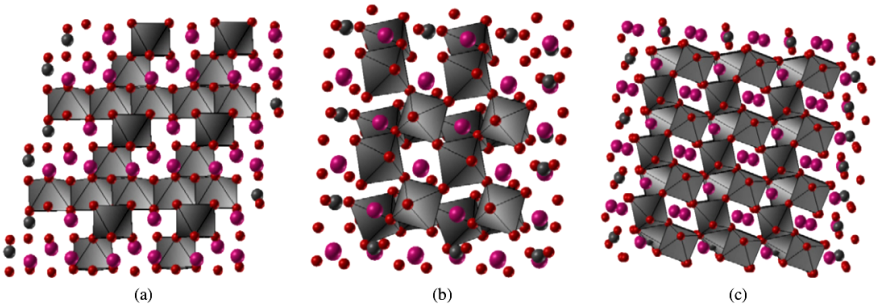

Figure 2.8: Example of heredity operator : (a) parent 1 (b) parent 2 and (b) newly generated offspring structure. The structures obtained after local optimization are shown here. [Taken from Ref [49].]

In this process, two parent structures are used to produce a new offspring structure. This operator considers two spatially coherent (in terms of fractional coordinate) fractions from each of the individual and combines them together to obtain a daughter structure. In more detail, a random number is chosen between 0 and 1 and is stored as the value for the fraction (x). Now from the first individual, atoms with fractional coordinates lying between 0 and x and that from the second individual having values between x and 1 are considered as two different slabs. Now these two slabs are joined together to form a new individual. If the number of atoms in the new individual is greater than original one, the

extra atoms are removed in a random manner. In case there is less number of atoms, the adjustment is made in the following way. The particular type of atom for which the adjustment is required is chosen in a random manner from the parent individuals which was absent originally in the offspring. This process is repeated until the number of atoms gets corrected. The lattice parameters of the offspring are weighted averages of two parent individuals. Fig. (2.8) shows an example of generation of offspring through heredity operator.

Mutation

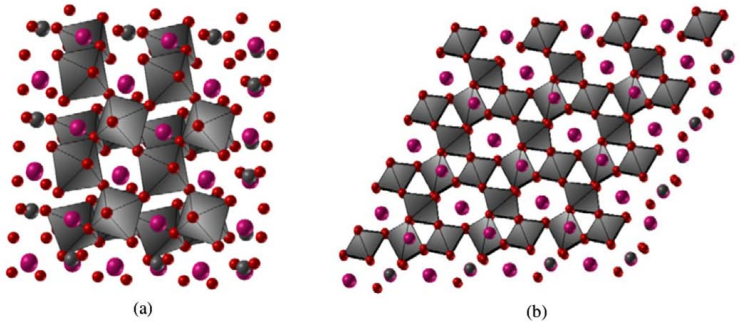

Figure 2.9: Structure produced by mutation : (a) Parent structure (b) Mutated structure presented after local optimization. [Taken from Ref [49].]

A new individual is produced from a single parent structure where a random symmetric strain matrix is applied to transform the lattice vector $\overrightarrow{a}$ of the parent structure to a new lattice vector $\overrightarrow{a'}$ of the offspring:

$$\overrightarrow{a'} = [I + \varepsilon_{ij}]\overrightarrow{a}$$

where I and ε_{ij} are unit matrix and symmetric strain matrix respectively, such that

$$[I + \varepsilon_{ij}] = \begin{bmatrix} 1+\varepsilon_{11} & \frac{\varepsilon_{12}}{2} & \frac{\varepsilon_{13}}{2} \\ \frac{\varepsilon_{12}}{2} & 1+\varepsilon_{22} & \frac{\varepsilon_{23}}{2} \\ \frac{\varepsilon_{13}}{2} & \frac{\varepsilon_{23}}{2} & 1+\varepsilon_{33} \end{bmatrix}$$

The strain components ε_{ij} are taken from Gaussian distribution having zero mean. An example of mutated structure is shown Fig. (2.9).

Permutation

One parent structure produces a offspring by swapping two heterogeneous atoms few times. Permutation is only possible for the systems where more than one

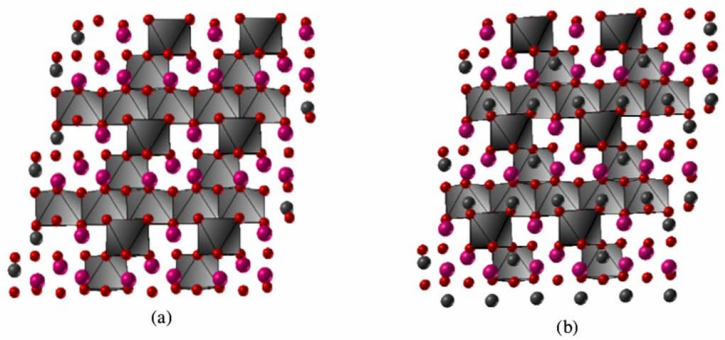

Figure 2.10: Structure produced by permutation : (a) Parent structure (b) permuted structure presented after local optimization. [Taken from Ref [49].]

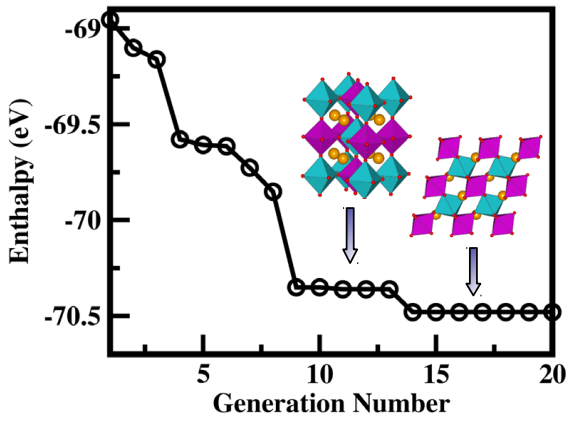

Figure 2.11: Evolution of structures as a function of generations.

type of atoms exist. Fig. (2.10) shows a offspring (b) which is produced from (a) by permutation.

In the next step, the offspring which are created by above mentioned variational operators, together with a few best structures from the previous generation, constitute the next generation. This process is repeated until no lower-energy structures are produced for sufficient number of generations as shown in Fig. (2.11). Another potential strategy can be adopted to reduce the computational cost significantly is "Seeding". In seeding different relevant structures of similar compounds are inserted in different generations in adhoc manner. The structures from previous calculations can also be provided as seed. While it incorporates bias in the search and can be misleading for the prediction, but careful implementation makes the method very efficient and helps to converge in correct ground state within a short time.

2.8 Finite temperature calculation

In this thesis besides DFT we also did finite temperature calculation. The model Hamiltonians were developed as per requirements of the problems and were solved using Monte Carlo and a combined method of exact diagonalization-Monte Carlo technique. Brief description of these methods are provided in the following sections.

2.8.1 Monte Carlo method

Monte Carlo is a widely used Metropolis algorithm where numerical results are obtained through repetitive random sampling. The central idea is based on the random walk through the generation of random number followed by acceptance or rejection decision. The algorithm is briefly described here for spin systems. Consider a system of Ising spins with two states S and S', obeying Boltzmann distribution.
The acceptance probability of S to S' can be written as,

$$A(S \to S') = \begin{cases} e^{-\triangle E/T}, if \triangle E = E(S') - E(S) > 0 & "uphill" \\ 1, else & "downhill" \end{cases} \tag{2.38}$$

Within this algorithm,

- The move is accepted if $e^{-\triangle E/T} > 1$
- In case of $e^{-\triangle E/T} < 1$, the value is compared with a random number r between 0 and 1 and the move is allowed if $r < e^{-\triangle E/T}$.

In practical purposes, to model any spin system one needs to specify the lattice size (cubic lattice of size $L \times L \times L$ is considered in this study) and also the proper periodic boundary condition. Next a primary spin configuration will be considered with either all spins are up or down. The self-consistency condition can be reached by following these steps,

- At first one lattice site i is selected randomly.
- The spin in this site is considered for flipping and corresponding energy difference $\triangle E$ is calculated.
- Then the transition probability is calculated from this energy difference.
- The decision of the spin flipping is made by a random number as described above. If the spin flip is allowed, then this configuration is considered as a new configuration.

- The properties of this resulting configuration is stored to calculate required averages. So, if one has interest on calculating the total magnetization M_{tot}, then it can be updated by M_{tot} by $M_{tot} + 2S_i$.

In this thesis, this method is employed to calculate the temperature dependent magnetic behaviour. The effective spin model [50] considered in this case is

$$H_{eff}\{\mathbf{S}\} \approx \sum_{<<ij>>} D_{ij}\sqrt{\frac{1+\mathbf{S}_i.\mathbf{S}_j}{2}}, \tag{2.39}$$

where D_{ij} are considered as nearest neighbour and next nearest neighbour magnetic interactions and were obtained from DFT total energies of the different magnetic configurations. The details can be found in Chapter 5.

2.8.2 Exact Diagonalization Monte Carlo (ED-MC) method

In exact diagonalization a finite size lattice is considered and few lowest energy eigenvalues and eigenvectors are determined to calculate the various ground state expectation value. The commonly used method in exact diagonalization is Lanczos method. [51] The main disadvantage of exact diagonalization is that the computational cost increases exponentially with the lattice size. Although most of the time the matrix is sparse but still it is beyond the computers memory storage. The way to solve the problem is block to diagonalize the Hamiltonian which produces smaller matrices along diagonal and to calculate the ground state properties one requires only the smallest eigenvalues from each of the small matrices.
Additionally Monte Carlo simulation combined with exact diagonalization method can help to study the behaviour of different physical properties as a function of temperature. Metropolis algorithm used in Monte Carlo simulation generates the equilibrium configuration at finite temperature. In classical system spin update costs $\mathcal{O}(zN)$, for N being the system size and z is coordination number. In case of spin-fermion problem the cost is determined by the fermion free energy. If one uses exact diagonalization of the Hamiltoninan for this purpose, the cost per site becomes $\mathcal{O}(N^3)$ and that of system update cost is $\mathcal{O}(N^4)$. Despite of this huge computational cost this method which is known as ED-MC is being used successfully to capture several aspects of magnanite physics. [52] To overcome this size limitation "travelling cluster approximation" (TCA) [53] is used which can handle the larger system. The following strategy is used in ED-MC: at first an arbitrary spin configuration $\{\eta\} = \{\eta_1, \eta_2, ..\}$ is considered and one needs to compute the total energy $\varepsilon\{\eta\}$ by exact diagonalization. Then it tries to update the spin configuration $\{\eta\}$ to $\{\eta'\}$ which is done within Metropolis algorithm. Total energy $\varepsilon\{\eta'\}$ of the corresponding spin configuration is computed in the next step. If $\varepsilon\{\eta'\}$ is already lower in energy than $\varepsilon\{\eta\}$, the new configuration

will be accepted. If $\varepsilon\{\eta'\}$ is greater than $\varepsilon\{\eta\}$, the move will be allowed with a probability $\propto exp(-\Delta E/KT)$ at finite temperature T. Thus it helps to reach the equilibrium and then different thermal averages can be computed. The results obtained using this method are discussed in detail in Chapter 3 and Chapter 4.

2.9 Machine Learning

Over past two decades, Machine learning (ML) has become a very useful tool in information technology and recently it has been used in the search for novel functional compounds. It is based on the principle where it finds pattern from the past (the available literature) and use it for prediction in future (material discovery). The procedure of ML adopted in this thesis can be described in four steps as shown schematically in Fig. (2.12). Brief description of each steps are described in the following section.

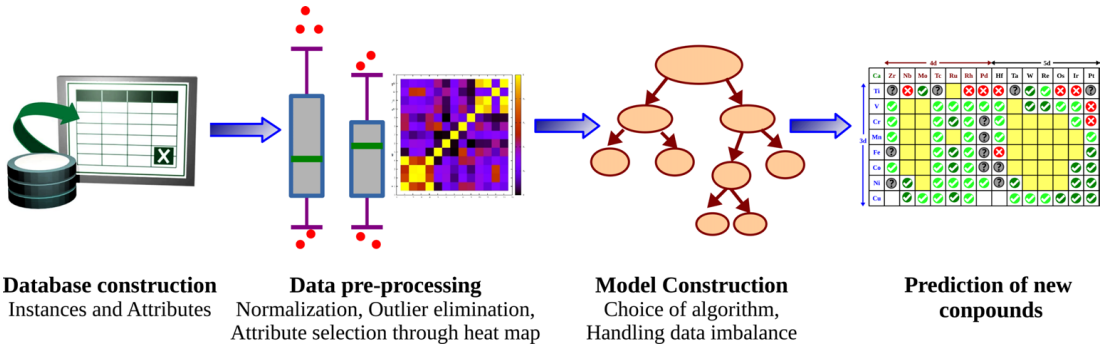

Figure 2.12: The steps adapted for screening of stable compounds, following the machine-learning algorithm. Shown are the schematic representations.

2.9.1 Database construction for model training

The database consists of (i) Instances : It can be thought as individual independent examples from which one needs to build the concept. Instances are collected from the existing literature and are classified or clustered based on some properties. (ii) Attributes : The corresponding features or characteristics which represent the uniqueness of a particular instance. The choice of proper set of attributes is an crucial part in machine learning. The attributes which are used in this work are based on either chemical or structural properties of the instances. The choice of such attributes make the database construction easier as these attributes can be obtained without any computational study.

2.9.2 Data preprocessing

Data preprocessing in machine learning is essential to improve the quality of the raw data by transforming it to a meaningful format. Besides, it helps in understanding the underlying trend in the dataset. In this study, data preprocessing comprised of normalization using bootstrapped sampling technique, removal of outliers and elimination of correlated attribute through heat map which can be summarized as follows:

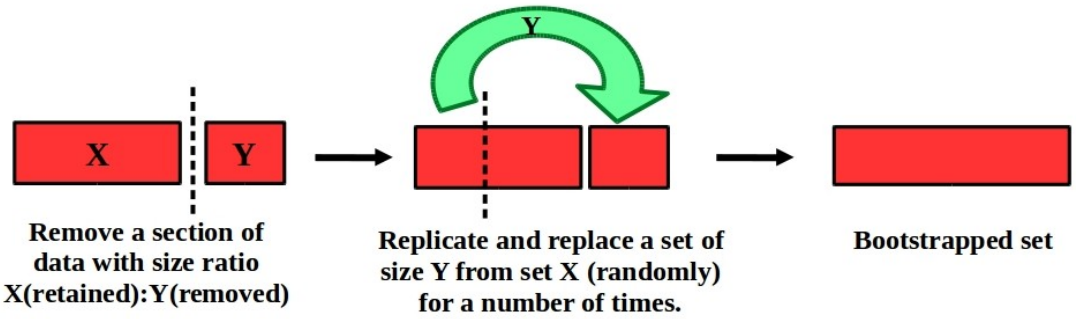

Figure 2.13: Creation of Bootstrapped dataset by random re-sampling and replacement in the original dataset

Bootstrapping and Z-score Normalization

Since the attributes in the dataset contain a wide range of numerical values, normalization helps in bringing them to an equal footing while keeping the difference in the range of the values unchanged. Normalization has been implemented through Z-score normalization method given by :

$$\tilde{X} = \frac{X - \mu_X}{\sigma_X}$$

where $\tilde{X}$ is the normalized attribute set, X is the original attribute set, μ_X and σ_X are population mean and variation. Since the true value of the population mean and variation cannot be calculated directly as we do not have the entire distribution, it has been estimated from the dataset itself. We have used a naive bootstrapping method which replicates several subsets of the actual dataset by re-sampling the dataset with random replacement. The bootstrapped datasets are created by replacing 1/4 of the original dataset with randomly picked values from the remaining part of the dataset. This process is continued until the averaged μ_X and σ_X of two consecutive steps differ by a threshold value. The final averaged μ_X and σ_X are used in normalization. A schematic representation of bootstrapped method is shown in Fig. (2.13).

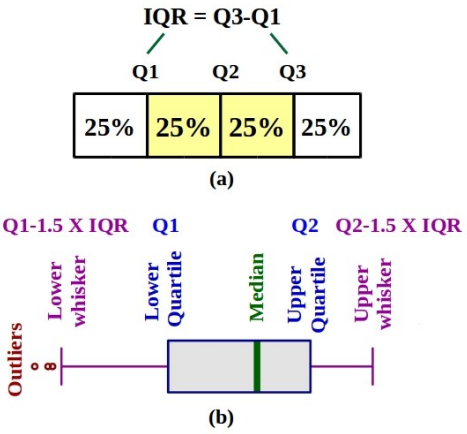

Figure 2.14: Determination of outlier data through box plot. (a) 50% of distribution lies between interquartile range and Q2 divides the distribution into two equal parts so it is the median of the distribution. (b) Lower whisker and upper whisker are determined by Q1-1.5×IQR and Q3+1.5×IQ respectively. For a Gaussian distribution 99.3% of values are found within this range and only 0.7% data are outliers.

Removal of outlier data

The next step of data preprocessing is removal of instances corresponding to outlier data in the normalized dataset. The entire normalized dataset is rank ordered and divided into four equal parts. Each part are named as first, second and third quartile with notation Q1, Q2 and Q3 respectively as shown in Fig. (2.14). Interquartile range (IQR) is defined as difference between Q1 and Q3 which measures the spread of the dataset. Box plot is a standard method to visualize the distribution of data in terms of quartile numbers. Any data point is considered to be an outlier if it lies below Q1-1.5×IQR or above Q3+1.5×IQR as shown in Fig. (2.14-b).

Attribute selection

The next and final step involves finding correlation between a pair of attributes using Pearson correlation coefficient, defined as,

$$r = \frac{\sum_{i=1}^{i=n}(x_i - \bar{x})(y_i - \bar{y})}{\sqrt{\sum_{i=1}^{i=n}(x_i - \bar{x})^2}\sqrt{\sum_{i=1}^{i=n}(y_i - \bar{y})^2}} \tag{2.40}$$

Here n is the sample size, x_i, y_i are sample points and $\bar{x}$ and $\bar{y}$ are the sample means. The range of absolute value of r lies between 0 and 1. If it is close to 1, the two corresponding attributes are highly correlated. To remove any possibility of

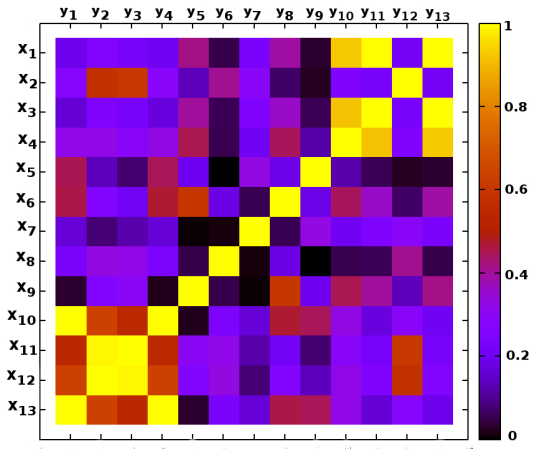

Figure 2.15: Heatmap representing correlation among different attributes. Different colors indicate the strength of their correlations. Weak or no correlation is represented by blue boxes in the plot and strong correlation is represented by yellow boxes in the plot.

introducing bias to the machine learning model, such correlation must be avoided, and so one of the correlated attributes is discarded. Fig. (2.15) represents a heat map where the correlations between different attributes are shown using Pearson correlation.

2.9.3 Model selection

The final and most crucial step is a suitable choice of machine learning algorithm that can efficiently capture the underlying pattern in the dataset. In this thesis the machine learning algorithms used for classification are based on decision tree which is described in the following section.

Decision tree

Decision tree is the most robust and frequently applied technique in machine learning used for classification and regression. The idea is based on the principle of "divide and conquer", where the entire population is divided into two or more sections in root node, each intermediate node performs test on a particular attribute, branches are generated as outcome of the test and leaf node or terminal node represents a single class level without any further splitting. The tree is drawn from top to bottom manner. At first one attribute is chosen and placed in the root node and splitting is done for all possible value of this particular attribute and each branch has a particular value of the attribute. The process is repeated in a recursive way until all the instances of a node are with

same class and it stops growing for that section of the tree. The crucial thing to

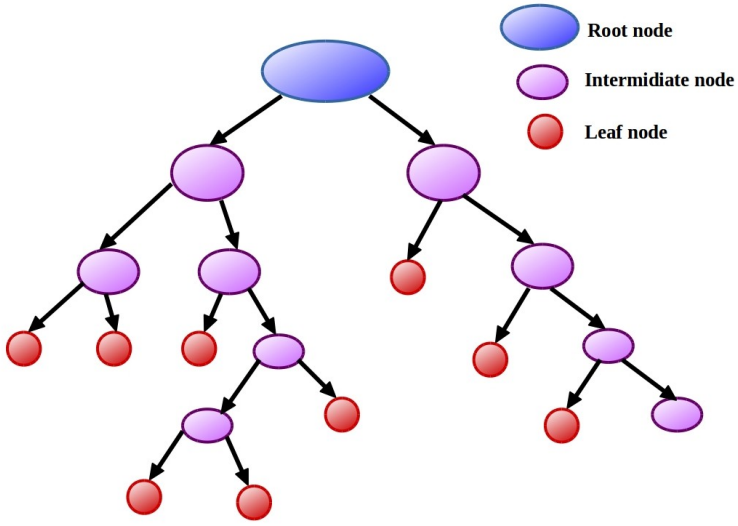

Figure 2.16: A schematic representation of decision tree.

determine which attribute to choose at root node and other intermediate nodes. This decision is taken by calculating information gain which can be obtained in terms of entropy estimated from the amount of uncertainty present in a data set S. The entropy can be written as,

$$Entropy = -\sum_{i=1}^{n} p_i log_2 p_i \tag{2.41}$$

where p_i is the proportion of a particular class i that is present in the considered node. The entropy is zero for a perfectly classified set. The information gain which can be measured by taking the difference between the entropies of before and after spiting into a node or in other words the reduction of entropy for a particular set S when it splits on the basis of a particular attribute. The attribute with highest information gain is considered in the root node and then the procedure is repeated for other sub trees until the desired tree is obtained. Decision tree has advantages as it is less expensive computationally, can handle both continuous and discrete variables, and one can get a clear understanding about the factors which is important for classification. A schematic of typical decision tree can be seen in Fig. (2.16).

Machine Learning Algorithm

Initially four tress algorithms namely J48 [54], random tree [55], random forest [56] and REP tree [57] have been considered to make the classification. It

is found that random forest algorithm provides the best result among these four algorithms. Random forest (introduced by Ho [58] and further developed by Leo Breiman [59]) by is found reliable for classification problems and it has been successfully used in many cases in material informatics. Random Forest algorithm is an example where multiple decision trees are build and their individual predictions are merged to provide a final prediction which is more precise and accurate. Each tree in the forest is grown in the following manner :

- Several data sets are required to create from original dataset. Let us consider the number of instances in the original set is N. Now to create a new data set with N instances, one needs to draw some samples randomly and replace them from the rest of the samples. Different trees are grown using these data sets.
- If there are K number of attributes, each node uses a variable n such that $n << K$ where n attributes will be picked from K at random and the best split is chosen for growing the node. During the development of forest, the value of n is kept invariant.
- No pruning is required for the growing of trees. Trees are allowed to grow to the largest possible extent.
- For prediction, one needs to count the votes for a predicted class from each tree, and the most voted one is considered as the finally predicted class.

Unlike other tree, it can overcome the disadvantage of data over-fitting. As Random forest creates multiple trees, it helps to incorporate additional randomness to the algorithm and delivers a more robust model. In this study random forest is built using 100 decision trees. The k fold cross validation is used to check the accuracy and dependability of the model.The method works by randomizing and splitting the entire learning set into k parts. Each part is held out once as a test set and the remaining $k-1$ fold are used to train the model. Finally, a cumulative accuracy measure from this k number of run are produced. The advantage of this method is, each instance is assigned to a group for the entire process, and hence, becomes a part of test set one time. A value of $k = 10$ has been used in our study, presented in Chapter 6.

Handling of class imbalance by cost sensitive method

In reality, class imbalance is one of problems that often arises and can hinder the performance of the ML algorithm. It incorporates bias in the model due to the fact that large number of samples belong to a particular class with respect to others. Cost sensitive learning is commonly used to over this class imbalance.

General classification algorithms work by minimizing the error rate which is the percentage of misclassified prediction and the cost of misclassification error is equal for all classes. But in practical cases especially when the data set having

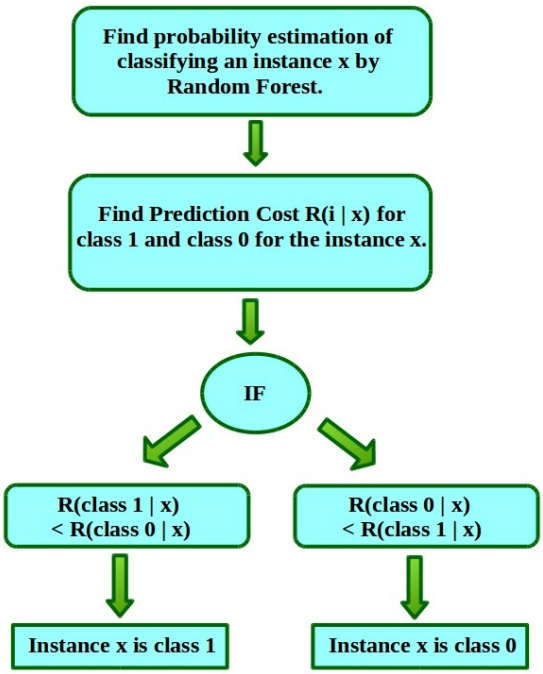

Figure 2.17: Flowchart of cost sensitive learning. Here Class 1 represents the positive class and Class 2 represents the negative class.

class imbalance, the difference of misclassification error between minority and majority classes become important. Hence cost sensitive learning considers cost of misclassification of different classes separately. The cost sensitive algorithm can be summarized as follows. Without loss of generality binary classification (positive class denoted by 1 and negative class denoted by 0) can be considered to describe the method. The cost matrix is a 2×2 matrix in this case where the diagonal elements denote true negative, true positive and off-diagonal elements represent false negative and false positive respectively. A instance x classified into class can be expressed in terms of expected cost $R(i|x)$ as:

$$R(i|x) = \sum_{i=1} P(j|x)C(i,j)$$

where $P(j|x)$ is the probability estimation for classifying an instance x into class j and $C(i,j)$ represents the elements of cost matrix. So an instance x will be classified into positive class if:

$$P(0|x)C(1,0) + P(1|x)C(1,1) \leqslant P(0|x)C(0,0) + P(1|x)C(0,1)$$

Considering the cost of correct classifications equal to zero, we can rewrite the previous expression as:

$$P(0|x)C(1,0) \leqslant P(1|x)C(0,1)$$

Since $P(0|x) = 1 - P(1|x)$, we can define a threshold p^* for classifying an instance x into class 1 if $P(1|x) \geqslant p^*$ with

$$p^* = \frac{C(1,0)}{C(1,0) + C(0,1)}$$

This can be implemented as follows. If negative examples are considered as majority class then all the components should be multiplied by $\frac{C(1,0)}{C(0,1)}$ which is less than 1. This is generally termed as "under-sampling of majority class". Cost sensitive learning can be achieved in two different ways. In the first case which is called direct cost-sensitive Learning where miss-classification cost is utilized within the learning algorithm itself. The second one is known as cost-sensitive meta learning [60] where cost sensitive (meta-learning) wrapper is used to convert cost insensitive classifier (in this thesis we used random forest algorithm) into a sensitive one as shown in Fig. (2.17).

2.9.4 Prediction of new compounds

Finally, the developed machine learning model is used to predict the class of new instances. For that one needs to create a dataset containing new instances and the corresponding attributes considered at the time of learning of the algorithm. The trained algorithm predicts the class of each instances in terms of some probability. The instances with high prediction rate are generally accepted for further investigation. In our case the instances are unknown compounds. The details are discussed in Chapter 6.

Bibliography

[1] M. Born and J. R. Oppenheimer, Ann. Physik **84**, 457 (1927).

[2] D. R. Hartree, Proc. Cambridge Phil. Soc. 24, **89**, 111 (1928).

[3] C. C. J. Roothaan, Rev. Mod. Phys. **23**, 69 (1951).

[4] Sherrill, C. D., An Introduction to Configuration Interaction Theory. 1995.

[5] P. Hohenberg and W. Kohn, Phys. Rev. B **136**, 864 (1964).

[6] W. Kohn and L. J. Sham, Phys. Rev. A **140**, 1133 (1965).

[7] Nobel Lecture: "Electronic structure of matter wavefunctions and density function- als by W. Kohn, Reviews of Modern Physics, **71**, 1253 (1999).

[8] L. H. Thomas, "The calculation of atomic fields". Proc. Cambridge Phil. Soc. 23 (5) 542548 (1927).

[9] E. Fermi, "Un Metodo Statistico per la Determinazione di alcune Priopriet dell'Atomo". Rend. Accad. Naz. Lincei **6** 602607 (1927).

[10] D.M. Ceperley and B.J. Alder, Phys. Rev. Lett. **45**, 566 (1980).

[11] J. P. Perdew and A. Zunger, Phys. Rev. B **23**, 5048 (1981).

[12] J. P. Perdew and Y. Wang, Phys. Rev. B, **45**, 13244 (1992).

[13] R .O. Jones and O. Gunnarson. The density functional formalism, its applications and prospects. Rev. Mod. Phys. **61**, 689 (1989).

[14] D .C.Langreth and M. Mehl, Phys. Rev. Lett. **47**, 446 (1981).

[15] J. P. Perdew and Y. Wang, Phys. Rev. B, **33**, 8800 (1986).

[16] J. P. Perdew, in Electronic Structure of Solids 91, edited by P. Ziesche and H. Eschrig (Akademie Verlag, Berlin, 1991), p. 11.

[17] A. D. Becke, Phys. Rev. A, **38**, 3098 (1988).

[18] C. Lee, W. Yang, and R. G. Parr, Phys. Rev. B, **37**, 785 (1988).

[19] J. P. Perdew, K. Burke and M. Ernzerhof, Phys. Rev. Lett. **77**, 3865 (1996).

[20] O. K. Andersen, Phys. Rev. B **12**, 3060 (1975).

[21] O. K. Andersen and O. Jepsen, Phys. Rev. Lett. **53** 2571 (1984).

[22] O. K. Andersen and T. Saha-Dasgupta, Phys. Rev. B **62**, R16219 (2000).

[23] G. Kresse and J. Furthmuller, Phys. Rev. B **54**, 11169 (1996).

[24] O. Jepsen, J. Madsen, and O. K. Andersen, Phys. Rev. B **18**, 605 (1978).

[25] P. Blaha, K. Schwarz, G. Madsen, D. Kvasnicka, and J. Luitz, in WIEN2k, An Augmented Plane Wave + Local Orbitals Program for Calculating Crystal Properties, edited by K. Schwarz (Technische Universitiat Wien, Vienna, 2001).

[26] O. K. Anderson, Phys. Rev. B **12**, 3060 (1975).

[27] D. R. Hamann, M. Schlter, and C. Chiang, Phys. Rev. Lett. **43**, 1494 (1979).

[28] D. Vanderbilt, Phys. Rev. B **41**, 7892 (1990).

[29] P. E. Blöchl, Phys. Rev. B **50**, 17953 (1994).

[30] A. I. Liechtenstein, V. I. Anisimov, and J. Zaanen, Phys. Rev. B **52**, R5467 (1995).

[31] O. Gunnarsson, O. K. Andersen, O. Jepsen and J. Zaanen, Phys. Rev. B **39**, 1708 (1989).

[32] V. I. Anisimov, and O. Gunnarsson, Phys. Rev. B **43**, 7570 (1991).

[33] S. L. Dudarev, G. A. Botton, S. Y. Savrasov, C. J. Humphreys and A. P. Sutton, Phys. Rev. B **57**, 1505 (1998).

[34] A. Georges, G. Kotliar, W. Krauth, and M. J. Rozenberg, Rev. Mod. Phys. 68, **13** (1996).

[35] W. Metzner and D. Vollhardt, Phys. Rev. Lett. **62**, 324 (1989).

[36] E. Müller-Hartmann, Z. Phys. B **74**, 507 (1989).

[37] M. Jarrell, Phys. Rev. Lett. **69**, 168 (1992).

[38] K. Held, Advances in Physics **6**, 829 (2007).

[39] A. Georges and G. Kotliar, Phys. Rev. B, **45**, 6479 (1992).

[40] E. Muller-Hartmann, Z. Phys. B **76**, 211 (1989).

[41] M. J. Rozenberg, X. Y. Zhang and G. Kotliar, Phys. Rev. Lett. **69**, 1236 (1992).

[42] M. Caffarel and W. Krauth, Phys. Rev. Lett. **72**, 1545 (1994).

[43] J. C. Schön, M. Jansen, First step towards planning of syntheses in solid-state chemistry: Determination of promising structure candidates by global optimization, Angew. Chem. Int. Ed. 35 (1996) 12871304.

[44] R. Martonk, A. Laio, M. Parrinello, Predicting crystal structures: The Parrinello-Rahman method revisited, Phys. Rev. Lett. **90**, 075503 (2003).

[45] S. Gödecker, Minima hopping: An efficient search method for the global minimum of the potential energy surface of complex molecular systems, J. Chem. Phys. 120 (2004) 99119917.

[46] Oganov A.R.; Glass C.W. *J Phys: Condens Matter* **20**, 064210 (2008).

[47] Oganov, A. R.; Glass, C.W. *J. Chem. Phys.* **124**, 244704 (2006).

[48] Lyakhov, A.O.; Oganov, A.R.; Valle, M. In *Modern Methods of Crystal Structure Prediction;* Oganov, A.R., Eds.; Wiley-VCH Verlag GmbH & KGaA : Weinheim, Germany, 2012.

[49] Colin W. Glass, Artem R. Oganov and Nikolaus Hansen, USPEX − Evolutionary crystal structure prediction, Computer Physics Communication **175** (2006).

[50] P. Sanyal and P. Majumdar, Phys. Rev. B, **80**, 054411 (2009).

[51] H.Q. Lin, J.E. Gubernatis, Harvey Gould, and Jan Tobochnik, Computers in Physics **7**, 400 (1993).

[52] S. Kumar and P. Majumdar, Eur. Phys. J. B **46**, 315 (2005).

[53] S. Kumar and P. Majumdar, Eur. Phys. J. B **50**, 571 (2006).

[54] Quinlan. J. R, C4.5: Programs for Machine Learning, Morgan Kaufmann Publishers, (1993).

[55] Mahmood. A. M., Satuluri. N , and Kuppa. M. R. , International Journal of Research and Reviews in Ad Hoc Networks **1**, (2011).

[56] Breiman. Leo, Machine Learning. **45**, 5 (2001).

[57] Mohamed. W. N. H. W., Salleh. M. N. M., and Omar. A. H., 2012 IEEE International Conference on Control System, Computing and Engineering, A comparative study of Reduced Error Pruning method in decision tree algorithms, **392** (2012).

[58] Ho, Tin Kam (1995). Random Decision Forests (PDF). Proceedings of the 3rd International Conference on Document Analysis and Recognition, Montreal, QC, 1416 August 1995. pp. 278282. Archived from the original (PDF) on 17 April 2016. Retrieved 5 June 2016.

[59] Breiman L (2001). "Random Forests". Machine Learning. 45 (1): 532. doi:10.1023/A:1010933404324.

[60] Francisco Azuaje, Ian Witten, and Frank E. Witten ih, frank e: Data mining: Practical machine learning tools and techniques. Biomedical Engineering Online - BIOMED ENG ONLINE, 5:12, 01 (2006).

Chapter 3

Magnetism in Sr_2CrMoO_6: A Combined Ab-initio and Model Study*

3.1 Introduction and motivation

The family of double perovskite compounds with general formula $A_2BB'O_6$ are in limelight after the report of low field magnetoresistance and half-metallicity in Sr_2FeMoO_6 (SFMO). The high magnetic transition temperatures (T_c) exhibited by the compounds like SFMO, open up the possibility of room temperature application. [1, 2] In this context to understand the dependence of $3d$ transition metal (TM) ion on the properties of these compounds, many double perovskites with $3d$ transition metal at B site have been investigated. Following this motivation, Cr-based double perovskites have been synthesized and studied, [3] in particular, the sister compound of SFMO, Sr_2CrMoO_6 (SCMO). [4] Like SFMO, SCMO is also a half metal with high transition temperature of $\sim 420K$. Unlike in SFMO, there can be no valence compensation between Cr and the Mo in SCMO: Cr can only be in the 3+ state making Cr^{3+}/Mo^{5+} only possible combination, while for SFMO, both Fe^{3+}/Mo^{5+} and Fe^{2+}/Mo^{6+} combinations are possible. Thus, one can expect SCMO as an even better candidate for room temperature spintronics. But unfortunately, the observed moment [5] and the magnitude of the tunneling magnetoresistance were found out to be disappointingly low although the measured transition temperature of SCMO is high. [4, 6] The large antisite disorder estimated to be as high as 43-50 %. [4, 7] together with oxygen vacancy [6]

*This chapter is based on publication : Prabuddha Sanyal, **Anita Halder**, L. Si, M. Wallerberg, K. Held and Tanusri Saha-Dasgupta, *Phys. Rev. B* **94**, 035132 (2016).

were held responsible for lowering the magnetic moment. To appreciate the role of $3d$ TM in the properties of double perovskites, it is thus highly desirable to understand the electronic and magnetic properties of pure, defect free SCMO.

There are few theoretical studies available on SCMO which were carried out within the framework of DFT. [8, 9] However in these studies, no microscopic analysis has been provided. The transition temperature has been calculated in a single study, where a mean field analysis of the finite temperature behavior has been carried out, [10] but based on classical Ising model, which neglects completely the itinerant electronic character of Mo $4d$ electrons, a crucial component in understanding the behavior of these $3d$-$4d$ double perovskites.

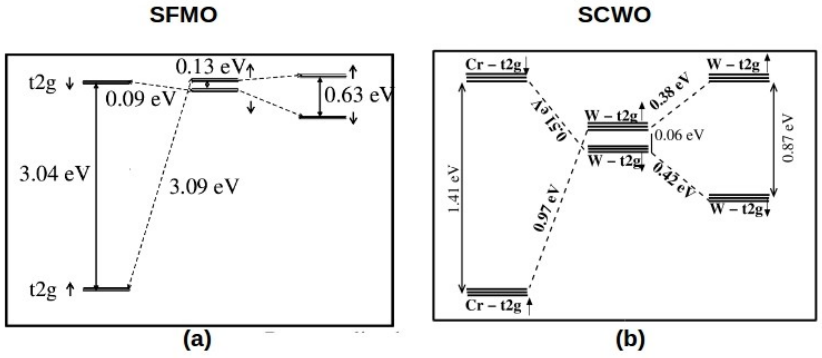

Figure 3.1: The energy level diagram for (a) SFMO and (b) SCWO, in the absence and presence of the B-B′ hybridization. The energies are in units of eV. Figures are adapted from Ref [11], [12].

Furthermore, the hybridization driven mechanism of magnetism has been identified [13] as the driving force in setting up the high Curie temperature in compounds like SFMO (see the energy level diagram of Fig. (3.1-a)) as already discussed in section 1.5.2. As it appears, SFMO is not only example showing hybridization driven magnetism. The energy level diagram of Sr_2CrWO_6 (SCWO) [3] which is a double perovskite from the Cr family but with $5d$ W instead of $4d$ Mo shows a remarkable similarity with SFMO. Note, SCWO is also a member of half metallic ferromagnetic double perovskite family with transition temperature of $\sim 458K$. The energy level diagram of SCWO as shown in Fig. (3.1-b) reveals that the W t_{2g} levels lie between the exchange split of Cr t_{2g} levels. Thus introduction of hybridization between Cr and W, induces a renormalized spin splitting at otherwise nonmagnetic W site, as found in SFMO.

Therefore to understand the mechanism of magnetism operative in SCMO, which is from Cr family as in SCWO, and from Mo family as in SFMO, we performed a microscopic study combining the state-of-art DFT calculations and exact diagonalization study of the ab-initio derived model Hamiltonian, comparison with SFMO and SCWO.

We further studied the effect of correlation on the half-metallic property of SCMO by including local correlations on top of DFT within the framework of dynamical mean field theory (DMFT).

3.2 Computational Details

The first-principles DFT calculations have been carried out using the plane-wave pseudopotential method implemented within the Vienna Ab-initio Simulation Package (VASP). [14] The exchange-correlation functional was considered within the generalized gradient approximation (GGA) in the framework of PW91 (Perdew - Wang 91) [15], local-density approximations (LDA) [16] as well as GGA within the framework of PBE (Perdew-Burke-Ernzerhof) [17]. The projector-augmented wave (PAW) potentials [18] were used and the wavefunctions were expanded in the plane-wave basis with a kinetic-energy cutoff of 500 eV. Reciprocal-space integrations were carried out with a k-space mesh of 8 × 8 × 8.

In order to extract a few-band tight-binding (TB) Hamiltonian out of the full DFT calculation which can be used as input to multiorbital, low-energy model Hamiltonian in exact diagonalization calculations we have carried out N-th order muffin tin orbital (NMTO) calculations. [19] In order to cross-check the TB parameters generated out of NMTO-downfolding calculations, further calculations were carried out using wien2wannier [20]. This generates maximally localized Wannier functions [21] from Wien2K [22] which employs a full potential linear augmented plane wave (FLAPW) basis. For self-consistent DFT calculation in the FLAPW basis the number of k-points in the irreducible Brillouin zone was chosen to be 64. The commonly used criterion relating the plane wave and angular momentum cutoff, $l_{max} = R_{MT} \times K_{max}$ was chosen to be 7.0, where R_{MT} is the smallest MT sphere radius and K_{max} is the plane wave cutoff for the basis. The chosen atomic radii for Sr, Cr, Mo and O were 1.43 Å, 1.01 Å, 1.01 Å, and 0.87 Å, respectively.

The DFT+DMFT calculations [23, 24] have been carried out using the wien2-wannier [20]-derived maximally localized Wannier functions of Wien2K as a starting point. For the interaction values we chose the typical values for $3d$ and $4d$ transition metal oxides. The choices were: interorbital Coulomb repulsion of $U' = 4\,\text{eV}$ (2.4 eV) and a Hund's coupling $J_H = 0.7\,\text{eV}$ (0.3 eV) for Cr (Mo) as estimated for neighboring vanadium [25](ruthenium [26]) perovskites. The intraorbital (Hubbard) repulsion follows from orbital symmetry as $U = U' + 2J_H$; and the pair hopping term is of equal strength as J_H. As a DMFT impurity solver, continuous-time quantum Monte-Carlo simulations [27] in the w2dynamics [28] implementation was used which includes the full SU(2) symmetry. The effect of electronic correlations beyond GGA, within the framework of static theory was

also checked by performing GGA+U calculations with choice of same U parameters, as in DMFT calculation. We have also checked the validity of our results by varying the U value by +/-1 eV at Cr site, and by +/-0.5 eV at Mo site. The trend in the results was found to remain unchanged.

3.3 Results

3.3.1 Basic DFT Electronic Structure

We first revisit the basic DFT electronic structure of SCMO, which has been calculated before using variety of basis sets, including plane wave, [29] LAPW [8] and LMTO. [9] SCMO crystallizes in the cubic Fm3m space group (225), with lattice parameter of 7.84 Å. [6] The crystal structure of ordered SCMO is shown in Fig. (3.2) where Cr and Mo octahedra are in rock salt ordering.

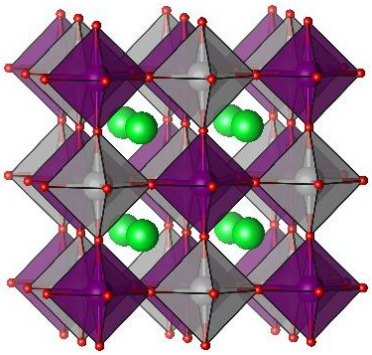

Figure 3.2: Crystal structure of SCMO: CrO_6 and MoO_6 octahedra are presented in violet and grey colour respectively. Sr and O atoms are shown in green and red balls respectively.

The Fig. (3.3) shows the spin polarized density of states (DOS) calculated in a plane wave basis. The basic features of the DOS are similar with previous studies [8, 9, 29]. The states close to Fermi level, E_F, (set as zero in the figure), are dominated by Cr and Mo d states hybridized with O p states. The states of dominant O p character are positioned further down in energy, separated by a small gap from Cr and Mo d states. Empty Sr states are not shown in the energy range of the figure, remain far above E_F. The empty Mo e_g states lie far above E_F as a result of the large octahedral crystal field at Mo sites. The Cr t_{2g} states are occupied in the up spin channel and empty in the down spin channel. Cr e_g states are empty in both spin channels, in agreement with the nominal Cr^{3+} (d^3) valence. The empty and highly peaked Mo t_{2g} states in the up spin channel appear in between the crystal field split Cr t_{2g} and Cr e_g states for the same spin.

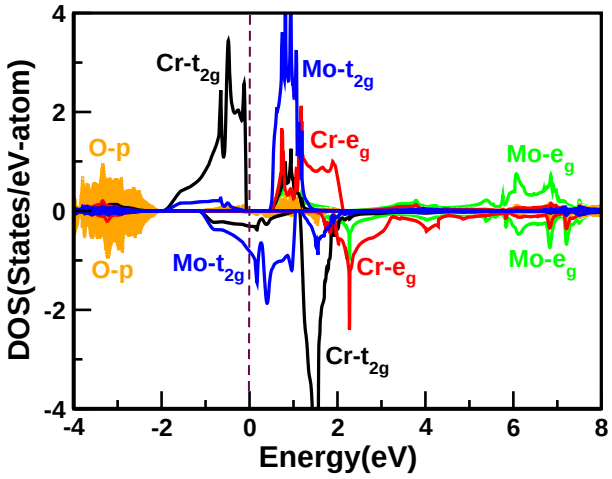

Figure 3.3: Spin-polarized DOS projected onto Cr t_{2g} (black solid line), Cr e_g (red solid line), Mo t_{2g} (blue solid line), Mo e_g (green solid line) and O p (shaded yellow area). The zero of the energy is set to the Fermi energy.

In contrast for the down spin channel, the Mo t_{2g} hybridize more strongly with Cr t_{2g}, which explains their much larger bandwidth.

The above described basic features for B and B$'$ states, are rather similar for SCMO and SFMO, [11] and in that respect also for SCWO. [12] We noticed that the main difference between the DOS of SCMO from both SFMO and SCWO is the hybridization between B t_{2g} and B$'$ t_{2g} in the down spin channel. It is found to be significantly lower in SCMO compare to that of SFMO or SCWO. [11, 12] A measure of this is the Cr contribution in the down spin bands crossing E_F of predominant Mo character. We estimated this contribution or admixture to be 35% for SCMO, while the corresponding estimates for SCWO and SFMO are much larger, 66% and 72 %, respectively.

The top rows in Table (3.1) show the calculated magnetic moments at Cr and Mo sites, as well as the total moment in three choices of exchange-correlation functionals, GGA-PW91, GGA-PBE as well as LDA in order to check any possible influence of the exchange-correlation functional on the calculated electronic structure. In all cases, the half-metallic nature of the ground state is found to be robust with the total magnetic moment of 2.0 μ_B/f.u. (cf. Table (3.1)) and finite moments residing at O sites. As is seen, while the individual moments on Cr and Mo are found to vary depending on the nature of approximation, the magnetic moments on Cr and Mo site being aligned in an antiparallel manner, the enhancement/reduction of individual moments cancel, thereby retaining the half-metallicity and net moment of 2 μ_B/f.u. We found that our calculated GGA magnetic moments at Cr and Mo sites are in good agreement with that reported by Liet *et al.* [29] whereas, the calculated site-specific moment reported

	Sr	Cr	Mo	total
LDA	0.00	-2.18	0.32	-2.00
GGA-PW91	0.00	-2.29	0.43	-2.00
GGA-PBE	0.00	-2.36	0.49	-2.00
GGA+U	0.00	-2.54	0.58	-2.00
DMFT	0.00	-2.84	0.84	-2.00

Table 3.1: Calculated magnetic moments (in μ_B) within LDA, GGA-PW91, GGA-PBE, GGA+U and DMFT. Note that within GGA there is also a moment on the oxygen sites which is accounted for in the Cr and Mo moment in DMFT as the predominately metal d Wannier functions also have some oxygen admixture.

by Wu [9] is much smaller than that of our as well as that of Liet *et al.* [29] This is presumably due to different choices of the muffin tin radii as well as the exchange-correlation functional.

The magnetic moments as measured in experiments are significantly smaller than the theoretical values. Experimentally, the total moment is only 0.5 μ_B [5] and the moment on the Cr sites is 0.8 μ_B. [30] This discrepancy can be argued in terms of the presence of large disorder in the sample. [6]

We notice that the value of the calculated GGA-PW91 magnetic moment at the Mo sites (0.43 μ_B) is larger than the calculated B$'$ site moment for SFMO (0.23 μ_B) and SCWO (0.30 μ_B). This indicates a weaker itinerancy of the Mo electrons in SCMO, compared to SFMO or to that of W in SCWO, which suggests that a small, but finite intrinsic moment develops at the Mo site as a consequence of the weaker hybridization between Cr and Mo. The suppression of the hybridization and the reduced itinerancy of the Mo t_{2g} electrons in SCMO has been also pointed out in the study by Wu, [9] though no detailed understanding of the mechanism of magnetism was provided.

3.3.2 DMFT Spectral Density

In order to study the effect of electronic correlations, specially the dynamical correlation which may be important for SCMO due to the metallic nature of the ground state, we further carried out DMFT calculations in the Wannier function basis. Fig. (3.4) shows the DMFT spectral density calculated at a temperature of 200 K. We restricted the DMFT to the low energy degrees of freedom, i.e., to the "t_{2g}" orbitals of Mo and the "t_{2g}" and "e_g" orbitals of Cr (These low energy orbitals are actually a mixture between predominately transition metal t_{2g} (e_g) character with some admixture of oxygen p character). We supplemented the DFT low-energy Hamiltonian in the Wannier basis by a local Coulomb interaction

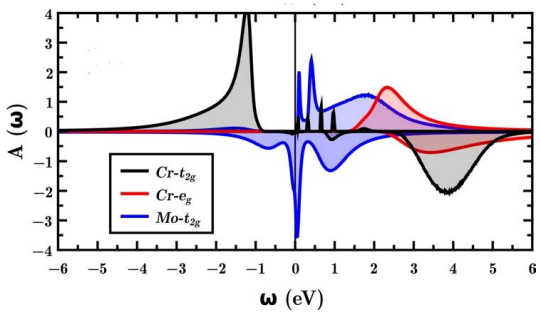

Figure 3.4: Upper panel: GGA-PW91 DMFT spectral density, calculated at 200 K within the Mo t_{2g} and Cr $t_{2g} + e_g$ Wannier basis. [31]

in Kanamori parametrization. For details see Ref. [28].

The spectrum shows qualitatively similar behavior to that obtained in DFT calculation, though the down spin spectrum shows the correlation physics with a feature resembling lower and upper Hubbard bands and a well defined quasiparticle peak at Fermi energy. This demonstrates the dual nature of the Mo down spin with localized electrons (Hubbard bands) and itinerant electrons (quasiparticle band) at the same time. The fully spin-polarized conducting electrons are Fermi-liquid-like with a linear frequency-dependence of the self energy (not shown). Hence the quasiparticle peak will lead to a Drude peak in the optical conductivity.

The DMFT magnetic moments are shown in the last row of Table (3.1). It is seen that the DMFT calculated magnetic moments are in the basis of Cr and Mo t_{2g} Wannier functions, which includes the effect of oxygen. This makes a direct comparison between DMFT and GGA values somewhat more difficult. However since the difference between GGA and DMFT magnetic moments is larger than the GGA oxygen contribution, it can be concluded that electronic correlations somewhat enhance the magnetic moment on both, Mo and Cr, sites. This is further supported by the magnetic moments calculated within the static theory of GGA+U, with choice of same U parameters as in DMFT calculation, shown in the second row of Table (3.1), which shows an enhancement of the moment both at Cr and Mo sites, compared to that of GGA.

3.3.3 Few-orbital, low-energy Hamiltonian

In order to understand the driving mechanism of magnetism in SCMO in a more quantitative manner, we carried out a NMTO downfolding in order to estimate the positions of exchange split Mo t_{2g} energy levels, before and after switching on the hybridization between the Mo t_{2g} and Cr t_{2g}. The former provides the estimate of intrinsic spin splitting at the Mo site, while the latter provides the information of the spin splitting at the Mo site renormalized by the hybridization effect from

Cr t_{2g}. As a first step of this procedure, we downfolded O p, Sr as well as Cr and Mo e_g degrees of freedom. This defines a few-orbital Hamiltonian consisting of Cr t_{2g} and Mo t_{2g} states. In the second step, we performed a massive downfolding, keeping only the Mo t_{2g} degrees of freedom, i.e., downfolding everything else including the Cr t_{2g} degrees of freedom. On site matrix elements of the few orbital Hamiltonian in real space representation defined in the Cr t_{2g} - Mo t_{2g} basis and the massively downfolded basis give the energy level positions before and after switching of the hybridization, respectively. The obtained result is presented in Fig. (3.5). First of all, we noticed that the Mo t_{2g} states are energetically situated in between the exchange-split energy levels of Cr t_{2g}'s. Thus switching of the hybridization between Cr and Mo, pushes the Mo up spin states down because these are below the Cr states of the same spin. In contrast, the Mo down spins are above their Cr counterpart and hence the hybridization shifts them upwards. Thus the hybridization induces a renormalization of the spin splitting at the Mo site, with renormalized value of about 0.70 eV, and being oppositely oriented (negative) with respect to that at Cr site. Note the intrinsic (in absence of hybridization) spin splitting at Mo site is small, having a value of 0.15 eV.

In this respect, the situation is very similar to SFMO or SCWO as can be seen from Fig. (3.1), for which also a negative splitting is induced at the itinerant B$'$ sites because of the hybridization with the large spin at the B sites. [1, 12, 13, 32] This supports that the hybridization-driven mechanism is operative in SCMO as well. While in all three cases of SFMO, SCWO and SCMO, the B$'$ t_{2g} states appear in between the strong exchange split energy levels of B site, which is an essential ingredient for hybridization-driven mechanism to be operative, we noticed the relative energy position of B$'$ t_{2g} states with respect to the exchange split B states is different in case of SCMO, as compared to SFMO or SCWO. For SFMO or SCWO, the down spin B$'$ t_{2g} states appear very close to B site down spin states, while for SCMO, they are shifted down. [1, 12] This hints towards a significantly different charge transfer energy in case of SCMO as compared to SFMO or SCWO. This will be elaborated in the next paragraphs. We further noticed that the intrinsic splitting at the Mo sites (0.15 eV) is somewhat larger than for SCWO (0.05 eV) (see Fig. (3.1-b)). [12] This further confirms the conclusion drawn from the calculated magnetic moment at Mo site that is in SCMO, unlike SFMO, Mo has a finite intrinsic moment. The magnetism in SCMO, as mentioned already, thus has an additional contribution, originating from the superexchange between the large moment at the Cr site and the intrinsic moment at the Mo site, on top of the hybridization-driven mechanism, as operative in SFMO. Note that the superexchange is antiferromagnetic, aligning the Cr and Mo moments antiparallely, *i.e.*, in the same way as for the hybridization-driven mechanism.

In this situation, the low-energy model Hamiltonian for SCMO in the Cr t_{2g} and Mo t_{2g} Wannier basis, describing the hybridization and super-exchange

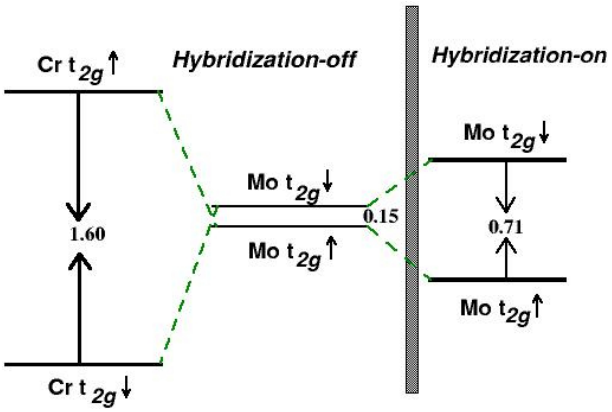

Figure 3.5: The energy level diagram for SCMO, in the absence and presence of the Cr-Mo hybridization. The energies are in units of eV.

mechanism is given by [12, 33]

$$\begin{aligned} H &= \epsilon_{Cr} \sum_{i\in B} f^{\dagger}_{i\sigma\alpha} f_{i\sigma\alpha} + \epsilon_{Mo} \sum_{i\in B'} m^{\dagger}_{i\sigma\alpha} m_{i\sigma\alpha} \\ &\quad -t_{Cr-Mo} \sum_{<ij>\sigma,\alpha} f^{\dagger}_{i\sigma,\alpha} m_{j\sigma,\alpha} \\ &\quad -t_{Mo-Mo} \sum_{<ij>\sigma,\alpha} m^{\dagger}_{i\sigma,\alpha} m_{j\sigma,\alpha} \\ &\quad -t_{Cr-Cr} \sum_{<ij>\sigma,\alpha} f^{\dagger}_{i\sigma,\alpha} f_{j\sigma,\alpha} + J \sum_{i\in Cr} \mathbf{S}_i \cdot f^{\dagger}_{i\alpha} \vec{\sigma}_{\alpha\beta} f_{i\beta} \\ &\quad +J' \sum_{i\in Cr, j\in Mo} \mathbf{S}_i \cdot \mathbf{s}_j \ . \end{aligned} \tag{3.1}$$

Here the f's and m's are second quantization operators for the Cr t_{2g} and Mo t_{2g} degrees of freedoms; σ is the spin index and α is the orbital index that spans the t_{2g} manifold; t_{Cr-Mo}, t_{Mo-Mo}, t_{Cr-Cr} represent the nearest neighbor Cr-Mo, the second nearest neighbor Mo-Mo and the Cr-Cr hopping, respectively. The on-site energy difference between Cr t_{2g} and Mo t_{2g} levels is $\Delta = \epsilon_{Cr} - \epsilon_{Mo}$. To take into account the dual nature of the electrons that are both, itinerant and localized, we include a large core spin $\mathbf{S}_i$ at the Cr site that couples with the itinerant electron delocalized over the Cr-Mo network, via a double-exchange like mechanism. The last term represents the superexchange mechanism in terms of coupling between the Cr spin ($\mathbf{S}_i$) and the intrinsic moment on the Mo site (s_j). All TB parameters of the model Hamiltonian, i.e., Δ, t_{Cr-Mo}, t_{Mo-Mo}, t_{Cr-Cr}, are extracted from a non-spin-polarized DFT calculations through two independent means: a) through the NMTO downfolding technique, and b) through the construction of maximally localized Wannier functions in the basis of the effective Cr and Mo t_{2g} degrees of

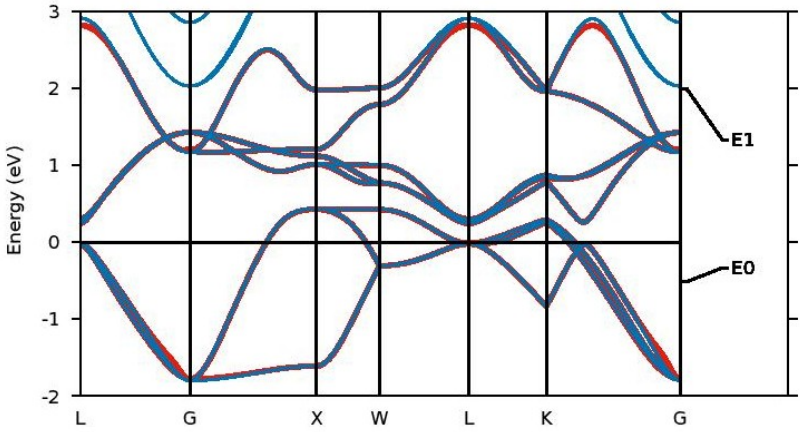

Figure 3.6: The downfolded, tight-binding band structure of SCMO in effective Cr-Mo t_{2g} basis (in red lines) in comparison with full band structure (in blue lines). Zero of the energy is set at Fermi energy. E0 and E1 represent the energy points about the expansion were carried out in NMTO calculation.

freedom. The latter scheme has been also employed in the DMFT study, presented before. In both cases we integrate out all other degrees of freedom except for the Cr and Mo t_{2g}'s states. The comparison of constructed real space bands and the full DFT bands in NMTO technique are shown in Fig. (3.6) whereas Fig. (3.7) shows the comparison of the full DFT non spin-polarized band structure and the few orbital TB bands in maximally localized Wannier function basis. The agreement between the two is found to be as good as possible, proving the effectiveness of the Wannier function projection.

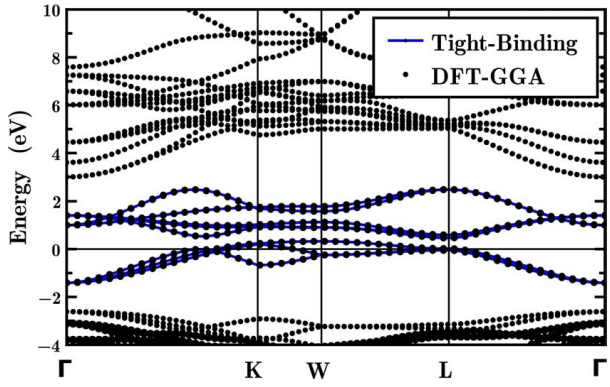

Figure 3.7: Comparison of the full paramagnetic DFT band structure (solid line) and the few orbital TB band structure (+) plotted along a high symmetry path through the Brillouin zone [Γ: (0 0 0), K: (3/8,3/4,3/8), W: (1/4,3/4,1/2), L: (1/2,1/2,1/2) and X: (0,1/2,1/2)].

	Δ	t_{Cr-Mo}	t_{Mo-Mo}	t_{Cr-Cr}
SCMO (NMTO)	-0.35	0.33	0.14	0.08
SCMO (Wannier90)	-0.42	0.30	0.12	0.06
SCWO	-0.66	0.35	0.12	0.08
SFMO	-1.04	0.26	0.11	0.04

Table 3.2: Tight-binding parameters (in eV) of the few orbital Hamiltonian for SCMO, SCWO [12], and SFMO [11] in Wannier function basis, extracted out of DFT calculations.

The DFT estimates of Δ, t_{Cr-Mo}, t_{Cr-Cr} and t_{Mo-Mo}, obtained by two different scheme of calculations are shown in Table (3.2). The agreement of the values in two independent scheme of calculations is remarkable and provides confidence regarding the results. The TB parameters for SCWO [12] and SFMO [11] are also listed in the table for comparison.

While the estimated hopping parameters of SCMO are rather similar to that reported for SCWO, [12] we found the charge transfer energy Δ (-0.4 eV) to be quite different from that estimated for SFMO (-1.0 eV) [11] and for SCWO (-0.7 eV). [12] This forms the most crucial observation of our study, which dictates the differences in electronic structure of SCMO and, SFMO and SCWO. Related discussions involving importance of Δ and t in hybridization driven mechanism were mentioned by another group for comparisons between SFMO and A-site B-site randomly doped Ti oxides although it was not a systematic one. [34]

The change in the bare, non-spin-polarized charge transfer energy (Δ), in turn, modifies the renormalized charge transfer energy Δ_R between Cr and Mo in the down spin channel in the spin-polarized phase. It is much larger in SCMO (0.81 eV) compared to that in SCWO (0.51 eV), [12] due to the moving down the column of the periodic table from the 4d element Mo in SCMO to the 5d element W in SCWO. As a consequence of the larger charge transfer splitting Δ_R the effect of the hybridization which is governed by t^2_{Cr-Mo}/Δ_R is significantly suppressed in SCMO, by about 63% compared to the corresponding value for SCWO.

The parameter involving J in Eqn. (3.1) corresponds to the spin-splitting at the Cr site, while $J^{'}$ is obtained from the enhanced intrinsic spin-splitting observed at Mo site in case of SCMO as compared to that for SCWO compound at the W site. As discussed below, frustration effects make the convergence of total energy calculations in different spin configurations difficult, prohibiting direct extraction of $J^{'}$ in a single system. Thus $J^{'}$ needs to be determined by comparison of the independently obtained intrinsic spin splittings (obtained by turning off the B-B$^{'}$ hybridization) at the B$^{'}$ sites of the related compounds. This approach was used earlier, [12] where three compounds Sr_2CrWO_6, Sr_2CrReO_6

and Sr_2CrOsO_6 were considered. It was pointed out [12] that the intrinsic splitting at the B site due to a purely hybridization driven mechanism should increase proportional to the electron filling at B$'$ site (the filling increases from 1 to 2 to 3 moving from W to Re to Os); the additional increase, if any, is due to the presence of the localized moment at B$'$ site giving rise to superexchange J' between B and B sites. In the present case, all the three compounds considered, namely SFMO, SCMO and SCWO have the same electron filling, namely 1. Hence considering the compound SCWO as the benchmark, the difference in intrinsic splitting between the Mo site of SCMO and the W site of SCWO is used to obtain the J' value for SCMO. [35]

3.3.4 Exact Diagonalization of Model Hamiltonian

As the magnetism of SCMO turns out to be driven by both hybridization-driven mechanism and superexchange mechanism, the calculation of magnetic transition temperature in a first-principles way is challenging. For example, an antiferromagnetic configuration of Cr spins leads to a frustration of the intrinsic Mo moment. On the other hand, the hybridization-driven mechanism, disfavors the stabilization of magnetic configurations with Cr spins aligned in parallel to the spins at Mo sites. This thus leads to a frustration effect which makes the convergence of different spin configurations to extract the magnetic exchanges a challenge within the framework of full blown DFT scheme.

Hence, we considered the model Hamiltonian approach in the following. To this end, we solved the ab-initio constructed model Hamiltonian Eqn. (3.1) using exact diagonalization on a finite lattice. In particular, we considered the stability of the ferromagnetic arrangements of Cr spins measured as the energy difference between the paramagnetic (PM) spin configuration and the ferromagnetic (FM) spin configuration. The PM phase was simulated as disordered local moment calculations, where the calculations were carried out for several (≈ 50) disordered configurations of Cr spin and were averaged to get the energy corresponding to PM phase. This energy difference provides an estimate of the magnetic T_c. The exact diagonalization were carried out for finite-size lattices of dimensions $4\times4\times4$, $6\times6\times6$, and $8\times8\times8$. The results presented in the following are for $8\times8\times8$ lattice.

In order to check the influence of the intrinsic moment at the Mo site on the magnetic transition, we first carried out exact diagonalization calculation considering the Mo site to be totally nonmagnetic, i.e., setting the last term of Hamiltonian (3.1) to zero. This boils down to a hybridization-only driven mechanism of magnetism, as suitable for SFMO or SCWO. [12, 36] The energy difference between the PM and FM in this calculation, turned out to be 0.067 eV/f.u., which is of the same order as, but less than, that obtained using the TB parameters of SCWO (0.085 eV/f.u). [12, 37] As mentioned already, the hopping parameters between SCMO and SCWO are very similar, thus the difference is

caused by the different charge transfer energy in the two compounds. Mapping this energy difference to the mean field transition temperature, one would get T_c in SCMO to be 79 % smaller compared to that of SCWO. [3] The calculated PM and FM energy difference, considering the full model Hamiltonian, describing both hybridization-driven and super-exchange driven mechanism, is 0.080 eV/f.u., which makes the calculated T_c of SCMO similar to that of SCWO. Mapping the PM and FM energy difference to the mean field T_c, one obtains the values 822 K for SCMO and 870 K for SCWO, which are an overestimation of the experimental values. [3,4,6] This is presumably due to non-local fluctuations beyond mean-field. However, the trend is very well reproduced with $\mathrm{T}_c^{SCMO}/\mathrm{T}_c^{SCWO} = 0.95$.

3.4 Summary

Starting from a DFT description we provided a microscopic analysis of the magnetic behavior of SCMO, a sister compound of SFMO. DFT calculations on pure, defect-free SCMO show that, like SFMO and SCMO, it is a half-metallic magnet. The calculated DMFT results confirm the robustness of the half-metallicity of SCMO upon inclusion of dynamical correlation effect. The DMFT results show a splitting of the Mo down spin band into Hubbard bands and quasiparticle peak. This indicates the dual nature of the Mo electrons having both, a local spin moment and itinerant behavior.

The origin of magnetism in SCMO turns out to be somewhat different than in SFMO. The charge transfer energy between Cr and Mo in the down spin channel of SCMO is found to be larger than that between Fe and Mo in SFMO. This suppresses the effect of hybridization between B and B$'$ sites in SCMO compared to SFMO and has two consequences: (i) the hybridization-driven mechanism for magnetism is reduced and (ii) a small but finite intrinsic moment develops at the Mo sites. The latter gives rise to a partial localized character of the Mo electrons, which was absent in SFMO. This in turn opens up a super-exchange contribution to magnetism in SCMO, which was absent for SFMO. We compared our results on SCMO to another Cr based double perovskite, SCWO. The magnetism in the latter, like SFMO, is well described by a hybridization-only picture. The computed T_c obtained through exact diagonalization of the ab-initio derived model Hamiltonian show the T_c of SCMO to be similarly high as in SCWO, only upon inclusion of both, super-exchange and hybridization-driven contribution in case of SCMO. Thus while magnetism in both, SCWO and SFMO, is governed by hybridization, the story in SCMO appears with a twist. It needs to be described by a combination of hybridization and superexchange mechanism.

We conclude that, in general, the magnetism in the double perovskite family has to be understood as an interplay between the hybridization and super-exchange between B and B$'$ sites. The relative contribution of one mechanism vs.

the other one is dictated by the charge transfer between the $3d$ transition metal at the B site and the $4d$ or $5d$ transition metal at the B$^{'}$ site.

Bibliography

[1] K.-I. Kobayashi, T. Kimura, H. Sawada, K. Terakura, and Y. Tokura, Nature (London) **395**, 677 (1998).

[2] D.D. Sarma, Current Opinion in Solid State and Materials Science, **5**, 261 (2001).

[3] J. B. Philipp, P. Majewski, L. Alff, A. Erb, R. Gross, T. Graf, M. S. Brandt, J. Simon, T. Walther, W. Mader, D. Topwal, and D. D. Sarma, Phys. Rev.B, **68**, 144431 (2003); H. Kato, T. Okuda, Y. Okimoto, Y. Tomioka, Y. Takenoya, A. Ohkubo, M. Kawasaki, and Y. Tokura, App. Phys. Lett **81**, 328 (2002); Y. Krockenberger, K. Mogare, M. Reehuis, M. Tovar, M. Jansen, G. Vaitheeswaran, V. Kanchana, F. Bultmark, A. Delin, F. Wilhelm, A. Rogalev, A. Winkler, and L. Alff, Phys. Rev. B **75**, 020404 (2007).

[4] F. K. Patterson, C. W. Moeller, and R. Ward, Inorg. Chem. **2**, 196 (1963).

[5] Y. Moritomo, Sh Xu, A. Machida, T. Akimoto, E. Nishibori, M. Takata and M. Sakata, Phys. Rev. B **61**, R7827 (2000).

[6] A. Arulraj, K. Ramesha, J. Gopalakrishnan, and C. N. R. Rao, J. Solid State Chem. **155**, 233 (2000).

[7] T.S. Chana, R.S. Liua, G.Y. Guoc, S.F. Hud, J.G. Line, J.-F. Leef, L.-Y. Jangf, C.-R. Changb, C.Y. Huangg, Solid State Commun. **131**, 531 (2004).

[8] C.M. Bonilla, D.A. Landnez Tellez, J. Arbey Rodrguez, E. Vera Lopez, J. Roa-Rojas, Physica B **398**, 208 (2007).

[9] H. Wu, Phys. Rev. B **64**, 125126 (2001).

[10] G. Dimitri Ngantso, A. Benyoussef, A. El Kenz, S. Naji, J Supercond Nov Magn **28**, 2589 (2015).

[11] Prabuddha Sanyal, Hena Das, and T. Saha-Dasgupta, Phys. Rev. B **80**, 224412 (2009).

[12] Hena Das, Prabuddha Sanyal, T. Saha-Dasgupta and D.D. Sarma, Phys. Rev. B, **83**, 104418 (2011).

[13] D.D. Sarma, P. Mahadevan, T. Saha Dasgupta, S. Ray, A. Kumar, Phys. Rev. Lett., **85**, 2549 (2000).

[14] G. Kresse and J. Hafner, Phys. Rev. B **47**, R558 (1993), G. Kresse and J. Furthmueller, Phys. Rev. B **54**, 11169 (1996).

[15] John P. Perdew, J. A. Chevary, S. H. Vosko, Koblar A. Jackson, Mark R. Pederson, D. J. Singh, and Carlos Fiolhais , Phys. Rev. B **46**, 6671 (1992).

[16] W. Kohn and L. J. Sham Phys. Rev. **140**, A1133 (1965); R. G. Parr and W. Yang Density Functional Theory of Atoms and Molecules Oxford University Press, Oxford (1989).

[17] J. P. Perdew, K. Burke, and M. Ernzerhof, Phys. Rev. Lett. **77**, 3865 (1996).

[18] P. E. Blöchl, Phys. Rev. B **50**, 17953 (1994).

[19] O. K. Andersen and T. Saha-Dasgupta, Phys. Rev. B **62**, R16219 (2000).

[20] J. Kunes, R. Arita, P. Wissgott, A. Toschi, H. Ikeda, abnd K. Held, Comp. Phys. Comm. 181, 1888 (2010).

[21] A. A. Mostofi, J. R. Yates, Y.-S. Lee, I. Souza, D. Vanderbilt and N. Marzari Comput. Phys. Commun. **178**, 685 (2008).

[22] S. P. Blaha, K. Schwartz, G. K. H. Madsen, D. Kvasnicka & J. Luitz. WIEN2K, An Augmented Plane Wave+ Local Orbitals Program for Calculating Crystal Properties. edited by K. Schwarz . Technische Universitaet Wien, Austria (2001).

[23] G. Kotliar, S. Y. Savrasov, K. Haule, V. S. Oudovenko, O. Parcollet, and C. A. Marianetti, Rev. Mod. Phys. **78**, 865 (2006).

[24] K. Held, Advances in Physics **56**, 829 (2007).

[25] C. Taranto, M. Kaltak, N. Parragh, G. Sangiovanni, G. Kresse, A. Toschi, and K. Held, Phys. Rev. B **88**, 165119 (2013).

[26] L. Si, Z. Zhong, J. M. Tomczak, and K. Held Phys. Rev. B **92**, 041108(R) (2015).

[27] E. Gull, A. J. Mills, A. I. Lichtenstein, A. N. Rubtsov, M. Troyer, P. Werner, Rev. Mod. Phys. **83**, 349 (2011).

[28] N. Parragh, A. Toschi, K. Held, and G. Sangiovanni, Phys. Rev. B **86**, 155158 (2012); M. Wallerberger (unpublished).

[29] Q. F. Li, X. F. Zhu and L. F. Chen, J. Phys.: Condens. Matter **20**, 255230 (2008)

[30] J Blasco, C Ritter, L Morellón, P A Algarabel, J M De Teresa, D Serrate, J García and R M Ibarra, Solid State Sci. **4**, 651 (2002).

[31] The sharp spikes in the Cr-t_{2g} up spin channel above the Fermi level might well be an artefact of the maximum entropy method employed for the analytical continuation.

[32] J. Kanamori and K. Terakura, J. Phys. Soc. Jpn. **70**, 1433 (2001).

[33] K. Samanta, P. Sanyal and T. Saha-Dasgupta, Scientific Reports **5**, 15010 (2015).

[34] H. Iwasawa, K. Yamakawa, T. Saitoh, J. Inaba, T. Katsufuji, M. Higashiguchi, K. Shimada, H. Namatame, M. Taniguchi, Phys, Rev. Lett **96**, 067203 (2006); H. Iwasawa, S. Kaneyoshi, K. Kurahashi, T. Saitoh, I. Hase, T. Katsufuji, K. Shimada, H. Namatame, and M. Taniguchi, Phys. Rev. B **80**, 125122 (2009).

[35] We have also repeated the NMTO calculation to obtain the energy level diagram and intrinsic spin splitting at the B' site, by carrying out calculations of SCWO with same crystal structure as SCMO, constructed by replacing Mo by W in the SCMO lattice. Comparison of the intrinsic spin-splitting observed at Mo site in case of SCMO as compared to that at W site of this hypothetical SCWO compound, captures solely the chemical effect, eliminating any possible lattice effect. The obtained result shows the intrinsic spin splitting at the W site of the hypothetical SCWO compound compound to be 0.05 eV, in good agreement with the value of 0.06 eV obtained for the SCWO [12] in its own crystal structure. This proves the dominance of chemical effect (W versus Mo) compared to the lattice effect.

[36] O. Navarro, E. Carvajal, B. Aguilar, M. Avignon, Physica B **384**, 110 (2006); L. Brey, M. J. Calderón, S. Das Sarma and F. Guinea, Phys. Rev. B **74**, 094429 (2006); J.L.Alonso,L.A. Fernandez, F. Guinea, F. Lesmes, and V. Martin-Mayor, Phys. Rev. B, **67**, 214423 (2003).

[37] The energy difference between PM and FM phases for different lattice sizes are found to scale with size, although the ratio between values for SCMO and SCWO is found to remain almost the same in calculations on different lattice sizes. These values are found to be 0.050 eV/f.u. for SCMO, 0.063

eV/f.u. for SCWO with a ratio of 79.2 % for a 4×4×4 lattice, 0.066 eV/f.u. for SCMO, 0.084 eV/f.u. for SCWO with a ratio of 78.5 % for a 6×6×6 lattice, and 0.067 eV/f.u. for SCMO, 0.085 eV/f.u. for SCWO with a ratio of 78.8 % for a 8×8×8 lattice. The values presented in the text are for 8×8×8.

Chapter 4

Magnetism in Cation Disordered 3d-4d/5d Double Perovskites*

4.1 Introduction and motivation

Double perovskites (DP) synthesized with choice of transition metals, one from 3d TM series and another from 4d or 5d TM series, have been reported to exhibit magnetic transition temperatures ranging from $\approx$ 200 K - $\approx$ 800 K. [1] The perfect ordering of B and B$^{'}$ cations (cf. left panel of Fig. (4.1)) in double perovskite compounds, however, is an idealized situation. In reality, the presence of B/B$^{'}$ disorder, commonly known as antisite disorder (ASD) where certain fraction of B and B$^{'}$ pair gets interchanged in a perfectly ordered arrangement, is inevitable. [2–4] Therefore, it is a matter of great concern to what extent ASD affects the fascinating magnetic properties of the DPs.

This discussion got further intrigued by the report of magnetic ordering with high transition temperature of more than 400K [5] in a CrRu based system in which apparently no Cr/Ru cation order was observed. This would amount to 50% ASD. [6] As pointed out in Ref. [5], any superexchange mechanism in presence of antisite disorder, would suppress magnetism with transition temperature dropping off rapidly and in extreme case may lead to spin glass like behavior. It is thus very surprising to find even this extreme disorder is not able to suppress magnetic ordering. Rather it supports magnetic ordering at temperature higher than room temperature. What is the clue to this puzzle?

The problem of cation disordering effect in magnetism of 3d-4d/5d is complex due to multiple reasons. Firstly, as discussed in Refs. [7,8] magnetism in DPs like

*This chapter is based on publication : **Anita Halder**, Prabuddha Sanyal and Tanusri Saha-Dasgupta, *Phys. Rev. B*, **99**, 020402(R) (2019).

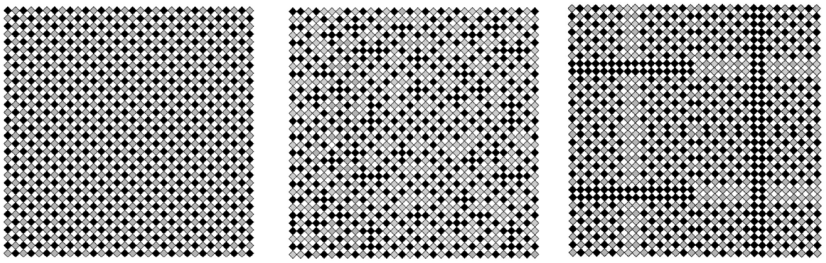

Figure 4.1: Left panel: Schematic view of in-plane projection of rock-salt ordering of BO_6 (black) and $B^{'}O_6$ (gray) octahedra in DP. Middle panel: The same, but in presence of random ASD. Right panel: The same, but in presence of correlated disorder, with well defined domains, separated by APB.

Sr_2FeMoO_6 is given by the two sublattice double-exchange mechanism operating between the core spin of Fe ion and the itinerant electron delocalized over Fe-O-Mo network thereby stabilizing parallel alignment of Fe core spins. Later on this mechanism is found to be operative in a number of 3d-4d/5d DPs. [9–12] The influence of disorder on such double exchange driven mechanism, which depends on the relative positioning of B-site levels and B′-O hybridized levels, is expected to be distinct from that arising due to commonly assumed superexchange mechanism. Secondly, the magnetism in certain class of 3d-5d DPs has been reported to be contributed by combined effect of double-exchange (DE) and superexchange mechanism (SE), [10] making the situation further complex. Thirdly, it is to be noted if two 3d TM ions with large core spin are on neighboring sites in an antisite disordered situation, the nearest-neighbor B-B antiferromagnetic (AFM) coupling becomes operative, which would be competitive to the two-sublattice DE driven parallel alignment of B core spins. Fourthly, the effect should also depend on the nature of ASD. The ASD can be placed randomly throughout the lattice leading to a homogeneous distribution of defects, or they can appear as patchy structure with locally ordered domains, separated by antiphase boundaries (APBs), as shown in middle and right panel of Fig. (4.1), respectively. X-ray absorption fine structure (XAFS) [13] or electron microscopy experiments [14] carried out on Sr_2FeMoO_6 (SFMO) DP strongly support the dominance of patchy structure formation over random distribution.

Though there has been attempt on theoretical study of disordering effect, [15, 16] to the best of our knowledge there has been no comprehensive microscopic investigation including all the aspects discussed above. In this work, we did so by using a multi-pronged approach of combining the first principles density functional theory (DFT) calculations to derive compound-specific model Hamiltonian together with Exact Diagonalization - Monte Carlo (ED - MC) solution of model Hamiltonian to obtain the finite temperature magnetic properties. Our

study encompassing a rather large set of six different known $3d-4d/5d$ compounds, is expected to provide a general picture of cation disordering effect on magnetism of $3d-4d/5d$ DPs. This in turn should also yield a solution to the CrRu puzzle.

Computational details

For extraction of few-band tight-binding Hamiltonian out of full DFT calculation which can be used as input to model Hamiltonian, NMTO-downfolding calculations were carried out based on self-consistent potentials borrowed from non spin-polarized linear muffin-tin orbital (LMTO) calculations. [18] LMTO calculation of hypothetical CrRu compound was done with the choice of muffin-tin (MT) radius of 2.304 $\mathring{A}$, 2.398 $\mathring{A}$ and 1.772 $\mathring{A}$ at Cr, Ru and O site respectively. For Ca_2CrWO_6, the corresponding choices were the following : 2.557 $\mathring{A}$, 2.713 $\mathring{A}$ for Cr and W respectively and 1.717 $\mathring{A}$, 1.725 $\mathring{A}$, 1.714 $\mathring{A}$ for three different O atoms. In the latter case, 10 empty spheres were used to achieve space filling. For SFMO, Sr_2CrMO_6, Sr_2CrWO_6, Sr_2CrReO_6 and Sr_2CrOsO_6, the details are given in the cited references. [10, 12, 17] The exchange-correlation functional for the self-consistent calculations was chosen to be generalized gradient approximation (GGA) as implemented in Perdew-Burke-Ernzerhof (PBE) prescription. [27]

The accuracy of LMTO calculations was cross checked in terms of further calculation in plane wave basis as implemented in Vienna ab Initio Simulation Package(VASP) [26] with projector-augmented-wave (PAW) pseudopotentials. [25] In plane wave basis, the choice of energy cut off of 600 eV and $8 \times 8 \times 8$ Monkhorst-Pack k-points mesh were found to provide a good convergence of the total energy. The electronic density of states and magnetic moments calculations were carried out within spin-polarized scheme taking into account the correlation effect at $3d$ transition metal site beyond GGA. The correlation energy at transition metal sites beyond GGA (e.g. at Cr and Ru/W sites) was taken into account through supplemented Hubbard U (GGA+U) approach as implemented within Liechetenstein method. [28] The calculations were performed with the choice of U of 4 eV at $3d$ B site and at $4d/5d$ B$'$ site to be 1 eV as estimated from previous study. [12] The value of $J_H = 0.6$ eV was kept fixed in all the calculations. The trend in the results was found to remain unchanged upon variation of U value 1 - 4 eV at B site.

The exact diagonalization calculations were carried out on lattice sizes of dimensions $4 \times 4 \times 4$, $6 \times 6 \times 6$ and $8 \times 8 \times 8$. The trend was found to be similar between calculations of different lattice sizes, though the quantitative values differed. The result presented in the text were obtained for ED calculations on $8 \times 8 \times 8$ lattice size, MC simulation equilibrated over 50,000 sweeps. The disordered averaging was done for 30 different configurations in case of random

ASD.

4.2 Results

4.2.1 Exchange Mechanism in 3d-4d/5d DPs

As mentioned already, the magnetism in a number of 3d-4d/5d DPs is found to be driven by a novel hybridization mediated mechanism. [7–12] This mechanism originates from the large exchange splitting at 3d TM in B site and the strong hybridization between B′ states and states at B site, which results in an induced negative spin splitting at B′ site when the B′ energy levels lie within the exchange split levels of B site. This essence is summarized schematically in Fig. (4.2) (Scenario - 1). However while the magnetism in compounds like Sr_2FeMoO_6 (SFMO), [9] Ba_2FeReO_6, [11] Sr_2CrWO_6 (SCWO) [10] etc turned out to be solely driven by the above described hybridization mediated mechanism, in case of double perovskite like Sr_2CrReO_6 (SCReO), Sr_2CrOsO_6 (SCOO) [10] an additional contribution comes into play which arises due to intrinsic spin splitting of the B′ states which adds on to the induced B-B′ hybridization driven spin splitting at B′ site (Scenario - 2). The most general form of the model Hamiltonian applicable for all $3d-4d/5d$ DPs thus can be written as, [10]

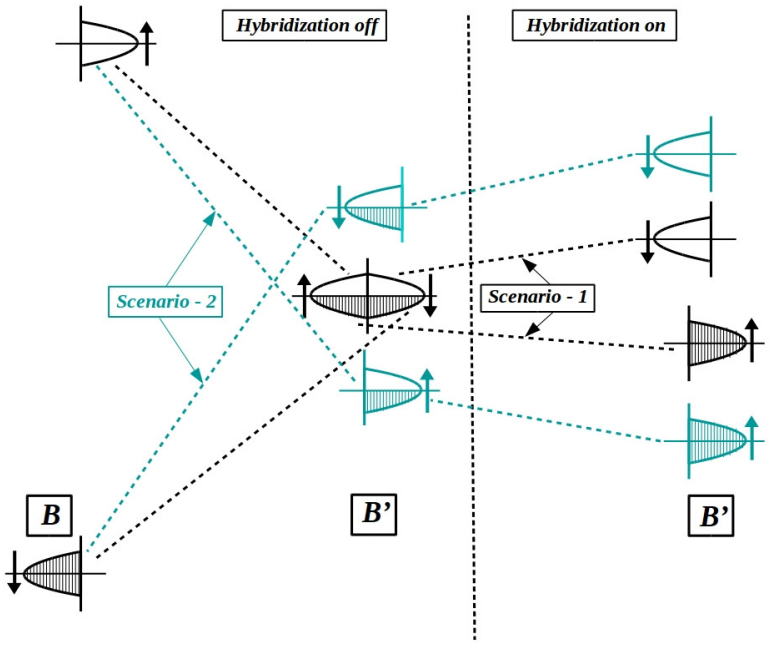

Figure 4.2: The two possible scenarios of driving mechanisms of exchange in 3d-4d/5d DPs.

$$
\begin{aligned}
H &= H_{DE} + H_{SE} \qquad (4.1)\\
&= \epsilon_B \sum_{i\in B} c^{\dagger}_{B,i\sigma} c_{B,i\sigma} + \epsilon_{B'} \sum_{i\in B'} c^{\dagger}_{B',i\sigma} c_{B',i\sigma}\\
&+ t_{B-B'} \sum_{<ij>\sigma} c^{\dagger}_{B,i\sigma} c_{B',j\sigma} + J \sum_{i\in B} \mathbf{S}_i \cdot c^{\dagger}_{B,i\alpha} \vec{\sigma}_{\alpha\beta} c_{B,i\beta} + J_2 \sum_{i\in B, j\in B'} \mathbf{S}_i \cdot \mathbf{s}_j
\end{aligned}
$$

where the first four terms of the Hamiltonian describe the hybridization-driven mechanism of exchange, resulting into two-sublattice double exchange Hamiltonian (H_{DE}) consisting of, (a) a large core spin of 3d TM B site ($\mathbf{S}_i$) considered to be classical spin, (b) effective hybridization between B and B$'$, decided by the onsite energies (ϵ_B, $\epsilon_{B'}$) and hopping integral ($t_{B-B'}$), which gives rise to delocalization of the itinerant electron over B-O-B$'$ network, and (c) strong coupling between the core spin $\mathbf{S}_i$ at B site and the itinerant electron through a coupling, $J \gg t_{B-B'}$. The last term of the Hamiltonian (H_{SE}) expresses SE interaction coupling (J_2) between the large core spin $\mathbf{S}_i$ at B site, and the intrinsic spin at B$'$ site ($\mathbf{s}_j$), which is antiferromagnetic in nature. Note H_{SE} would be operative for systems like SCReO or SCOO, and would be absent for SFMO or SCWO.

Given the fact that $J \gg t_{B-B'}$, the Hamiltonian in Eqn. (4.1) can be cast into form appropriate for $J \to \infty$, having spinless fermionic degrees of freedom at B site, and itinerant electrons having both spin channels, [17] as given below,

$$
\begin{aligned}
H &= \epsilon_{B'} \sum_{i\sigma} c^{\dagger}_{B',i\sigma} c_{B',i\sigma} + \tilde{\epsilon}_B \sum_i \tilde{c}^{\dagger}_{B,i} \tilde{c}_{B,i} \qquad (4.2)\\
&+ t_{B-B'} \sum_{<ij>} (sin\frac{\theta_i}{2} \tilde{c}^{\dagger}_{B,i} c_{B',j\uparrow} - cos\frac{\theta_i}{2} e^{i\phi_i} \tilde{c}^{\dagger}_{B,i} c_{B',j\downarrow}) + J_2 \sum_{i\in B, j\in B'} c^{\dagger}_{B',j\alpha} \vec{\sigma}_{\alpha\beta} c_{B',j\beta} \cdot \vec{S}_i
\end{aligned}
$$

θ and ϕ dictate the relative alignment of core spins in B sublattice. While the above Hamiltonian is sufficient for description of the perfectly ordered compound, for the disordered compound, additional terms are needed for description of antisite regions, as given below,

$$
\begin{aligned}
H_{disord} &= t_{B-B} \sum_{<ij>} \left[cos\frac{\theta_i}{2} cos\frac{\theta_j}{2} + e^{i(\phi_j - \phi_i)} sin\frac{\theta_i}{2} sin\frac{\theta_j}{2} \right] \tilde{c}^{\dagger}_{B,i} \tilde{c}_{B,j}\\
&+ t_{B'-B'} \sum_{<ij>\sigma} c^{\dagger}_{B',i\sigma} c_{B',j\sigma} + J_{AS} \sum_{<ij>} \vec{S}_i \cdot \vec{S}_j \qquad (4.3)
\end{aligned}
$$

where J_{AS} is an antiferromagnetic B-B antisite superexchange, and t_{B-B}, $t_{B'-B'}$ are the nearest neighbor B-B and B$'$-B$'$ hopping that arise in presence of ASD. The complete Hamiltonian was solved using ED - MC technique as discussed in subsection 2.8.2, the Hamiltonian H (H_{disord}) being used in the ordered (disordered) region.

Compound	$t_{B-B'}$	$\triangle$	t_{B-B}	$t_{B'-B'}$	J_2	J_{AS}
SCWO [10]	0.350	0.510	0.210	0.450	0.000	0.001
CCWO	0.210	0.470	0.170	0.450	0.000	0.0006
SCMO [12]	0.330	0.800	0.210	0.320	0.007	0.001
SCOO [10]	0.350	1.350	0.210	0.470	0.026	0.001
SFMO [17]	0.260	0.090	0.144	0.320	0.000	0.002
SCRuO	0.290	1.651	0.210	0.350	0.031	0.001
SCReO [10]	0.350	0.900	0.210	0.460	0.014	0.001

Table 4.1: DFT derived model parameters in eV; $t_{B-B'}$, nearest neighbor B-B$'$ hopping, $\Delta = \epsilon_B$ - $\epsilon_{B'}$, onsite energy difference between B and B$'$, $t_{B-B}/t_{B'-B'}$ nearest neighbor B-B/B$'$-B$'$ hopping in ASD region, J_2, the intrinsic spin-splitting at B$'$ site. J_{AS} has been estimated from corresponding Neél temperatures of the corresponding ABO_3 perovskites.

4.2.2 Model Hamiltonian

To obtain a material specific description, the input parameters of model Hamiltonian, ϵ_B, $\epsilon_{B'}$, $t_{B-B'}$, J_2 need to be evaluated. In order to provide realistic estimates of ϵ_B, $\epsilon_{B'}$, $t_{B-B'}$, we carried out muffin-tin orbital (MTO) [18] based NMTO-downfolding calculations [19] to derive low-energy Hamiltonian starting from non spin-polarized DFT calculations, and reading off the onsite and off-site matrix elements of the real-space representation of the low-energy Hamiltonian. [12] The derived parameters are thus expected to capture correct structural and chemical information of the compounds under consideration. We considered a total of six different 3d-4d/5d DPs, with Fe or Cr at 3d site, which were studied most extensively, namely SFMO, Sr_2CrMoO_6 (SCMO), SCWO, SCReO, SCOO, and Ca_2CrWO_6 (CCWO). DFT calculations [9, 10, 12] as well as experimental investigations [8, 20–24] in all these cases reveal that B cation is in nominal 3+ valence state which means d^5 configuration for Fe and d^3 configuration for Cr. This puts the 4d/5d B$'$ cation in nominal 5+ valence state. The minimal, low-energy Hamiltonian was thus constructed by retaining all five d orbitals of Fe, only t_{2g} orbitals in case of Cr, and 4d/5d ions like W, Re, Os, Mo. The extracted parameters, some of which have been taken from our existing work, [9,10,12] and some of which have been freshly calculated, are listed in Table. (4.1). The J_2 parameter was obtained from the information of extra spin-splitting at B$'$ site in B-B$'$ low energy Hamiltonian, compared to that expected from Stoner I of

the B′ element and its nominal filling. [10] t_{B-B}, $t_{B'-B'}$, J_{AS} were obtained from calculation of corresponding simple perovskite compounds.

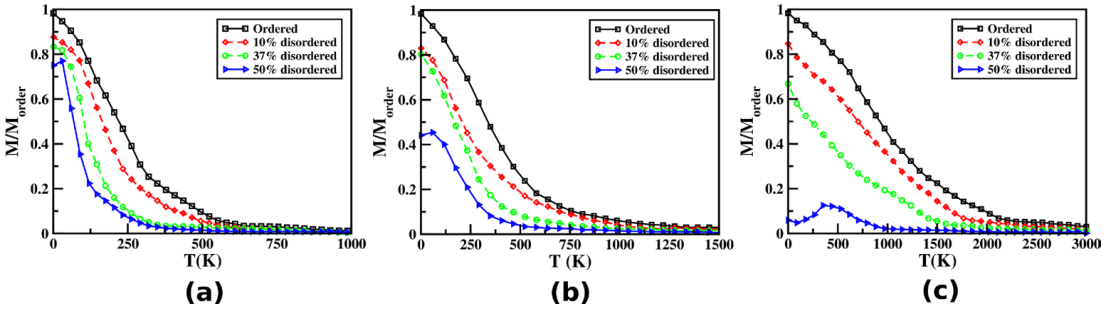

Figure 4.3: M/M_{ord} plotted as a function of temperature T at different concentration of disorder strength. The results are shown for compounds, (a) SCWO representing weak/no super-exchange (SE), (b) SCReO representing moderate super-exchange and (c) SCOO having strong SE.

4.2.3 Calculated Magnetic Properties of Disordered 3d-4d/5d DPs

The magnetization data obtained from ED - MC method by solving H (for ordered compound) and H_{disord} (additional terms for antisite regions) for representative cases of SCWO, SCReO and SCOO are shown in Fig. (4.3) upon varying degrees of ASD, which are assumed to be random.

The magnetic transition temperatures (T_c) estimated from these plots together with the average magnetic moment at the B sublattice (M) with respect to that of fully ordered compound (M_{ord}) is shown in Fig. (4.4) for all six DPs for random ASD with disorder strength of 10%, 37 % and the maximum limit of 50%. We observed a distinctly different behavior between DPs exhibiting solely DE driven magnetism and those having combined DE - SE driven magnetism. In case of solely DE driven compounds like SFMO, SCWO ($J_2 = 0$) or SCMO having only weak SE contribution ($J_2 < 0.01$), the ordered magnetic moment is retained to a large extent, showing about 25-35% drop from that of the fully ordered compound to the extreme case of 50% disorder, the corresponding drop in magnetic transition temperature being about 60-70%. Keeping in mind, the high transition temperatures of the perfectly ordered compounds with calculated T_c values e.g. 350 K for SFMO, 410 K for SCWO, and 424 K for SCMO, even the disordering induced reduced T_c for 50% turns out to be above 100 K. *This is markedly different from expected behavior of SE driven magnetic systems, for which such heavily disordered situation will completely suppress the magnetic order.* Indeed the influence of SE term becomes evident in magnetic behavior of

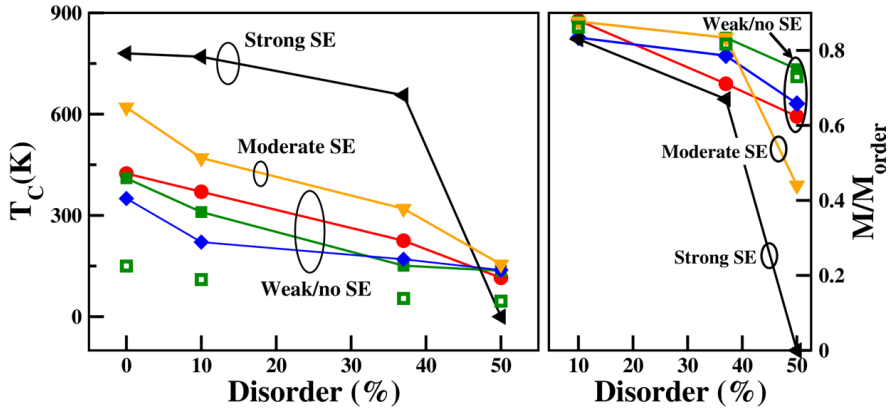

Figure 4.4: Variation of T_c (left panel) and M/M_{ord} (right panel) plotted as a function of concentration of random ASD. The data points with black left triangle, yellow down triangle, red circle, green square and blue diamond correspond to SCOO, SCReO, SCMO, SCWO and SFMO, respectively. The green open squares represent data for CCWO.

compounds like SCOO for which the substantial SE contribution ($J_2 \approx 0.03$) makes the magnetic order completely vanish for the extreme limit of 50% disorder. SCReO, for which the effect of SE is relatively weaker compared to SCOO ($J_2 \approx 0.02$) though stronger compared to SFMO or SCWO or SCMO, the disordering effect is found to be intermediate between SFMO or SCWO or SCMO and SCOO, with a suppression of ordered moment by 56% and a suppression of T_c value by 85% for 50% disorder strength. The Ca counterpart of SCWO, CCWO, shows a similar trend as SCWO, though the corresponding temperatures are suppressed due to reduction in B-O-B$'$ bond angle, and the consequent reduction in hopping interaction.

4.2.4 *CrRu* Puzzle

Having understood the role of disorder on magnetism in 3d-4d/5d DPs of large variety, and the crucial role of the exchange mechanism, it becomes pertinent to investigate the case of $SrCr_{0.5}Ru_{0.5}O_3$. [5] The first step towards that will be understanding the driving exchange mechanism in CrRu system. For this purpose, we carried out DFT calculation of hypothetical perfectly ordered double perovskite counterpart of $SrCr_{0.5}Ru_{0.5}O_3$, *i.e.* Sr_2CrRuO_6 (SCRuO) with fully ordered alternating array of Cr and Ru. The crystal structure of SCRuO was assumed to be cubic (space group Fm-3m) as shown in inset of Fig. (4.7) and the structural parameters in the cubic symmetry were obtained by starting from the structure of SCOO, replacing Os by Ru, followed by structural relaxation which

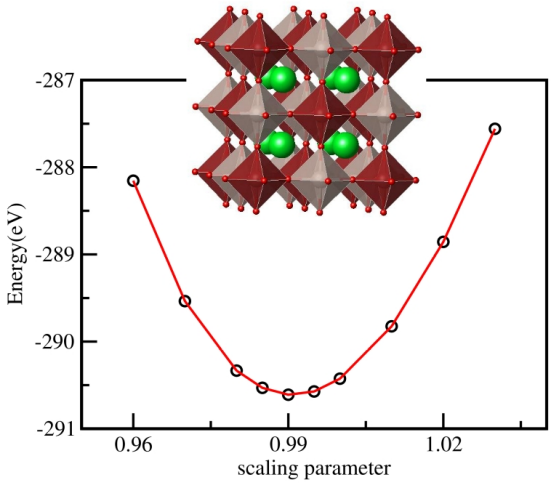

Figure 4.5: Structure determination of hypothetical perfectly ordered compound from volume optimization. The obtained crystal structure SCRuO compound is shown in inset.

involved volume as well as optimization of ionic positions of oxygen. The energy vs volume (here it is scaling parameter which is ratio of the volume of SCRuO and SCOO) plot is shown in Fig. (4.7). During ionic relaxations, internal positions of oxygens were allowed to relax until Hellman-Feynman forces became less than 0.01 eV/$\mathring{A}$. The cell parameter of the relaxed structure was found to be 7.829 $\mathring{A}$, with internal parameter of oxygen given by 0.2471. The DFT calculation [25, 26] within the generalized gradient approximation [27] (GGA) with supplemented Hubbard U (GGA+U) [28] resulted in an insulating, compensated ferrimagnetic solution (cf. Fig. (4.6)). Calculated magnetic moments, 2.42 μ_B at Cr site, -1.65 μ_B at Ru site and a rather large moment of -0.11 μ_B at O site, are similar to that obtained for corresponding isoelectronic compound SCOO. [10, 29]

In order to have an understanding of the exchange mechanism in case of CrRh, we estimated the energy level positions of exchange split Ru t_{2g} energy levels, before and after switching on the hybridization between Ru t_{2g} and Cr t_{2g} from NMTO-downfolding calculations within a spin-polarized scheme. As a first step of this procedure, all the states like O p and Sr as well as Cr and Ru e_g states except Ru t_{2g} and Cr t_{2g} states were downfolded, which defined a few orbital Hamiltonian consisting of Cr and Ru t_{2g} states. In the next step a massive downfolding was done, keeping on Ru t_{2g} degrees of freedom active and downfolding all the rest including Cr t_{2g} degrees of freedom. The former step provides on-site matrix elements of the real space Hamiltonian defined in the Cr - Ru t_{2g} basis

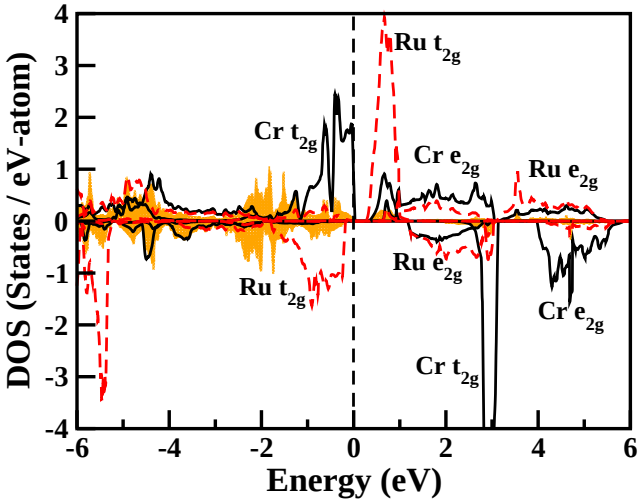

Figure 4.6: The DFT density of states for the hypothetical fully ordered structure of Sr_2CrRuO_6, projected to Cr d (black solid), Ru d (red dashed) and O p (yellow shaded) states. The zero of the energy is set at E_F.

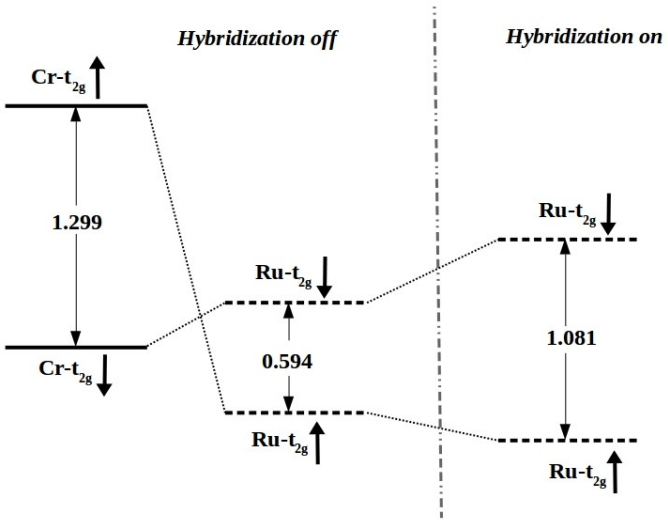

Figure 4.7: Positions of various energy levels (in eV) as obtained by NMTO-downfolding calculation before and after switching on the hybridization between Cr and Ru. The energies are in units of eV.

before switching on the hybridization and the second step gives the energy level positions of renormalized Ru t_{2g} states after switching on the hybridization between the Cr and B states. The obtained result is presented in Fig. (4.7). We observed that unlike other double perovskites Sr_2CrWO_6 [10], Sr_2CrReO_6 [10],

Sr_2FeMoO_6 [17], Sr_2CrMoO_6 [12] only up spin state of Ru t_{2g} lies between the exchange split of Cr t_{2g} states. But hybridization mechanism is still active in this compound, as after switching on the hybridization between Cr and Ru allows the states of same symmetry and spin to interact. This leads to Ru t_{2g} down state been pushed up and the Ru t_{2g} up state been pushed further down by hybridization with the corresponding Cr states. Thus hybridization enhances the spin splitting at Ru site due to these opposite movement of Ru spin up/down states with a renormalized value of about 1.081 eV being oriented in opposite direction with respect to that at the Cr sites. The intrinsic spin splitting at Ru site is quite significant, having a value of 0.594 eV. This establishes the presence of intrinsic, local moment at the Ru site similar to that of Os site for Sr_2CrOsO_6, thus the exchange mechanism being of combined DE-SE kind. The estimated

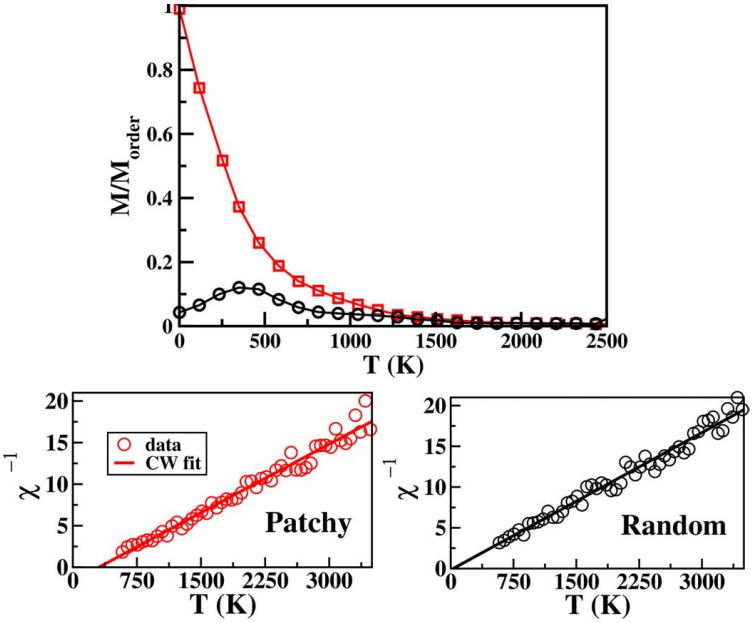

Figure 4.8: Top panel : The B-sublattice magnetism plotted as a function of temperature for the fully disordered situation with 50% random ASD (black circles) and for correlated disordered situation with patchy structure of ordered domains (red squares). Bottom panel: The calculated inverse susceptibility, along with Curie-Wiess (CW) fit.

model parameters, presented in Table. (4.1) along with six other naturally occurring DP compounds, show a remarkable similarity with SCOO, suggesting a similar disordering effect on magnetism. Indeed consideration of 50% random ASD led to a complete suppression of magnetic order, with T_c droping down to 0 K, as found in case of SCOO. This is however in complete contradiction with observation made in Ref. [5]. It is important to note here, the above conclusions

have been drawn based on the assumption of ASD to be random. The limited experimental studies, [13, 14] carried out only for SFMO, suggest the ASD to be correlated generating a patchy structure, as in right panel of Fig. (4.1). Strikingly, the temperature dependent magnetization at Cr sublattice of SCRuO is found to be strongly influenced by assuming correlated disorder instead of random (cf. top panel Fig. (4.8)). As shown in bottom pannel of Fig. (4.8) , Curie-Weiss fit to inverse of high temperature magnetic susceptibility leads to a 0 K magnetic ordering temperature for random disorder, while the assumption of correlated disorder yields a value of about 370 K, in close agreement to observed value. [5]

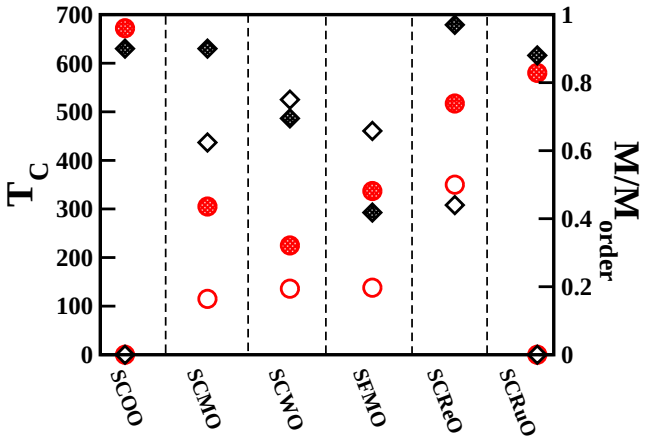

Figure 4.9: Comparison of T_c (red circle) and M/M_{ord} (black diamond) between the 50% random ASD case (open symbols) and correlated disorder with patchy domain structure (closed symbols).

We finally checked the influence of correlated ASD for 50% disorder strength in all DPs in this study. Remarkably, we found that consideration of patchy structure consisting of ordered domains, separated by APBs enhances T_c substantially in all cases. The B-sublattice ordered moment also shows a substantial enhancement, especially for cases where magnetism is driven by combined DE and SE as shown in Fig. (4.9). This strongly suggests that in combined DE and SE driven magnetic material like SCRuO, the cationic order remains preserved to a high degree in a local scale, although the global cationic order gets disrupted due to presence of APBs separating locally ordered regions. While the global probe like X-ray or neutron diffraction will be unable to detect any $B/B^{'}$ order signaled by presence of superstructure peak, as reported in Ref. [5], local probes like XAFS [13] or microscopy study [14] should be able to reveal presence of such locally ordered structure. This resolves the apparently puzzling situation of $SrCr_{0.5}Ru_{0.5}O_3$.

4.3 Conclusion

In conclusion, our exhaustive study encompassing a large number of 3d-4d/5d DP compounds, reveals that the influence of B cation anti-site disorder on their magnetic properties, which is unavoidable in any sample, crucially depends on the exchange mechanism. The magnetic behavior is far less susceptible to disorder for DE, while its effect is severe for compounds in which SE becomes operative in addition to DE. Interestingly, even in case of compounds, having SE contribution, the magnetic behavior of ordered situation may be regained if the disorder is correlated with high degree of short range order. [13] This strongly suggests that although the absence of long range chemical order was reported for CrRu compound, [5] high degree of short range order must have been preserved as in case of SFMO.

Finally, our study does not take into account the effect of oxygen vacancy or excess B/B$'$ [30, 31] which needs to be considered separately. As discussed in Refs [32,33] the oxygen vacancy acts as effective electron doping, which populates the delocalized electronic state of B and B$'$ in the down spin, thereby causing shift in valences of cations. This is expected to increase the magnetic transition temperature with some reduction in moment, [32] as demonstrated in Ref. [17] in context of La-doping of Sr_2FeMoO_6.

Bibliography

[1] T. K. Mandal, C. Felser, M. Greenblatt, and J. Kübler, Phys. Rev. B 78, 134431 (2008).

[2] V. P. Sakhnenko and N. V. Ter-Oganessian, Acta Crystallographica Section B, **74**, 264 (2018).

[3] Q. Chen, C. Svoboda, Q. Zheng, B. C. Sales, D. G. Mandrus, H. D. Zhou, J.-S. Zhou, D. McComb, M. Randeria, N. Trivedi, and J.-Q. Yan, Phys. Rev. B, **96**, 144423 (2017).

[4] J. Yang, P. Zhang, and S-H. Wei, J. Phys. Chem. Lett., **9**, 31 (2018).

[5] J. A. Rodgers, A. J. Williams, M. J. Martinez-Lope, J. A. Alonso and J. P. Attfield, Chem Mater **20** 4797 (2008).

[6] The disorder strength is measured by the percentage of wrong B or B$'$ sites (B site occupying B$'$ site of the ordered configuration and vice versa), thus maximum ASD being of 50%.

[7] D.D. Sarma, P. Mahadevan, T. Saha-Dasgupta, S. Ray and A. Kumar, Phys. Rev. Lett. **85**, 2549 (2000).

[8] K-I. Kobayashi, T. Kimura, H. Sawada, K. Terakura and Y. Tokura, Nature **395** 677 (1998).

[9] T. Saha-Dasgupta, M. De Raychaudhury, and D. D. Sarma, Phys. Rev. B **76**, 054441 (2007).

[10] H. Das, P. Sanyal, T. Saha-Dasgupta, and D. D. Sarma, Phys. Rev. B **83**, 104418 (2011).

[11] S. Baidya, U. V. Waghmare, A. Paramekanti, and T. Saha-Dasgupta, Phys. Rev. B **92**, 161106(R) (2015).

[12] P. Sanyal, A. Halder, L. Si, M. Wallerberger, K. Held, and T. Saha-Dasgupta, Phys. Rev. B 94, 035132 (2016).

[13] C. Meneghini, Sugata Ray, F. Liscio, F. Bardelli, S. Mobilio, and D. D. Sarma Phys. Rev. Lett. **103**, 046403 (2009).

[14] Y. H. Huang, M. Karppinen, H. Yamauchi, and J. B. Goodenough, Phys. Rev. B **73**, 104408 (2006).

[15] V. N. Singh and P. Majumdar, Euro. Phys. Lett. **94** 47004 (2011).

[16] S. K. Das, V. N. Singh, and P. Majumdar, Phys. Rev. B, **88**, 214428 (2013).

[17] P. Sanyal, H. Das, and T. Saha-Dasgupta, Phys. Rev. B **80**, 224412 (2009).

[18] O. K. Andersen, Phys. Rev. B **12**, 3060 (1975).

[19] O. K. Andersen and T. Saha-Dasgupta, Phys. Rev. B **62**, R16219 (2000).

[20] A. Arulraj, K. Ramesha, J. Gopalakrishnan, and C. N. R. Rao, J. Solid State Chem. **155**, 233 (2000).

[21] J. B. Philipp, P. Majewski, L. Alff, A. Erb, R. Gross, T. Graf, M. S. Brandt, J. Simon, T. Walther, W. Mader, D. Topwal, and D. D. Sarma, Phys. Rev.B, **68**, 144431 (2003).

[22] H. Kato, T. Okuda, Y. Okimoto, and Y. Tomioka, App. Phys. Lett **81**, 328 (2002).

[23] Y. Krockenberger, K. Mogare, M. Reehuis, M. Tovar, M. Jansen, G. Vaitheeswaran, V. Kanchana, F. Bultmark, A. Delin, F. Wilhelm, A. Rogalev, A. Winkler, and L. AlffY. Krockenberger, Phys. Rev. B **75**, 020404 (2007).

[24] P. Majewski, S. Gepraegs, A. Boger, M. Opel, A. Erb, R. Gross, G. Vaitheeswaran, V. Kanchana, A. Delin, F. Wilhelm, A. Rogalev, L. Alff, Phys. Rev. B **72**, 132402 (2005).

[25] P. E. Blöchl, Phys Rev B **50**, 17953 (1994).

[26] G. Kresse and J. Hafner, Phys. Rev. B **47**, 558(R) (1993); G. Kresse and J. Furthmuller, *ibid.* **54**, 11169 (1996).

[27] J. P. Perdew, K. Burke, and M. Ernzerhof, Phys. Rev. Lett. **77**, 3865 (1996).

[28] V. I. Anisimov, F. Aryasetiawan, and A. I. Liechtenstein, J. Phys.: Condens. Matter. **9**, 767-770 (1997).

[29] The influence of spin-orbit coupling (SOC), specially on 4d TM, Ru has been checked through GGA+U+SOC calculation, which yielded an orbital moment of 0.05 μ_B at Ru site, giving rise to a small net moment of 0.02 μ_B, making the situation nearly compensated, as opposed to fully compensated solution with net magnetic moment of 0 μ_B in GGA+U calculation.

[30] O. Erten, O. N. Meetei, A. Mukherjee, M. Randeria, N. Trivedi, and P. Woodward, Phys. Rev. B, **87**, 165105 (2013).

[31] O. N. Meetei, O. Erten, A. Mukherjee, M. Randeria, N. Trivedi, and P. Woodward, Phys. Rev. B, **87**, 165104 (2013).

[32] M. Hoffmann, V. N. Antonov, L. V. Bekenov, K. Kokko, W. Hergert and A. Ernst, J. Phys. Condens Matter, **30**, 305801 (2018).

[33] C. Etz and D. Stoeffler, Eur. Phys. J. B **54**, 429 (2006).

Chapter 5

Computer predictions on Rh-based double perovskites with unusual electronic and magnetic properties*

5.1 Introduction and motivation

The magnetic materials are technologically important and useful in every day life, although they are rare in reality. Thus demand for new magnetic materials is endlessly growing. The double perovskite (DP) family of compounds is well-known for providing magnetic compounds with spectacularly high magnetic transition temperature as already discussed in chapter 1. In spite of such large number of DP compounds already being synthesized, they form a small percentage of all the possible compounds that may be synthesized (see Fig. 2 in Ref. [1]). In particular, there is surprising scarcity of Rh-based DPs. There are only a few Rh based double perovskites known. While among the Ca^{2+} based compounds, there is none known, among the Sr^{2+} based compounds, there are compounds like Sr_2NbRhO_6, [2] Sr_2TaRhO_6, [2] Sr_2SbRhO_6, [3] which are reported to be nonmagnetic [4] with d^0 and low-spin d^6 combination of valences at B and Rh sites, respectively.

In this work, we focused on computer prediction of double perovskites with B and B$'$ TM cations, being 3d TM and Rh respectively. At A site, we considered Sr^{2+} or Ca^{2+}, as most of the DP compounds found in literature have a divalent

*This chapter is based on publication : **Anita Halder**, Dhani Nafday, Prabuddha Sanyal and Tanusri Saha-Dasgupta, *npj Quantum Materials*, **3**, 17 (2018).

cation at A site, the number of such compounds being over 700. For B site element, we considered Cr, Mn and Fe, which are neighboring elements in $3d$ TM series.

The first step towards this project, is the prediction of crystal structure. We used the algorithm of evolutionary crystal structure prediction [5], as implemented in Universal Structure Predictor: Evolutionary Xtallography (USPEX) [6] for this purpose. The evolutionary algorithm for crystal structure prediction has been highly successful as a method for the discovery of minerals and materials. [7] However, to the best of our knowledge, this method has not been applied to double perovskites, which are multi-component with four different element, out of which two are magnetic transition metal ions with strong electron-electron correlation effect. After the clarification on crystal structure, we performed electronic structure calculation which is followed by the study of magnetic properties of the compounds by considering different possible magnetic structures. We also calculated the magnetic transition temperatures within the framework of model Hamiltonian.

Finally, we estimated the growth conditions of these compounds in terms of temperature and partial pressure of reactants from extensive thermodynamic stability analysis [8, 9] which should be an useful guide for future synthesis of predicted compounds.

5.2 Computational Methodology

To investigate the structures of Sr_2BRhO_6 and Ca_2BRhO_6 (B=Cr, Mn, Fe) compounds, we used a genetic evolutionary algorithm which is implemented in USPEX [6]. We considered fixed composition mode with 10 atoms/unit cell and all the calculations are performed at zero pressure. In order to minimize the computational effort, we restricted our initial search to some specific space groups ($P2_1/n$, I2/m, P4/mnc, I4/m, $R\bar{3}$, $Fm\bar{3}m$) in which double perovskite are primarily found. [1] The structures in the first generation were picked up randomly from the restricted space group as mentioned above. In the succeeding generations, the structures were produced employing 40% from heredity operations, 20% from lattice mutation, 10% from permutation and few structures (30%) were produced randomly. For structural relaxations and total energy calculations, first-principle density functional (DFT) based calculations were carried out in plane wave basis as implemented in Vienna Ab initio Simulation Package (VASP) [10, 11] which is interfaced with USPEX. We used projected augmented wave(PAW) potential [12]. Exchange correlation functional is chosen to be that of generalized gradient approximation (GGA) in the implementation of Perdew-Burke-Ernzerhof (PBE) [13]. Additional calculations were carried out taking into account the electronic correlation effect at B (Cr/Mn/Fe) and Rh sites beyond

GGA through supplemented Hubbard U (GGA+U) calculation [14] as prescribed in Liechtenstein formulation. [15] The U value at B site (U_B) were chosen to vary between 1 and 8 eV, keeping the U value at Rh site and Hund's coupling J_H fixed at 1 eV, and at 0.8 eV, respectively. Structural relaxations were carried out stepwise from low to high precession, where at the last stage we use a full relaxation with a high threshold of energy cut off set at 500 eV and a force convergence of 10^{-3} eV/A^0. Then few good structures were considered on the basis of enthalpy. These structures were further relaxed extensively in three steps where relaxation of ions, volume and cell shape were allowed step by step. For ionic relaxations, the positions of the atoms were allowed to relax until the Hellman-Feynman forces become less than 0.001 eV/A^0. In the final step, one single self consistency calculation was performed to obtain the accurate enthalpies. Energy cut off of 600 eV and $8 \times 8 \times 8$ Monkhorst-Pack k-points mesh were found to provide a good convergence of the total energy. Finally, we compared the energies and the crystal structure corresponding to the lowest energy is considered as the chosen structure. The validity of the above described method were checked for two well known double perovskites, namely Sr_2CrMoO_6 and Sr_2FeMoO_6. The method reproduced the correct space groups of the compounds, $Fm\bar{3}m$ for Sr_2CrMoO_6 [16] and I4/m for Sr_2FeMoO_6 [17] with good agreement between measured and predicted lattice parameters, [18] giving us confidence in our adapted method.

After determining the crystal structures, their electronic and magnetic structure were studied using DFT in plane wave basis. The ground state magnetic structures were determined by comparing the energies of $2\times2\times2$ supercells having eight formula unit. These supercells with eight inequivalent B atoms can accommodate the ferromagnetic (FM) spin alignment of B atoms as well as A-type and G-type antiferromagnetic (AFM) alignment of B atoms. Upon clarification of magnetic structure, the magnetic transition temperatures were obtained from Monte Carlo study of a model spin Hamiltonian defined on a $16 \times 16 \times 16$ system, containing 4096 spins. The growth conditions of the predicted compounds were obtained by calculating the formation enthalpy of the possible competing phases, as elaborated in the result section.

5.3 Results and Discussions

In the results and discussions section, we reported a) the crystal structures of the compounds, as predicted theoretically, b) their electronic structure defined in terms of magnetic moments, assigned valence states and density of states, c) the magnetic ground state, d) the driving mechanism of magnetism, the DFT derived model Hamiltonian and calculated magnetic transition temperatures obtained through Monte Carlo study of model Hamiltonian, and e) the predicted growth conditions of the compounds. The section is divided into different sub-sections

accordingly.

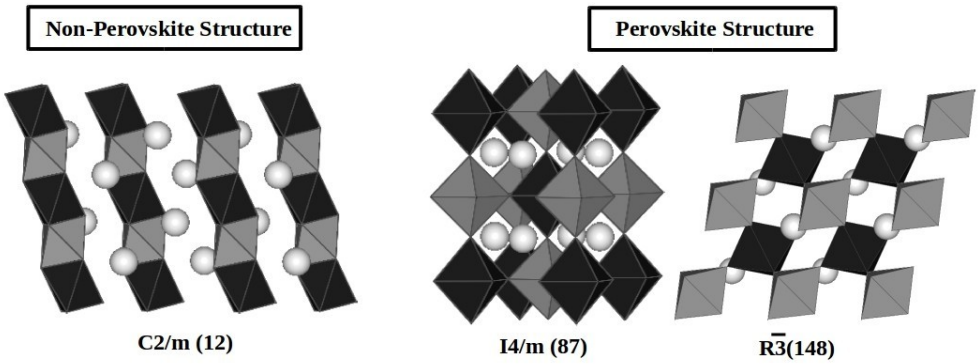

Figure 5.1: Schematic representation of three different low-energy crystal structures of Sr_2BRhO_6 and Ca_2BRhO_6 (B=Cr, Mn, Fe) compounds, as given by the evolutionary search. The BO_6 and RhO_6 polyhedra are shown as dark and light gray polyhedra, respectively, while the Sr^{2+} or Ca^{2+} ions are shown as balls. Left panel: Non-perovskite structure of C2/m symmetry derived from hexagonal P-3m1 symmetry. The structure consists of face-sharing chains of alternating BO_6 and RhO_6 octahedra running along crystallographic *c*-axis. Middle panel: Double perovskite structure of I4/m symmetry. The structure consists of corner-sharing BO_6 and RhO_6 octahedra alternating in all three directions with 180^o out-of-plane Rh-O-B bond angle, and in-plane Rh-O-B bond angle deviating from 180^o. Right panel: Double perovskite structure of $R\bar{3}$ symmetry having corner-shared BO_6 and RhO_6 octahedra alternating in all three directions with equal-valued bent Rh-O-B bond angles in out-of-plane and in-plane directions.

5.3.1 Predicted Crystal Structures

As mentioned above, we employed the evolutionary algorithm, as implemented in USPEX in conjunction with DFT in plane-wave basis for total energy calculations, to predict the crystal structures of yet-to-be synthesized Sr_2BRhO_6 and Ca_2BRhO_6 (B = Cr, Mn, Fe) compounds. Compilation of crystal structure data of so-far synthesized DP compounds shows [1] that while compounds with relatively smaller tolerance values, 0.93 or less, are predominantly of monoclinic $P2_1/n$ symmetry, compounds with relatively larger tolerance factors, 0.97 and beyond form in either cubic Fm-3m, or tetragonal I4/m or rhombohedral $R\bar{3}$ symmetry. Our search based on evolutionary algorithm results into either I4/m or $R\bar{3}$ symmetry of the compounds, in agreement with this general expectation. We note here that larger size of Sr^{2+} compared to Ca^{2+} drives the tolerance factor

t, defined as $t = \frac{r_A + r_O}{\sqrt{2}(\frac{r_B + r_{B'}}{2} + r_O)}$ where r_A, r_O, r_B, $r_{B'}$ are the ionic radii of A, O, B and B$'$ ions respectively, > 1 (1.03 - 1.01) for Sr based compounds and < 1 (0.98 - 0.97) for Ca compounds, with 3+/5+ combinations having somewhat smaller tolerance factor compared to 4+/4+ combinations. This makes non-perovskite structures possible candidates for Sr based compounds, which compete with perovskite structure, posing a challenge to the evolutionary algorithm. While for all Ca-based compounds, low-energy structures are found to be of perovskite-based R$\bar{3}$ symmetry, in case of Sr-based compounds, a non-perovskite structure with C2/m symmetry is found to be a strongly competing phase along with R$\bar{3}$ for Sr_2CrRhO_6 and Sr_2FeRhO_6, and I4/m for Sr_2MnRhO_6. The structural informations containing space group symmetry, lattice parameters(a, b, c), cell volume(V), cell angles(α, β, γ), Wyckoff positions and the atomic coordinates of the perovskite structures are listed in Table (5.1) and (5.2).

The left most panel of Fig. (5.1) shows the schematic diagram showing the crystal structure of non-perovskite C2/m symmetry. This monoclinic structure can be derived from the hexagonal P-3m1 symmetry by introduction of distortion, with their lattice constants connected by the transformation $a' = -a + b$, $b' = -a$ - b, and $c' = c$, a' (a), b' (b) and c' (c) being the lattice constants of the monoclinic (hexagonal) unit cell. The distorted BO_6 and RhO_6 octahedra are found to face-share and form chain-like structures with alternating BO_6 and RhO_6 units running along crystallographic c-direction. The Sr atoms sit in between the chains, and in the crystallographic ab-plane the neighboring chains form hexagonal packing.

The I4/m symmetry of the perovskite-based structures, as shown in the schematic diagram in middle panel of Fig. (5.1), shows $a^0a^0c^-$ Glazer tilt pattern resulting into 180^o B-O-Rh bond angles along the crystallographic c-axis and in-plane B-O-Rh bond angle bent from 180^o. The R$\bar{3}$ symmetry of the perovskite-based structures, shown in the schematic diagram in right most panel of Fig. 1, on the other hand shows $a^-a^-a^-$ Glazer tilt pattern resulting into equal valued B-O-Rh bond angles along in-plane and out-of-plane directions, which deviate from 180^o. The deviation of $\angle$ B-O-Rh from 180^o for perovskite-structures of Sr_2BRhO_6 compounds is found to be around 20^o, while for Ca_2BRhO_6 compounds this deviation is found to be increase to about 30^o. The B-O and Rh-O bond lengths show interesting evolution as a function of U value applied at B site. While B-O bond lengths are found to be less than 2 Å for GGA calculations with a value of about 1.88-1.90 Å, within GGA+U calculations for choice of $U_B = 4$ eV or more, the B-O bond lengths are found to be more than 2 Å with a value of about 2.01-2.02 Å. This occurs with a concomitant decrease of Rh-O bond length from a value 2.03-2.04 Å obtained within GGA calculation to a value 1.98-1.99 Å in GGA+U calculations for $U_B = 4$ eV or more. The observed U_B dependent evolution of bond length has important implications in valences of B cation and Rh cation, as will be discussed in the following subsection.

Sr-based Compound	SCRO	SMRO	SFRO
Symmetry	Rhombohedral	Tetragonal	Rhombohedral
Spacegroup	$R\bar{3}$	I4/m	$R\bar{3}$
a=b/Å	5.551	5.458	5.574
c/Å	5.551	8.282	5.574
$\alpha = \beta = \gamma$	60.860	90	60.546
$V/\mathring{A}^3$	123.293	246.719	123.968
Sr site	2c	4d	2c
Sr_x	0.2499	0.0	-0.2499
Sr_y	0.2499	0.5	-0.2499
Sr_z	0.2499	0.25	-0.2499
B site	1a	2b	1a
B_x	0	0	0
B_y	0	0	0
B_z	0	0.5	0
Rh site	1b	2a	1b
Rh_x	0.5	0	0.5
Rh_y	0.5	0	0.5
Rh_z	0.5	0	0.5
O1(O2) site	6f	8f(4e)	6f
$O1_x(O2_x)$	0.2525	0.2005(0.0)	0.2946
$O1_y(O2_y)$	-0.1974	-0.3065(0.0)	0.2073
$O1_z(O2_z)$	0.6984	0.00(-0.2419)	-0.2518

Table 5.1: Predicted crystal structures of Sr_2BRhO_6 compounds.

Ca-based Compound	CCRO	CMRO	CFRO
Symmetry	Rhombohedral	Rhombohedral	Rhombohedral
Spacegroup	$R\bar{3}$	$R\bar{3}$	$R\bar{3}$
a=b=c/Å	5.418	5.391	5.422
$\alpha = \beta = \gamma$	61.343	61.567	61.336
V/$\mathring{A}^3$	115.855	114.683	116.094
Ca site	2c	2c	2c
Ca_x	-0.2489	-0.2506	-0.2517
Ca_y	-0.2489	-0.2506	-0.2517
Ca_z	-0.2489	-0.2506	-0.2517
B site	1b	1a	1a
B_x	0.5	0	0
B_y	0.5	0	0
B_z	0.5	0	0
Rh site	1a	1b	1b
Rh_x	0	0.5	0.5
Rh_y	0	0.5	0.5
Rh_z	0	0.5	0.5
O site	6f	6f	6f
O_x	0.2462	0.3326	-0.1677
O_y	-0.1637	0.1624	0.6667
O_z	0.6657	-0.2482	0.2535

Table 5.2: Predicted crystal structures of Ca_2BRhO_6 compounds.

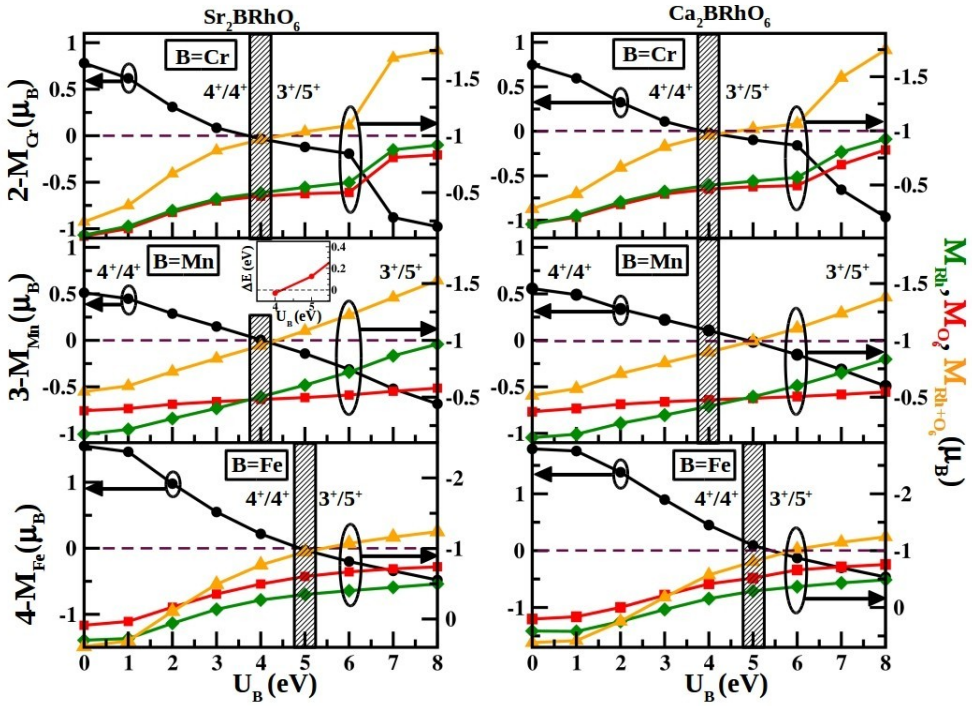

Figure 5.2: B site magnetic moment (M_B), shown in left y-axis, Rh site magnetic moment (M_{Rh}), magnetic moments on oxygen sites (M_{O_6}), the combined moment at Rh and O sites (M_{Rh+O_6}), all three quantities shown in right y-axis, plotted as a function of Hubbard U at B site (U_B), for Sr_2BRhO_6 and Ca_2BRhO_6 (B=Cr, Mn, Fe) compounds. M_B, M_{Rh}, M_{O_6}, M_{Rh+O_6} are shown in black, green, red and yellow lines, respectively. For the moment on B site, plotted are the quantities, ΔM = 2 - M_{Cr}, 3 - M_{Mn} or 4 - M_{Cr}. The change of valence at B site from 4+ to 3+ is signaled by change in ΔM from a value within +1 μ_B to 0 μ_B to a value within 0 μ_B to -1 μ_B. The hatched bar in each panel signals the critical value of U_B at which such change-over happens. At this critical value of U_B, M_{Rh+O_6}also changes from a value less that -1 μ_B to a value within -1 μ_B to -2 μ_B. The inset in left, middle panel of the figure shows the plot of energy difference between non-perovskite C2/m symmetry and perovskite I4/m symmetry plotted as a function of U_B for Sr_2MnRhO_6. Note that crossover from the non-perovskite C2/m symmetry to perovskite I4/m symmetry happens that at same critical U_B value at which crossover of valences from 4+/4+ to 3+/5+ at B/Rh happens.

5.3.2 Magnetic moment, Valence States, Electronic Structure

In order to discuss the electronic properties of B ion and Rh ion in Sr_2BRhO_6 and Ca_2BRhO_6 (B = Cr, Mn, Fe) compounds, we start with discussion of calculated magnetic moments at B, Rh and O sites, as given in GGA+U calculations. Calculated magnetic moments in plane wave basis and in linear muffin-tin orbital basis (in parenthesis) are listed in Table 5.3. The moments at Sr or Ca sites

Compound	U_B in eV	B	Rh	O	Total
Sr_2CrRhO_6	3	-1.915(-1.935)	0.426(0.440)	0.074(0.079)	-1.00
	4	-2.034(-2.050)	0.468(0.560)	0.083(0.081)	-1.00
	5	-2.121(-2.163)	0.490(0.604)	0.091(0.091)	-1.00
Sr_2MnRhO_6	3	-2.851(-2.918)	0.461(0.438)	0.067(0.081)	-2.00
	4	-3.008(-3.053)	0.488(0.458)	0.084(0.098)	-2.00
	5	-3.142(-3.197)	0.497(0.479)	0.101(0.118)	-2.00
Sr_2FeRhO_6	4	-3.782(-3.811)	0.497(0.574)	0.045(0.038)	-3.00
	5	-4.027(-4.112)	0.604(0.637)	0.058(0.065)	-3.00
	6	-4.200(-4.312)	0.670(0.702)	0.067(0.079)	-3.00
Ca_2CrRhO_6	3	-1.890(-1.886)	0.416(0.475)	0.073(0.067)	-1.00
	4	-2.017(-2.015)	0.462(0.518)	0.083(0.081)	-1.00
	5	-2.098(-2.129)	0.484(0.552)	0.089(0.093)	-1.00
Ca_2MnRhO_6	3	-2.779(-2.873)	0.459(0.486)	0.057(0.066)	-2.00
	4	-3.002(-3.010)	0.480(0.509)	0.079(0.081)	-2.00
	5	-3.015(-3.123)	0.490(0.528)	0.084(0.098)	-2.00
Ca_2FeRhO_6	4	-3.550(-3.680)	0.416(0.439)	0.026(0.032)	-3.00
	5	-4.012(-4.021)	0.527(0.534)	0.053(0.059)	-3.00
	6	-4.129(-4.221)	0.661(0.697)	0.061(0.075)	-3.00

Table 5.3: Calculated total magnetic moment and moments at B (Cr/Mn/Fe), Rh and O site for Sr_2BRhO_6 and Ca_2BRhO_6 compounds at different U values from plane-wave calculation and from linear muffin-tin orbital (LMTO) basis calculations (in parenthesis). Moments are listed for three different U_B values, chosen around the critical U_B value at which predicted transition of valence state of B/Rh from 4+/4+ to 3+/5+ happens.

are found to be negligible small. Interestingly, we find the computed magnetic moment to be strongly dependent on the choice of U value at the B site. The results are presented in Fig. (5.2). For reference, the plot also includes the result of GGA calculation, shown as the data point corresponding to $U_B = 0$ eV. We note that for nominal valence of 4+ at B site in Sr_2BRhO_6 or Ca_2BRhO_6, the magnetic moment at B site (M_B) is expected to be 1 μ_B < M_B <2 μ_B for B =

Cr, 2 μ_B <M_B <3 μ_B for B = Mn and 3 μ_B < M_B < 4 μ_B for B = Fe, corresponding to d^2, d^3 and d^4 nominal occupancies, respectively. Decrease of nominal valence from 4+ to 3+ at B site, should result into magnetic moments at B site, 2 μ_B <M_B < 3 μ_B for B = Cr, 3 μ_B < M_B <4 μ_B for B = Mn and 4 μ_B < M_B < 5 μ_B for B = Fe, corresponding to d^3, d^4 and d^5 nominal occupancies, respectively. As is seen from Fig. (5.2), upon increasing U value of B site, a transition from nominal valence of 4+ to 3+ happens at B site, at critical value of U_B, estimated to be 4 eV for Cr-Rh and Mn-Rh compounds, and 5 eV for Fe-Rh compounds. Concomitantly, the magnitude of magnetic moment at Rh site, together with moments at O sites are also found to increase, which are found to be aligned in opposite direction to that of M_B. At the critical value of U_B, the net moment on Rh and six O sites in the formula unit, M_{Rh+O_6}, is also found make a transition from M_{Rh+O_6} <1 μ_B to 1 μ_B < M_{Rh+O_6} < 2 μ_B. The total moment in the formula unit is found to be 1 μ_B, 2 μ_B and 3 μ_B respectively, irrespective of the choice of U_B, due to cancellation of moments between M_B and that of M_{Rh+O_6}. We thus conclude a transition of nominal 4+/4+ valence of B/Rh to 3+/5+ valence of B/Rh happens beyond critical value of U_B.

As is also evident, the unusual 5+ valence of Rh gets stabilized having a large contribution of moment from oxygen sites. Thus ideally the valence should be written as $Rh^{4+}\underline{L}$. [19] The U_B dependent change in Rh-O bond-length, as described in previous sub-section, further supports the change of nominal valence from 4+/4+ to 3+/5+. [20]

The microscopic mechanism of U_B assisted stabilization of unusual 5+ valence of Rh may be rationalized in the following manner. Increase of U_B shifts the *d* energy level position of B site with respect to O *p* level, thereby destabilizing the O *p* states, promoting increased orbital overlap with Rh *d* states, which facilitates the formation of ligand hole. Very interestingly, we find also at this critical U_B value, a transition from non-perovskite structure to perovskite structure happens for Sr based compound. This is seen in the plot of energy difference between non-perovskite and perovskite structures, as a function of U_B, the representative case of Sr_2MnRhO_6 being presented as inset in left, middle panel of Fig. (5.2) Similar cross-over of structural stability is observed between C2/m and $R\bar{3}$ for Sr_2CrRhO_6 and Sr_2FeRhO_6 (see Fig. (5.3)). We note that a transition from 4+/4+ to 3+/5+ also effectively reduces the tolerance factor slightly, e.g. from 1.03 to 1.01 for Sr_2MnRhO_6, making the formation of perovskite structure more favorable. In the following, we present the results considering the perovskite $R\bar{3}$ structure for Sr_2CrRhO_6 and Sr_2FeRhO_6, and I4/m structure for Sr_2MnRhO_6.

In order to check the influence of spin-orbit coupling (SOC), which might be important for 4*d* Rh ion, we also repeat calculations within the framework of GGA+U+SOC. The trend, as described above is found to remain valid. The orbital moment at Rh site is found to be around 0.10 - 0.13 μ_B, aligned in the same direction to that of the spin moment at Rh site, in agreement with more

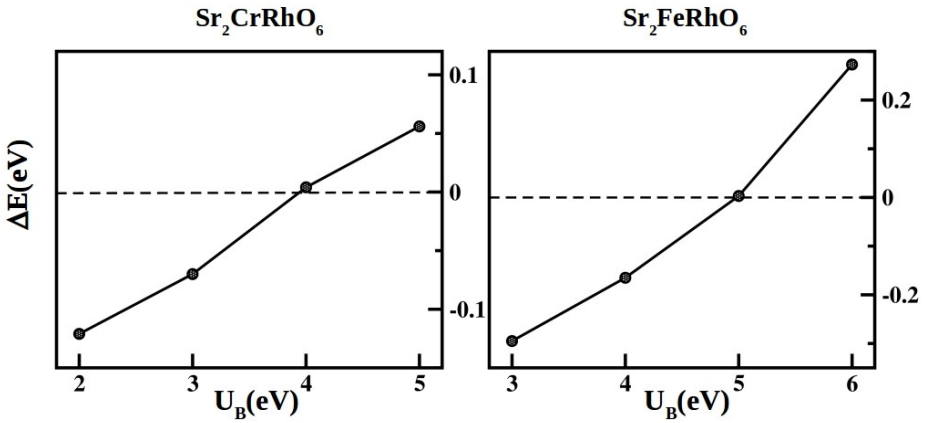

Figure 5.3: Energy difference between non-perovskite C2/m symmetry and perovskite R$\bar{3}$ symmetry plotted as a function of U_B for Sr_2CrRhO_6 (left panel) and Sr_2FeRhO_6 (right panel).

than half-filled nature of Rh t_{2g} occupancy. The orbital moments at B and O sites are found to be negligible (see Table. 5.4).

The spin-polarized density of states (DOS) of the compounds in double-perovskite space groups, R$\bar{3}$ for Sr_2CrRhO_6, Sr_2FeRhO_6, Ca_2CrRhO_6, Ca_2MnRhO_6 and Ca_2FeRhO_6 compounds, and I4/m for Sr_2MnRhO_6 are shown in Fig. (5.4). The states close to Fermi level are dominantly of B d and Rh d character which are both crystal field split into t_{2g} and e_g, and spin-split. First observation to be made is that that the spin-splitting at Rh site is oppositely oriented to that at B site in agreement with oppositely directed moments at B and Rh sites, as described previously. We further find that DOS plots of Ca and Sr compounds show similar features for choice of same B site element, except small decrease in band width in Ca compounds compared to corresponding Sr counterparts.

We find that the Rh e_g states are empty in both spin channels in all compounds, in conformity with low spin nominal d^4 state of Rh. This makes Rh t_{2g} states completely filled in down spin channel and Rh t_{2g} - O p hybridized state in the up spin channel partially filled with about 1 electron. This creates a gap in down spin channel, while in up spin channel partially filled Rh t_{2g} - O p states cross the Fermi energy strongly admixed with Cr t_{2g} states or Mn e_g states or Fe e_g states in case of Cr-Rh compounds or Mn-Rh compounds or Fe-Rh compounds. This drives half-metallic solution in all cases. The inset in the left, middle panel of Fig. (5.4) shows the plot of charge density with an energy window set between Fermi level and 0.5 eV above Fermi level. This shows that the unfilled low energy states, which are completely spin-polarized due to the half-metallic character of the ground state, have a rather large contribution from the oxygen

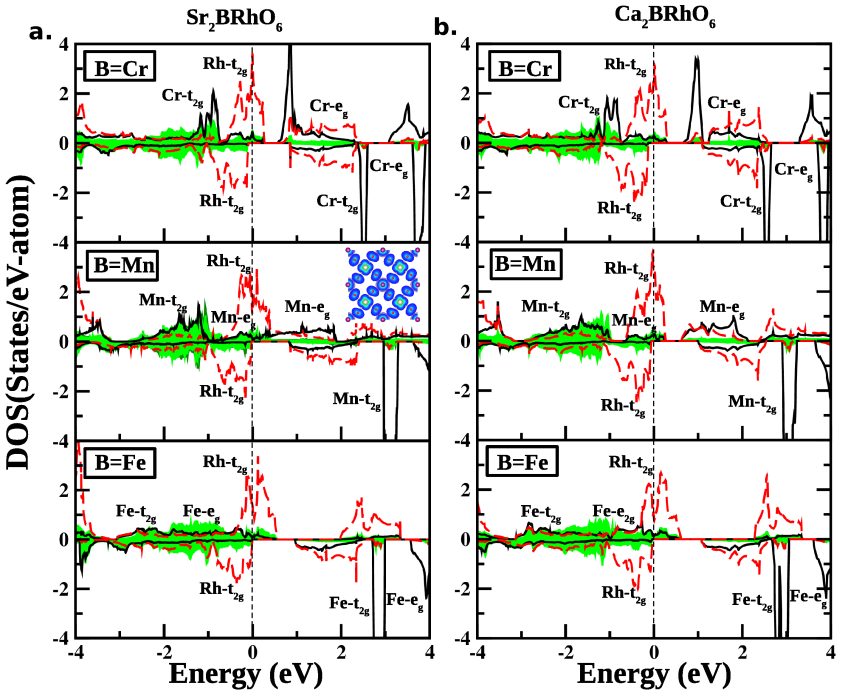

Figure 5.4: GGA+U (U_B = 5 eV, U_{Rh} = 1 eV, J_H = 0.8 eV) density of states, projected onto B d states (black, solid line), Rh d states (red, dashed lines) and O p states (green, shaded area) for Sr_2BRhO_6 and Ca_2BRhO_6 (B=Cr, Mn, Fe) compounds. The zero of the energy is set at GGA+U Fermi energy in each case. The inset in left, middle panel shows the plot of charge density calculated for the energy window from 0 eV to 0.5 eV. The isosurface value in the charge density plot is set at 0.015 $e^-/Å^3$.

Compound	Total Magnetic moment	Magnetic moments	B	Rh	O
Sr_2CrRhO_6	0 0 -1.00	Spin	-2.122	0.478	0.089
		Orbital	0.011	0.087	0.006
Sr_2MnRhO_6	0 0 -2.00	Spin	-3.143	0.485	0.167
		Orbital	0.000	0.131	0.007
Sr_2FeRhO_6	0 0 -3.00	Spin	-4.201	0.663	0.065
		Orbital	-0.014	0.095	0.010
Ca_2CrRhO_6	0 0 -1.00	Spin	-2.098	0.475	0.087
		Orbital	0.014	0.094	0.006
Ca_2MnRhO_6	0 0 -2.00	Spin	-3.016	0.490	0.081
		Orbital	0.000	0.111	0.006
Ca_2FeRhO_6	0 0 -3.00	Spin	-4.131	0.654	0.059
		Orbital	-0.014	0.101	0.007

Table 5.4: GGA+U+SOC (U_B = 5 eV, U_{Rh} = 1 eV, J_H = 0.8 eV) calculated spin and orbital magnetic moments for Sr_2BRhO_6 and Ca_2BRhO_6 compounds.

orbitals, thereby establishing the scenario of the ligand hole formation.

5.3.3 Magnetic Ground State

The literature of magnetic double-perovskites shows that they exhibit ferromagnetism as well as antiferromagnetism. While compounds like Ca_2CrMoO_6, Sr_2CrMoO_6, Ba_2CrMoO_6, Ca_2CrReO_6, Sr_2CrReO_6, Ca_2CrWO_6, Sr_2CrWO_6, Sr_2FeMoO_6, Sr_2MnReO_6 etc are reported to be ferromagnets, the compounds like Sr_2MnMoO_6, Ca_2MnWO_6, Sr_2MnWO_6, Ba_2MnWO_6, Sr_2FeWO_6 etc are reported to be antiferromagnets. [21] Also based on model calculations [22] as well as DFT calculations [23] competing ferromagnetic, and A-type and G-type antiferromagnetic (AFM) phases, driven by kinetic energy, have been predicted for doped double-perovskites. The signature of such competing antiferromagnetic phase has been further verified experimentally upon large doping of Sr_2FeMoO_6 by La. [24] In view of the above we carry out total energy calculations considering the ferromagnetic (FM) alignment of B site spins, together with A-type and G-type antiferromagnetic arrangement of B spins within a 2 × 2 × 2 supercell of the compounds. In case of A-type antiferromagnetism (A-AFM) the B spins in-plane are ferromagnetically coupled, while B spins between two adjacent plans are antiferromagnetically coupled. For G-type antiferromagnetism (G-AFM), the B spins are antiferromagnetically coupled both out-of- plane and in-plane. The A-type, G-type and ferromagnetic arrangements are shown in Fig. (5.5).

Comparison of the GGA+U total energy of the three magnetic structures

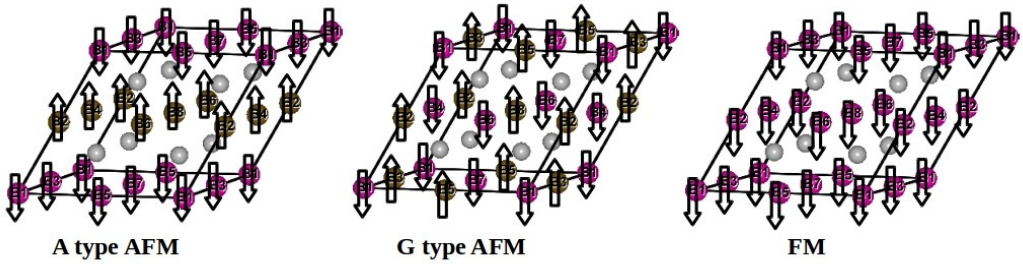

Figure 5.5: A type (left panel), G type (middle panel) antiferromagnetic (AFM) and ferromagnetic (right panel) (FM) arrangement of B (Cr/Mn/Fe) site spins in SCRO, SMRO, SFRO, CCRO, CMRO and CFRO. Oxygen and A site (Sr/Ca) atoms in the structures are not shown for clarity. The spin structure of only B site (pink and brown balls) have been shown, while the induced spins at Rh sites (shown as light gray balls) have not been shown.

shows the ferromagnetic state to the minimum energy state among the three considered magnetic structures for SCRO, SMRO, CCRO and CMRO. For choice of $U_B = 5$ eV, the FM state is found to be favored compared to A-AFM and G-AFM states by energy difference of 39.3 (49.1) meV/f.u. and 39.7 (49.4) meV/f.u., respectively, for SCRO (CCRO). SMRO and CMRO show the similar trend as SCRO and CCRO, in terms of FM state being the minimum energy state, with Ca-counterparts showing enhanced stability of FM state with respect to AFM states, compared to Sr-compounds. The calculated magnetic moments in the A-AFM and G-AFM phases, show the magnetic moment at Cr/Mn site to be robust showing little variation between FM and AFM phases, while the the moments at Rh and O sites are found to be vanishingly small in AFM phases (see Table. 5.5 for calculated magnetic moments in FM and AFM phases) indicating the induced nature of moments at Rh and O sites, as will be discussed in the following.

Very interestingly, moving to Fe-Rh compounds, both for Sr and Ca-counterparts, the AFM structures came out to be minimum energy states, with slight preference of A-AFM over G-AFM, and separated by an energy difference of 109.1 meV/f.u. from the FM solution for SFRO and 43.1 meV/f.u. for CFRO. We find this antiferromagnetic state to be metallic as seen in Fig. (5.6). This makes the situation as one among the rare cases of antiferromagnetic metal, deviating from established wisdom of relation between magnetic order and electrical conductivity, *i.e.* antiferromagnets are insulators and ferromagnets are metals. There are only few examples of this exceptional situation, reported in case of compounds with low-dimensional electronic structure, [25] and only one known so far in perovskite family. [26]

Since the above results have been obtained for a specific choice of U_B value,

Compound	Magnetic ordering	B	Rh	O	Total
Sr_2CrRhO_6	A-AFM	2.017	0.000	0.006	0.00
	G-AFM	2.015	0.007	0.01	0.00
	FM	2.122	-0.490	-0.091	1.00
Sr_2MnRhO_6	A-AFM	3.092	0.206	0.020	0.00
	G-AFM	3.058	0.172	0.01	0.00
	FM	3.144	-0.499	-0.090	2.00
Sr_2FeRhO_6	A-AFM	4.001	0.000	0.060	0.00
	G-AFM	3.997	0.000	0.055	0.00
	FM	4.026	-0.602	-0.06	3.00
Ca_2CrRhO_6	A-AFM	2.006	0.000	0.018	0.00
	G-AFM	2.003	0.000	0.016	0.00
	FM	2.098	-0.484	-0.089	1.00
Ca_2MnRhO_6	A-AFM	2.931	0.00	0.008	0.00
	G-AFM	2.935	0.00	0.010	0.00
	FM	3.015	-0.490	-0.080	2.00
Ca_2FeRhO_6	A-AFM	3.866	0.000	0.030	0.00
	G-AFM	3.860	0.00	0.029	0.00
	FM	3.906	-0.573	-0.040	3.00

Table 5.5: GGA+U ($U_B = 5$ eV, $U_{Rh} = 1$ eV, $J_H = 0.8$ eV) total magnetic moment and moments at B, Rh and O site for A-AFM, G-AFM, FM for Sr_2BRhO_6 and Ca_2BRhO_6 compounds.

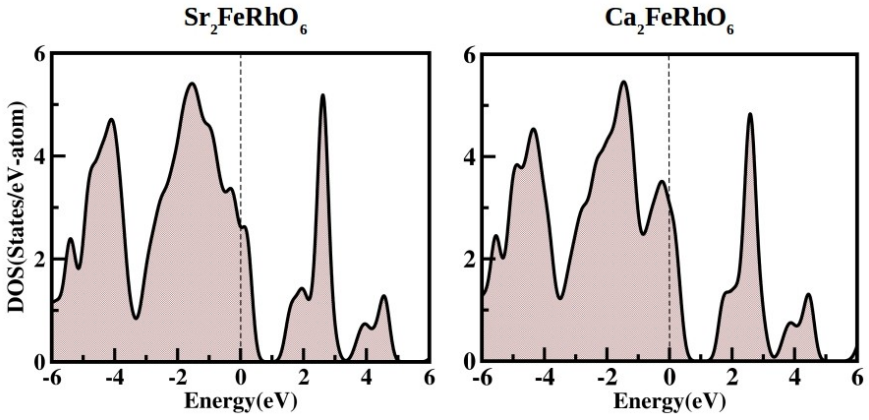

Figure 5.6: A-AFM GGA+U ($U_B = 5$ eV, $U_{Rh} = 1$ eV, $J_H = 0.8$ eV) total density of states for Sr_2FeRhO_6 and Ca_2FeRhO_6 compounds. The zero of the energy is set at GGA+U Fermi energy in both cases.

the natural question to ask is that how robust is the obtained ground state upon variation of U_B value. In order to answer this, we have carried out calculations of ground state magnetic structures, over the entire studied range of U_B = 1-8 eV. In all cases, the ferromagnetic state turns out to be the ground state for Cr-Rh and Mn-Rh compounds, while the antiferromagnetic state is found to be the ground state for Fe-Rh compounds (cf. Fig. (5.7)).

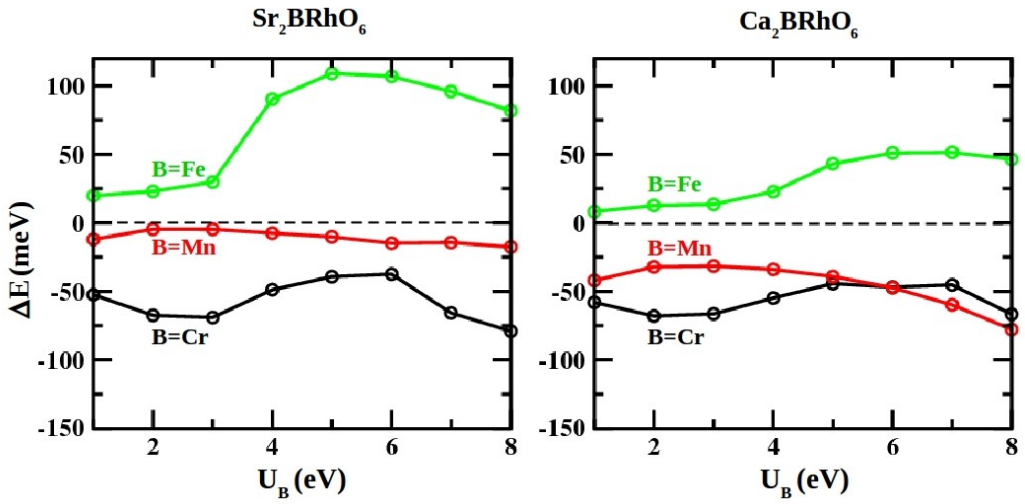

Figure 5.7: Energy difference per formula unit (ΔE) between FM and AFM structures plotted as a function of U_B for SCRO (black line), SMRO(red line), and SFRO(green line) in the left panel and for CCRO (black line) and CMRO(red line) and CFRO(green line) in the right panel.

5.3.4 Mechanism of magnetism and Model calculation of magnetic Transition Temperature

The fact that the moments at Rh and O site are strongly dependent on the arrangement of B site spins in Sr_2BRhO_6 and Ca_2BRhO_6 compounds indicates that the moment on the Rh-O network is induced by the magnetism at B site. This scenario was first described in the context of Sr_2FeMoO_6 in terms of hybridization driven mechanism. [27] Within this mechanism, if the effective energy levels of the 4*d* or 5*d* TM *d* - O *p* fall within the exchange split energy levels of 3*d* TM *d*, due to the hybridization between states of same spin and symmetry at the two sites, a negative spin-polarization is induced at the 4*d* or 5*d* - O network re-normalizing the intrinsic spin-polarization at the 4*d* or 5*d* - O network. Following this, in the ferromagnetic configuration of B (Cr/Mn/Fe) site spins, this gives rise to an intrinsic spin splitting at 3*d* TM site and an induced, negative spin splitting at

Rh network. In the antiferromagnetic structure, on the other hand, where the intrinsic spins at neighboring $3d$ TM (Cr/Mn/Fe) sites are oppositely aligned, the induced spin splitting at the Rh - O network due to the effect of two neighboring $3d$ TM sites cancel out resulting into vanishing magnetic moments at Rh and O sites. Calculated energy level diagrams of B site d level and effective Rh t_{2g} - O p levels of Sr_2BRhO_6 or Ca_2BRhO_6 series, shows that effective Rh t_{2g} - O p states appear within the spin-split energy levels of B sites, further supporting the hybridization-driven mechanism of magnetism to be operative in Sr_2BRhO_6 and Ca_2BRhO_6 series.

Interesting enough, the hybridization-driven mechanism supports filling driven FM-AFM transition, which was predicted theoretically [23] and verified experimentally [24] for La doped Sr_2FeMoO_6. As opposed to super-exchange driven insulating antiferromagnetic state found in DPs [28], the antiferromagnetic phase within the hybridization-driven mechanism of magnetism is metallic. The increase of filling upon moving from Cr or Mn in Cr-Rh or Mn-Rh compounds to Fe in Fe-Rh compounds, drives the Fe-Rh DPs antiferromagnetic with Fe spins aligned antiparalelly in A-AFM manner with vanishing moment at Rh, O sites, as opposed to FM ground state of Cr-Rh or Mn-Rh DPs with parallel alignment of B site moments and induced moment on Rh. As schematically shown in Fig. (5.8), in case of Cr-Rh or Mn-Rh compounds, the minority spins on Rh site, which are parallel to the majority spins on the B site, can hop via the majority spin t_{2g} - e_g hybridization, provided all the B site moments are parallel, and all the Rh site moments are antiparallel to them (cf. top two panels of Figs. (5.8)). In case of Fe-Rh compounds, the e_g states in majority spin channel at B site gets filled, thus prohibiting B-Rh hybridization in the majority spin channel of B site, unlike Cr-Rh or Mn-Rh compounds. In an antiferromagnetic arrangement of B site spins on the other hand (cf. bottom panel of Fig. (5.8)), both the minority and majority spin electrons at the Rh site can hybridize with the B sites in either down (Scenario 1 in the figure) or up spin (Scenario 2 in the figure) sublattices, thus maximizing the kinetic energy of hybridization. This makes Fe-Rh DPs one of the rare example of undoped DPs in AFM metallic phase.

Furthermore, it is interesting to note that the magnetism in the compounds under discussion, being governed by hybridization-driven mechanism, as opposed to more conventional superexchange mechanism, is almost insensitive to the change in the valences from 4+/4+ to 3+/5+, as long as energy levels of Rh d states fall within the spin-split d energy levels of B site. The predicted magnetic properties, thus turned out to be robust upon variation of U_B over large range, as demonstrated above.

The important ingredients in the hybridization-driven mechanism, as pointed out in Refs. [22, 29], are (i) a large core spin (S) at B site, (ii) strong coupling between B site core spin and the itinerant electron on B′-O network when it hops onto the B site, inducing preferred polarization of the itinerant electron in

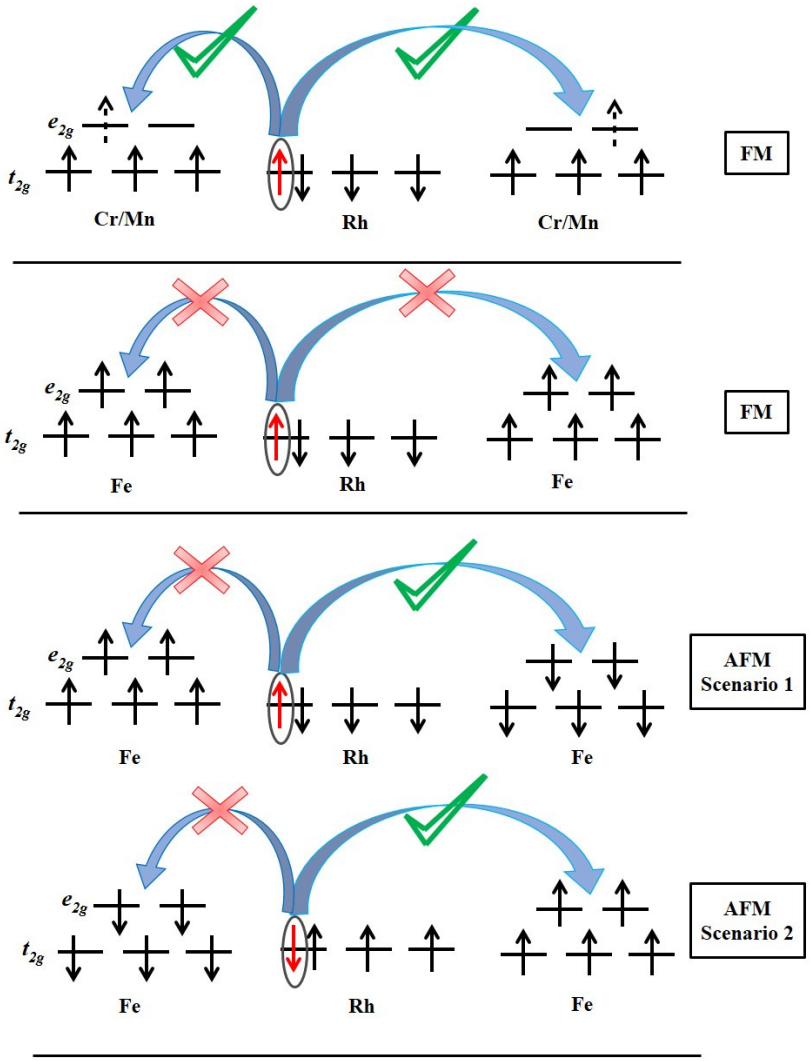

Figure 5.8: The schematic representation of allowed and dis-allowed hybridization between B (Cr/Mn or Fe) and Rh sites within the hybridization-driven mechanism.

Compound	Structure	D_{NN} (meV)	D_{NNN} (meV)	T_C (K)	T_N (K)
SCRO	rhombohedral	-6.62	-6.54	135	
SMRO	tetragonal	-2.05	-1.79	40	
SFRO	rhombohedral	16.6	18.9		145
CCRO	rhombohedral	-8.23	-8.16	170	
CMRO	rhombohedral	-6.18	-6.71	135	
CFRO	rhombohedral	5.78	7.88		60

Table 5.6: T_c, T_N and exchanges D_{NN} and D_{NNN} (see text) for the model spin Hamiltonian corresponding to Sr_2BRhO_6 and Ca_2BRhO_6 compounds.

one spin channel over other, and (iii) delocalization of the itinerant electron on the B-O-B$^{'}$ network. This can be written in terms of a B and effective B$^{'}$ site two-sublattice double-exchange model, given by,

$$\begin{aligned} H &= \epsilon_B \sum_{i\in B,\sigma} c_{i\sigma}^{B\dagger} c_{i\sigma}^{B} + \epsilon_{B'} \sum_{i\in B',\sigma} c_{i\sigma}^{B'\dagger} c_{i\sigma}^{B'} \\ &+ t \sum_{<ij>\sigma} c_{i\sigma}^{B\dagger} c_{j\sigma}^{B'} + J \sum_{i\in B,\alpha\beta} \vec{\mathbf{S}}_i \cdot c_{i\alpha}^{B\dagger} \vec{\sigma}_{\alpha\beta} c_{i\beta}^{B} \end{aligned} \tag{5.1}$$

where ϵ_B and $\epsilon_{B'}$ represent onsite energies on the B and B$^{'}$ sublattices. The third term in the Hamiltonian represents the kinetic energy of the itinerant electrons, t being the effective B-B$^{'}$ hopping. $c_{i\sigma}^{B\dagger}$ and $c_{i\sigma}^{B'\dagger}$ create B and B$^{'}$ site fermions respectively at the i-th site with spin σ. $\mathbf{S}_i$'s are the classical (large) core spins at B site, coupled to the itinerant electrons through a coupling $J >> t$. In the limit $J \to \infty$, the above Hamiltonian can be recast to an effective model involving only the core spin $\mathbf{S}$ of the B sites, integrating out the fermionic degrees of freedom of the itinerant electron using the procedure of self-consistent renormalization [22], given by,

$$H_{eff}\{\mathbf{S}\} \approx \sum_{<<ij>>} D_{ij} \sqrt{\frac{1+\mathbf{S}_i.\mathbf{S}_j}{2}} \tag{5.2}$$

While the original Hamiltonian given by Eqn. (Eq. (5.1)) contains only nearest neighbor hopping, the effective model, given by Eqn.(Eq. (5.2)) contains the nearest neighbor (D_{NN}) as well as next nearest neighbor (D_{NNN}) interactions.

In the present work the Hamiltonian, H_{eff}, has been used phenomenologically, and the parameters D_{ij} have been obtained from DFT total energies of the FM, A-AFM and G-AFM configurations. The calculated values for D_{NN} and D_{NNN} for Sr_2BRhO_6 and Ca_2BRhO_6 compounds are listed in Table 5.6. With the DFT inputs for D_{NN} and D_{NNN}, the core spin Hamiltonian was simulated using Monte Carlo algorithm. It was confirmed that for each of the compounds same

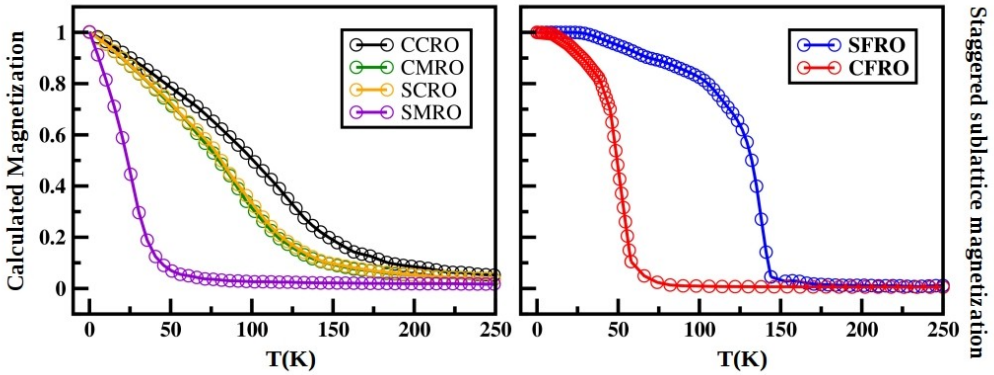

Figure 5.9: Calculated magnetization from Monte Carlo simulation plotted as a function of temperature, for SCRO (yellow line), CCRO (black line), SMRO(violet line), and CMRO(green line) in the left panel and for SFRO (blue line) and CFRO(red line) in the right panel.

magnetic ground state was obtained from the Monte Carlo simulation as obtained from DFT.

From the Monte Carlo simulation, the magnetization was calculated as a function of temperature (cf. Fig. (5.9)), and the ferromagnetic transition temperatures, T_c was obtained for SCRO, CCRO, SMRO, and CMRO. Similarly, the staggered sublattice magnetization was calculated as a function of temperature from Monte Carlo simulation, and antiferromagnetic transition temperatures, T_N's were obtained for SFRO and CFRO. Following the same procedure, T_c for well-known double perovskite compound Sr_2CrMoO_6 was computed, which was found to be about 430K, in good agreement with experimentally measured T_c, [16] thereby providing confidence in the adapted procedure. The calculated T_c and T_N values for the Sr_2BRhO_6 and Ca_2BRhO_6 compounds are listed in Table 5.6, which show that other than SMRO and CFRO, the magnetic transition temperatures to be above 100K.

5.3.5 Predicted growth conditions

Our computational prediction for the unknown Sr_2BRhO_6 and Ca_2BRhO_6 (B = Cr, Mn, Fe) compounds employing USPEX in conjunction with DFT resulted in ground state structures belonging to the double perovskite family. The predicted oxidation state of the Rh ion is 5+ which is different from the conventional 3+ or 4+ oxidation state of Rh, known for Rh-based perovskites and thus unusual. For guiding the future synthesis of these compounds, analysis of the thermodynamic stability of the predicted Rh-based DP compounds is important. This will ascer-

tain the possibility of their formation in reality, allowing one to determine, among other things, the thermodynamic stability of the predicted compounds with respect to decomposition into their competing phases. In particular, we follow the formalism outlined in Ref. [8, 9], based on the computation of the formation enthalpies ΔH_f of both the predicted compound and it's competing phases.

The enthalpy of formation ΔH_f, defined as the energy needed to form a compound from it's constituent elements, is given by

$$\Delta H_f(A_{n_1}B_{n_2}\ldots) = E^{DFT}(A_{n_1}B_{n_2}\ldots) - \sum_I n_I\mu_I$$

where, $E^{DFT}(A_{n_1}B_{n_2}\ldots)$ is the total ground state energy per formula unit of the predicted compound and μ_I is the chemical potential of the constituent elements A, B, ... in their elemental reference phase. If ΔH_f is negative, then it is possible to estimate chemical potential ranges of the constituent elements within which the predicted compound is thermodynamically stable. This is achieved by formulating a set of equalities and inequalities in terms of the chemical potentials within the grand canonical ensemble, which need to be satisfied.

For the A_2BRhO_6 compounds, these set of equalities and inequalities are as follows,

$$2\Delta\mu_A + \Delta\mu_B + \Delta\mu_{Rh} + 6\Delta\mu_O = \Delta H_f(A_2BRhO_6) \tag{5.3}$$

where A = {Sr,Ca} and B = {Cr, Mn, Fe}

$$\Delta\mu_A \leq 0;\ \Delta\mu_B \leq 0;\ \Delta\mu_{Rh} \leq 0,\ \Delta\mu_O \leq 0 \tag{5.4}$$

and a set of inequalities for the number of competing phases given by

$$\begin{aligned} n^{(i)}\Delta\mu_A + m^{(i)}\Delta\mu_B + p^{(i)}\Delta\mu_{Rh} + q^{(i)}\Delta\mu_O \quad &\leq \Delta H_f(A_{n^{(i)}}B_{m^{(i)}}Rh_{p^{(i)}}O_{q^{(i)}}), \\ n, m, p, q &= 0, 1, 2, \ldots \\ i &= 1, \ldots, Z \end{aligned} \tag{5.5}$$

where A = {Sr, Ca} and B = {Cr, Mn, Fe}, $\Delta\mu_I = \mu_I - \mu_I^0$ is the deviation of the chemical potential of a component from it's elemental-phase reference, and Z is the number of competing phases with chemical formula $A_{n^{(i)}}B_{m^{(i)}}B'_{p^{(i)}}O_{q^{(i)}}$ with formation enthalpies $\Delta H_f(A_{n^{(i)}}B_{m^{(i)}}B'_{p^{(i)}}O_{q^{(i)}})$.

Eqn. (5.3) above represents the condition of thermodynamic equilibrium between the A_2BRhO_6 compound and it's constituent elements. Eqn. (5.3) along with the inequality (5.4), determine the allowed range of values for $\Delta\mu_I$ which can be represented as a triangle in the three-dimensional $(\Delta\mu_B, \Delta\mu_{Rh}, \Delta\mu_O\ )$ phase-space. We assume the A-rich limit i.e. $\Delta\mu_A = 0$. Eqn. (5.4) define a set of conditions which needs to be satisfied for the predicted $A_2BRh'O_6$ compound to

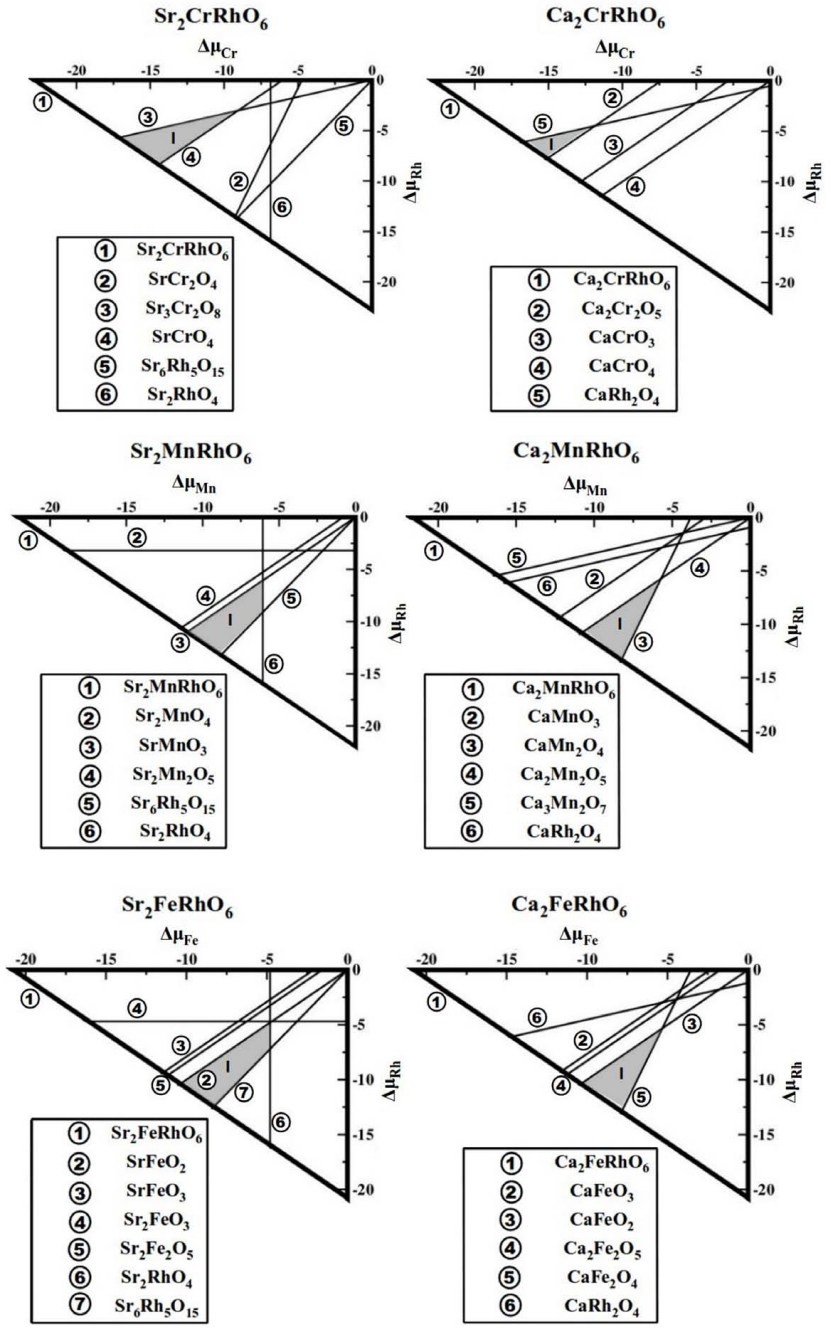

Figure 5.10: Projection of the allowed ranges of chemical potentials on the $(\Delta\mu_B, \Delta\mu_{Rh})$ plane with the shaded part representing the region of thermodynamic stability for the Sr_2BRhO_6 and Ca_2BRhO_6 compounds.

to be thermodynamically stable. For example, if one of the inequalities in Eqn.

Compound	$\Delta\mu_O$(min)/$\Delta\mu_O$(max) (eV)
SCRO	-1.79/0.00
SMRO	-1.65/0.00
SFRO	-1.86/0.00
CCRO	-0.46/0.00
CMRO	-1.69/0.00
CFRO	-1.68/0.00

Table 5.7: The calculated range of chemical potential of oxygen, necessary for growth of Sr_2BRhO_6 and Ca_2BRhO_6 (B = Cr, Mn, Fe) compounds.

(5.5) remains unsatisfied within the region defined by the triangle, then the predicted A_2BRhO_6 compound is unstable and it is energetically more favorable for the corresponding competing phase to be formed.

In Fig. (5.10), we show the projection of the triangle in the three-dimensional ($\Delta\mu_B, \Delta\mu_{Rh}, \Delta\mu_O$) phase-space into two-dimensional ($\Delta\mu_B, \Delta\mu_{Rh}$) phase-space for Sr_2BRhO_6 and Ca_2BRhO_6 (B = Cr, Mn, Fe) compounds, shown by thick, black line in each panel. The value of $\Delta\mu_O$ is equal to 0 on this line. Solving the inequality (5.5) simultaneously with Eqn.(5.3) for each of the competing phases leads to a set of inequalities that can plotted in ($\Delta\mu_B, \Delta\mu_{Rh}, \Delta\mu_O$) space. Their projections on the ($\Delta\mu_B, \Delta\mu_{Rh}$) plane are represented by thin, black lines, with each line corresponding to a single competing phase. The shaded region defines the stability region within which the compounds Sr_2BRhO_6 and Ca_2BRhO_6 (B = Cr, Mn, Fe) are stable.

The points of intersection ($\Delta\mu_B$, $\Delta\mu_{Rh}$), of the straight lines which enclose the stability region, define the allowed range of $\Delta\mu_O$, obtained by substituting the values of $\Delta\mu_B$ and $\Delta\mu_{Rh}$ in Eqn (5.3). Table. 5.7 lists the range of $\Delta\mu_O$ obtained for Sr_2BRhO_6 and Ca_2BRhO_6 (B = Cr, Mn, Fe) compounds. The allowed range of $\Delta\mu_O$ when recast in terms of oxygen partial pressure (p_{O_2}) and temperature (T) provide a gauge of the growth conditions for the Rh DP compounds. The dependence of the oxygen chemical potential on pressure and temperature can be obtained from equation [9]

$$\mu_O(T,p) = \mu_O(T,p_0) + \frac{1}{2}kTln\frac{p}{p_0}$$

where k is the Boltzmann constant and p_0 is taken as the standard pressure (1 atm).

Fig. (5.11) in SI shows the p_{O_2} vs T plot for a range of values of $\Delta\mu_O$. The shaded region in Fig. (5.11) indicates the conditions for growth of the predicted Rh-DP compounds, from which we assess that formation of Sr_2BRhO_6 and Ca_2BRhO_6 (B = Cr,Mn,Fe) compounds require high temperature synthesis for

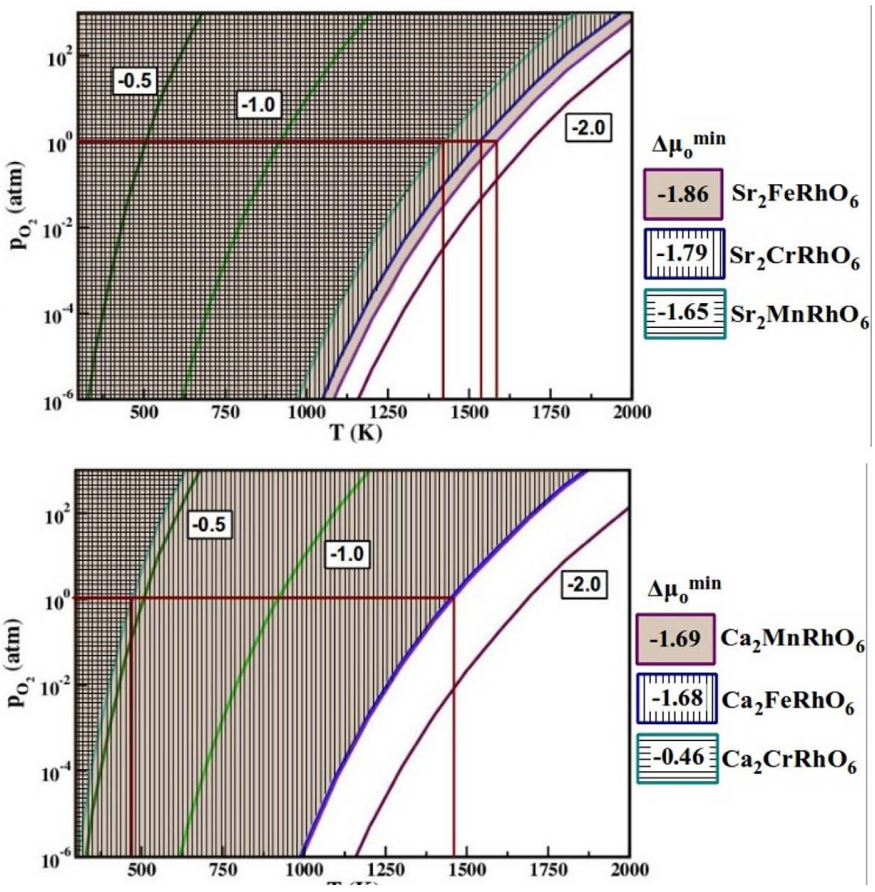

Figure 5.11: Plot of oxygen partial pressure p_{O_2} vs temperature T at different values of $\Delta\mu_O$. The shaded (hatched) area denotes the region corresponding to the allowed range of $\Delta\mu_O$ obtained for the predicted Sr_2BRhO_6 compounds (B = Cr/Mn/Fe) (top panel) and Ca_2BRhO_6 compounds (B = Cr/Mn/Fe) (bottom panel). The temperatures required to grow the compounds at standard atmospheric pressure are indicated by the dotted red line.

ambient pressure condition, or low pressure condition at room temperature.

5.4 Conclusions

In this study we considered the case of yet-to-synthesized Rh family of magnetic double perovskites, namely $Sr(Ca)_2BRhO_6$, where B is Cr or Mn or Fe. While Rh double-perovskites, having Nb, Ta or Sb at B site position have been synthesized, so far Rh based double perovskites having 3d TM ions at B site position have not been reported.

Through our computational study, we predicted the crystal structure, electronic, magnetic properties and growth conditions of these compounds, which should form a useful basis for attempts in synthesizing these compounds. In particular, we used the evolutionary algorithm to predict the crystal structure. To the best of our knowledge, such an algorithm has not been applied previously to complex, four component magnetic oxides. We validated our approach through prediction of crystal structure of well-known double perovskite like Sr_2CrMoO_6. The excellent comparison between predicted and measured structure provided confidence in our prediction. Considering the example of Sr_2BRhO_6 we discovered the competition between non-perovskite and perovskite structure, which is found to be dictated by change of nominal valence from 4+/4+ at B/Rh sites to 3+/5+. Very interestingly, we find that that 3+/5+ scenario is favored for choice of Hubbard U parameter at B site, U_B beyond a critical value. The unusual valence of Rh5+ is found to be stabilized through U_B-assisted change in the position of B *d* level, thereby destabilizing O *p* levels, effecting the Rh-O covalency, and creating oxygen ligand hole. The stabilization of Rh^{5+} through formation of the ligand hole would be possible to verify through spectroscopic techniques if these compounds can be synthesized, as in case of cuprates or nickelates. [30] Studying the electronic and magnetic structure of the compounds in predicted crystal structures, we further show that while Cr-Rh and Mn-Rh combinations give rise to ferromagnetic, half-metallic solutions, the Fe-Rh combinations are rare examples of antiferromagnetic metals. Analyzing the electronic structure further, we found that the magnetism in this compounds to be driven by hybridization-mediated mechanism, first discussed in context of Sr_2FeMoO_6. [27] Based on this analysis, we derived a model Hamiltonian, which we solved through Monte Carlo simulation to compute the magnetic transition temperature. The calculated values of magnetic transition temperatures turn out to be above 100 K for most compounds, except Sr_2MnRhO_6 and Ca_2FeRhO_6. Following this, we analyzed the favorable growth conditions from consideration of the formation enthalpies of the predicted compounds and their competing phases. Our analysis indicates that high temperature and low partial pressure oxygen would be required to synthesis the predicted materials.

Bibliography

[1] Vasala, S. & Karppinen, M. $A_2B'B''O_6$ Perovskites: A review. *Prog. in Solid State Chem.* **43**, 1-36 (2015).

[2] Jung, D-Y.; Demazeau, G. Structural and Magnetic Study on the Perovskite Rhodium(III) Oxides, $Sr_2MRh(III)O_6$ (M = Nb, Ta). *Solid state Commun.* **1995**, 12, 963-967.

[3] Blasse, G. New Compounds with Perovskite-like Structures. *J. Inorg. Nucl. Chem.* **1965**, 27, 993-1003.

[4] Arribi, P. V.; García-Fernández, P.; Junquera, J.; Pardo, V. Efficient thermoelectric materials using nonmagnetic double perovskites with d^0/d^6 band filling. *Phys. Rev.B: Condens. Matter Mater. Phys.* **2016**, 94, 035124.

[5] Lyakhov, A.O.; Oganov, A.R.; Valle, M. In *Modern Methods of Crystal Structure Prediction;* Oganov, A.R., Eds.; Wiley-VCH Verlag GmbH & KGaA : Weinheim, Germany, 2012; Chapter Crystal structure prediction using evolutionary approach, pp 147-180.

[6] Oganov, A. R.; Glass, C.W. Crystal structure prediction using ab initio evolutionary techniques: Principles and applications. *J. Chem. Phys.* **2006**, 124, 244704.

[7] Oganov A.R.; Glass C.W. Evolutionary crystal structure prediction as a tool in materials design. *J Phys: Condens Matter* **2008**, 20, 064210.

[8] Zhang, X.; Stevanović, V.; d'Avezac M.; Lany, S.; Zunger, A. Prediction of A_2BX_4 metal-chalcogenide compounds via first-principles thermodynamics. *Phys. Rev. B: Condens. Matter Mater. Phys.* **2012**, 86, 014109.

[9] Osorio-Gullién, J.; Lany, S.; Barabash, S.V.; Zunger, A. Magnetism without Magnetic Ions: Percolation, Exchange, and Formation Energies of Magnetism-Promoting Intrinsic Defects in CaO. *Phys. Rev. Lett: Condens. Matter Mater. Phys.* **2006**, 96, 107203.

[10] Kresse, G.; Hafner, J. Ab initio molecular dynamics for liquid metals. *Phys. Rev. B: Condens. Matter Mater. Phys.* **1993**, 47, 558-561.

[11] Kresse, G.; Furthmuller, J. Efficient iterative schemes for ab initio total-energy calculations using a plane-wave basis set. *Phys. Rev. B: Condens. Matter Mater. Phys.* **1996**, 54, 11169-11186.

[12] Blöchl, P. E. Projector augmented-wave method. *Phys. Rev. B: Condens. Matter Mater Phys.* **1994**, 50, 17953-17979.

[13] Perdew, J. P.; Burke, K.; Ernzerhof, M. Generalized Gradient Approximation Made Simple. *Phys. Rev. Lett.* **1996**, 77, 3865-3868.

[14] Anisimov, V. I.; Aryasetiawan, F.; Liechtenstein A. I. First-principles calculations of the electronic structure and spectra of strongly correlated systems: the LDA+U method. *J. Phys.: Condens. Matter.* **1997**, 9, 767.

[15] Liechtenstein, A. I.; Anisimov, V. I.; Zaanen, J. Density functional theory and strong interactions: Orbital ordering in Mott Hubbard insulators. *Phys. Rev. B: Condens. Matter Mater. Phys.* **1995**, 52, R5467-5470.

[16] Patterson, F. K.; Moeller, C. W.; Ward, R. Magnetic Oxides of Molybdenum(V) and Tungsten(V) with the Ordered Perovskite Structure. Inorg. Chem. **1963**, 2, 196-198.

[17] Kobayashi K. -I.; Kimura, T.; Sawada, H.; Terakura, K.; Tokura, Y. Room-temperature magnetoresistance in an oxide material with an ordered double-perovskite structure. *Nature.* **1998**, 395, 677-680.

[18] The predicted lattice parameters, a, b, c for Sr_2CrMoO_6 were 7.834Å, 7.834Å, 7.834 Å, respectively, compared to the experimentally measured values of 7.840Å, 7.840Å, and 7.840Å, respectively. This gave rise to Cr-O and Mo-O bond lengths of 1.933 $\mathring{A}$ and 1.984 $\mathring{A}$, respectively in the predicted structure, compared to 1.933 $\mathring{A}$ and 1.986 $\mathring{A}$, respectively in experimental structure. A similar level of agreement was also obtained for Sr_2FeMoO_6.

[19] Etourneau, J.; Portier, J; Ménil, F. The role of the inductive effect in solid-state chemistry - how the chemist can use it to modify both the structural and the physical properties of the materials. *J. Alloys Compd.,* **1992**, 188, 1-7.

[20] Reisner, B. A.; Stacy, A. M. Sr_3ARhO_6 (A = Li, Na): Crystallization of a Rhodium(V) Oxide from Molten Hydroxide. *J. Am. Chem. Soc.* **1998**, 120, 9682-9683.

[21] Philipp, J. B.; Majewski, P.; Alff, L.; Erb, A.; Gross, R.; Graf, T.; Brandt, M. S.; Simon, J.; Walther, T.; Mader, W.; Topwal, D.; Sarma D. D. Structural and doping effects in the half-metallic double perovskite A_2CrWO_6 (A=Sr, Ba, and Ca). *Phys. Rev.B: Condens. Matter Mater. Phys.* **2003**, 68, 144431.

[22] Sanyal, P.; Majumdar, P. Magnetic model for the ordered double perovskites. *Phys. Rev. B: Condens. Matter Mater. Phys.* **2009**, 80, 054411.

[23] Sanyal, P.; Das, H.; Saha-Dasgupta, T. Evidence of kinetic-energy-driven antiferromagnetism in double perovskites: A first-principles study of La-doped Sr_2FeMoO_6. *Phys. Rev. B: Condens. Matter Mater. Phys.* **2009**, 80, 224412.

[24] Jana, S.; Meneghini, C.; Sanyal, P.; Sarkar, S.; Saha-Dasgupta, T.; Karis, O.; Ray, S. Signature of an antiferromagnetic metallic ground state in heavily electron-doped Sr_2FeMoO_6. *Phys. Rev. B: Condens. Matter Mater. Phys.* **2012**, 86, 054433.

[25] Yoshida, Y. *et al.* Crystal and magnetic structure of $Ca_3Ru_2O_7$ *Phys. Rev. B: Condens. Matter Mater. Phys.* **72**, 054412-054418 (2005).

[26] Komarek, A. C. *et al.* $CaCrO_3$: An Anomalous Antiferromagnetic Metallic Oxide *Phys. Rev. Lett.* **101**, 167204-167207 (2008).

[27] Sarma,D. D.; Mahadevan, P.; Saha-Dasgupta, T.; Ray, S.; Kumar, A. Electronic Structure of Sr_2FeMoO_6. *Phys. Rev. Lett.: Condens. Matter Mater. Phys.* **2000**, 85, 2549.

[28] Fang, Z.; Terakura, K.; Kanamori, J. Strong ferromagnetism and weak antiferromagnetism in double perovskites: Sr_2FeMO_6 (M=Mo, W, and Re). *Phys. Rev. B: Condens. Matter Mater. Phys.* **2001**, 63, 180407(R).

[29] Chattopadhyay, A; Millis, A. J. Theory of transition temperature of magnetic double perovskites *Phys. Rev. B: Condens. Matter Mater. Phys.* **2001**, 64, 024424.

[30] Sawatzky, G.; Green, R. In *Quantum Materials: Experiments and Theory*; Pavarini, E., Koch, E., van den Brink, J., Sawatzky, G., Eds., Forschungszentrum Jülich GmbH Institute for Advanced Simulation: Forschungszentrum Jülich, 2016; Chapter 1: The Explicit Role of Anion States in High Valence Metal Oxides, Modeling and Simulation, pp 9-44.

Chapter 6

Machine-learning Assisted Prediction of Magnetic Double Perovskites*

6.1 Introduction and motivation

Prediction of new double perovskite compounds is important in order to add more compounds with interesting magnetic properties to this family. This is however challanging. Use of ab-initio calculations for this purpose is very tedious due to various level of complexities. The reasons are the following. First of all, this would involve testing the stability of a hypothetical compound against all other possible phases including those that could result from the decomposition of the hypothetical compound. Secondly, the enthalpies of formation should include the vibrational contributions for prediction of stable phases at finite temperature, making the computation further expensive. This would allow us to broaden the material-base of magnetic compounds, which is urgently needed for technological purpose. The other alternative could be the use of machine learning algorithm to check the stability criteria instead of any direct ab-initio calculation. The method is very simple yet powerful to reach the goal. It tries to learn underlying pattern from the existing compounds and predict new stable compounds by using this pattern. Careful screening of the possibilities helps to synthesize and characterize the compounds experimentally.

Most common double perovskites have a divalent alkaline-earth cation, Ca, Sr or Ba at A-site. There are also reports of double perovskites with trivalent rare-

*This chapter is based on publication : **Anita Halder**, Aishwaryo Ghosh and Tanusri Saha-Dasgupta. (Manuscript accepted in Phys. Rev. Materials.)

earth cations at A-site, but they are significantly smaller in number, which may be rationalized by smaller sizes of A^{3+} cations compared to A^{2+} cations, limiting the choice of B/B$'$ cations. Focusing on the alkaline-earth based double perovskites, the average B-site cation oxidation state will be four, which can be achieved by a combination of B^{4+}/B'^{4+}, B^{3+}/B'^{5+}, B^{2+}/B'^{6+} or B^{1+}/B'^{7+} cations. Therefore, cations with oxidation states ranging from one to seven can be inserted into the B site, covering all the cations in the periodic table, opening up a vast possibilities. Among them, only about 640 compounds have been synthesized and structurally characterized. For a detailed review see Vasala et al. [1] Understandably, there are several possible combinations of B/B$'$ that have remained unexplored so far.

In order to make a headway in this complex problem, we applied a multi-pronged approach to this problem, by first applying machine learning technique, using the known double perovskite compounds as a training set, to screen the most probable B/B$'$ combinations giving rise to stable double perovskite structure. This is followed by prediction of the crystal structure by employing evolutionary algorithm based on density functional theory (DFT) total energies, calculation of the nominal valences of the transition metal cations, the magnetic state, and the mean field estimation of the transition temperatures. Since most known magnetic double perovskites with high magnetic transition temperatures have combination of $3d$ and $4d$ or $5d$ transition metal (TM) cations at B and B$'$ sites, we restricted our search to B/B$'$ combinations to $3d/4d(5d)$ TMs. Our exhaustive study, taking into account a large number of possibilities, should form an useful reference for future experimental research with a goal to synthesize new magnetic double perovskites.

6.2 Machine learning approach

In order to screen the unexplored B/B$'$ combinations for possible prediction of new stable, double perovskite compounds we used machine learning (ML) algorithm. The adapted ML scheme can be described in terms of four basic steps, shown schematically in chapter 2, Fig. (2.12). In the following, we provide the calculation details based on these steps.

6.2.1 Database construction

As already mentioned in chapter 2, two crucial ingredients for database construction are, instances and attributes.

Instances are the existing compounds having chemical formula of $A_2BB'O_6$, reported in literature. Since we focus our search on double perovskites with divalent rare-earth cations at A-site, our choice of instances included the compounds where A is divalent cation with three different possibilities, Ca/Sr/Ba, and B and

B′ are mostly transition metals, with some choices of lanthanides and actinides. The existing $A_2BB'O_6$ compounds were classified into two categories: (a) Double perovskites (DPs) : where B/B′ form octahedra, and corner-shared BO_6 and $B'O_6$ octahedra are arranged in an ordered manner. (b) Non-double perovskites (NDPs) : where the compounds either exhibit disordered B/B′ arrangement, or do not form perovskite structure with corner-shared arrangement of BO_6 and $B'O_6$ octahedra. This gave rise to 641 compounds in the training data set, among which 115 compounds are Ca-based, 224 compounds are Sr-based and 302 compounds are Ba-based. 515 compounds were classified as DP and 126 compounds as NDP. For effectiveness of the training data set, both the quality and quantity of the data set are important. The quantity of data in this case is limited as is often the case in materials science projects. To reinforce the quality of the data that can reduce noise and bias in the constructed model, we have cross-checked our data base among different sources like Inorganic Crystal Structure Database (ICSD), Ref. [1], and other available literature. Any questionable/doubtful instance is removed from the database.

Attribute	Notation	Value range
av. radius of B/B′	$< r_{BB'} >$	0.51-1.04 Å
radii diff. of B and B′	$\Delta r_{BB'}$	0.00-0.85 Å
radii ratio of B and B′	$r_B/r_{B'}$	1.00-2.61
tolerance factor	t	0.85-1.08
valence diff. of B and B′	$\Delta Val_{BB'}$	0-6
column B	C_B	1-15
column B′	$C_{B'}$	2-17
Row B	R_B	2-7
Row B′	$R_{B'}$	2-7
Row diff. of B/B′	$\Delta R_{BB'}$	0-5
Atomic mass diff. of B and B′	$\Delta M_{BB'}$	1.78-229.02 a.m.u
Electronegativity diff. of B and B′	$\Delta \chi_{BB'}$	0.01-1.84
Atomic number diff. of B and B′	$\Delta Z_{BB'}$	1-88

Table 6.1: The description, notation and range of 13 different attributes used in the study. Tolerance factor is defined as $t = \frac{r_A + r_O}{\sqrt{2}(\frac{r_B + r_{B'}}{2} + r_O)}$ where r_A, r_O, r_B, $r_{B'}$ are the ionic radii of A, O, B and B′ ions respectively.

The features or characteristics which represent the uniqueness of a particular instance, are termed as attributes. The choice of proper set of attributes is a crucial part in machine learning. The attributes that have been used in this study are based on either chemical or structural properties of the instances. The choice of such attributes make the database construction easier and the entire process

inexpensive as these attributes can be obtained without involving computation. Table. 6.1 lists the 13 attributes used in this study, along with their notation and ranges.

6.2.2 Data preprocessing

Data preprocessing is an important part in ML technique before model construction, which has been discussed elaborately in chapter 2 (cf. section 2.9). One of the important steps of data preprocessing is removal of outlier data. In the Fig. 6.1, box plot is showing the diversity of 13 attributes, along with their mean and median. The long whisker are set at Q1-1.5IQR and Q4-1.5IQR, where Q1,Q4 are first and forth quartiles and IQR is known as interquartile range. Any data point outside the whisker was considered as an outlier data and was discarded. Fig. 6.1 shows that the attributes like $C_{B'}$, $R_{B'}$, $r_B/r_{B'}$ and $\Delta r_{BB'}$ have outlier data which were removed from the training dataset.

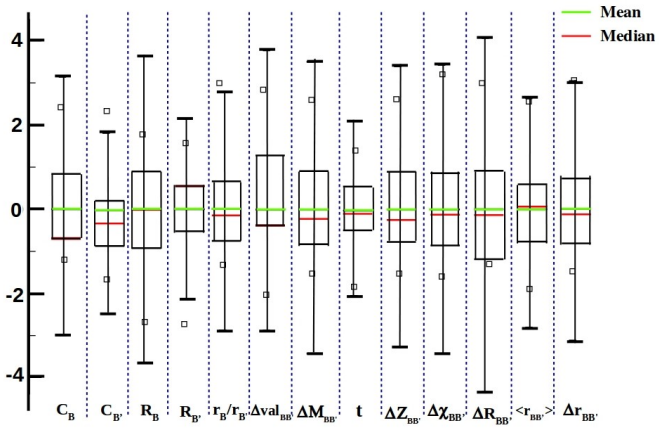

Figure 6.1: Box plot showing the spread of the 13 attributes which were considered initially. The green and red line show the mean and median respectively. The lower and upper whisker are set at Q1-1.5IQR and Q4-1.5IQR respectively. The small squares indicate the maximum and minimum range of the data.

In the next step to remove correlated attributes, the heatmap drawn among initial choice of attributes using Pearson correlation exhibits that a few attributes are strongly correlated to each other, as shown in Fig. 6.2. From the created heatmap of the present problem, it has been observed that:

1. Tolerance factor (t) and radius average of B site ($< r_{BB'} >$) are highly correlated.

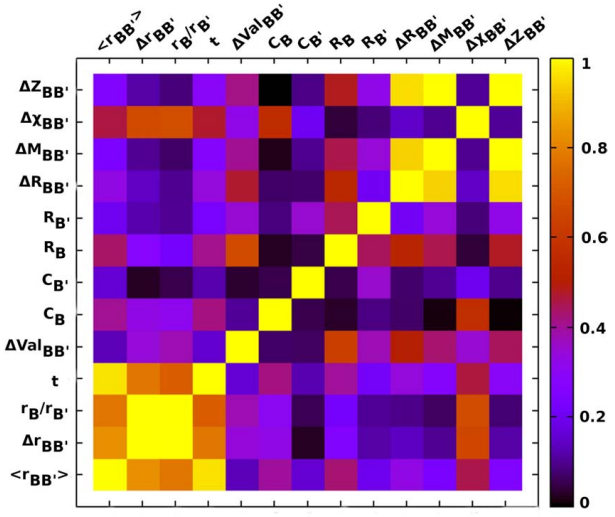

Figure 6.2: Heatmap representing correlation among different attributes. Different colors indicate the strength of their correlations. Weak or no correlation is represented by blue boxes in the plot and strong correlation is represented by yellow boxes in the plot.

2. Radius difference between B sites ($\Delta r_{BB'}$) and radius ratio $r_B/r_{B'}$ are highly correlated.

3. $\Delta Z_{BB'}$ and $\Delta M_{BB'}$ in B site are correlated.

We thus retained (i) t, discarding $< r_{BB'} >$, (ii) $r_B/r_{B'}$, discarding $\Delta r_{BB'}$, and (iii) $\Delta M_{BB'}$, discarding $\Delta Z_{BB'}$ from the list of attributes. Based on this input, out of initial choice of 13 attributes, 10 attributes were used for the model construction.

6.2.3 Model construction

The crucial step after data set construction and its preprocessing, is the suitable choice of machine learning algorithm that can efficiently capture the underlying pattern in the dataset. We initially used four different tree algorithms, namely J48 [2], random tree [3], random forest [4] and REPtree [5], to make the classification between DP/NDP compounds. We used standard k-fold cross validation technique to characterize accuracy of the model. A value of $k = 10$ was found to be sufficient in the present context. Fig. (6.3) shows the accuracy of four different algorithms. The accuracy of a model can be calculated from confusion matrix, which summarizes the prediction results while building a machine learning model. During cross validation, it enlists the number of correct and incorrect predictions

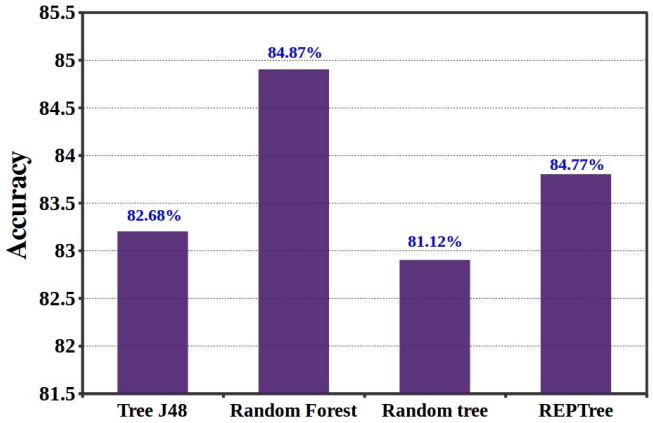

Figure 6.3: Plot of calculated accuracy in four different tree algorithms. It can be seen that random forest algorithm provides best prediction probability among them.

made to each class. In our case, the confusion matrix represents the number of training set DP instances that have been predicted correctly as DP (True positive or TP) or wrongly as NDP (False negative or FN) and the number of instances that are originally NDP (True negative or TN) and have been predicted correctly as NDP or wrongly as DP (False positive or FP). The off diagonal terms in the confusion matrix give the number of wrongly predicted instances. The confusion matrix can be written as,

$$M = \begin{bmatrix} TP & FN \\ FN & TN \end{bmatrix}$$

Thus, accuracy in this model can be defined as $\frac{TP+TN}{Total\,number} \times 100\%$. It was found that random forest algorithm, which has been successfully used in many cases in material informatics, [6, 7] provides the best result among these four algorithms from consideration of misclassified instances as shown in Fig. (6.3).

We also calculated the misclassification rate in a random forest calculation as a function of number of instances as shown in Fig. (6.4). It is seen that misclassification rate saturates as one increases the number of instances in the training set. This plot assures that in our case, the model performance would not be further affected by the quantity of data.

In passing we note that our training set shows imbalance [8] between DP and NDP classes. As most often the unsuccessful experiments are not reported in literature the number of known NDP compounds is much less than that of DP compounds. To overcome the effect of this imbalance in building the model, we made use of the cost sensitive (meta-learning) wrapper. [9, 10] It considers the

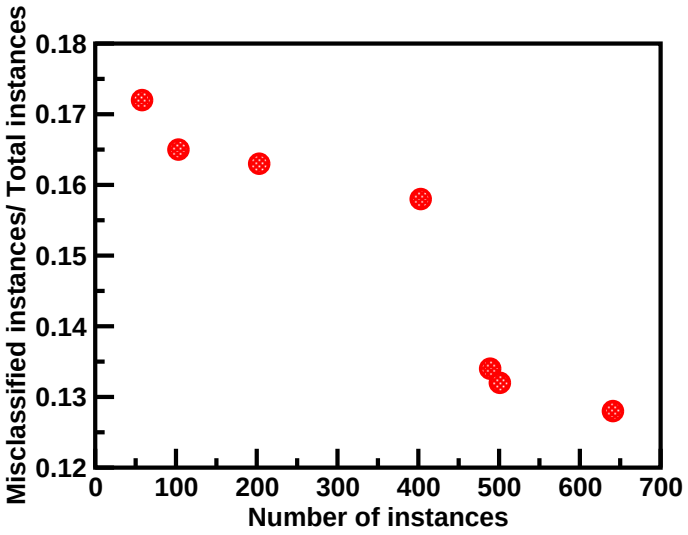

Figure 6.4: Learning curve shows the misclassification rate as a function of number of instances in the dataset, which confirms whether the quantity of data is sufficient for robust model as predicted by ML algorithm.

fact that the "cost" of misclassification of NDP compounds are more than the misclassification cost of DP compounds. We found that the true negative rate in a cost insensitive model is 46% whereas in cost sensitive model it has been increased to 59%. The calculated confusion matrix for cost sensitive random forest algorithm applied to our problem,

$$M = \begin{bmatrix} 470 & 45 \\ 52 & 74 \end{bmatrix}$$

Accuracy in this model as seen in Fig. (6.3) is 84.87%. We may also define F1 score in terms of precision and recall is given by $\frac{2\times Recall \times Precision}{Recall + Precision} = 90.60\%$. F1 score gives a better evaluation of a model than accuracy when FP and FN have different costs as in our case. The model obtained using cost sensitive random forest algorithm has been finally used to predict the stability of unknown DP compounds, reported in the following.

6.2.4 Prediction of new compounds

The developed machine learning model was used to predict the stability of unknown $A_2BB'O_6$ composition in double perovskite structure, by applying model on the test dataset of size 412. The unknown dataset was constructed considering all possible combination of B cations from $3d$ transition metal series and $B^{'}$ cations from $4d$ or $5d$ transition metal series that have not been reported in

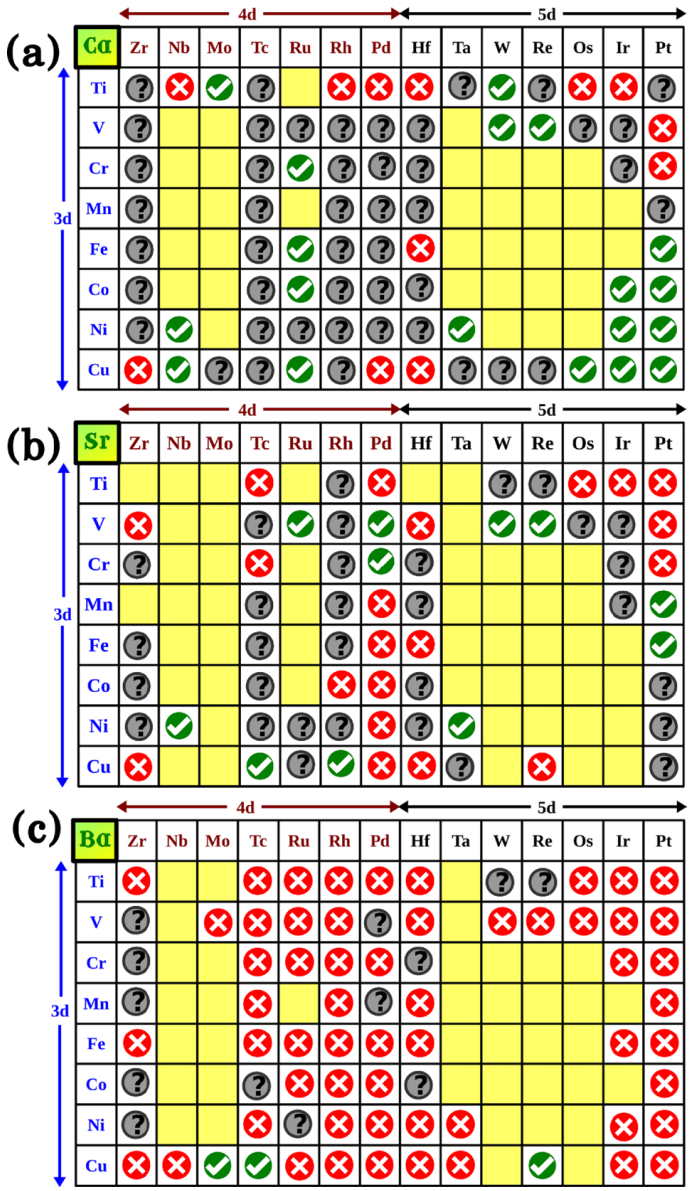

Figure 6.5: $A_2BB'O_6$ compositions with A = Ca, Sr, Ba, and B/B$'$ = $3d/4d(5d)$ TMs. Left most column represents the $3d$ B cation and top most row the B$'$ cation. Different colors indicate known compounds (yellow), predicted double perovskite compounds (green with "right" symbol), predicted compounds with either disordered B/B$'$ arrangement, or non-perovskite structure with the $A_2BB'O_6$ stoichiometry (red with "wrong" symbol), undecided predictions (grey with "question" symbol).

literature.

Fig. (6.5) shows a summary of known and predicted $A_2BB'O_6$ compounds with A = Ca/Sr/Ba and B/B$^{'}$ = 3*d*-4*d*/5*d* TMs. The known B/B$^{'}$ DP combinations are marked as yellow. The B/B$^{'}$ combinations predicted to be NDPs are marked with "wrong" symbol. The B/B$^{'}$ combination is predicted to be DP if the prediction probability is high (0.8-1.0). The B/B$^{'}$ combinations with prediction probability (0.6-0.7) are considered as moderately probable, while those with prediction probability (0.5-0.6) are considered as undecided situations. The DPs are marked with "right" symbol, while both moderately probable and undecided situations are marked with "question" symbol. Our machine-learning screening predicts 33 compounds to be DPs with strong probability, 89 compounds with unresolved prediction and 54 compounds as NDPs among all the studied 3*d*-B/4*d*(5*d*)B$^{'}$ combinations together with 119 known cases.

In the following, we consider the predicted DPs compounds, [11] and characterize them in terms of their crystal structure, electronic and magnetic properties.

6.3 DFT details

The structural optimizations were performed in plane wave basis with projector-augmented wave (PAW) [12] potentials. During optimization, the position of the atoms were allowed to relax until the Hellman-Feynman forces became less than 0.001 eV/$\mathring{A}$. Energy cut-off of 600 eV and Monkhorst pack k-points mesh of $6 \times 6 \times 4$ for monoclinic and tetragonal, $6 \times 6 \times 6$ for cubic and rhombohedral compounds were found to provide good convergence.

In all electron LAPW method, APW + lo was used as the basis set, and the spherical harmonics were expanded upto $l = 10$ and the charge density and potentials were represented upto $l = 6$. The criterion for the number of plane waves in LAPW basis were chosen considering the muffin tin radius R_{MT} multiplied by K_{max} (plane wave cut off for basis) producing a value of 7.0.

The magnetic structure was determined by comparing the energies of A type and FM arrangements of B spins. Here a larger supercell was considered which can accommodate more than one inequivalent B atoms.

6.4 Properties of Predicted Compounds

6.4.1 Crystal Structure

The first step towards characterization of any compound is the information of its crystal structure. To predict the structures, we employed genetic algorithm as implemented in "USPEX" (Universal Structure Predictor: Evolutionary Xtallography) which is known for its accurate prediction of crystal structure of different

multinary compounds, and has been also validated by testing on known DPs [13] as discussed in chapters 2 and 3. Necessary information about the crystal structure of all the compounds have been provided from Table 6.5 to Table 6.11 at the end of this chapter. Each table corresponds to a particular space group symmetry with the compounds belong to this particular space group. In the tables we listed lattice parameters, wyckoff positions and atomic positions of the free parameters of the compounds.

Compound	Space group	t	d_{B-O} ($\mathring{A}$)	$d_{B'-O}$ ($\mathring{A}$)	$\langle$ B-O-B$'$ (^{0})
Ca_2TiMoO_6	$P2_1/n$ (14)	0.956	2.006	2.029	151.379°
Ca_2VReO_6	I2/m (12)	0.964	2.012	1.977	151.122°
Sr_2NiNbO_6	R-3 (148)	1.004	1.981	1.991	168.669°
Sr_2NiTaO_6	Fm-3m (225)	1.004	2.006	1.985	180°
Ca_2CuRuO_6	R3 (146)	0.961	2.056	1.959	151.198°
Ca_2CuOsO_6	R-3 (148)	0.951	2.101	1.931	151.121°
Sr_2VRuO_6	Fm-3m (225)	0.999	1.907	2.009	180°
Ca_2CrRuO_6	$P2_1/n$ (14)	0.974	1.947	1.999	151.394°
Ca_2FeRuO_6	$P2_1/n$ (14)	0.966	2.017	1.984	149.969°
Ca_2CoRuO_6	$I4_/m$ (87)	0.975	1.997	1.964	150.226°
Ca_2CoIrO_6	$P2_1/n$ (14)	0.954	2.011	1.959	148.123°
Ca_2NiIrO_6	$P2_1/n$ (14)	0.967	2.079	1.959	148.250°
Ca_2CuIrO_6	$P2_1/n$ (14)	0.958	2.094	1.968	147.037°
Ca_2VWO_6	$P2_1/n$ (14)	0.925	2.125	1.947	149.304°
Sr_2VWO_6	$P2_1/n$ (14)	0.959	2.110	1.947	162.809°
Ca_2NiNbO_6	$P2_1/n$ (14)	0.959	2.014	1.990	151.488°
Ca_2NiTaO_6	$P2_1/n$ (14)	0.959	1.984	1.993	153.082°
Ba_2CuMoO_6	I4/mmm (139)	1.033	2.168	1.953	180°
Sr_2CuRhO_6	I4/m (87)	1.032	2.093	1.985	150°
Ca_2TiWO_6	$P2_1/n$ (14)	0.947	2.015	2.003	153.571°
Sr_2VReO_6	Fm-3m (225)	0.999	1.953	1.982	180°
Ca_2CuNbO_6	I2/m (12)	0.974	2.179	1.999	140.118°
Ba_2CuReO_6	I4/m (87)	1.038	2.256	1.919	164.355°
Sr_2CuTcO_6	R-3 (148)	0.973	2.147	1.930	159.063°
Ba_2CuTcO_6	R-3 (148)	1.031	2.154	1.944	176.863°

Table 6.2: The space group symmetry, the tolerance factor (t), the average B-O bond-length (d_{B-O}) in BO_6 octahedra, the average B$'$-O bond-length ($d_{B'-O}$) in $B'O_6$ octahedra, the average B-O-B$'$ bond angle of the predicted DP compounds.

In Table 6.2, we list the important structural parameters of the predicted

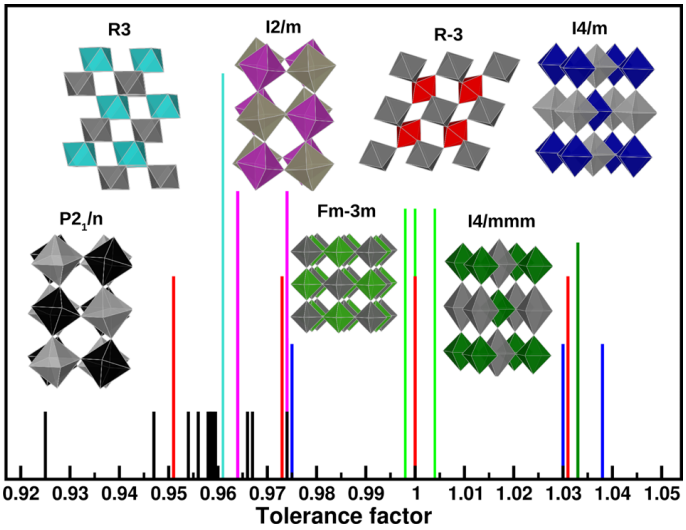

Figure 6.6: Tolerance factors of the predicted compounds, along with their space group symmetries. The representative crystal structures for each structure types are shown as insets, with monoclinic $P2_1/n$ symmetry in black, I2/m in magenta, rhombohedral R3 in cyan, R-3 in red, tetragonal I4/m in blue, cubic Fm-3m in light green and I4/mmm in dark green.

DP compounds along with their theoretical space-groups, as given by the genetic algorithm. Analysis of the crystal structure data of the known DP compounds shows [1] that the space group symmetries are dictated by the tolerance factors. Compounds with relatively smaller tolerance values, 0.93 or less, are predominantly of monoclinic symmetry, while compounds with relatively larger tolerance factors, 0.97 and beyond form in either cubic, or tetragonal I4/m or rhombohedral symmetry. Our predicted space group symmetries are in agreement with this general expectation, as shown in Fig. (6.6) where the tolerance factors of the predicted compounds are shown along with their predicted space groups. Our study predicts most of the compounds into $P2_1/n$ symmetry, in accordance with the fact over 300 DPs are found to be formed in this space group. We found 11 compounds in $P2_1/n$ symmetry, 4 compounds in R-3, 3 compounds in Fm-3m, 3 compounds are in I4/m, 2 compounds in I2/m and 1 each in I4/mmm and R3 symmetry. Though the space group R3 has no inversion symmetry and may lead to disorder but recently a double perovskite [14] has been found in this space group where unusual cation ordering has been reported.

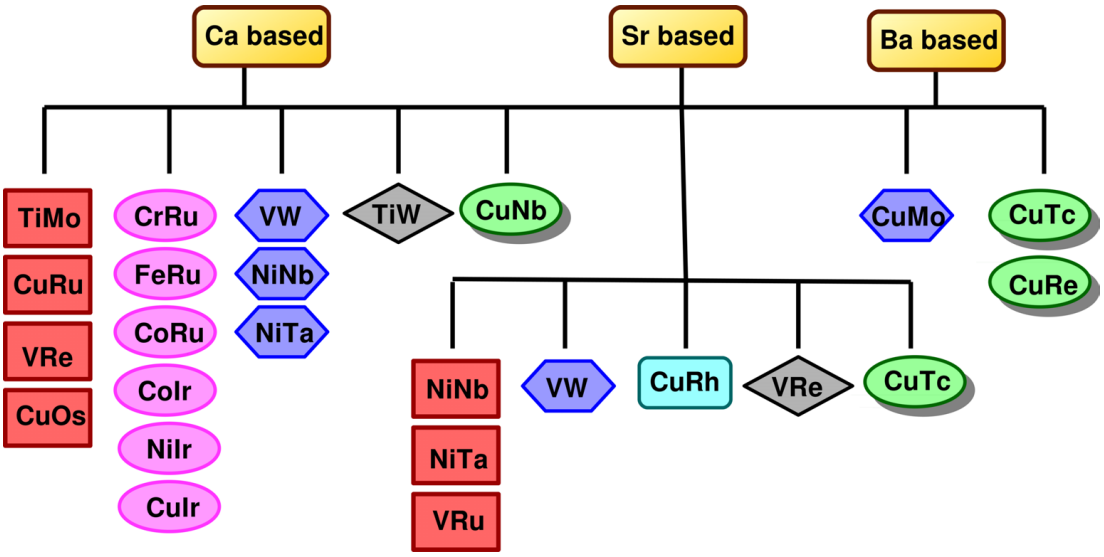

Figure 6.7: Classification of predicted double perovskites, $(Ca/Sr/Ba)_2BB'O_6$, based on their electronic and magnetic properties. The color codes represent FM-HM: red rectangle, FiM-I: magenta ellipse, AFM-I: blue hexagon, AFM-M: cyan rounded rectangle, NM: green shaded ellipse and FM-M: grey diamond.

6.4.2 Electronic and Magnetic State

We calculated the electronic and magnetic state of the predicted compounds within the density functional theory in generalized gradient approximation (GGA) [15] of exchange-correlation functional in two different basis sets a) the plane-wave pseudo-potential basis as implemented in Vienna Ab initio Simulation Package (VASP) [16] and b) The full potential linear augmented plane wave (FLAPW) basis as implemented in WIEN2k [17] code. The consistency of the calculations in these two different basis set were cross-checked in terms of magnetic moments, total and partial density of states. In order to include the electron-electron correlation beyond GGA at $3d/4d/5d$ transition metal sites which is found to be crucial to capture the correct electronic and magnetic properties, we considered supplemented Hubbard U correction following Liechetenstein [18] formulation. The choice of U value at B sites was chosen as 6-7 eV for late $3d$ transition metals, 3-4 eV for early $3d$ transition metals. For $4d$ or $5d$ TM B′ sites, the value of U was kept fixed at 1 eV. The Hund coupling J_H was chosen 0.8 eV for both B and B′ sites. The influence of variation of U value on the electronic and magnetic structures have been carefully considered, and the trend is found to remain the same for the chosen ranges. We checked the effect of spin-orbit coupling (SOC), which is expected to be important for $4d/5d$ TMs by repeating the calculations within GGA+U+SOC. No significant changes were found in the

qualitative description of electronic or magnetic states upon inclusion of SOC.

The calculated first-principles electronic structure, along with total energy calculation of magnetic structure with ferromagnetic and antiferromagnetic alignment of transition metal spins, established that the predicted compounds can be classified in six broad groups (cf. Fig. (6.7)): ferromagnetic half-metal (FM-HM), ferrimagnetic insulator (FiM-I), antiferromagnetic insulator (AFM-I), antiferromagnetic metal (AFM-M), ferromagnetic metal (FM-M) and nonmagnetic (NM). Out of predicted seven FM-HMs, four are Ca based and three are Sr based. Three of AFM-Is are Ca based, one is Sr based and one is Ba based. All six FM-Is are Ca based. One example of AFM-M is Sr based, and two examples of FM-M are one Ca based and another Sr-based. There are four NM compounds, two Ba based, one Ca based and one Sr based. In the following we provide a brief account of each of the groups, the predicted compounds belonging to the group, their electronic density of states, magnetic moment, magnetic state and mean field estimate of magnetic transition temperatures. For a concise summary, see Table 6.3. Total and projected magnetic moments at B, B$'$ and O sites are listed in Table 6.4.

Ferromagnetic half-metal

The largest group among six different classes is that of ferromagnetic half-metal, which consist of seven compounds, Ca_2TiMoO_6, Sr_2NiNbO_6, Ca_2CuRuO_6, Ca_2VReO_6, Sr_2NiTaO_6, Ca_2CuOsO_6 and Sr_2VRuO_6.

Ca_2TiMoO_6- Panel (a) of Fig. (6.8) shows the density of states (DOS) of the compound projected onto Ti d, Mo d and O p states. As is seen from the figure, the Mo t_{2g} states are partially filled in the majority spin channel, and completely empty in the down spin channel, with Mo e_g states being empty in both spin channels (not shown in the figure). Ti d states are empty, apart from the covalency driven mixing with partially filled Mo t_{2g} states. This is in accordance with the calculated magnetic moments, with a value of 1.50 μ_B at Mo site, and total moment of 2 μ_B in the formula unit, the residual moment being distributed between Ti site (0.33 μ_B) and O sites ($\approx$ 0.01 μ_B) due to covalency effect. This stabilizes a half-metallic ground state with nominal 4+/4+ valences of Ti/Mo. While such isovalent combinations tend form disordered structure, recent advances in high pressure synthesis has been reported to be able to stabilize ordered structure of double perovskites with isovalent B/B$'$ combinations. [14]

Total energy calculation of ferro, and antiferromagnetic alignment of Mo spins show the stability of FM state over AFM state by a relatively small energy difference of 15 meV, which would translate to a mean field T_c of about 30 K. This may be rationalized through Stoner instability driven ferromagnetism in a metallic system.

Compound	Nominal Charges	Electronic state	Band gap (eV)	Magnetic state	T_c/T_N in K
Ca_2TiMoO_6	4+/4+	Half metal	-	FM	30
Ca_2VReO_6	3+/5+	Half metal	-	FM	220
Sr_2NiNbO_6	3+/5+	Half metal	-	FM	400
Sr_2NiTaO_6	3+/5+	Half metal	-	FM	14
Ca_2CuRuO_6	2+/6+	Half metal	-	FM	483
Ca_2CuOsO_6	2+/6+	Half metal	-	FM	125
Sr_2VRuO_6	3+/5+	Half metal	-	FM	102
Ca_2CrRuO_6	3+/5+	Insulator	0.570	FiM	135
Ca_2FeRuO_6	3+/5+	Insulator	0.660	FiM	547
Ca_2CoRuO_6	3+/5+	Insulator	0.220	FiM	365
Ca_2CoIrO_6	2+/6+	Insulator	0.090	FiM	95
Ca_2NiIrO_6	2+/6+	Insulator	0.120	FiM	39
Ca_2CuIrO_6	2+/6+	Insulator	0.200	FiM	132
Ca_2VWO_6	2+/6+	Insulator	0.830	AFM	67
Sr_2VWO_6	2+/6+	Insulator	0.780	AFM	130
Ca_2NiNbO_6	3+/5+	Insulator	0.580	AFM	11
Ca_2NiTaO_6	3+/5+	Insulator	1.110	AFM	39
Ba_2CuMoO_6	2+/6+	Insulator	1.030	AFM	2
Sr_2CuRhO_6	2+/6+	Metal	-	AFM	184
Ca_2TiWO_6	3+/5+	Metal	-	FM	14
Sr_2VReO_6	3+/5+	Metal	-	FM	10
Ca_2CuNbO_6	3+/5+	Insulator	0.609	NM	-
Ba_2CuReO_6	1+/7+	Insulator	0.499	NM	-
Sr_2CuTcO_6	1+/7+	Insulator	0.175	NM	-
Ba_2CuTcO_6	1+/7+	Insulator	0.079	NM	-

Table 6.3: The nominal valences of B/B$'$, the electronic, magnetic state and the band gap for the predicted double perovskites.

Compound	Total	M_B (μ_B)	$M_{B'}$ (μ_B)	M_O (μ_B)
Ca_2TiMoO_6	2.00 (1.991)	0.337 (0.336, -0.008)	1.503 (1.499, -0.107)	0.005
Ca_2VReO_6	0.00 (0.198)	1.674 (1.499, -0.056)	-1.391 (-0.99, 0.341)	-0.041
Sr_2NiNbO_6	1.00	1.450	0.056	-0.075
Sr_2NiTaO_6	1.00	1.458	0.043	-0.075
Ca_2CuRuO_6	1.00 (0.989)	-0.649 (-0.761, 0.050)	1.441 (1.214, -0.044)	0.033
Ca_2CuOsO_6	1.00 (0.867)	-0.451 (-0.662, -0.091)	0.963 (0.963, -0.292)	0.028
Sr_2VRuO_6	1.00 (0.985)	-1.122 (-1.118, -0.022)	1.350 (1.340, 0.023)	0.105
Ca_2CrRuO_6	0.00 (0.109)	2.711 (2.778, -0.018)	-1.797 (-1.819, 0.018)	-0.126
Ca_2FeRuO_6	2.000 (2.020)	4.194 (4.195, 0.019)	-1.781 (-1.775, -0.021)	-0.042
Ca_2CoRuO_6	1.000 (1.010)	3.129 (3.180, 0.046)	-1.750 (-1.708, 0.020)	-0.031
Ca_2CoIrO_6	2.000 (2.001)	2.743 (2.708, 0.044)	-0.431 (-0.377, 0.004)	-0.038
Ca_2NiIrO_6	1.000 (1.043)	-1.721 (-1.727, -0.046)	1.432 (1.325, -0.040)	0.160
Ca_2CuIrO_6	2.000 (2.002)	-0.612 (-0.622, -0.006)	1.410 (1.304, -0.029)	0.149
Ca_2VWO_6	3.000 (2.990)	2.586 (2.575, -0.032)	0.236 (0.239, -0.022)	0.001
Sr_2VWO_6	3.000 (2.992)	2.559 (2.549, -0.032)	0.247 (0.249, -0.020)	0.003
Ca_2NiNbO_6	3.000	2.070	0.023	0.133
Ca_2NiTaO_6	3.000	2.133	0.095	0.122
Ba_2CuMoO_6	1.000 (0.993)	0.714 (0.710, 0.192)	0.047 (0.047, 0.003)	0.040
Sr_2CuRhO_6	2.000 (1.976)	0.580 (0.662, 0.129)	-1.236 (-1.236, -0.003)	0.172
Ca_2TiWO_6	0.027 (0.157)	-0.267 (-0.247, 0.009)	0.419 (0.397, -0.036)	0.015
Sr_2VReO_6	0.567 (0.157)	1.671 (1.592, -0.405)	-0.893 (-0.958, 0.317)	-0.034
Ca_2CuNbO_6	0.000	0.000	0.000	0.000
Ba_2CuReO_6	0.000	0.000	0.000	0.000
Sr_2CuTcO_6	0.000	-0.027	0.032	-0.001
Ba_2CuTcO_6	0.000	0.000	0.000	0.000

Table 6.4: GGA+U, and GGA+U+SOC calculated total magnetic moment, moment at B (M_B), B$'$ (M'_B) and average magnetic moment at O (M_O) site, for Sr_2BRhO_6 and Ca_2BRhO_6 compounds. For GGA+U calculations only the spin moment is provided, while the spin and orbital moments at B and B$'$ sites as given in GGA+U+SOC is shown in brackets. Total moment in GGA+U+SOC is shown in bracket. In cases where the GGA+U+SOC has only marginal effect, the GGA+U+SOC results are not shown.

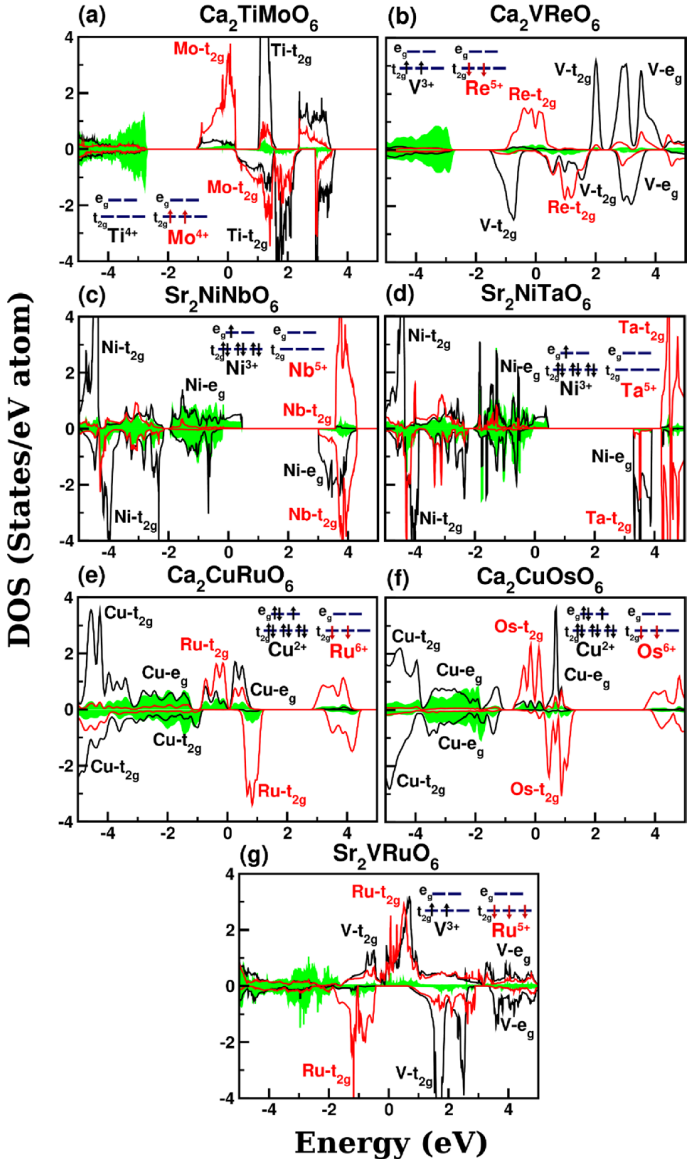

Figure 6.8: The density of states projected to B d (black), B$'$ d (red/grey) and O p (shaded green/grey) character for compounds predicted to ferromagnetic half-metals. Energy is measured with respect to E_F. Octahedrally split dominant t_{2g} and e_g character of TM d states are marked. Inset shows the schematics of orbital occupancies at B and B$'$ sites, neglecting the distortion-induced splitting within t_{2g} and e_g manifolds and covalency effect with oxygen.

Ca_2VReO_6- The DOS (cf. Fig. (6.8)-(b)) shows that the V t_{2g} states to be partially filled in the majority spin channel, and Re t_{2g} states to be partially

filled in the minority spin channel, all other d states being empty. The calculated magnetic moment gives rise to a value of 1.67 μ_B at V site and 1.39 μ_B at Re site, suggestive of d^2 occupancies of both the sites. The net moment without consideration of SOC turned to be zero due to cancellation of moments at V and Ru, which turn out to be antiparallel driven by the two-sublattice double exchange mechanism of ferromagnetism, as discussed for Sr_2FeMoO_6. [19] Introduction of strong SOC effect at Re site, gave rise to be net moment of 0.198 μ_B.

The FM configuration is found to be stabler compared to AFM configuration by 115 meV, giving rise to a mean field T_c of $\approx$ 220 K.

Sr_2NiNbO_6- The density of states, projected to Ni d, Nb d and O p states are shown in panel (c) of Fig. (6.8). We find Nb d states are mostly empty (Nb e_g states not shown in the scale of the figure), suggestive of Nb^{5+} nominal valence with d^0 occupancy. This forces Ni to be in nominal 3+ valence, with 2+ and 2- nominal valences of Sr, and O. Focusing on the DOS, we find the half-metallic character, with filled Ni t_{2g} states in both spin channels, empty Ni e_g states in the minority spin channel and highly dispersive Ni e_g states strongly admixed with oxygen character crossing the Fermi level (E_F) in majority spin channel. Interestingly, the strong admixture gives rise to the configuration where the spin of the ligand hole aligns antiparallel of the Ni spin, thereby stabilizing the low-spin state of nominal Ni^{3+} with net moment of 1 μ_B in the unit cell, which may be better viewed as Ni^{2+} and ligand hole. The calculated magnetic moments of 1.45 μ_B at Ni, -0.08 μ_B at O and 0.06 μ_B at Nb site supports the above mentioned scenario.

The calculated energy difference between ferro, and antiferromagnetic alignment of Ni spins, turn out to be very large, $\approx$ 210 meV with stability of FM state over AFM state, suggestive of a high mean-field T_c of $\approx$ 400 K.

Sr_2NiTaO_6- The DOS projected to Ni d, Ta d and O p states, as presented in panel (d) of Fig. (6.8), shows striking similarity to that of Sr_2NiNbO_6. This is expected since Ta is in same column as Nb, one being $5d$ element and another being $4d$ element. As in case of Sr_2NiNbO_6, the low-spin state of nominal Ni^{3+} is stabilized with calculated magnetic moments of 1.46 μ_B at Ni, -0.08 μ_B at O and 0.04 μ_B at Ta site, and net moment of 1 μ_B in the unit cell.

The calculated energy difference between ferro, and antiferromagnetic alignment of Ni spins, turn out to be $\approx$ 7.2 meV with stability of FM state over AFM state, suggestive of a low mean-field T_c of $\approx$ 14 K.

Ca_2CuRuO_6- The DOS, presented in panel (e) of Fig. (6.8), projected to Cu d, Ru d and O p states, reveals less than half-filled t_{2g} states of Ru, and partially empty high spin Cu e_g states. The calculated magnetic moments of 0.65 μ_B at Cu site, and 1.44 μ_B indicates the stabilization of nominal 2+ state of Cu, Ru

being in its nominal 6+ state, with d^9 and d^2 occupancies, respectively. The magnetic moment of Ru is found to align antiparallely to that Cu, driven by the two sublattice DE mechanism. The Jahn-Teller (JT) activity of Cu^{2+} ion drives the low-symmetry rhombohedral structure of the compound, splitting the three-fold degeneracy of Ru t_{2g} and two fold degeneracy of Cu e_g states, which creates a pseudo-gap in the majority spin channel, with significantly reduced DOS at E_F. Inclusion of spin-orbit coupling retains the pseudo-gap, although disordering effect like anti-site disorder may localize the low DOS at E_F inducing an activated semiconducting behavior.

The FM state is found to be lower than the AFM configuration by about 250 meV, giving rise to high T_c with mean-field estimate of 483 K.

Ca_2CuOsO_6- The DOS project to Cu d, Os d and O p states , presented in panel (f) of Fig. (6.8), is of similar nature, as in Ca_2CuRuO_6, Os being below Ru in the periodic table. This suggests nominal valences to Cu and Os in Ca_2CuOsO_6 to be identical to that of Cu and Ru in Ca_2CuRuO_6, being 2+ and 6+ respectively, giving rise to one hole in the crystal-field split and JT split $d_{x^2-y^2}$ state of d^9 Cu and one hole in the t_{2g} states of Os. The computed magnetic moments at 3d Cu, 5d Os and O sites, as listed in Table IV, are similar to that of 3d Cu, 4d Ru and O sites of Ca_2CuRuO_6, with large orbital moment developed at 5d B$'$ site upon introduction of SOC.

The mean-field T_c calculated out of total energy between ferro and antiferromagnetic configuration turn out to be 125 K.

Sr_2VRuO_6- The DOS, presented in panel (g) of Fig. (6.8) shows a half-metallic behavior, with empty V d state and occupied Ru t_{2g} states in the insulating down spin channel (e_g being empty) and V t_{2g} states strongly hybridized with Ru t_{2g} states crossing E_F in the up spin channel. Following the two sublattice DE model, the spin splitting of V and Ru sites are found to be oppositely aligned with magnetic moments of -1.12 μ_B at V site and 1.35 μ_B at Ru site, giving rise to a integer net moment of 1 μ_B.

The ferromagnetic alignment of V and Ru sublattice spins was found to be stabler compared to anti ferro alignment by an energy difference of about 53 meV, making the mean field T_c of 102 K.

Ferrimagnetic Insulator

The next large group consisting of six compounds, Ca_2CrRuO_6, Ca_2FeRuO_6, Ca_2CoRuO_6, Ca_2CoIrO_6 Ca_2NiIrO_6, and Ca_2CuIrO_6 is that of magnetic insulators with net moment. We note that insulators with net moment are rare, as magnets we know of are ferromagnetic metals. Some of the examples are EuO [20], $CdCr_2S_4$ [21], $SeCuO_3$ [22]. All of them have T_c less than 100 K. Net

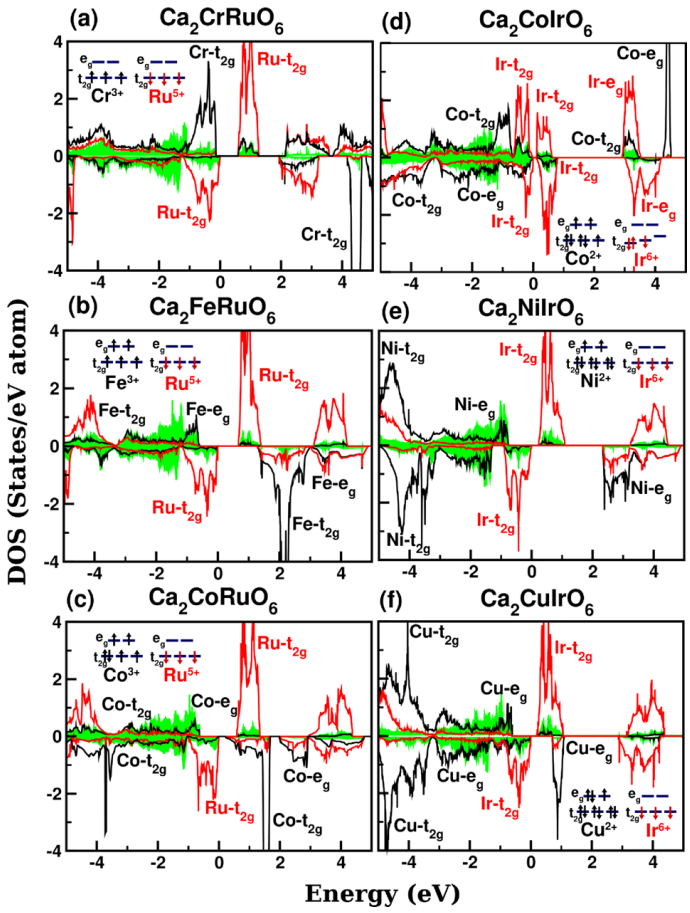

Figure 6.9: Same as in Fig. (6.8), but shown for compounds predicted to be ferromagnetic insulators.

moment magnetic insulators with high T_c are offered by double perovskite family itself, the prominent examples being La_2NiMnO_6 [23,24] and La_2CoMnO_6 [25,26], having T_c more than 200 K. As we see in the following, many of the predicted ferrimagnetic insulating double perovskites are predicted to be high T_c materials with large net moment. [27]

Ca_2CrRuO_6- The calculated electronic structure (cf DOS in Fig. (6.9)-(a)) shows filled t_{2g} states of Cr in the up spin channel, it being empty in the down spin channel. The opposite happens for Ru t_{2g} states which is filled in down spin channel and empty in up spin channel. The nominal valences of Cr and Ru are thus estimates to be 3+ and 5+ respectively, with half-filled t_{2g} states of both Cr and Ru, each having 3/2 spin, which are aligned antiparallely due to antiferromagnetic super-exchange (SE) between half-filled states. Magnetic

moments at Cr and Ru sites are found to be 2.7 μ_B and -1.8 μ_B with large moment of about 0.13 μ_B aligned in the direction of Ru spin due to large Ru-O covalency. This gives rise to a compensated ferrimagnetic situation with net moment of 0 μ_B in absence of SOC. Inclusion of SOC, produces a total moment of 0.11 μ_B.

The mean-field T_c is estimated to be 135 K.

Ca_2FeRuO_6- The computed DOS of Ca_2FeRuO_6 (cf Fig. (6.9)-(b)) confirms the nominal 3+ and 5+ valences of 3*d* cation and Ru, as found for Ca_2CrRuO_6. This leads to half-filled *d* shell of Fe with a magnetic moment of 4.19 μ_B and half-filled t_{2g} states of Ru with a moment of -1.78 μ_B, aligned antiparallely due to antiferromagnetic SE. Due to d^5 and d^3 occupancies of 3*d* cation and Ru in Ca_2FeRuO_6, as opposed to d^3 and d^3 occupancies of 3*d* cation and Ru in Ca_2CrRuO_6, a partial compensation happens, giving rise to a net GGA+U moment of 2 μ_B in the unit cell.

The estimated mean-field T_c turn out to be 547 K, much larger than that of Ca_2CrRuO_6, due to strong core spin of 5/2 of Fe.

Ca_2CoRuO_6- Moving to next TM in 3*d* series after Fe, *i.e.* Co, the calculated DOS (cf Fig. (6.9)-(c)) confirms that 3+/5+ nominal valences of B/B$'$ is maintained in Ca_2CoRuO_6, as found for Ca_2CrRuO_6 and Ca_2FeRuO_6. This puts Co in d^6 configuration with Ru in half-filled t_{2g} of d^3 configuration. The calculated magnetic moment of 3.13 μ_B ascertains the high-spin configuration of Co^{3+} d^6. The magnetic moment of 1.75 μ_B at Ru site is aligned antiparallely to 3*d* moment, as in Ca_2CrRuO_6 and Ca_2FeRuO_6, giving rise to a net GGA+U moment of 1.0 μ_B in the unit cell. The tetragonal space group of the crystal structure, driven by JT nature of high-spin Co d^6 in octahedral environment, makes the in plane metal-oxygen bond-lengths of CoO_6, significantly different from that in out-of-plane, which opens up a gap in the Co t_{2g} manifold in down spin channel, making the solution insulating.

The calculated mean field estimate of magnetic T_c turned out to be 365 K, in between the estimated T_c of Ca_2CrRuO_6 and Ca_2FeRuO_6.

Ca_2CoIrO_6- Replacement of Ru by Ir at B$'$ site of $Ca_2CoB'O_6$ makes the charge transfer between Co and B$'$ stronger, setting the nominal valences of Co/B$'$ to 2+/6+ as opposed to 3+/5+ for Ca_2CoRuO_6. The monoclinic distortion breaks the degeneracy of t_{2g} and e_g states, resulting into either filled or empty states in both spin channels, the spin splitting at Co and Ir sites being oppositely aligned (cf Fig. (6.9)-(d)). This gives rise to a net uncompensated moment of 2 μ_B. The T_c was estimated to be reasonably high (95 K).

Ca_2NiIrO_6- Panel (e) of Fig. (6.9) shows the DOS of the compound, pro-

jected to Ni d and Ir d states together with O p states. We find Ir t_{2g} states to be filled and empty in majority and minority spin channels, respectively. This sets the nominal valence of Ir to be 6+ with half filled t_{2g} d^3 occupancy of Ir. This in turn, fixes the 2+ nominal valence of Ni, which is its d^8 configuration gives rise half-filled e_g bands. The antiparallel alignment of Ni and Ir moments, driven by SE mechanism, produces a net uncompensated GGA+U moment of 1 μ_B in the unit cell.

The mean field estimate of T_c turned out to be 39 K.

Ca_2CuIrO_6- Moving from Ni to Cu along the 3d series of the periodic table, the nominal 2+/6+ description of valences for B/B$'$ is found to remain valid, with d^9 configuration of Cu and half-filled t_{2g} d^3 configuration of Ir (cf Fig. (6.9)-(f)). The JT active Cu^{2+} makes the Cu $d_{x^2-y^2}$ half-filled, which becomes gaped upon introducing spin-splitting. The solution thus turns to be insulating, where Cu and Ir moments align antiparallely, as found for all the compounds listed in this class. This gives rise to a net GGA+U moment of 2 μ_B in the unit cell. A large moment on oxygen ($\approx$ 0.15 μ_B) aligned in the direction of Ir moment is found. The estimated mean-field T_c is found to be 132 K.

Antiferromagnetic Insulator

Our analysis gave rise to five antiferromagnetic insulators, Ca_2VWO_6, Sr_2VWO_6, Ca_2NiNbO_6, Ca_2NiTaO_6 and Ba_2CuMoO_6. As discussed in the following, in all cases the B$'$ site turned out to be in d^0 configuration with B site in half-filled situation. The antiferromagnetic insulating state is thus driven by antiferromagnetic super-exchange mechanism between half-filled states mediated by essentially non-magnetic O-B$'$-O path.

Ca_2VWO_6- Examination of the projected spin-polarized DOS (cf. Fig. (6.10)-(a)) reveals W d states to be empty, confirming its 6+/d^0 configuration, which sets the configuration of V to be 2+ with half filled t_{2g}^3 configuration. This is supported by magnetic moment of 2.59 μ_B at V site, with a moment of 0.24 μ_B at W due to covalency effect, giving rise to a total GGA+U moment of 3 μ_B in the unit cell.

The super-exchange interaction between half filled t_{2g}^3 states of V^{2+} ions stabilizes the antiferromagnetic state over the ferromagnetic state by an energy gain of 35 meV. The DOS corresponding to antiferromagnetic insulating state is shown as inset. The antiferromagnetic Neél temperature (T_N) estimated in a mean field way from total energy differences of ferro and antiferromagnetic spin arrangements, turned to be 67 K.

Sr_2VWO_6- Replacement of Ca by Sr at A-site is found to keep the essen-

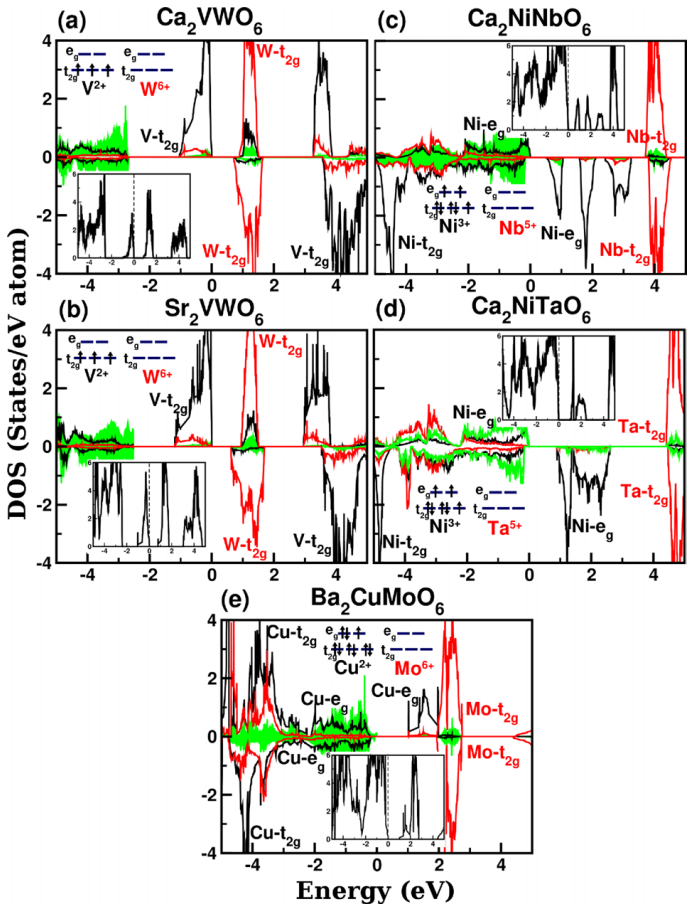

Figure 6.10: Same as in Fig. (6.8), but shown for compounds predicted to be antiferromagnetic insulators. Additional insets show the antiferromagnetic DOS.

tial features of the electronic structure same (compare panels (a) and (b) of Fig. (6.10)) with d^0 and half filled t_{2g}^3 configurations of W and V. The calculated mean-field antiferromagnetic Neél temperature of Sr compound is estimated to be about double (130 K) compared to that of Ca compound, in line with strengthening of super-exchange path by straightening of V-O-W bond angle due replacement of Ca by bigger Sr cation at A-site.

Ca_2NiNbO_6- The spin polarized density of states, projected to Ni d, Nb d and O p states are shown in panel (c) of Fig. (6.10). As in case of Sr_2NiNbO_6, we find Nb d states are mostly empty, confirming the Nb^{5+} nominal valence with d^0 occupancy also in case of Ca compound. Strikingly, the nominal Ni^{3+} shows stabilization of a high spin configuration, with oxygen moment, arising due to strong admixture, aligning parallel to Ni moment, as opposed to antiparallel alignment

for Sr counterpart. This gives rise to a net GGA+U moment of 3 μ_B in the unit cell, with moment of 2.10 μ_B at Ni site, average moment of +0.13 μ_B at O and 0.02 μ_B at Nb site. This interesting cross-over from ferromagnetic, half-metal to antiferromagnetic, insulating state upon replacement of Sr^{2+} by Ca^{2+} deserves further attention. The antiferromagnetic state (DOS shown as inset), stabilized by super-exchange interaction between the high spin state of Ni-O complex, with half-filled orbitals, gives a mean-field T_N of $\approx$ 11 K.

Ca_2NiTaO_6- Ca_2NiTaO_6 follows the same trend as Ca_2NiNbO_6, in terms of nominal d^0 configuration of Nb, stabilization of high spin configuration of Ni^{3+}, strongly admixed with oxygen, the moments of Ni (2.13 μ_B) and oxygen (0.12 μ_B) being oriented parallely, as opposed to antiparallel alignment in case of Sr_2NiTaO_6. Thus, the cross-over from ferromagnetic, half-metal to antiferromagnetic, insulating state between Sr and Ca sister compounds, is seen also for 5*d* Ta compounds. The antiferromagnetic state (DOS shown as inset of Fig. (6.10)-(d), stabilized by super-exchange interaction between the high spin state of Ni-O complex, with half-filled orbitals, gives a mean-field T_N of $\approx$ 39 K in this case.

Ba_2CuMoO_6- The last example of this category is Ba_2CuMoO_6, with Cu in its nominal 2+, d^9 configuration and Mo in its nominal 6+, d^0 configuration, as evident from the DOS plot in panel (e) of Fig. (6.10). The calculated total and site projected moments (cf Table III) supports this. The antiferromagnetic Neél temperature, however is found to be tiny (< 2 K).

Antiferromagnetic metal

Antiferromagnetic metals are considered to be rare since the examination of a wide class of transition-metal oxides gives rise to general relation between magnetic order and electrical conductivity, that ferromagnetism typically coexists with metallic conductivity, whereas insulators usually exhibit antiferromagnetism. There are only few exceptions discovered so far, e.g., $(La/Sr)_3Mn_2O_7$ [28] or $Ca_3Ru_2O_7$ [29], characterized by low dimensionality. The only perovskite compound with three-dimensional connectivity showing antiferromagnetic metallic behavior is $CaCrO_3$. [30] In recent time, we have made predictions of Sr_2FeRhO_6 and Ca_2FeRhO_6 to be antiferromagnetic metals, which is yet to be confirmed experimentally. Our present study includes one more compound in this rare series, Sr_2CuRhO_6. The nominal valences of $B/B^{'}$ predicted [13] for Sr_2FeRhO_6 compound was 3+/5+. Replacement of Fe by further late TM, Cu, effects charge transfer between B and $B^{'}$. Examination of the spin-polarized DOS (cf Fig. (6.11)) shows the Cu states to be mostly filled in the majority spin channel and one of the Cu e_g states being empty in the minority spin channel, suggesting 2+

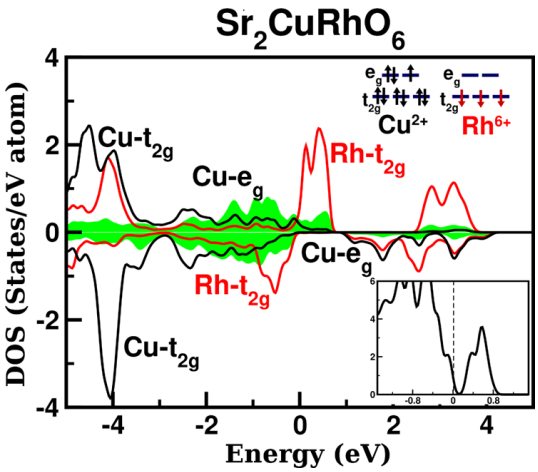

Figure 6.11: The density of states projected to Cu d (black), Rh d (red) and O p (shaded green) character for Sr_2CuRhO_6, the only compound predicted to antiferromagnetic metals. As in Figs 5, 6, and 7, energy is measured with respect to E_F (marked by dotted line). Octahedrally split dominant t_{2g} and e_g character of Cu and Rh d states are marked. Insets show the AFM DOS, and orbital occupancies at Cu and Rh sites, neglecting the distortion-induced splitting within t_{2g} and e_g manifolds and covalency effect with oxygen.

valence of Cu. This in in accordance of 0.66 μ_B magnetic moment of Cu. This puts Rh in its unusual state of 6+, which presumably is stabilized by creation of ligand hole, with moment of -1.24 μ_B at Rh site and a large moment of 0.17 μ_B at O site. Similar to two-site double-exchange driven magnetism as found for Sr_2FeRhO_6, the magnetism in case of Sr_2CuRhO_6 is driven by the same mechanism, with antiparallel alignment of Rh-O moment to that of Cu moment. The antiferromagnetism, metallic state (cf DOS in inset of Fig. (6.11)) is driven by filling driven transition from ferro to antiferro, as explained for Sr_2FeRhO_6. [13] The mean-field estimate of Neél temperature turned out to be reasonably high, $\approx$ 184 K.

Ferromagnetic metal

Our exercise provided two examples of ferromagnetic metals, Ca_2TiWO_6 and Sr_2VReO_6.

Ca_2TiWO_6-The DOS presented in Fig. (6.12-a), shows the oppositely oriented spin-splitting at Ti and W sites. In down spin channel a rather strong mixing between Ti and W t_{2g} states is observed, producing highly dispersive

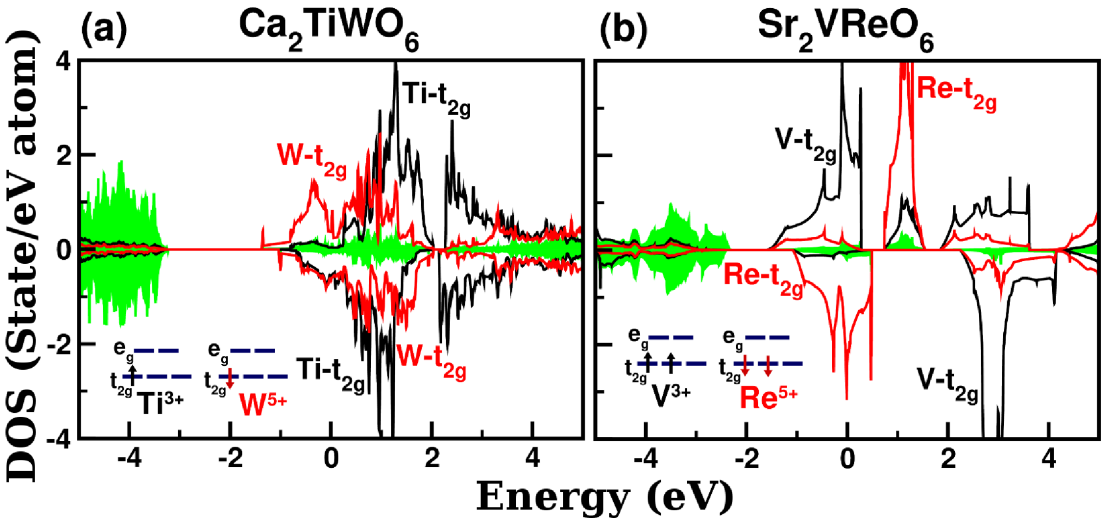

Figure 6.12: Same as in Fig. (6.8), but shown for compounds predicted to be ferromagnetic metals.

states crossing E_F. In the up spin channel, split out segment of Ti t_{2g} from the rest of Ti t_{2g} states produces a pseudo-gap at E_F, rather than a gap, making the solution metallic, rather than half-metallic. The large covalency effect and metallicity produces a net magnetic moment of 0.27 μ_B, and substantially reduced moment at Ti site, of -0.24 μ_B compared to its nominal 1 μ_B value, expected for Ti^{3+} (d^1), with W moment of 0.42 μ_B as expected for W in it nominal 5+ valence, aligned antiparallely to Ti moment, possibly driven by DE mechanism. The mean field T_c is estimated to be 14 K.

Sr_2VReO_6- Sr_2VReO_6 in its cubic structure with degenerate, partially filled V t_{2g} states in up spin channel, partially filled Re t_{2g} states in down spin channel is metallic (cf. Fig. (6.12-b)). The occupancies of filled V and Re states suggest nominal d^2 occupanies of both sites, amounting to nominal valences of 3+ and 5+, respectively. The spin spilttings at V and Re sites are found to be oppositely aligned, driven by possible DE mechanism. Switching of SCO, introduces a large orbital moment at 5*d* Re site within the partially filled t_{2g} manifold, as also observed for Ca_2VReO_6. The calculated mean field T_c gives a value of 10 K.

Nonmagnetic compounds

Out of our studied compounds, four were predicted to be nonmagnetic, all of them being Cu based, Ca_2CuNbO_6, Sr_2CuTcO_6, Ba_2CuTcO_6 and Ba_2CuReO_6. In all cases, the d^0 states of B′, driven by high oxidation states (Nb^{5+}, Tc^{7+},

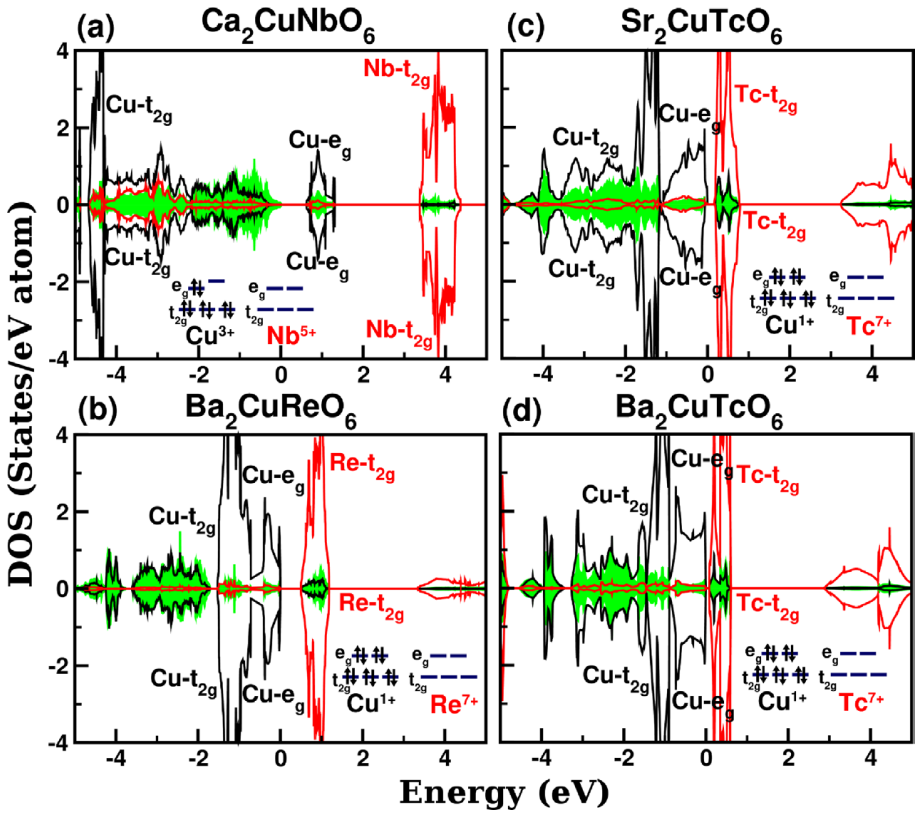

Figure 6.13: Same as Fig. (6.8), but shown for predicted compounds with NM character.

Re^{7+}) are found to be realized. This drives the unusual oxidation states of Cu, Cu^{3+} with low-spin (S=0) d^{8+} configuration for Ca_2CuNb_6, and filled shell Cu^{1+} for Sr_2CuTc_6, Ba_2CuTc_6 and Ba_2CuRe_6, as seen in the projected DOS presented in Fig. (6.13). In all cases, a nonmagnetic, insulating solutions are obtained consisting of only filled and empty states.

6.5 Summary and Discussion

In conclusion, we used a multi-pronged approach of machine-learning assisted evolutionary and first-principles calculations to predict new magnetic double perovskites. In the first step, we employed a random-forest regression of machine learning technique to develop an effective classification model for prediction of stable double perovskite compounds. The ML study was based on a training set constructed out of existing double-perovskite compounds, characterized by a set of 10 structure and chemistry based attributes. The developed classification model was applied to a unknown set consisting of 412 combinations of 3*d* B and

$4d$ or $5d$ B$'$ cations with A-sites occupied by divalent rare-earth cations Ca or Sr or Ba. This screening exercise resulted in 33 compounds with high chance of being formed in stable double-perovskite structure, out of which 25 was chosen for the next stage of investigation. In the following steps, the crystal structure of the predicted double-perovskites were theoretically calculated within the framework of evolutionary algorithm, the nominal valences and occupancies of B and B$'$ TM sites were assigned based on first-principles electronic structure results, the magnetic state was calculated and the magnetic transition temperature was estimated in a mean field way from the energy difference of FM and AFM states. Our analysis finds 7 FM half-metallic, 6 FiM insulating, 5 AFM insulating, 2 FM metallic, 1 AFM metallic and 4 NM insulating double-perovskites. Our exhaustive computational study, considering all possible combinations of $3d$ B and $4d$ or $5d$ B$'$ cations should form an useful guide for future synthesis and experimental study of new magnetic compounds in double-perovskite structure.

It is to be noted that some of the predicted compounds like Ca_2NiIrO_6, [31] Ca_2CoIrO_6, [32] Ca_2CuIrO_6, [33] Ca_2VWO_6, [34] Ca_2TiWO_6 [35] have been theoretically investigated under materials project. The space group symmetry used in materials projects are in agreement with our predictions except for Ca_2CuIrO_6. Our genetic algorithm predicted $P2_1/n$ while the symmetry used in materials project is a low symmetry C2. The total energy calculation of the two structures find $P2_1/n$ to be lower, confirming the prediction of genetic algorithm. There were also differences in magnetic states in case of Ca_2NiIrO_6 and Ca_2TiWO_6. Ca_2NiIrO_6 was reported in ferromagnetic state, [31] while our study finds ferrimagnetic state to be stabler compared to ferromagnetic state. Similarly Ca_2TiWO_6 was reported as non-magnetic [35] in contrast to the ferromagnetic state as found in our study. There also exists mention of high-pressure synthesis of Ca_2NiIrO_6 compound in an unpublished thesis, [36] without details of its structure or properties. However this work claims Ir to be 6+ nominal valence state which is in agreement with our prediction. Compensated magnetism in Sr_2VReO_6 was theoretically predicted by Pardo and Pickett [37], which though ignored the significant SOC at Re site. The future experiments are essential in order to clarify the accuracy of our predictions.

Compound	Lattice parameters	Atom	Wycoff positions	Atomic positions (x y z)
Ca_2CoRuO_6	a = 5.492 $\mathring{A}$	O1	8h	-0.189 -0.322 0.000
	c = 7.696 $\mathring{A}$	O2	4e	0.000 0.000 0.245
Sr_2CuRhO_6	a = 5.348 $\mathring{A}$	O1	8h	-0.187 0.321 0.000
	c = 8.806 $\mathring{A}$	O2	4e	0.000 0.000 0.225
Ba_2CuReO_6	a = 5.704 $\mathring{A}$	O1	8h	0.202 -0.268 0.000
	c = 8.775 $\mathring{A}$	O2	4e	0.000 0.000 0.219

Table 6.5: Compounds with I4/m symmetry.

Compound	Lattice parameters	Atom sites	Wycoff positions	Atomic positions (x y z)
Ca_2VReO_6	a = 5.502 $\mathring{A}$	A	4i	-0.518 0.000 -0.249
	b = 5.544 $\mathring{A}$	O1	8j	-0.247 0.251 0.055
	c = 7.798 $\mathring{A}$	O2	4i	0.102 0.000 0.244
	β = 90.43°			
Ca_2CuNbO_6	a = 5.156 $\mathring{A}$	A	4i	-0.535 0.000 -0.247
	b = 5.317 $\mathring{A}$	O1	8j	0.737 0.260 0.433
	c = 9.192 $\mathring{A}$	O2	4i	0.109 0.000 0.298
	β = 90.08°			

Table 6.6: Compounds with I2/m symmetry.

Compound	Lattice parameters	Atom sites	Wycoff positions	Atomic positions (x y z)
Ba_2CuMoO_6	a = 5.617 $\mathring{A}$	O1	8h	-0.247 -0.247 0
	c = 8.835 $\mathring{A}$	O2	4e	0 0 -0.219

Table 6.7: Compound with I4/mmm symmetry.

Compound	Lattice parameters	Atom sites	Wycoff positions	Atomic positions (x y z)
Sr_2NiTaO_6	7.981 $\mathring{A}$	O	24e	0.251 0 0
Sr_2VRuO_6	7.835 $\mathring{A}$	O	24e	0.256 0 0
Sr_2VReO_6	7.869 $\mathring{A}$	O	24e	0.252 0 0

Table 6.8: Compounds with Fm-3m symmetry.

Compound	Lattice parameters	Atom sites	Wycoff positions	Atomic positions (x y z)
Sr_2NiNbO_6	5.577 $\mathring{A}$	A	2c	-0.249 -0.249 -0.249
	60.30°	O	6f	0.284 -0.249 0.214
Ca_2CuOsO_6	5.449 $\mathring{A}$	A	2c	0.246 0.246 0.246
	61.75°	O	6f	0.672 0.229 -0.149
Sr_2CuTcO_6	5.626 $\mathring{A}$	A	2c	0.249 0.249 0.249
	61.04°	O	6f	0.672 0.271 0.801
Ba_2CuTcO_6	5.798 $\mathring{A}$	A	2c	-0.249 -0.249 -0.249
	59.86°	O	6f	0.261 -0.253 0.727

Table 6.9: Compounds with R-3 symmetry.

Compound	Lattice parameters	Atom sites	Wycoff positions	Atomic positions (x y z)
Ca_2CuRuO_6	a= 5.509 $\mathring{A}$	A1	3a	0.000 0.000 0.417
	c = 13.419 $\mathring{A}$	A2	3a	0.000 0.000 -0.082
		O1	9b	-0.247 -0.333 0.113
		O2	9b	0.244 0.312 0.278

Table 6.10: Compound with R3 symmetry.

Compound	Lattice parameters	Atom sites	Wycoff positions	Atomic positions (x y z)
Ca_2TiMoO_6	a = 7.799 Å	A	4*e*	-0.249 0.049 -0.011
	b = 5.610 Å	O1	4*e*	-0.454 0.292 -0.297
	c= 5.463 Å	O2	4*e*	-0.454 0.795 -0.205
	β = 90.05 °	O3	4*e*	-0.251 -0.025 0.413
Ca_2CrRuO_6	a = 5.350 Å3	A	4*e*	0.489 0.448 0.750
	b = 5.484 Å	O1	4*e*	0.295 0.700 0.542
	c= 7.647 Å	O2	4*e*	0.303 0.706 0.958
	β = 89.84°	O3	4*e*	0.082 0.482 0.253
Ca_2FeRuO_6	a = 7.699 Å	A	4*e*	-0.750 0.445 -0.012
	b = 5.559 Å	O1	4*e*	-0.546 0.201 -0.297
	c= 5.392 Å	O2	4*e*	-0.547 0.705 -0.197
	β = 90.02°	O3	4*e*	-0.751 0.526 -0.591
Ca_2CoIrO_6	a = 7.614 Å	A	4e	-0.251 0.062 0.015
	b = 5.508 Å	O1	4e	-0.747 0.023 -0.596
	c= 5.307 Å	O2	4e	-0.549 0.704 -0.311
	β = 90.25°	O3	4e	-0.548 0.197 -0.198
Ca_2NiIrO_6	a = 7.713 Å	A	4*e*	-0.752 0.439 -0.484
	b = 5.615 Å	O1	4*e*	0.052 0.210 0.811
	c= 5.408 Å	O2	4*e*	-0.452 0.807 0.206
	β = 90.22°	O3	4*e*	-0.243 0.469 -0.097
Ca_2CuIrO_6	a = 5.427 Å	A	4e	0.485 0.934 0.249
	b = 5.706 Å	O1	4e	0.179 0.709 0.052
	c= 7.624 Å	O2	4e	0.297 0.187 0.049
	β = 89.89°	O3	4e	0.902 0.034 0.247
Ca_2VWO_6	a = 7.829 Å	A	4*e*	-0.247 0.054 0.487
	b = 5.657 Å	O1	4*e*	-0.761 0.031 0.094
	c= 5.467 Å	O2	4*e*	-0.455 0.3075 0.212
	β = 90.28°	O3	4*e*	0.052 0.717 0.811
Sr_2VWO_6	a = 5.687 Å	A	4*e*	0.996 0.480 0.749
	b = 5.679 Å	O1	4*e*	0.786 0.735 0.971
	c= 8.025 Å	O2	4*e*	0.263 0.784 0.027
	β = 90.06°	O3	4*e*	0.946 0.992 0.239
Ca_2NiNbO_6	a = 7.691 Å	A	4*e*	-0.748 0.452 -0.011
	b = 5.584 Å	O1	4*e*	-0.547 0.213 -0.299
	c= 5.473 Å	O2	4*e*	-0.544 0.707 -0.205
	β = 90.07°	O3	4*e*	-0.752 0.526 -0.587
Ca_2NiTaO_6	a = 5.414 Å	A	4*e*	0.489 0.953 0.247
	b = 5.516 Å	O1	4*e*	0.207 0.707 0.043
	c= 7.749 Å	O2	4*e*	0.295 0.208 0.041
	β = 89.60°	O3	4*e*	0.919 0.021 0.250
Ca_2TiWO_6	a =7.797 Å	A	4*e*	0.267 0.007 0.045
	b = 5.459 Å	O1	4*e*	0.961 0.712 0.714
	c= 5.572 Å	O2	4*e*	0.462 0.293 0.292
	β = 90.10°	O3	4*e*	0.249 0.575 0.980

Table 6.11: Compounds with $P2_1/n$ symmetry.

Bibliography

[1] S. Vasala and M. Karppinen, Progress in Solid State Chemistry **43**, 1 (2015).

[2] Quinlan. J. R, C4.5: Programs for Machine Learning, Morgan Kaufmann Publishers, (1993).

[3] Mahmood. A. M., Satuluri. N , and Kuppa. M. R. , International Journal of Research and Reviews in Ad Hoc Networks **1**, (2011).

[4] Breiman. Leo, Machine Learning. **45**, 5 (2001).

[5] Mohamed. W. N. H. W., Salleh. M. N. M., and Omar. A. H., 2012 IEEE International Conference on Control System, Computing and Engineering, A comparative study of Reduced Error Pruning method in decision tree algorithms, **392** (2012).

[6] Oliynyk. Anton O, Antono. Erin, Sparks. Taylor D, Ghadbeigi. Leila, Gaultois. Michael W, Meredig. Bryce, and Mar. Arthur, Chemistry of Materials **28**, 7324 (2016).

[7] Carr. D. Andrew, Lach-hab. Mohammed, Yang. Shujiang, Vaisman. Iosif I, and Blaisten-Barojas. Estela, Microporous and Mesoporous Materials **117**, 339 (2009).

[8] Japkowicz. Nathalie, and Stephen. Shaju, Intelligent Data Analysis **6**, 429 (2002).

[9] X Ling. Charles and Sheng. Victor, Encyclopedia of Machine Learning, 2010.

[10] Witten, I.H., and Frank, E. 2005. Data Mining − Practical Machine Learning Tools and Techniques with Java Implementations. Morgan Kaufmann Publishers.

[11] There are 25 predicted new DPs, leaving out the rather atypical cases of Pd and Pt based compounds, which showed highly distorted structures.

[12] P. E. Blöchl, Phys. Rev. B **50**, 17953 (1994).

[13] A. Halder, D. Nafday, P. Sanyal and T. Saha-Dasgupta, npj Quantum Materials **3**, 17 (2018).

[14] C. De, Á. M. Arévalo-López, F. Orlandi, P. Manuel, J.P. Attfield and A. Sundaresan, Angew. Chem. Int. **57**, 16099 (2018).

[15] John P. Perdew, J. A. Chevary, S. H. Vosko, Koblar A. Jackson, Mark R. Pederson, D. J. Singh, and Carlos Fiolhais , Phys. Rev. B **48**, 4978(E) (1993).

[16] G. Kresse and J. Hafner, Phys. Rev. B **47**, R558 (1993), G. Kresse and J. Furthmueller, Phys. Rev. B **54**, 11169 (1996).

[17] P. Blaha, K. Schwarz, G. K. H. Madsen, D. Kvasnicka, and J. Luitz, WIEN2k, An Augmented Plane WaVe + Local Orbitals Program for Calculating Crystal Properties; Technische Universitat Wien: Wien, Austria, 2001.

[18] V. I. Anisimov, F. Aryasetiawan and A. I. Liechtenstein, J. Phys. Condens. Matter **9**, 767 (1997).

[19] D.D. Sarma, P. Mahadevan, T. Saha Dasgupta, S. Ray, A. Kumar, Phys. Rev. Lett. **85**, 2549 (2000).

[20] B. T. Matthias, R. M. Bozorth, J. H. Van Vleck, Phys.Rev. Lett. **7**, 160 (1961).

[21] P. K. Baltzer, H. W. Lehmann, M. Robbins, Phys. Rev.Lett. **15**, 493 (1965).

[22] M. A. Subramanian, A. P. Ramirez, W. J. Marshall, Phys.Rev. Lett. **8**, 21558 (1999).

[23] A. Wold, R. J. Arnott, J. B. Goodenough, J. Appl. Phys. **29**, 387 (1958).

[24] H. Das, U. V. Waghmare, T. Saha-Dasgupta, and D. D. Sarma, Phys. Rev. B **79**, 144403 (2009).

[25] V. L. Joseph Joly, Y. B. Khollam, P. A. Joy, C. S. Gopinathand S. K. Date, J. Phys. Condens. Matt. **13**, 11001 (2001).

[26] S Baidya and T Saha-Dasgupta, Phys. Rev. B **84**, 035131 (2011).

[27] The insulating nature of DOS described in the text, has been confirmed in both GGA+U and GGA+U+SOC calculations.

[28] R. Seshadri, C. Martin, M. Hervieu, B. Raveau, C. N. R. Rao. Chemistry of Materials **9**, 270 (1997).

[29] Y. Yoshida, I. Nagai, S. I. Ikeda, N. Shirakawa, M. Kosaka and N. Mori, Physical Review B, **69**, 220411 (2004).

[30] A. C. Komarek et al. Phys. Rev. Lett. **101**, 167204 (2008).

[31] https://materialsproject.org/materials/mvc-5855/

[32] https://materialsproject.org/materials/mvc-5820/

[33] https://materialsproject.org/materials/mvc-11828/

[34] https://materialsproject.org/materials/mvc-5055/

[35] https://materialsproject.org/materials/mvc-5090/

[36] Y. Yahua, High-Pressure Synthesis, Crystal Structures, and Magnetic Properties of Perovskite-Related Os and Ir Oxides, Doctor of Science, Graduate School of Chemical Sciences and Engineering,Hokkaido University, (2015).

[37] V. Pardo and W. E. Pickett, Phys. Rev. B **80**, 054415 (2009).

Chapter 7

Conclusion

7.1 Summary

In this thesis, we have investigated the structural as well as the microscopic origin of different exciting and facinating properties of double perovskites which is a special class of transition metal oxides. As discussed in chapters 3 - 6, our studied double perovskite compounds can be divided into two broad categories, namely (i) known double perovskite compounds which are already synthesized, and (ii) yet to be synthesized double perovkites. In order to have microscopic understanding of the properties of known double perovskites, we have mainly used density functional theory and first-principles derived model Hamiltonians which have been solved by using techniques likes Monte Carlo (MC) and exact diagonalization (ED). For the study on unknown double perovskites, we have used genetic algorithm to determine the crystal structure of the unknown double perovskite compounds, while first principles calculations and finite temperature model Hamiltonian study have been used to predict their properties. We used machine learning algorithm to screen the stable double perovskite compounds from a large number of possible combinations.

In this chapter we summarize the main conclusions of our study. Following which we discuss the future directions.

7.1.1 Chapter 3 : Magnetism in Sr_2CrMoO_6 : A Combined Ab-initio and Model Study

In this chapter, we have investigated the microscopic origin of magnetism of Sr_2CrMoO_6 (SCMO) which can be considered as a sister compound of much discussed double perovskite Sr_2FeMoO_6 (SFMO). We used a combination of density functional theory and first-principle derived model Hamiltonian approach. We also used dynamical mean field theory (DMFT) along with density functional theory to capture the correlated nature of the electrons. The main findings are:

- The spin-polarized density of states calculated in plane wave basis on pure, defect-free SCMO shows that like SFMO [1], SCMO is a half-metallic ferromagnet. The main difference between the electronic structure of SCMO and SFMO is the hybridization between B t_{2g} and B$^{'}$ t_{2g} which is found to be reduced in SCMO compared to SFMO.

- The calculated spectra from DMFT also confirms the robustness of the half-metallic behaviour of SCMO upon inclusion of dynamical correlation effect. The presence of lower, upper Hubbard bands and quasiparticle peak in the spectrum indicate the dual nature of the Mo electrons having both, a local spin moment and itinerant behavior.

- The origin of magnetism in SCMO turns to be somewhat different than in SFMO. [2] The charge transfer energy between Cr and Mo in SCMO is found to be larger than that between Fe and Mo in SFMO. This suppresses the effect of hybridization between B and B$^{'}$ sites in SCMO compared to SFMO and has two consequences: (i) the hybridization-driven (HD) mechanism for magnetism is reduced and (ii) a small but finite intrinsic moment develops at the Mo sites. The latter gives rise to a partial localized character of the Mo electrons, which was absent in SFMO. This in turn opens up a super-exchange (SE) contribution to magnetism in SCMO, which was absent in SFMO.

- The magnetic transition temperature (T_c), obtained through solution of the ab-initio derived model Hamiltonian by exact diagonalization, shows that estimated T_c in SCMO to be similar to measured T_c only if one includes both super-exchange and hybridization-driven contribution.

7.1.2 Chapter 4 : Magnetism in Cation Disordered 3d-4d/5d Double Perovskites

In this chapter, we have considered a variety of $3d-4d/5d$ DP compounds which have been reported to exhibit magnetic transition temperatures ranging from $\approx$ 200 K - $\approx$ 800 K [3] and investigated the effect of B/B$^{'}$ cation disorder (antisite disorder) on magnetic properties employing exact diagonalization-Monte Carlo (ED-MC) solution of the first-principles drivered model Hamiltonian. The major findings are:

- The influence of B cation anti-site disorder on their magnetic properties crucially depends on the mechanism of magnetism, being distinctly different for solely double exchange driven or combined superexchange-double exchange driven.

- The magnetic behaviour is far less susceptible to disorder for hybridization-driven magnetism (compounds like Sr_2FeMoO_6, Sr_2CrWO_6, Sr_2CrMO_6, Ca_2CrWO_6), while its effect is severe for compounds in which super-exchange becomes operative (compounds like Sr_2CrReO_6, Sr_2CrOsO_6).

- Further magnetic properties noticeably depend on the nature of disorder. Uncorrelated or random disorder affects magnetism severely, especially when super-exchange is present whereas correlated disorder with high degree of short range order retains to a large extent the magnetic properties of the fully cation ordered case.

- This provides a natural solution to the puzzle of unexpected magnetic ordering found in fully cation disordered $Sr_2Cr_{0.5}Ru_{0.5}O_3$. [4] The driving mechanism of magnetism operative in the fully ordered counterpart of compound is found to be combined double exchange and superexchange driven, hence magnetic ordering vanishes in case of 50% random disorder whereas it sustains only in the case of correlated disorder. This strongly suggests that despite of long range ordering as reported in the mentioned compound, magnetic ordering is preserved due to high degree of local ordering as in case of SFMO [5].

7.1.3 Chapter 5 : Computer Predictions on Rh-based Double Perovskites with Unusual Electronic and Magnetic Properties

In this chapter, we have predicted six yet-to-synthesized Rh based magnetic double perovskites, namely $Sr(Ca)_2BRhO_6$, where B is Cr or Mn or Fe. We have used a combination of computational algorithm for this purpose, which involves evolutionary crystal structure predictor, density functional theory and finite temperature Monte Carlo simulation of DFT derived spin model. The major findings of this study are as follows:

- The larger size of Sr^{2+} compared to Ca^{2+} drives the tolerance factor $t \geq 1$ for Sr based compounds and < 1 for Ca compounds. This makes non-perovskite structures possible candidates for Sr based compounds which is found to be a strongly competing phase along with perovskite phases like $R\bar{3}$ for Sr_2CrRhO_6 and Sr_2FeRhO_6, and $I4/m$ for Sr_2MnRhO_6. For all Ca-based compounds, on the otherhand low-energy structures are predicted to be of perovskite-based $R\bar{3}$ symmetry.

- Our calculated electronic structure shows that in Sr_2BRhO_6 compounds perovskite structure gets favoured over non-perovskite, dictated by change of nominal valence at B/Rh sites from 4+/4+ to 3+/5+. Very interestingly,

we found that that 3+/5+ scenario is favored for choice of Hubbard U parameter at B site U_B, beyond a critical value $U_B^{critical}$.

- The unusual valence of Rh^{5+} gets stabilized through U_B-assisted change in the position of B d level, thereby destabilizing O p levels, effecting the Rh-O covalency, and creating oxygen ligand hole.
- While the Cr-Rh and Mn-Rh compounds are predicted to be ferromagnetic half-metals, the Fe-Rh compounds are found to form rare examples of antiferromagnetic metals with magnetic transition temperatures above 100 K for most compounds.
- Analysis of the favourable growth conditions from consideration of the formation enthalpies of the predicted compounds and their competing phases, indicates that high temperature and low partial pressure of oxygen may promote the synthesis of predicted materials.

7.1.4 Chapter 6 : Machine-learning Assisted Prediction of Magnetic Double Perovskites

In the last chapter, we have combined the techniques of machine learning with quantum-chemical calculations to predict new double perovskite compounds. We have created a dataset from known literature of double perovskite compounds and each of the compounds (called instances), characterized by a choice of attributes, have been used to train the algorithm. Our dataset contains about 641 double perovskites, of which 115 have Ca at A site, 224 are Sr based and 302 are Ba based. After data preprocessing and attribute selection, we have built a model using Random forest algorithm. The model was used in making prediction of possible new double perovskites. Finally, using computational tools like density functional theory together with techniques of genetic algorithm to characterize the crystal structure, the electronic and magnetic properties of the predicted compounds have been studied. The main findings are

- 33 B/B′ combinations show high chance of being stablilized in double-perovskite structure, out of which 25 was chosen for the next stage of investigation.
- The predicted crystal structure using evolutionary algorithm shows that most of the compounds into $P2_1/n$ symmetry, the other space groups are R-3, Fm-3m, I2/m, I4/m, I4/mmm, R3.
- Our analysis finds 7 FM half-metallic, 6 FiM insulating, 5 AFM insulating, 2 FM metallic, 1 AFM metallic and 4 NM insulating double-perovskites.

7.2 Outlook

- **Effect of disorder on magnetotransport property:** Some double perovskites like Sr_2FeMoO_6 exhibit high ferromagnetic transition temperature, half metallicity and large low field magnetoresistance. Experimental results in few cases pointed out that magnetoresistance decreases with the increase of antisite disorder, [6] whereas others indicated an increment. [7] Theoretical study by P. Majumdar et al. [8] showed that the double perovskite compounds with magnetisation driven by hybridization driven mechanism, moderate amount of correlated antisite disorder slightly affects T_c but can adequately increase the low field magnetoresistance. So as an extension of our work we plan to investigate the effect of antisite disorder on magnetoresistance in the compounds where superexchange contribution is present along with hybridization driven mechanism.

- **Prediction of more Rh-based double perovskites:** In chapter 5, we have predicted six Rh based double perovskites, four of which are predicted to be half metallic ferromagnet and rest two are rare example of antiferromagnetic metals. To predict new double perovskite with such exotic property, we wish to extend our study in this series of Rh based double perovskite compounds. In particular we want to focus on four yet to be synthesized compositions with B sites occupied by very late $3d$ transition metals like Co and Ni, namely Sr_2NiRhO_6, Sr_2CoRhO_6, Ca_2NiRhO_6 and Ca_2CoRhO_6. These compounds are way more complex with respect to previously discussed Rh based compounds in terms of increased charge transfer with possible stabilization of 2+/6+ valances of B/Rh in contrast to 3+/5+ found in other six Cr, Mn and Fe based Rh double perovskites. Also possible effect of JT distortions need to be studied carefully.

- **Prediction of new rare earth based permanent magnet using machine learning algorithm :** Search for high performance permanent magnets is everlasting due to their potential applications in different fields. The quality of a permanent magnet depends on a) high spontaneous or saturation magnetization M_s with high remanence, b) high Curie temperature T_c, c) strong uniaxial magneto-crystalline anisotropy which offers high coercitivity, and d) thermodynamic stability. [9] On the basis of the above criteria, rare earth transition metal inter-metallics are ideal candidate for modern permanent magnets. It is generally consist of $3d$ transition metal M (offers high saturation magnetization as well as high curie temperature), and rare earth element R (responsible for strong magnetocrystalline anisotropy as a result of spin-orbit interaction (SOC) in $4f$ electrons of rare earth elements). It is seen that performance of a magnet strongly depends on the proportion of rare earth and transition metal. With the increase of rare earth

concentration, although coercivity increases but there is reduction in magnetic moment, as the $4f$ magnetic moment cancels the magnetic moment of $3d$ transition metals. There are huge number of materials belong to this family as it is seen that more than 10 intermetallics can be obtained from the combination of a single rare earth element and one transition metal. The rare-earth intermetallic compounds can be classified mainly in three categories: binary compounds, interstitial compounds and multicomponent systems. [10] The series of binary compounds having different compositions are R_3M, R_7M_3, R_4M_3, RM, RM_2, RM_3, R_2M_7, R_6M_{23}, RM_5, RM_{12}, RM_{13}, R_2M_{17}. Interstitial intermetallic compounds are those in which small nonmetallics atoms are placed in the interstitial region of the elemental or host intermetallic compounds to fill the void space without replacing the metal atoms. [11] Though interstitial modification provides high saturation magnetization with high Curie temperature but it suffers from thermodynamical stability. Presence of another non magnetic transition metal ion (Ti, V, Nb, Mo, Ta, W) in multicomponent rare-earth intermetallic compounds provides structural stabilization in cost of reduction of saturation magnetization. So the search for a suitable candidate in terms of above mentioned charectaristics is a challenge for making new permanent magnets. Machine learning algorithm can help us to overcome this problem, as it can find out the underlying pattern from the existing intermetallic compounds and therfore the trained model can find out the correct combination for an ideal magnet.

Bibliography

[1] K.-I. Kobayashi, T. Kimura, H. Sawada, K. Terakura, and Y. Tokura, Nature (London) **395**, 677 (1998).

[2] D.D. Sarma, P. Mahadevan, T. Saha Dasgupta, S. Ray, A. Kumar, Phys. Rev. Lett. **85**, 2549 (2000).

[3] T. K. Mandal, C. Felser, M. Greenblatt and Jrgen Kbler, Phys. Rev. B **78**, 134431 (2008).

[4] J. A. Rodgers, A. J. Williams, M. J. Martinez-Lope, J. A. Alonso and J. P. Attfield, Chem Mater **20** 4797 (2008).

[5] C. Meneghini, Sugata Ray, F. Liscio, F. Bardelli, S. Mobilio, and D. D. Sarma Phys. Rev. Lett. **103**, 046403 (2009).

[6] J. Navarro, L. Balcells, F. Sandiumenge, M. Bibes, A. Roig, B. Martnez and J. Fontcuberta, J. Phys.:Condens. Matter, **13**, 8481 (2001).

[7] Y. H. Huang, H. Yamauchi and M. Karppinen, Phys.Rev. B, **74**, 174418 (2006).

[8] V. N. Singh and P. Majumdar, Europhysics Letters, **94**, 47004 (2011).

[9] Takashi Miyake, and Hisazumi Akai, J. Phys. Soc. Jpn. **87**, 041009 (2018).

[10] H. H. Stadelmaier Intermetallics for Permanent Magnets IEEE transactions on magnetics, **29**, 6 (1993).

[11] Fujii, H., M. Akayama, K. Nakao and K. Tatami, J. Alloys Comp. **10**, 219 (1995).